NUREG/CR-6623

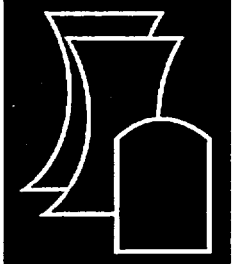

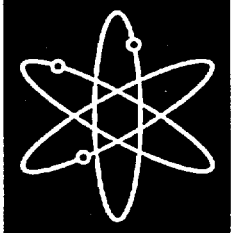

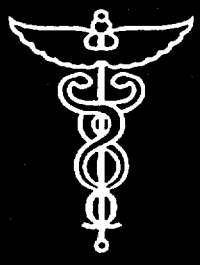

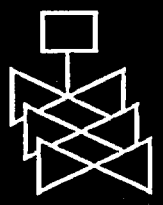

Vapor Explosions in a One-Dimensional Large-Scale Geometry With Simulant Melts

University of Wisconsin - Madison

U.S. Nuclear Regulatory Commission
Office of Nuclear Regulatory Research
Washington, DC 20555-0001

AVAILABILITY NOTICE

Availability of Reference Materials Cited in NRC Publications

NRC publications in the NUREG series, NRC regulations, and *Title 10, Energy,* of the *Code of Federal Regulations,* may be purchased from one of the following sources:

1. The Superintendent of Documents
   U.S. Government Printing Office
   P.O. Box 37082
   Washington, DC 20402–9328
   <http://www.access.gpo.gov/su_docs>
   202–512–1800

2. The National Technical Information Service
   Springfield, VA 22161–0002
   <http://www.ntis.gov/ordernow>
   703–487–4650

The NUREG series comprises (1) brochures (NUREG/BR-XXXX), (2) proceedings of conferences (NUREG/CP-XXXX), (3) reports resulting from international agreements (NUREG/IA-XXXX), (4) technical and administrative reports and books [(NUREG-XXXX) or (NUREG/CR-XXXX)], and (5) compilations of legal decisions and orders of the Commission and Atomic and Safety Licensing Boards and of Office Directors' decisions under Section 2.206 of NRC's regulations (NUREG-XXXX).

A single copy of each NRC draft report is available free, to the extent of supply, upon written request as follows:

Address: Office of the Chief Information Officer
Reproduction and Distribution
Services Section
U.S. Nuclear Regulatory Commission
Washington, DC 20555–0001
E–mail: <DISTRIBUTION@nrc.gov>
Facsimile: 301–415–2289

A portion of NRC regulatory and technical information is available at NRC's World Wide Web site:

<http://www.nrc.gov>

All NRC documents released to the public are available for inspection or copying for a fee, in paper, microfiche, or, in some cases, diskette, from the Public Document Room (PDR):

NRC Public Document Room
2120 L Street, N.W., Lower Level
Washington, DC 20555–0001
<http://www.nrc.gov/NRC/PDR/pdr1.htm>
1–800–397–4209 or locally 202–634–3273

Microfiche of most NRC documents made publicly available since January 1981 may be found in the Local Public Document Rooms (LPDRs) located in the vicinity of nuclear power plants. The locations of the LPDRs may be obtained from the PDR (see previous paragraph) or through:

<http://www.nrc.gov/NRC/NUREGS/SR1350/V9/lpdr/html>

Publicly released documents include, to name a few, NUREG-series reports; *Federal Register* notices; applicant, licensee, and vendor documents and correspondence; NRC correspondence and internal memoranda; bulletins and information notices; inspection and investigation reports; licensee event reports; and Commission papers and their attachments.

Documents available from public and special technical libraries include all open literature items, such as books, journal articles, and transactions, *Federal Register* notices, Federal and State legislation, and congressional reports. Such documents as theses, dissertations, foreign reports and translations, and non-NRC conference proceedings may be purchased from their sponsoring organization.

Copies of industry codes and standards used in a substantive manner in the NRC regulatory process are maintained at the NRC Library, Two White Flint North, 11545 Rockville Pike, Rockville, MD 20852–2738. These standards are available in the library for reference use by the public. Codes and standards are usually copyrighted and may be purchased from the originating organization or, if they are American National Standards, from—

American National Standards Institute
11 West 42nd Street
New York, NY 10036–8002
<http://www.ansi.org>
212–642–4900

NUREG/CR-6623

Vapor Explosions in a One-Dimensional Large-Scale Geometry With Simulant Melts

Manuscript Completed: October 1999
Date Published: October 1999

Prepared by
H.-S. Park, R. Chapman, M.L. Corradini

University of Wisconsin - Madison
1500 Engineering Drive
Madison, WI 53706

S. Basu, NRC Project Manager

Prepared for
Division of Safety Analysis and Regulatory Effectiveness
Office of Nuclear Regulatory Research
U.S. Nuclear Regulatory Commission
Washington, DC 20555-0001
NRC Job Code W6183

Abstract

In light water reactors after a prolonged lack of cooling, vapor explosions could occur when molten fuel is generated and contacts residual water coolant within the reactor vessel or below in the containment reactor cavity. The experimental objectives for this work were to obtain well-characterized data for the explosion propagation/escalation phases, while systematically investigating the effect of a comprehensive set of initial and boundary conditions on the explosion energetics; i.e., trigger strength, fuel mass, composition and temperature, coolant mass, viscosity and temperature and system constraint. First, a vapor explosion apparatus, WFCI, was developed which allowed for well-characterized explosion data and demonstrated reproducible explosions with a simulant fuel. Second, the explosion energetics was examined as a function of varying initial and boundary conditions for this tin simulant. Finally, the simulant fuel was changed to a molten iron-oxide, which was more prototypic of the actual molten fuel compositions and explosion energetics were reexamined and FCI were found to be quite weak.

With respect to reactor safety issues, this experimental work has quite important safety implications. First, this work has provided clear evidence of the reproducibility of vapor explosion energetics for a controlled set of initial and boundary conditions. This suggests empirically that this phenomenon is predictable if one can establish and control the initial and boundary conditions. Second, the experiments demonstrate that geometric scaling can be properly specified; e.g., a rigid radial constraint for one-dimensional tests is conservative for energetics when compared to full-scale, while the axial constraint scale factor from test to prototype needs to be unity to preserve energetics. Finally and most importantly, the data suggests that once the fuel-coolant initial conditions are within an envelope for triggered events, the energetics is much less than thermodynamic, apparently due to the small amount of fuel that participates in an explosion timescale. And this envelope of triggerability is much smaller for a simulant molten oxide with low superheat, such as molten iron-oxide in our tests (corium in the KROTOS tests). This suggests that material scaling for reactor safety issues must preserve the same fuel composition and superheat from the test to the prototype.

The current work has limited data at larger scales with more prototypic molten oxides. It is recommended that further tests could be carried out under these conditions to empirically verify our findings. Models developed from our analysis can also be used to analyze these experiments. Finally, it is known that the mixing conditions determine the envelope of explosivity for the vapor explosion. Thus, it is of fundamental interest to better measure the mixture local conditions just prior to the explosion to correlate with the explosion energetics; i.e., void fraction profiles, fuel volume fractions and mixing diameters. Our future work in vapor explosion research is specifically targeted toward this purpose.

Contents

List of Figures

List of Tables

EXECUTIVE SUMMARY

Vapor explosions have occurred in various industrial processes following some accidental contact of a hot liquid with a cold more volatile liquid. In light water reactors after a prolonged lack of cooling, this process could occur when molten fuel is generated and contacts residual water coolant within the reactor vessel or below in the containment reactor cavity. Past studies have demonstrated the explosive nature of certain liquid pairs, but have not systematically examined explosion energetics at larger scales as a function of controlled initial and boundary conditions. This has hampered basic understanding and has been a major deficiency in the database for modelling purposes. Without such a systematic study one cannot verify the interrelationships between competing effects on explosion energetics, given a specific set of initial and boundary conditions.

Our objectives for this work were to obtain well-characterized data for the explosion propagation/escalation phases, while systematically investigating the effect of a comprehensive set of initial and boundary conditions on the explosion energetics; i.e., trigger strength, fuel mass, composition and temperature, coolant mass, viscosity and temperature and system constraint. This objective was subdivided into three specific stages. First, a vapor explosion apparatus, WFCI, was developed which allowed for well-characterized explosion data and demonstrated reproducible explosions with a simulant fuel. Second, the explosion energetics was examined as a function of varying initial and boundary conditions for one simulant fuel composition. Finally, the simulant fuel was changed from a metal to a molten oxide, which was more prototypic of the actual molten fuel compositions and explosion energetics were reexamined.

The experimental investigation was subdivided into smaller test series to better understand specific vapor explosion mixing and propagation behavior. First, a series of experiments were performed to demonstrate the reproducibility of the explosion phenomena with molten tin as the fuel simulant. Initial conditions similar to the KROTOS-21 experiment were chosen as the nominal case for these tests, for comparison to independent data. The explosion behavior in the WFCI facility showed good reproducibility and agreement with KROTOS-21. Dynamic pressures had peak values of 10 MPa and quasi-steady values of 2-3 MPa, while explosion propagation speeds were about 200 m/s. The explosion conversion ratios were about 0.2 to 0.5 percent. The next three test series investigated the effect of the external trigger on the vapor explosion; i.e., spontaneous explosions and triggered explosions with specific impulse strengths. The tests showed that as the external trigger was reduced and then eliminated, multiple propagation events occurred during the explosion. The energetics of the complete interaction was relatively independent of trigger strength, but the detailed behavior of propagation process became more complex with spontaneous triggers. Once the trigger strength exceeded 3 MPa no multiple propagation events were observed and single propagation events of similar energetics were observed.

The next test series investigated the effect of axial constraint. The WFCI facility was originally designed with a rigid radial constraint to maximize the energetics for any given

set of mixing conditions, but the axial constraint could be varied. The axial constraint was varied by changing the slug mass in the horizontal expansion tube by an order of magnitude. Results indicated that there was an optimal degree of axial constraint to maximize explosion energetics. This could be explained by the competing effects of rapid vapor production during the propagation and quenching in surrounding coolant liquid as the explosion mixture expands. This effect suggests that the actual axial constraint needs to be used in tests when considering reactor safety issues.

The sixth and seventh test series investigated the effect of the fuel and coolant temperatures on energetics. The results indicated that once the fuel temperature was above a threshold value its effect on energetics was of second-order importance. The same result was noted for a variation in the coolant temperature. This suggests that if the fuel and coolant temperature are large enough to satisfy the qualitative requirements of a molten fuel and stable film boiling at the time of triggering, then an energetic explosion can result, with temperature having a small quantitative effect within this envelope of conditions. This should be scale independent and KROTOS tests also suggest this based on the scale for KROTOS-21 and for compositions with alumina fuels. This is also consistent with the lack of energetics from our later observations in iron-oxide tests as well as the KROTOS corium tests.

The eighth test series was performed to investigate the suppression effect of polymer additives by an increase in the coolant viscosity. Polymer additives suppressed spontaneous vapor explosions in this larger scale geometry in qualitative agreement with past small scale tests. This was the first time that explosion suppression was demonstrated at relatively large scale. Also, the post-test fuel debris generated in the absence of the explosion may be quite representative of the fuel debris during the mixing process. This experimental technique should be considered as useful for subsequent fuel-coolant mixing studies.

In the ninth series the fuel jet diameter and the timing of the external trigger were altered to vary the ratio of coolant mass to fuel mass in the mixture at the time of the explosion. Varying this mass ratio of coolant to fuel indicated that the explosion conversion ratio exhibited a broad maximum in energy conversion. These values were more than an order of magnitude lower value than one predicts from ideal thermodynamic situations. Analysis again indicated that the broad maximum is created by competing effects related to the development of the fuel-coolant mixture prior to triggering. The location of this maximum relative to mass ratio is secondary to its qualitative existance. However, the value of this coolant to fuel ratio can be understood relative to mixing kinetics. The small energy conversion ratio can only be explained by the observation that only a few percent of the fuel mass fragments into small enough debris (<0.1mm) to directly participate in explosion timescales. This conclusion is applicable for all of our test data and seems to be scale independent, and thus, has important implications for reactor safety issues.

Finally, in the tenth test series, the effect of changing the fuel composition from molten tin to a more prototypic simulant (iron-oxide) was observed. These tests indicated that the triggering of energetic fuel-coolant interactions with more prototypic fuel materials and superheats was quite difficult and no propagating vapor explosions were observed. This

observation is consistent with those of JRC staff and their corium tests in KROTOS at atmospheric pressures in which weak vapor explosions were observed.

With respect to reactor safety issues, this experimental work using fuel simulants has yielded a number of results that have potentially quite important safety implications. First, this work has provided clear evidence of the reproducibility of vapor explosion energetics for a controlled set of initial and boundary conditions. This suggests empirically that this phenomenon is predictable if one can establish and control the initial and boundary conditions. Second, the experiments demonstrate that geometric scaling can be properly specified; e.g., a rigid radial constraint for one-dimensional tests is conservative for energetics when compared to full-scale, while the axial constraint scale factor from test to prototype needs to be the unity to preserve energetics. Finally and most importantly, the data suggests that once the fuel-coolant initial conditions are within an envelope for triggered events, the energetics is much less than thermodynamic, apparently due to the small amount of fuel that participates in an explosion timescale. And this envelope of triggerability is much smaller for a simulant molten oxide with low superheat, such as molten iron-oxide in our tests or corium in the KROTOS tests. This suggests that material scaling for reactor safety issues must preserve the same fuel composition and superheat from the test to the prototype.

The current work has limited data at larger scales with more prototypic molten oxides; i.e., larger fuel volumes than 0.5 liters, larger chamber geometries, prototypic molten oxide compositions and superheats. It is recommended that further tests could be carried out under these conditions to empirically verify our findings. Models developed from our analysis can also be used to analyze these experiments. Finally, it is known that the mixing conditions determine the envelope of explosivity for the vapor explosion. Thus, it is of fundamental interest to better measure the mixture local conditions just prior to the explosion to correlate with the explosion energetics; i.e., void fraction profiles, fuel volume fractions and mixing diameters. Our future work in vapor explosion research is specifically targeted toward this purpose.

Acknowledgements

The support from the U.S Nuclear Regulatory Commission under contract for this work is gratefully acknowledged. In particular the suggestions by Dr. Sudhamay Basu have been quite helpful. In addition, the authors wish to express their gratitude to the JRC research staff, in particular, Drs. H. Hohmann, D. Magallon, A. Yerkess, A. Annunziato and I. Huhtiniemi for fruitful discussions. Much of this report could not have been done without the help of Dr. Rosa Marina Bilbao and her detailed knowledge of the NSRC computer systems.

Nomenclature

A	Area
A_m	Fuel volumetric surface area
Bo	Bond number
C_D	local drag coefficient
C_f	local friction factor
C_o	Drift flux coefficient or Proportionality constant
CR	Conversion Ratio
D_{fo}	Initial fuel diameter
D_h	Hydraulic diameter
D_{po}	Pouring diameter
DSE	Delayed spontaneous vapor explosion
E	Thermal energy
ESE	Early spontaneous vapor explosion
F	Compensation factor for the fragmentation time
F_r	Fragmentation rate
H_c	Depth of coolant pool
H(t)	Heaviside function
Ja	Jacob number, $C_p \frac{\Delta T}{h_{lv}}$
J_v	Volumetric vaporization rate
MW_t	Thermal Mega-Watt Power
NE	No vapor explosion
N_p	Number of fuel particle
N_{fr}	Number of fuel fragments
P	Pressure
$\dot{Q}$	Heat transfer rate
R_{vi}	Transfer coefficient between the vapor and vapor-liquid interface
R_{ci}	Transfer coefficient between the coolant and coolant-liquid interface
R_f	Final radius of the fuel after mixing occurred
Ra	Rayleigh number, $\frac{gD^3\Delta\rho}{\nu_v \alpha_v \rho_v}$
S	Surface Area
SE	Spontaneous vapor explosion
T	Temperature
TE	Triggered vapor explosion
ΔT_{sub}	Degree of subcooling
U	Velocity
U_r	Relative velocity
V_f	Initial volume of the fuel mass to be mixed
V_{jet}	Average coolant jet velocity

We	Weber number or Mechanical equilibrium work of the bubble
c_f	Specific heat of fuel
c_p	Constant pressure specific heat
e	Internal Energy
f_d	The fraction of the fragmentation debris energy
f_r	Enhancement factor
g	Gravity constant
h	Overall heat transfer coefficient
$h_{c,sat}$	Heat transfer coefficient of the coolant
h_{gb}	Heat transfer coefficient with a gas blanket
h_{ff}	Heat transfer coefficient with a finite fragmentation rate
h_{qss}	Quasi-steady-state heat transfer coefficient
$h_{v,sat}$	Heat transfer coefficient of the vapor at saturated condition
i	Enthalpy
i_{fg}	Latent heat of Vaporization
i_{fus}	Heat of fusion
i_{rc}	Heat of reaction
k	Thermal conductivity
m	Fuel mass
$\dot{m}_{fr}$	Fuel fragmentation rate
$\dot{m}_v$	Vapor generation rate
q''_d	Heat flux from the fuel droplet
q''_{CHF}	Critical heat flux
$\dot{q}_{net,f}$	Net heat transfer from the fuel to vapor and coolant
$\dot{q}_{frag}$	Net heat transfer from the fragmented fuel to generate vapor
r_d	Fuel drop radius
t^*_b	Dimensionless break-up time
t_{lag}	Lag time
t_{mix}	Mixing time
t_m	Fragmentation or mixing time
u	Velocity
v	Specific volume
x	Mass fraction
m/o	Mole fraction
w/o	Weight fraction

Greek

α	Volume fraction vapor
β	Constant, $(k_f \rho_f c_f / k_c \rho_c c_c)^{0.5}$
γ	Specific heat ratio
Γ_p	Surface area source due to primary break up
Γ_e	Surface area source due to surface entrainment
δ_b	Gas blanket thickness
μ	Viscosity
ρ	Density
σ	Surface tension

Superscript

min	Minimum
1	One-step

Subscript

a,∞	Ambient
c	Coolant
ch	Chamber
cr	Critical
cv	Interface between the coolant and vapor
e	Equilibrium
f	Fuel
fr	Fuel Fragment
g	Gas or vapor
hm	Homogeneous nucleation
i	Initial or interface
m, mlt	Melt
max	Maximum
min	Minimum
p	Fuel Particle
r	Relative
ref	Reference
sat	Saturate
sn	Spontaneous nucleation
sp	Specific
v	Vapor
vol	Volumatric

Chapter 1

Introduction

1.1 Background and Motivation

Consider the case of a hot liquid rapidly releasing its energy into a surrounding cold, volatile liquid under direct contact, with excessive amounts of vapor production. If this event occurs within a timescale short compared to vapor expansion, it can cause local pressurization similar to an explosion and threaten the surroundings by the subsequent high pressure vapor expansion. From a historical point of view, this process has occurred since man began to work with molten metals. Berman *et al.*[1] used the term "Thermal Explosion" to contrast it from a chemical explosion. Condiff[2] suggested the term "Thermal Detonation" as a self-sustaining thermal explosion involving propagating shock waves. In the nuclear industry, the terms, energetic " Fuel-Coolant Interaction (FCI)" and "Vapor Explosion", are widely used in severe accident safety analyses, since molten materials being considered are nuclear fuel and associated metals in the reactor core.

FCIs can be produced by different modes of contact, generally categorized in three different types as shown in Figure 1.1; *i.e.*, pouring mode, injection mode and stratified mode. In the pouring mode, the hot liquid enters into the cold liquid, the hot liquid breaks up into small fragments and is mixed with the cold liquid. In the injection mode, however, the cold liquid is injected into the hot liquid and can be vaporized within the hot liquid. In the stratified mode, one liquid is separated from the other due to density differences and by the vapor generated at the interface; i.e., both liquids exist as stratified layers.

In the nuclear industry, the vapor explosion phenomenon has been an issue in safety analyses for almost three decades. If a complete and prolonged failure of normal and emergency cooling systems in a nuclear reactor occurs, the reactor core could melt due to the fission product decay heat. There may be two possible modes of contact after the molten corium [1] is formed: the pouring and stratified modes of contact. In the pouring mode, the molten corium drops into the residual water coolant either inside or outside the reactor pressure vessel (RPV), and can result in energetic FCIs. The stratified mode, however, can be established during refilling of emergency water to the molten corium residing inside or outside the RPV. Experimental results[3] have suggested that the pouring mode of contact produces more energetic FCIs than the stratified mode of contact.

[1]Material formed after the core melt, which includes fuel, partially oxidized cladding material and structural material

After the contact between both liquids, a significant fraction of the thermal energy in the hot liquid is transferred into the cold liquid and in turn, converted into destructive mechanical energy due to the explosive vapor production and expansion. If the FCI thermal to mechanical work conversion is efficient, it may threaten the integrity of the containment by missile generation [2] or dynamic shock pressures, thereby leading to release of radioactive materials to the environment[5].

This type of explosive interaction has occurred in other industrial processes[6]; molten metal-water contact in the metal-casting industry[7], LNG (Liquefied Natural Gas) spilling over water during its transportation[8], leakage of cooling water onto molten salts, "smelt", in the paper industry[9], and lava flow into sea water[10].

A vapor explosion is a phenomenon which combines several different physical processes which occur in sequence. From several decades of research into the vapor explosion phenomenon, these phases have been conceptually identified as four different stages [11]: (1) Mixing, (2) Triggering, (3) Explosion propagation and (4) Expansion.

In the mixing phase, if a hot liquid pours into a cold liquid, the hot liquid is broken down into smaller sizes due to fragmentation processes as it interpenetrates the coolant; separated from the cold liquid by a stable vapor film (*i.e.*, the surface temperature of the hot liquid needs to be sufficient to maintain this film). In the triggering phase, if this metastable vapor film collapses locally due to a disturbance, very rapid heat transfer occurs due to the direct contact between the hot and cold liquid, and produces local high pressures due to the rapid vaporization process. This local explosion provides a trigger source to generate more fuel surface area and vapor generation in the adjacent mixture. These reactions produce a spatial propagation of the explosion as a shock wave passes through the melt-water mixture. With this shock passage in the mixture, fuel fragmentation and heat release occur near the shock front and reinforce the shock wave strength. During the expansion phase, high heat transfer rates from hot to cold liquid produce rapid vapor volume increases which may cause mechanical damage against the surrounding system constraint.

During a postulated severe accident in a light water nuclear reactor (LWR), vapor explosions may occur at two different locations; inside of the reactor pressure vessel, RPV (In-Vessel) and outside of the RPV (Ex-Vessel). For the case of the in-vessel vapor explosion, Theofanous *et al.*[12] estimated that an excessive explosion energy release could cause the RPV to rupture in the lower head region. In addition, a liquid slug is accelerated upward by the explosion expansion. Following some dissipation of energy as the slug passes through the upper internals, it impacts the RPV upper head and loads the head bolts. This may endanger the integrity of the containment since the vessel head (or portions of it) may become a missile with sufficient energy to penetrate the containment. There are other possible hazards from the vapor explosions that indirectly threaten containment: *e.g.*, the explosion causes fuel dispersal into the containment and generates dynamic pressures that could induce a local RPV wall failure, significantly altering melt entry into the containment.

[2]This specific sequence is termed α mode failure in WASH-1400 [4]

For an ex-vessel vapor explosion, the damage potential differs somewhat from an in-vessel event. Because the explosion occurs in a much larger volume, beneath the vessel in the LWR, the likelihood of direct containment failure due to missile generation is very small. In this case the major concern for an ex-vessel explosion centers on dynamic pressures produced in the water pool adjacent to the fuel-coolant mixture. If such pressures can be coupled to the containment pressure boundary or critical structures, then significant damage may occur. However, such a process is quite geometry dependent and is now being examined in safety studies.

In most accident situations for current LWRs, the pouring mode of contact is the predominant geometric condition, since fuel melting can only occur in the absence of water; thus requiring a pouring of fuel into coolant for the FCI to occur. Since the vapor explosion phenomenon is a highly transient, nonequilibrium and multi-phase problem, there are many difficulties in uncovering its basic mechanisms from either experimental or theoretical approaches. From an experimental point of view, numerous small scale experiments for investigating the fundamental mechanisms causing a vapor explosion have been carried out [13]. These experiments provided some ideas to develop better models of the basic mechanism of the vapor explosion [14, 15, 16].

1.2 Objectives and Scope

Attempting to explain large scale behavior using these small scale data, however, remains an issue since there is no well-defined scaling relationship for the vapor explosion process. In this context large scale experiments are defined as those in which spatial propagation occurs in the fuel-coolant mixture. The fuel mass is approximately equal to the coolant mass in the FCI with length scales much larger than the mixing length scale; *i.e.*, length scales much greater than 1cm and fuel masses greater than a kilogram. It is almost impossible to carry out prototypic scale experiments, with fuel masses in the tons. Because of these facts, many researchers have been working on developing more mechanistic models of the vapor explosion instead of building prototypic experimental facilities. In theory, using a computer model for parametric and sensitivity studies with controlled input data is easier than conducting a large scale experiment, if the computer models can be believed; i.e., verified and validated at different scales. However, in order to develop such models, at least some well-controlled larger scale experiments are required in which the initial and boundary conditions are known and the key dependent quantities are measured.

Such a situation provides the impetus for the present investigation of large scale vapor explosion phenomena under well-controlled experimental initial and boundary conditions. The main objectives of our present study are as follows:

1. to obtain well-characterized data for the explosion propagation/escalation phases using simulant fuel compositions,

2. to investigate the effect of particular initial and boundary conditions (*e.g.*, triggering, fuel mass, temperature and composition, coolant mass, temperature and additives as well as system constraint effects) on the explosion energetics and

3. to use well-understood methods of analysis to understand our experimental results.

In section two, previous experimental and theoretical studies are reviewed. These reviews support the necessity of this work and indicate its appropriate direction. The experimental facility designed for accomplishing the objectives is described in section three. The experiments are discussed in section four, and subdivided into a number of smaller test series to investigate specific initial and boundary conditions. The first four test series examine the reproducibility of the vapor explosion under well-controlled conditions, and the influence of an external trigger on the explosion behavior. The next test series determines the effect of the system constraint on the explosion energetics. The next four experiments demonstrate the effect of the fuel and coolant temperatures on FCI behavior as well as the ability to suppress the explosion with coolant additives. Finally, the fuel composition is changed to a more prototypic simulant, iron-oxide, to see its effect on explosion energetics. In section five, the discussion of the experimental results is presented, along with our supporting analyses. Finally, the conclusions for this work and recommendations are given in section six. Some detailed experimental data are presented in Appendices.

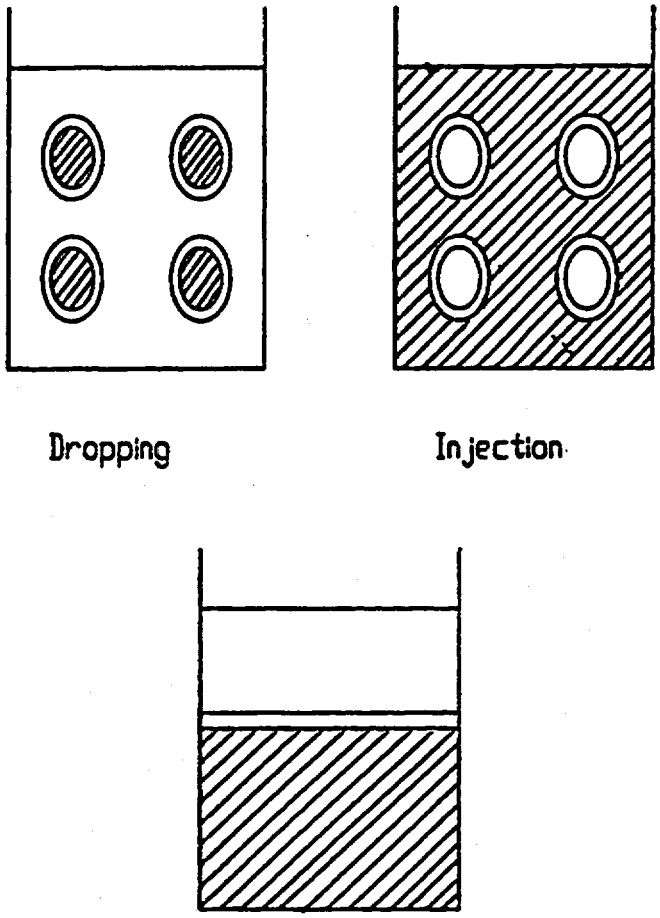

Figure 1.1: Typical Geometries of Fuel-Coolant Interactions

Chapter 2

Literature Review

2.1 Perspectives on Vapor Explosions

From 1950 to 1960, accidental pouring of molten materials [7, 17] into water resulted in energetic FCIs causing massive structural damage in the metal-casting industry. From the middle of the 1950's a new improved ingot continuous-casting method was introduced in the aluminum industry which cooled the hot metal very rapidly with water. Accidental contact of the water and molten aluminum also resulted in vapor explosions as the number of hazardous events increased. Such vapor explosion hazards have been noted in a number of other process industries over the last fifty years; *e.g.*, paper pulping, ferroalloys manufacturing, and liquified natural gas.

In the nuclear industry, several incidents associated with this phenomenon in test reactors were reported[18]; *e.g.*, BORAX-I (1954), SL-1 (1961), SPERT (1964), *etc.* One notable accident occurred at the SL-1 test reactor[18]. The SL-1 reactor was a 3 MWt aluminum clad-aluminum alloy fueled prototype natural circulation boiling water reactor. Rapid steam production caused a high pressure buildup which accelerated the body of the water upwards above the core. The water slug hit the vessel lid, collapsed the extension tube housings around the control rods and bulged the pressure vessel. A major reason for the destructive potential of this FCI was that a significant amount of the premixed aluminum melt was oxidized on this explosive timescale and this enormously increased the explosion yield.

In the 1970s, the vapor explosion process was intensively studied for the fast breeder reactor, in which uranium oxide and sodium were fuel and coolant, respectively. While research was continued on vapor explosions for the safety of the fast breeder reactor, a comprehensive risk assessment to estimate the likelihood of containment failure in Light Water Reactors (LWR) was conducted in 1975 and reported in WASH-1400[4]. This study focused on two specific reactor designs; the Surry PWR and the Peach Bottom BWR-Mark I. The hazard from a vapor explosion was considered in this assessment. It was determined that the containment could be threatened by three possible damage mechanisms; (a) dynamic liquid phase pressures on structures, (b) static overpressurization of the containment by steam production, and (c) solid missile generation from the impact of a liquid slug accelerated by the vapor explosion. In this analysis, the primary concern was a direct failure of containment caused by an energetic FCI causing missile generation (designated "α-mode" failure).

In WASH-1400, the possibility of a large-scale vapor explosion which would threaten the containment of a light-water reactor was estimated to be about 10^{-2} per reactor year with the likelihood of water availability and triggering of the explosion as the major uncertainties. Conservative results were obtained from this analysis because it was conducted under some bounding assumptions. Those assumptions were: first, all the fuel inventory in the core was melted and well-dispersed with half of the water in the lower plenum. Second, the remaining half of the water was above this fuel-coolant mixture when it exploded. And third, the piston of water was driven upwards through a clean vessel without internal structure and then impacted coherently on the top of the vessel.

Corradini *et al.* [19] developed a discretized Monte Carlo probablistic analysis to estimate the WASH-1400 vapor explosion failure mode with models for fuel-coolant mixing and explosion, *i.e.*, expansion work and associated dissipation and lower head failure models to estimate the α mode failure probability. Given a core melt, the probability of α mode failure was estimated to be less than 10^{-4} per reactor year. In 1985, in NUREG-1116[20], the Steam Explosion Review Group (SERG) estimated the probability of the α mode failure. This group of experts performed independent analyses and estimated that the conditional probability of the α mode failure was much less likely than in WASH-1400 ($10^{-2} \sim 10^{-4}$/yr as upper bound given a core melt). This group also recognized that these estimates were founded on the judgment that the amount of fuel-coolant mixture was limited and/or the explosion yield was less than the maximum thermodynamic values. Included in their findings was the consensus recommendation that fundamental experiments needed to be performed at larger scales to characterize fuel-coolant mixing and measure explosion yield as well as the effect of mixing on yield.

Theofanous *et al.* [12] performed a comprehensive analysis of α mode failure and found the upper bound value to be much lower than past estimates. Recently, Turland *et al.* [21] investigated a methodology for quantifying the conditional probability of the α mode failure in the Sizewell B PWR. They estimated that the probability was approximately 10^{-4} and the effect of the system pressure elevation on the probability of this mode of failure was modest. Theofanous *et al.* [22] updated their original risk assessment[12] and concluded that even vessel failure by vapor explosions might be regarded as physically unreasonable.

Almost ten years after SERG-1 the same group of experts convened in 1995 for SERG-2 [24, 23]. Their consensus opinion was that the probability of α mode failure was $<10^{-4}$ per reactor year given a core melt accident and was essentially resolved from a risk perspective. Other FCI issues were identified by the experts, specifically those that related to the energetics of vapor explosions and their impact on lower head failure and structural integrity. Further experimental research and associated analysis was recommended to address these issues.

This historical perspective on this phenomenon indicates that one needs to better understand the energetics of the explosion as a function of the initial and boundary conditions. Specifically, one needs to be able to correlate the expected energetics to variations in these conditions. There have been past experiments and analyses that could be examined with this purpose in mind. A comprehensive summary is presented below to aid the reader for

this particular purpose.

2.2 Past Vapor Explosion Studies

2.2.1 Large Scale Experiments

In this work, we provide the current status of large scale experiments and organize the data based on the research group as well as on various fuel simulants, *e.g.*, tin, salt, thermite, corium, *etc.*, for a pouring mode of contact. More comprehensive reviews for other topics have appeared in several review papers[5, 13, 25, 26, 27]. The review of small scale experiments is brief and limited to experiments performed with tin as the simulant fuel material.

2.2.1.1 Argonne National Laboratory

Recently, Spencer *et al.* [28] reanalyzed two experimental series, designated as CWTI[29] and CCM[30]. These experiments were performed in the COREXIT facility. The facility allowed for FCI studies of 1-10 kg of corium and consisted of a containment cell, the experimental apparatus, instrumentation, control systems, optical photography and flash X-ray as shown in Figure 2.1. The CWTI tests focused on FCIs occurring in the ex-vessel reactor cavity and the associated containment pressurization from high and low pressure melt ejections into the cavity region. The CCM tests were performed to investigate the coarse mixing and melt jet breakup for an in-vessel geometry. The detailed experimental conditions and results are summarized in Table 2.1. Major conclusions from the work were:

1. energetic FCIs did not occur in these tests, rather vigorous vapor generation during the FCI was observed under all circumstances;

2. the CWTI test series indicated that the presence of water exhibited a mitigative effect on containment pressurization for the range of initial conditions studied;

3. the CCM test series clearly showed that fuel jet breakup occurred at the leading edge of the jet as well as along its upstream surface due to hydrodynamic instabilities induced by relative velocity and vaporization.

The latter experimental observations were used in the development of the THIRMAL mixing model for the fuel-coolant interaction.

2.2.1.2 Winfrith

Four different series of large scale experiments were performed at Winfrith by Fry using corium thermite *et al.* [31], SUW[32], WUMT[33] and MIXA series[34, 35]. Both the SUW and WUMT series of experiments were conducted in the MFTF facility and MIXA in the MIXA facility.

The MFTF facility was a large pressure vessel with a volume of 1.7 m^3, equipped with the thermite charge container as shown in Figure 2.2. To release the melt from this thermite container, two different methods were applied; free and restricted release modes. In the free release mode, the melt was released freely into the surrounding water, and in the restrict release mode, the melt was constrained by an open catchpot and ejected with the end cap of the charge container.

The SUW series of experiments focused on the investigation of the effects of melt mass, ambient pressure and subcooling of water. A total of twelve tests in the SUW series were performed including nine tests with the melt mass of 24 kg and three tests with the melt mass of 8 kg as shown in Table 2.2. Spontaneous explosions and triggered explosions were observed in all the experiments, but two (SUW-02 and SUW-10). Some experiments were triggered by the impact of the catchpot on the bottom of the vessel; *i.e.*, impulsive trigger from this impact. Bird[32] observed in this series of tests that the conversion ratio tended to increase with decreasing water subcooling and increasing system pressure even though the likelihood of an explosive interaction decreased. Note that the unusual contact geometry makes these tests difficult to interpret for reactor safety considerations.

In the WUMT tests, 24 kg of melt was poured into water by gravity through a circular orifice with a diameter ranging from 40 to 100 mm. Two experiments produced a spontaneous explosion in water at 80 K subcooling and saturated water. As shown in Table 2.3, no explosive interactions occurred in any other tests. These tests provided little insight into explosion energetics.

In the MIXA series of tests, the facility was designed for studying the mixing phase of FCIs. In particular, the corium melt poured through a droplet former installed at the top of the mixing vessel, which produced various diameters of melt droplets before melt-water contact. In the MIXA series of tests, Denham *et al.* [34, 35] reported five experiments as shown in Table 2.3. Melt and water masses were about 3 kg and 80 kg respectively. There were no spontaneous explosions in any of these series of tests, even with water subcooled by 20 K.

2.2.1.3 Sandia National Laboratories

Fuel-coolant interaction data are available from many large scale experiments conducted by Sandia National Laboratories (SNL). These tests focused on estimating the FCI energy

conversion ratio, determining the triggering behavior and explosion threshold, and identifying the effects of various parameters on FCIs. Tables 2.4, 2.5, 2.6 and 2.7 show the detailed experimental conditions and results.

The purpose of this Open Geometry test series [36, 37] was to estimate the conversion ratio of vapor explosions at large scale geometry. About sixty experiments were conducted in the open-geometry facility (OG) with minimal instrumentation as shown in Figure 2.3. The two sets of experiments were performed with different fuel materials (thermitically generated $Fe - Al_2O_3$ and Corium). The thermite melt consisted of 55 w/o Fe and 45 w/o Al_2O_3, at a theoretical (maximum) temperature of approximately 3100 K. These tests resulted in spontaneous explosions with conversion ratios ranging from 0.1 to 1.5 %, with small correlation to initial and boundary conditions. In the second set of experiments[37], with a prototypic reactor material of Corium-A+R[1], no energetic explosions were observed. Corradini[38] explained the reason for the lack of an explosion for the corium test as the solidification of the molten Corium due to relatively low superheat of molten fuel. In this series of tests, however, the precise data measurement was limited due to the lack of instrumentation and the facility geometry.

The tests performed in the EXO-FITS facility focused on instrumentation development and pre-tests for the FITS series. Even though the experimental data were limited due to the lack of instrumentation, it provided qualitative information on the effects of fuel composition, the characteristics of spontaneous explosions and selected explosion propagation data.

The MD series of experiments[39] was performed primarily to study melt delivery methods. A total of thirteen experiments as shown in Table 2.4 were conducted. A 0.6 to 5.11 kg quantity of Fe-Al_2O_3 melt was poured into subcooled water at an ambient pressure of 0.083 MPa. In highly subcooled conditions, the spontaneous explosions showed random characteristics. In most of the spontaneous explosion cases, the propagation velocities were estimated by visual observation and ranged from 300 to 550 m/s, with shock pressures as high as 34 MPa. The conversion ratio of the explosions were estimated to be quantitatively greater than the nominal 1.0 % in the Open-Geometry tests. The MDC tests[40] were also performed to test various compositions of corium melt with a fuel mass from 4 to 20 kg injected into a water mass from 77 to 276 kg. A wide variation in the explosivity was observed with no pattern observed. This again suggests that reproducibility in test conditions was lacking and may have caused scatter in the explosion data.

Five tests in the MDF series of tests[40] were conducted for examining a new iron oxidic simulant (Fe_3O_4). The oxidic melt was produced by mixing appropriate quantities of iron powder and potassium perchlorate followed by a thermite reaction. There were no spontaneous explosions, although an external trigger (0.635g of explosive) was applied in three tests. Berman *et al.* [40] observed that the melts were dispersed before entering the water

[1] 53 w/o UO_2, 16 w/o ZrO_2, 2 w/o NiO 27 w/o SS and 2 w/o Mo

and individual single drops were locally interacted. They suggested that energetic explosions were dependent on void fraction in the mixture (*i.e.*, melt dispersion) and explosive propagations were not triggered if local triggers were weak.

The CM series tests[40] were designed to investigate the coarse mixing behavior of FCIs with extensive visual observation. For this coarse mixing study, tests shown in Table 2.5 were mostly conducted at nearly saturated water conditions with subcooling from 1 to 9 K, without an external trigger. All twelve experiments produced violent eruptions at approximately 20 to 70 ms after the melt contacted the surface of the water. Multiple explosions were observed in some of the spontaneous triggered tests and provided damage to the water chamber. In these tests, the difference between the eruption and explosion was defined by the duration time of the interaction; the eruption lasted for an extended period of time longer than 50 ms with little pressurization.

Two RC tests[40] were conducted by replacing the weak constraint lucite interaction water chamber with a steel pipe (0.6 m diameter and 25 mm thick) to estimate the effect of the rigid radial constraint on FCIs. The Fe-Al_2O_3 fuel was poured into subcooled water. The first experiment produced a violent surface eruption as observed in the CM tests. In the second test, however, the largest recorded vapor explosion in the EXO-FITS tests occurred. Rough estimates of the conversion ratio for this test ranged from 0.8 to 14 percent. This strong explosion was explained at that time by the radially confined geometry enhancing liquid-liquid contact by driving the liquids together as they approached the wall, thereby providing more fragmentation. It is interesting to note that these test conditions were not replicated again in any Sandia experiments. Detailed experimental conditions and results are shown in Table 2.5. These results were an impetus to consider the current experimental series.

Based on experiences from the EXO-FITS tests, the FITS series of tests[39, 40, 41] were performed in the chamber shown in Figure 2.5. The chamber gas pressure, water phase pressures were measured, debris was collected and analyzed from the resulting fuel-coolant interaction and the explosion process was observed. The purposes of these tests were to determine the trigger behavior, explosion threshold and estimate of the conversion ratio as a function of ambient pressure, fuel composition, and other initial conditions.

The FITS-A test series was performed with similar conditions as some of the earlier EXO-FITS experiments with iron-alumina thermite and weak wall constraint (MD-15 and MD-16). In these tests the effect of the system ambient pressure was demonstrated. It was found that a system pressure increase suppressed explosions (FITS4A). However, the explosion suppression did not persist against an external trigger with a trigger pressure of 4 MPa (FITS5A).

The FITS-B test series was primarily performed to investigate the effect of the coolant to fuel mass ratio on spontaneous vapor explosions, at an ambient pressure of 0.083 MPa and a coolant temperature of 300 K. The mass of the fuel was increased from 2 kg (FITS-A series) to 18.7 kg. The mass ratio was controlled by altering the dimension of the interaction chamber and water depth. The conversion ratios of these tests were calculated by using

the estimated coolant slug kinetic energies from observations. Among these tests, two experiments (5B and 6B) were performed at temperatures near water saturation and the energetics was small. Most experiments were spontaneously triggered at the surface of the coolant and/or the base of the chamber in a subcooled coolant. For the range of the mass ratio, M_c/M_f, from 3 to 15, conversion ratios estimated from the coolant slug kinetic energies were relatively unaffected by this variation. Once again data scatter was large and this inhibited a clear understanding of the effect of initial conditions on energetics.

The FITS-C series tests were performed to study the effects of fuel composition and system pressure on energetics of FCIs, the resultant debris formation and hydrogen production. The experiments were conducted in an inert nitrogen environment to sample post-test hydrogen content. No external trigger was applied as shown in Table 2.7. The FITS1C test was conducted with similar conditions to the FITSB series of tests with an iron-alumina fuel. None of these series of tests, except two, produced explosions. Fletcher[27] suggested that both low-melt superheat and dispersion of the melt before contact with the coolant reduced the likelihood of triggering.

The FITS-D series[42] investigated the effects of the coolant to fuel mass ratio, water subcooling and ambient pressure and measuring of the hydrogen generation. In this series as shown in Table 2.7, no external trigger was provided. Increases in ambient pressure again suppressed the explosion. Only one explosive interaction (FITS5D) was observed. This test was performed at atmospheric pressure with highly subcooled water and produced a double explosion separated by about 3 ms. In past experiments double explosions were observed with a delay time of about 100 ms.

2.2.1.4 JAERI

In the 1990's the ALPHA program was initiated at JAERI (Japan Atomic Energy Research Institute) in Japan to investigate phenomena that may threaten containment integrity during postulated severe accidents. One experimental program examines the vapor explosion using a chamber type facility, named ALPHA as shown in Figure 2.6. The ALPHA facility[43, 44, 45] simulates the containment with an inner volume of 50 m^3 and a weak-walled interaction chamber. The melt is generated in the melt generator by a thermite reaction with iron-oxide and aluminum. This melt is identical to what was used in the Sandia tests. All detailed conditions and results are shown in Table 2.8. The results from over twenty experiments are qualitatively similar to what had been observed in the Sandia FITS tests. Similar data scatter can also be noted and this may again be due to the lack of precise control on the constraint and initial conditions.

2.2.1.5 JRC-Ispra

At the European Joint Research Center (JRC) at Ispra, two different sets of experiments (KROTOS and FARO) related to fuel-coolant interactions are being conducted. These experiments began over fifteen years ago applied to fast reactors. Since 1990, these tests have focused on light water reactor safety. These test facilities are unique because they have the capability to use prototypic reactor materials; *i.e.*, urania and other high temperature oxides.

The FARO facility shown in Figure 2.7 was designed to provide an experimental data base on molten fuel jet and water quenching and mixing phenomena. These tests are performed with about150 kg of corium in prototypical conditions; *e.g.*, early test series shown in Table 2.10. The tests simulate a corium pour into a water pool in the lower plenum of a reactor pressure vessel (RPV), or in the reactor cavity, its debris settling on the chamber bottom and its long term quench behavior.

The KROTOS facility shown in Figure 2.8 was built to obtain experimental information on explosive fuel-coolant interactions for various fuel-coolant pairs. Several different types of simulant fuels were utilized; *e.g.*, tin, aluminum oxide and corium (mixture of urania and zirconia). These tests mainly focused on studying the effects of initial and mixing conditions on the energetics of the FCIs. These experiments are complimentary to the experiments performed in our WFCI facility.

In these tests[47, 48, 49], the objective was to prepare and deliver a known molten fuel material into a water pool under controlled conditions . To accomplish this purpose the facility was designed to produce an explosion propagation in a one-dimensional geometry. The melt is prepared in a radiation furnace to a desired temperature, the melt crucible is then delivered to a location where melt release produces a fuel jet pour of 30 mm diameter into the test section. At a prescribed time the diaphragm to a pressurized gas volume is ruptured at the chamber bottom and a shock propagates vertically upwards through the mixture to trigger the explosion. Dynamic pressures and ambient pressures are recorded during the explosion transient to ascertain the explosion energetics. Debris is collected in the surrounding containment vessel (free volume of 275 liters). Two different inner diameters of the explosion test tube have been used (95 mm and 200mm with a tube length of about 1.2 meter) for the various experimental conditions as shown in Table 2.9.

About ten years ago the KROTOS tests utilized molten tin as the simulant. These were prepatory experiments for high temperature oxide melts. As the heating furnace was upgraded, molten aluminum-oxide was used as the fuel simulant. Most recently, molten corium is the fuel simulant and is quite prototypical of the molten core material; *i.e.*, 80 % urania and 20 % zirconia. Since this transition to molten oxide fuels, over two dozen tests have been conducted to investigate the explosivity of alumina and corium and to understand the effect of certain initial conditions. The experimental results can be summarized in the following manner:

1. Molten alumina melts produced explosive interactions under all conditions except for nearly saturated water. These explosions were both triggered and spontaneous. The general characteristics were supercritical pressures (20 - 100 MPa) with large propagation velocities (about 400 - 600 m/s) with narrow pressure pulse widths (1 msec) and energy conversion ratios of a few percent (1 - 3 %).

2. The effect of altering the fuel temperature or coolant temperature (below saturation) had little effect on energetics for alumina. Modest increases in ambient pressure below 2 bar also did not affect energetics. Nearly saturated water appeared to cause much larger vapor formation and thus may have substantially increased the void in the mixture.

3. Molten corium melts did not produce an explosion under atmospheric pressure conditions. Only when the ambient pressure rose above 2 bar could the FCI be externally triggered and be energetic enough to become a propagating explosion. Peak pressures were much lower (20 - 40 MPa) and associated pulse widths (<1 msec) and conversion ratios were quite small (0.02 - 0.05 %). The reason for this behavior is not totally clear, but is attributed to low melt superheat for corium and large void fractions in the mixture at the time of triggering. An increase in ambient pressure seems to be sufficient to reduce the mixture void to allow the explosion to be triggered.

2.2.2 Experiments using Tin as a Fuel

As a simulant fuel, tin has been widely used for investigating fuel-coolant interaction phenomena because it has a relatively low melting point of 231.9 °C, low toxicity and produces vapor explosions at subcritical pressures, when it contacts water. Initial FCI experiments were performed at small scales where small masses of tin were dropped into water to identify regions of spontaneous interactions (Figure 2.9). In Table 2.11, tin and other simulant fuels used in past experiments are compared [51] with respect to their mechanical and thermal properties. Tin has a similar energy content per unit volume as aluminum, while alumina and corium are also quite similar. However, we know from empirical evidence that aluminum and alumina result in much more energetic explosions.

Hall *et al.* [60] investigated vapor explosions in a long tube geometry as shown in Figure 2.10. The main test tube was 0.85 to 1.0 m in length and a 25 mm inner diameter; the outer tube had a 50 mm inner diameter. The test vessel was filled with water at 85 to 95 °C and tin as fuel material at 600 to 750 °C was poured into the top of the inner tube. They observed self-sustaining shock propagations and escalation. All detailed conditions and a brief summary of results are shown in Table 2.12.

Briggs[61] investigated the metal/water interaction including aluminum/water and tin/water as the first stage of the THERMIR experimental program. These experiments as shown in Table 2.12, had no external trigger device because of the scoping nature of the tests. Three experiments (8,9, and 10) with a molten tin mass of 2 kg produced localized interactions

with peak pressures of 0.2 - 0.3 MPa.

Fry and Robinson[31] continued the experimental studies in the THERMIR facility to investigate explosion propagation. In their experiments, explosions were initiated by an external trigger using a mechanical impact or detonator. Molten metal up to 16 kg at about 800 °C was poured into water at a temperature between 44 and 86 °C. The first five experiments in Table 2.12 produced coherent explosions at high melt temperatures. These tests suggested that coherent explosions might occur for a large mass system (several kilograms) even when the interface temperature was below the homogeneous nucleation temperature.

More recently Baines[62] conducted an experiment to investigate vapor explosion propagation and work yields in a constrained system. This apparatus (shown in Figure 2.11) was equipped to measure the explosion work output, which was the expansion tube attached horizontally to the upper part of the vertical test section. The vertical test tube (~1 m long) and the horizontal cylinder (~3 m long) were made of stainless steel tubing with an inner diameter of 29.5 mm. The tin (~1 kg) is heated to about 800 °C and pours into the water in the test section. After a preset time delay (~2 s) to allow the tin to almost reach the bottom of the test section, the gate valve at the top of the test section closes and a steel plate simultaneously cuts off the flows of tin into the funnel. A fraction of a second later, molten tin reaches the cold water in the triggering section, which causes the vapor film to collapse, initiating a steam explosion. The resulting mixture then expands to cause the magnet piston in the horizontal cylinder to move. He observed that the explosion efficiencies were low with work yields less than 0.4 % of the thermal energy in the fuel, propagation velocities were about 100 m/s and the explosion mixtures produced were relatively "weak" with the tin volume fractions in the range of 0.08 to 0.14. This experiment is of note because it is the only test apparatus which took great care in measuring the energetics under controlled conditions.

A total of twenty-two tests for a tin-water vapor explosion were performed in the KROTOS facility. Only the KROTOS-21 test[63], however, was reported in the open literature and used as a benchmark data for the verification of several computer models. In this test, a test section with an inner diameter of 95 mm was chosen for investigating one dimensional explosion propagation eliminating the explicit radial distribution of the fragmented melt. As shown in Table 2.13, about 6.5 kg of the melt was poured into the water and explosive interactions were initiated by the gas trigger with a magnitude of 12 MPa. The propagation of the coherent explosion with a peak pressure of 6.5 MPa moved upward with velocities ranging from 150 to 270 m/s. The post-test analysis showed that approximately 0.85 kg, *i.e.* 13 % of the tin mass, had fragmented to diameters below 250 μm. No direct measurement of work yield was available, although estimates could be made based on impulse and chamber pressurization of 1-2 kilojoules.

2.2.3 Experiments using Iron-Oxide as a Fuel

Iron-oxide is not commonly used as a fuel simulant in vapor explosion experiments. It has a fairly high melting temperature (1550 °C), and though it is chemically inert in water, it is very corrosive to containers holding it in its molten state. The cases where it has been used have been small scale single droplet experiments [58, 59, 66, 67, 68]. where the fuel was prepared in the form of Fe_3O_4. These experiments are considered small scale because the mass of the fuel is small when compared to the mass of the coolant, thus there is no spatial propagation of the explosion through the fuel-coolant mixture. The fuel droplet was prepared by melting a small piece of iron foil with a heat source like a laser at above 1850 °C. At these high temperatures, the iron oxidizes in air to a composition of magnetite similar to Fe_3O_4, which represents its equilibrium state. This small droplet of material is usually held by surface tension to a wire made of iridium, and is easily dropped on demand. This method is reliable and easy to perform for repeated experiments, since it eliminates the need for a crucible and large furnace, but it is always limited to very small masses (<0.1gm), and hence is only used for small scale experiments.

At Sandia National Laboratories, many single droplet experiments were performed, with iron-oxide as the principal fuel composition. Nelson and coworkers [58] performed a series of experiments with small iron-oxide droplets (< 0.1 g and 3mm in diameter) at temperatures close to 2000 °C, dropped into water at 30-50 °C. The coolant test section was transparent, which allowed filming of the experiment with a high-speed camera. As the droplets contacted the water, a stable vapor film could be seen forming around the fuel droplet. This vapor film was destabilized by a pressure pulse, thereby forcing liquid-liquid contact and initiating the local vapor explosion. Triggering of the explosion was achieved by electrically vaporizing a thin gold wire, and pressure traces were acquired with submerged pressure transducers. It was found that multiple explosions would occur from the single droplet. The high-speed film allowed measurement of the size of the vapor bubble that was created as a result of the explosion. Conversion ratios of the explosions were found to be in the range of 1 - 3 %, and peak pressures were estimated to be above 10 MPa near the drop surface. If the trigger pulse was less than 0.2 MPa, no explosion would occur, and with trigger pulses of 0.4 MPa or greater, a prompt explosion would always occur. For trigger pressure peaks in the range of 0.2 - 0.4 MPa, the drops would undulate, then show delayed cyclic explosions. Based on debris sizes of less than 250 microns, it was determined that the explosion occurred due to the interaction of the coolant with liquid fuel, with no evidence present that solidified fuel participated in the explosion. Electron microscope images of the debris confirmed this, with no evidence of sharp edges on the particles that would have indicated that a solid fuel particle had fragmented. All the particles were spherical in shape, indicating that they were in a liquid state during the interaction.

At the University of Wisconsin, Kim [67] performed a series of single droplet experiments very similar to Nelson with 0.1 g or less of iron-oxide at 1900 °C, as the fuel dropped into water at 15 °C. Pressure histories at three different locations in the container were measured, and the entire experiment was filmed with a high-speed camera. In addition to baseline experiments and investigations into the effect of variation in trigger pressure, the

effect of changing the coolant viscosity on the explosion energetics was to be observed by adding a cellulose gum solution to the water. Conversion ratios for the baseline experiments ranged from 1- 6 %. The results showed that an increase in coolant viscosity reduced the conversion ratio of the explosions, and in some cases, suppressed the explosion altogether. Also, an increase in trigger pressure seemed to offset the effects of the viscosity increase, but only to a limited extent. Even with a 0.4 MPa trigger pulse, if the viscosity was larger than 150 centipoise (cp), the conversion ratio was very low (< 0.5 %). Peak pressures were higher with a lower viscosity, with a maximum of about 2 MPa for a 40 cp solution, and a maximum of about 0.5 MPa for a 240 cp solution. This suggests that the addition of an additive to the coolant which increases viscosity could help suppress or mitigate vapor explosions.

Baker [68] added to the work of Kim by using the same apparatus to investigate the effect of surfactant additives (substances that affect surface tension) to the coolant on the energetics of single droplet vapor explosions with iron oxide. Two different surfactants, ethoxilated-nonyle-phenole and sodium-dodecyl-benzene, were investigated. The peak pressure data was inconclusive with values ranging from 0.1 to 1.2 MPa. Also, the conversion ratio data indicated the possibility of a slight decrease in the explosion intensity with higher concentrations of either surfactant. Conversion ratios were in the range of 0.5 to 12 % at low concentration, but dropped to around 0.2 % at 10 wppm. The particle debris size data (Sauter mean diameter), which is used as a measure of fuel participation in the explosion, was inconclusive for ethoxilated-nonyle-phenole, but showed some evidence of a suppressive effect for sodium-dodecyl-benzene.

2.2.4 Related Experimental Parameters

Coolant Additives

To reduce the potential hazard of the FCIs, many methods have been investigated [7, 66, 67, 69]. In the aluminum industry in late 50's the causes and prevention of these explosive interactions were studied by Long[7]. He performed large scale tests with aluminum and various combinations of materials. In these experiments, a sudden discharge of 22.7 kg of molten aluminum through an 89 mm diameter hole into a clean degreased steel container partially filled with water at 12.8~25.6 °C, always produced an explosion. Based on his results, Long suggested that the cause of these explosive interactions was the rapid vaporization of water entrapped between the melt and container surface. In order to reduce the amount of water entrapment, he coated the inside wall with grease, oil or a bituminous paint and found that the explosion did not occur with the coated container surface.

Nelson *et al.* [70] investigated the reason for these non-explosive interactions. They suggested the hypothesis that the initiating action at a wet surface was caused by a thin layer of liquid water enclosed beneath the molten metal and solid surface. Nonwettable ("coated") surfaces did not have the thin layer of water between the melt and surface, and offered little or no assistance to triggering during the interaction.

Recently, in the nuclear industry, numerous efforts in suppressing or mitigating the FCI risk have been made [66, 67, 69, 71, 72]. Most of the work has focused on the effect of additives in the coolant, which changed the characteristics of the coolant, resulting in suppression of explosive interactions. As one of many possible additives, water-soluble polymers, which change coolant properties such as viscosity and heat transfer characteristics, were previously investigated. Kotchaphakdee *et al.* [73] studied the nucleate pool boiling of dilute aqueous polymer solutions on a heated flat plate. Paul *et al.* [74, 75] measured nucleate boiling curves for aqueous solutions of nine different drag-reducing polymers on a platinum wire. They found that nucleate boiling heat flux for the polymer solutions was substantially increased.

Most of the past work focused on the investigation of the boiling heat transfer characteristics in dilute polymeric solutions. One of the early studies for investigating the threshold viscosity of polymeric solutions was performed by Flory *et al.* [76]. They prepared a dilute polymeric solution by the addition of carboxymethylcellulose and dropped molten lead, tin and bismuth into the solution. They observed that the interaction between the molten metal and solution was substantially reduced or totally eliminated at a viscosity ratio of approximately five. The viscosity ratio is defined in this study as the ratio of the viscosity of the solution to that of pure water. Nelson *et al.* [70] performed experiments by pouring 12 g of molten tin at 923 K into 1.8 kg of aqueous glycerol or cellulose gum solution. They found that there was a threshold solution viscosity near a viscosity ratio of 15, above which spontaneous explosions no longer occurred. Also they performed one field-scale experiment in which 50 kg of molten Fe-Al_2O_3 were poured into 190 kg of an aqueous solution of cellulose gum at the viscosity of about 0.080 Pa s. They observed that only a gentle breakup of some of the melt occurred. Kim[67] investigated the effect of external trigger strength on the explosion of molten iron oxide drops in aqueous solutions of cellulose gum and associated efficiencies. He applied external trigger pressures of 200 and 400 kPa and varied the viscosity ratio from 40 to 240. He observed that the explosion efficiency decreased from about 6 % to 0 % as the viscosity ratio of the solution increased from 40 to 240. Kim noted that the threshold for suppression was dependent on trigger strength. Recently, Dowling *et al.* [69] examined the ability of a dilute aqueous solution of polyethylene oxide (PEO) to suppress spontaneous explosions. Twelve grams of molten tin at temperatures from 600 to 1000 °C were poured into a solution-filled container at 25 °C with a viscosity ratio from 1.01 to 2.0. They showed that spontaneous explosions were markedly suppressed and entirely eliminated when the polymer solution was twice as viscous as pure water.

Note that all this previous work has been conducted at small scales. Thus, it is important for us to verify that these suppressive effects can be realized at large scales. The analysis performed in conjunction with these tests suggest scale independence, but this has not been empirically observed. This will be one of the important parameters investigated in this experimental body of work.

Radial Constraint

The geometry surrounding the fuel-coolant mixture plays an important role in FCI energetics. Early research on explosion propagation recognized the role of the radial constraint.

One of the experiments, Board *et al.* [16], produced a coherently propagating explosion using two types of chambers with a different degree of constraint; one is a 'V' shape channel (or trough) and another is a narrow channel. Board produced a coherently propagating explosion with a narrow channel which had a higher degree of radial constraint. Previously mentioned, the RC tests performed by Sandia investigated the effect of the radial constraint on the vapor explosion. These tests produced the most energetic explosion recorded by the Sandia researchers.

Recently, Frost *et al.* [77] investigated more systematically the degree of geometrical constraint required to sustain vapor explosion propagation. In their experiments an array of melt droplets were injected into a narrow channel as a radial constraint (or confinement). The explosive interaction produced a shock propagation with a speed of about 100 m/s. Without the radial constraint, incoherent sequential explosions of the drops still occurred. If there was no confinement, the propagation velocity was decreased by an order of magnitude to 5~10 m/s. They found a high degree of radial constraint was required to sustain a propagating explosive interaction. Also, they observed interactions initiated in a radially unconstrained cylindrical geometry always failed to propagate after a short distance. In the KROTOS tests and our WFCI tests[78], this high degree of radial constraint has been maintained resulting in reproducible propagating vapor explosions. Conceptually, the presence of a strong radial wall constraint in these one-dimensional experiments is necessary to simulate a "slice" of a larger scale fuel-coolant mixture which would provide the radial confinement in larger scale explosions that approaches a rigid wall constraint. In reality, at larger scales the compressibility of the surrounding mixture would reduce the rigidity of the radial constraint. The relationship between the scale of experimental geometries and fuel-coolant mixtures is a crucial factor in deciding the degree of geometrical constraint needed to bound the effect of larger scales and sustain propagations. It is a believed that a strong radial constraint maximizes the energetics for a particular fuel-coolant mixture at any given geometric scale.

2.3 Key Findings of the Experimental Review

- One of the key experimental results needed to understand the energetics of FCIs is the resulting work output. The data associated with precise measurement of this work output are extremely limited. Over the last two decades each experiment has used its own method to estimate the work output and because of experimental imprecision has led to large uncertainties. Such uncertainties in measuring the work output precludes any direct data comparison on key effects. This is the major improvement we plan to make with this work.

- In FCI experiments, various materials are used as a simulant of the core melt. Even with a large amount of experimental data associated with various simulant materials and variations in initial and boundary conditions, it is difficult to extrapolate their data to prototypic conditions. Again this is because of insufficiently defined measurements and differing definitions of work yield.

- Large amounts of experimental data are available from small and large scale experiments both triggered and spontaneous. However, experimental data associated with the systematic effects of the trigger on energetics in FCIs is very limited This is especially the case in large scale tests where most experimental data are not obtained with well controlled measurements.

- The study of vapor explosion suppression, using some additive, in large scale systems is nonexistant. Historically, only the suppressive effect of ambient pressure are known. Most previous work has been performed on small scale geometries (single drop experiments). The effects of polymer additives on the FCI looks promising and it is necessary to verify scale effects.

Table 2.1: Summary of the ANL Experiments

Test Facility & Run No.	Fuel/Coolant Fuel	$T_f/\Delta T_{sub}$ °C	M_f/M_c kg	Test-section H_c cm	D_{po} cm	Trigger Type	Trigger MPa	Results Exp.[2] Type	P_{pk} MPa	V_p m/s	α %	CR %	Remarks
ANL : Chamber Type													
CWTI	P_a : 0.1 MPa												
CWTI-09	Corium	2800/6	2.18/11	31	2.20	-	-	NE[3]	0.245	-		-	
CWTI-10	Corium	2800/75	1.31/11	32	2.54	-	-	NE	-	-		-	
CCM	P_a : 0.1 MPa												
CCM-1	Corium	2800/43	2.15/37	106	2.54	-	-	NE	0.139	-		-	ID : 0.21m
CCM-2	Corium	2800/1	11.15/22	63	2.02	-	-	NE	0.386	-		-	Single jet ID : 0.21m
CCM-3	Corium	2800/0	3.34/39	110	2.54	-	-	NE	0.389	-		-	Four jets ID : 0.21m
CCM-4	Corium	2800/37	9.24/38	107	5.08	-	-	NE	0.430	-		-	Single jet ID : 0.21m
CCM-5	Corium	2800/45	11.34/525	107	5.08	-	-	NE	0.246	-		-	Single jet ID : 0.76m
CCM-6	Corium	2800/0	12.89/510	107	5.08	-	-	NE	0.417	-		-	ID : 0.76m

[2]Explosion
[3]No Explosion

Table 2.2: Summary of the SUW Experiments

Test Facility & Run No.	Fuel/Coolant Fuel	$T_f/\Delta T_{sub}$ °C	M_f/M_c kg	Test-section H_c cm	D_{po} cm	P_a MPa	Trigger Type	Trigger MPa	Results Exp. Type	P_{pk} MPa	CR %	Remarks
SUW : Chamber Type, M_c/M_f: 63-188												
01	UO_2+Mo	3300/78	24/1500			0.1	-	-	SE		2.8	FR[4]
02	UO_2+Mo	3300/87	24/1500			0.4	-	-	NE		-	FR
03	UO_2+Mo	3300/80	24/1500			0.1	-	-	SE		1.6	FR
04	UO_2+Mo	3300/80	24/1500			0.1	-	-	SE		2.3	RR[5]
05	UO_2+Mo	3300/61	24/1500			0.1	-	-	SE		3.2	RR
06	UO_2+Mo	3300/31	24/1500			0.1	-	-	SE		3.1	RR
07	UO_2+Mo	3300/0	24/1500			0.1	-	-	SE		4.3	RR
08	UO_2+Mo	3300/60	24/1500			0.5	-	-	SE		2.8	RR
09	UO_2+Mo	3300/60	24/1500			1.0	-	-	SE	17.2	3.0	RR
10	UO_2+Mo	3300/60	8/1500			0.1	-	-	SE		1.1	RR
11	UO_2+Mo	3300/60	8/1500			1.0	-	-	NE		-	RR
12	UO_2+Mo	3300/60	8/1500			1.0	-	-	SE		-	RR

[4]Free Release
[5]Restricted Release

Table 2.3: Summary of the WUMT Experiments

Test Facility & Run No.	Fuel/Coolant Fuel	$T_f/\Delta T_{sub}$ °C	M_f/M_c kg	Test-section H_c cm	D_{po} cm	P_a MPa	Trigger Type	Trigger MPa	Results Exp. Type	V_p m/s	CR %	Remarks
WUMT : Chamber Type, M_c/M_f: 0.33-7.5												
01	UO_2+Mo	3300/0	24/80[6]	50	7	0.1	-	-	NE			
03	UO_2+Mo	3300/80	24/180	50	7	0.1	-	-	SE			
04	UO_2+Mo	3300/0	24/180	50	4	0.1	-	-	NE			
05	UO_2+Mo	3300/0	24/72	20	10	0.1	-	-	NE			
06	UO_2+Mo	3300/0	24/20	50	4	0.1	-	-	NE			
07	UO_2+Mo	3300/0	24/8	20	10	0.1	-	-	NE			
08	UO_2+Mo	3300/0	24/180	50	10	1.0	-	-	NE			
09	UO_2+Mo	3300/0	24/180	50	10	0.1	-	-	SE			
MIXA : Chamber Type, V_e: 5 m/s, M_c/M_f: 27 Dimension: 0.37 m Vessel Side												
01	UO_2+Mo	3300/0	2.84/82	60		0.1	-	-	NE			
04	UO_2+Mo	3300/0	2.75/82	60		0.1	-	-	NE			
05	UO_2+Mo	3300/20	3.00/82	60		0.1	-	-	NE			
06	UO_2+Mo	3300/0	3.00/82	60		0.1	-	-	NE			
07	UO_2+Mo	3300/20	3.00/82	60		0.1	-	-	NE			

[6]Water mass was calculated by the dimension of the chamber given in ref. [33, 35]

Table 2.4: Summary of the SNL Experiments (Part I)

Test Facility & Run No.	Fuel/Coolant Fuel	$T_f/\Delta T_{sub}$ °C	M_f/M_c kg	Test-section H_c cm	D_{po} cm	Trigger Type	Trigger MPa	Results Exp. Type	P_{pk} MPa	V_p m/s	CR %	Remarks
EXO-FITS : Open Chamber Type												
MD	V_e : 5.3-6.4, E_m : 3.3, P_a : 0.083											
07	Fe-Al_2O_3	2800/-	4.80/75	45.7		-	-	SE		-		Base[7]
08	Fe-Al_2O_3	2800/90	4.70/258	71.0		-	-	SE	>34	415	>1	Base
09	Fe-Al_2O_3	2800/91	0.60/56	61.0		-	-	NE		-		
10	Fe-Al_2O_3	2800/90	1.31/56	61.0		-	-	NE		-		
11	Fe-Al_2O_3	2800/89	4.70/267	71.1		-	-	SE	>34	365	>1	Above Base
12	Fe-Al_2O_3	2800/89	1.46/42	45.7		-	-	NE		-		
13	Fe-Al_2O_3	2800/89	1.69/66	30.5		-	-	NE		-		
14	Fe-Al_2O_3	2800/90	4.70/264	71.1		-	-	SE		555		Above Base
15	Fe-Al_2O_3	2800/90	1.88/90	43.2		-	-	SE		249		Base
16	Fe-Al_2O_3	2800/90	1.85/90	43.2		-	-	SE		429		Base
17	Fe-Al_2O_3	2800/82	2.85/152	53.3		-	-	NE		-		
18	Fe-Al_2O_3	2800/80	2.74/152	53.3		-	-	SE	9	313		Base
19	Fe-Al_2O_3	2800/74	5.11/224	61.0		-	-	SE	17.5	427		Base

[7]Spontaneous Explosion occurred at the Base of the Chamber

Table 2.5: Summary of the SNL Experiments (Part II)

Test Facility & Run No.	Fuel/Coolant Fuel	$T_f/\Delta T_{sub}$ °C	M_f/M_c kg	Test-section H_c cm	D_{po} cm	Trigger Type	Trigger MPa	Results Exp. Type	P_{pk} MPa	V_p m/s	τ_{er}/τ_{se}[8] ms	Remarks
EXO-FITS : Open Chamber Type												
CM	V_e : 2.4-5.9, M_c/M_f: 6-55											
01	$Fe\text{-}Al_2O_3$	2800/9	18.5/109.7	122	-	-	-	NE			30/-	Eruption
02	$Fe\text{-}Al_2O_3$	2800/4	18.0/109.3	122	-	-	-	NE			73/-	Eruption
03	$Fe\text{-}Al_2O_3$	2800/3	18.0/437.0	122	33	-	-	NE			43/-	Eruption
04	$Fe\text{-}Al_2O_3$	2800/3	18.9/218.5	61	53	-	-	NE			18-89/-	Eruption
05	$Fe\text{-}Al_2O_3$	2800/4	7.6/218.7	61	28	-	-	NE			27/-	Eruption
06	$Fe\text{-}Al_2O_3$	2800/3	4.0/218.5	61	18	-	-	NE			22-159/-	Eruption
07	$Fe\text{-}Al_2O_3$	2800/73	18.5/169.6	46	-	-	-	SE		301	43/69,503	
08	$Fe\text{-}Al_2O_3$	2800/2	18.6/218.4	61	23	-	-	SE			37/216	
09	$Fe\text{-}Al_2O_3$	2800/3	18.6/218.6	61	26	-	-	SE			65/105	
10	$Fe\text{-}Al_2O_3$	2800/1	18.4/109.3	31	19	-	-	SE			43/112,311	
11	$Fe\text{-}Al_2O_3$	2800/1	18.7/218.6	61	20	-	-	NE			52/-	Eruption
12	$Fe\text{-}Al_2O_3$	2800/69	18.5/112.9	31	20	-	-	SE			37/69,125	
OM	V_e : 3.3-3.8, M_c/M_f: 11-24											
01	Fe_xO_y	-/69	-/66.10	36		-	-	SE		-	-	
02	Fe_xO_y	-/69	9.00/100.9	36		-	-	SE		193	47	
03	Fe_xO_y	-/69	10.0/131.7	36		-	-	SE		785	141	
04	Fe_xO_y	-/4	9.00/218.6	61		-	-	SE		332	19-360	Multiple Explosions
RC	V_e : 5.8, M_c/M_f: 6											
01	$Fe\text{-}Al_2O_3$	2800/69	19.0/111.7	46		-	-	NE	-	-	86/-	Eruption
02	$Fe\text{-}Al_2O_3$	2800/64	18.5/111.6	46		-	-	SE	76	1100	56/180	

[8]Event Time of Eruption/Spontaneous Explosion after Melt Entry

Table 2.6: Summary of the SNL Experiments (Part III)

Test Facility & Run No.	Fuel/Coolant Fuel	$T_f/\Delta T_{sub}$ °C	M_f/M_c kg	Test-section H_c cm	D_{po} cm	Trigger Type	Trigger MPa	Results Exp. Type	P_{pk} MPa	CR %	Remarks
FITS : Chamber Type											
FITS-A	V_e : - , M_c/M_f:42-53										
1A	Fe-Al_2O_3	2500/85	1.94/90	43.2		-	-	SE		-	Mild Explosion
2A	Fe-Al_2O_3	2500/82	2.87/152	53.3		-	-	SE		< 1	Surface Explosion
3A	Fe-Al_2O_3	2500/81	5.30/226	61.6		-	-	SE		1-2	Above Base
4A	Fe-Al_2O_3	2500/80	4.29/226	61.0		-	-	NE		-	P_a: 1.02 MPa
5A	Fe-Al_2O_3	2500/81	5.38/226	61.0				TE		1-2	P_a: 1.09 MPa, 0.64g PETN detonator
FITS-B	V_e :5.4-7.2, M_c/M_f:1.5-15, P_a: 0.083 MPa										
1B	Fe-Al_2O_3	2500/70	18.7/226	61.0	5	-	-	SE		3.7 (5.1)	Double Explosion at surface and base
2B	Fe-Al_2O_3	2500/70	18.6/113	30.0	20	-	-	SE		4.4	Single Explosion
3B	Fe-Al_2O_3	2500/67	18.6/57	30.0	22	-	-	SE		5.3	Single Explosion
4B	Fe-Al_2O_3	2500/69	18.7/226	61.0	18	-	-	SE		7.0 (9.0)	Double Explosion at surface and base
5B	Fe-Al_2O_3	2500/1	14.5/ -	37.0	-	-	-	NE		-	
6B	Fe-Al_2O_3	2500/1	18.7/63	30.0	-	-	-	NE		-	Weak Interactions
7B	Fe-Al_2O_3	2500/78	18.7/28	15.0	-	-	-	SE		0.5	
7BR	Fe-Al_2O_3	2500/79	18.7/ -	15.0	22	-	-	SE		-	EXO-FITS facility
8B	Fe-Al_2O_3	2500/81	18.7/284	77.0	19	-	-	SE		7.4 (9.2)	Double Explosion at surface and base
9B	Fe-Al_2O_3	2500/80	18.7/170	46.0	20	-	-	SE		5.5	Single Explosion

Table 2.7: Summary of the SNL Experiments (Part IV)

Test Facility & Run No.	Fuel/Coolant Fuel	$T_f/\Delta T_{sub}$ °C	M_f/M_c kg	Test-section H_c cm	D_{po} cm	Trigger Type	Trigger MPa	Results Exp. Type	P_{pk} MPa	CR %	Remarks
FITS : Chamber Type											
FITS-C	V_e :, M_c/M_f: 5-15										
1C	Fe-Al_2O_3	2500/69	17.1/115	31.0		-	-	SE			P_a: 0.083 MPa, Surface Explosion
2C	C-A+R	2500/72	16.0/227	61.0		-	-	SE			P_a: 0.083 MPa, Surface Explosion, Base
3C	C-A+R	2500/68	11.5/128	38.0		-	-	NE			P_a: 0.083 MPa, Mild interaction
4C	Fe-Al_2O_3	2500/67	19.0/115	31.0		-	-	NE			P_a: 0.550 MPa, Mild interaction
5C	Fe-Al_2O_3	2500/69	19.5/115	31.0		-	-	NE			P_a: 0.520 MPa, Mild interaction
FITS-D	V_e :, M_c/M_f: 5-15										
0D	Fe-Al_2O_3	2400/0	17.8/182	51.0		-	-	NE			P_a: 0.085 MPa
2D	Fe-Al_2O_3	2400/169	19.0/95	66.0		-	-	NE			P_a: 1.100 MPa, Mild interaction
2DR	Fe-Al_2O_3	2400/158	18.7/95	66.0		-	-	NE			P_a: 1.100 MPa, Mild interaction
3D	Fe-Al_2O_3	2400/37	18.9/16.2	15.0		-	-	NE			P_a: 0.700 MPa, Mild interaction
5D	Fe-Al_2O_3	2400/83	19.2/383	66.0		-	-	SE			P_a: 0.083 MPa
8D	Fe-Al_2O_3	2400/0	19.5/21.3	15.0		-	-	NE			P_a: 0.083 MPa

Table 2.8: Summary of the ALPHA Experiments

Test Facility & Run No.	Fuel/Coolant Fuel	$T_f/\Delta T_{sub}$ °C	M_f/M_c kg	Test-section H_c cm	D_{po} cm	Trigger Type	Trigger MPa	Results Exp. Type	P_{pk} MPa	V_p m/s	α %	CR %	Remarks
ALPHA	Chamber Type Dimension : 3.9m D x 5.7m H, M_c/M_f: 10-80												
STX001	$Fe\text{-}Al_2O_3$	10/785	2450/20	100	20	-	-	NE					P_a: 0.1 MPa
STX002	$Fe\text{-}Al_2O_3$	20/785	2450/16	100	20	-	-	SE					P_a: 0.1 MPa
STX003	$Fe\text{-}Al_2O_3$	20/784	2450/19	100	20	-	-	SE				1.10	P_a: 0.1 MPa
STX005	$Fe\text{-}Al_2O_3$	20/774	2450/27	100	20	-	-	SE					P_a: 0.1 MPa
STX006	$Fe\text{-}Al_2O_3$	20/774	2450/25	100	20	-	-	NE					P_a: 0.1 MPa, D.D[9]
STX008	$Fe\text{-}Al_2O_3$	20/774	2450/186	100	20	-	-	NE					P_a: 1.6 MPa
STX009	$Fe\text{-}Al_2O_3$	20/774	2450/16	100	20	-	-	SE				1.50	P_a: 0.1 MPa
STX010	$Fe\text{-}Al_2O_3$	10/774	2450/24	100	20	-	-	SE				2.20	P_a: 0.1 MPa
STX011	$Fe\text{-}Al_2O_3$	20/774	2450/27	100	20	-	-	SE					P_a: 0.1 MPa, D.D
STX012	$Fe\text{-}Al_2O_3$	20/774	2450/184	100	20	-	-	NE					P_a: 1.6 MPa
STX013	$Fe\text{-}Al_2O_3$	10/774	2450/11	100	20	-	-	NE					P_a: 0.1 MPa
STX014	$Fe\text{-}Al_2O_3$	20/816	2450/99	100	20	-	-	NE					P_a: 0.1 MPa
STX015	$Fe\text{-}Al_2O_3$	20/774	2450/171	100	20	-	-	NE					P_a: 1.0 MPa
STX016	$Fe\text{-}Al_2O_3$	20/174	2450/22	100	20	-	-	SE				0.86	P_a: 0.1 MPa
STX017	$Fe\text{-}Al_2O_3$	20/174	2450/87	90	20	-	-	SE				0.66	P_a: 0.1 MPa
STX018	$Fe\text{-}Al_2O_3$	20/174	2450/90	90	20	-	-	SE			20-25	3.33	P_a: 0.1 MPa
STX019	$Fe\text{-}Al_2O_3$	20/392	2450/92	90	20	-	-	SE			42-50	5.67	P_a: 0.1 MPa D.D
STX020	$Fe\text{-}Al_2O_3$	20/774	2450/92	100	20	-	-	NE			58-68	-	P_a: 0.1 MPa D.D
STX021	$Fe\text{-}Al_2O_3$	20/697	2450/92	90	20	-	-	SE			63-80	4.05	P_a: 0.1 MPa D.D in Water

[9]Dispersion Device

TEST ID	K26	K27	K28	K29	K30	K38	K40	K41	K42	K43	K44	K49	K50	K51
Melt: Alumina														
Mass [kg]	1.0	1.43	1.43	1.45	1.52	1.53	1.47	1.43	1.54	1.5	1.5	1.74	1.57	1.8
Temp [K]	2573	2573	2573	2573	2573	2665	3073	3073	2465	2625	2673	2415	2200	2475
Brake Disk	yes	yes	yes	yes	yes	no	no	no	no	no	no	no	no	no
Jet Diam [mm]	30	30	30	30	30	30	30	30	30	30	30	30	30	30
Coolant:Water														
Mass [kg]	7.2	7.2	7.2	7.2	7.2	34.5	34.5	34.5	34.5	34.5	34.5	34.5	34.5	34.5
Depth [m]	1.08	1.08	1.08	1.08	1.08	1.11	1.11	1.11	1.11	1.11	1.11	1.11	1.11	1.11
Temp [C]	60	90	80	20	20	21	17	95	20	22	90	20	87	95
Fall Distance [m]	0.46	0.46	0.46	0.46	0.46	0.46	0.46	0.46	0.46	0.46	0.46	0.46	0.46	0.46
Press [bar]	1.0	1.0	1.0	1.0	1.0	1.0	1.0	1.0	1.0	2.0	1.0	3.5	1.0	1.0
Ves'l ID [mm]	95	95	95	95	95	200	200	200	200	200	200	200	200	200
Gas Trigger	yes	no	yes	no	no	no	no	no	no	no	yes	no	no	no
RESULTS														
Penet.Melt Jet	T5	T0	T1	T0	T1	T3	<T1	T0	T2	T1	<T2	T3	T0	T0
Steam Explosion	yes	no	yes	yes	yes	yes	yes	no	yes	yes	yes	yes	no	no
Max.Press. [MPa]	>26	--	>50	>104	>106	67	83	--	57	117	65	82	---	---
Conv. Ratio [%]	0.35	--	0.85	0.72	1.1	1.45	0.9	--	1.9	1.3	2.6	2.2	---	---
Total Debris [kg]	<1	1.1	1.36	1.5	1.43	1.5	1.45	1.43	1.5	1.5	1.5	1.7	1.55	1.8
Debris<0.25 mm [%]	31	0.1	62	62	88	60	35	--	60	47	75	60	---	---
Debris<0.1 mm [%]	22	--	40	39	73	35	25	--	35	30	50	35	---	---

Table 2.9: Summary of KROTOS Experiments with Alumina

TEST ID	K32	K33	K35	K36	K37	K45	K46	K47	K52	K53
Melt: UO_2ZrO_2	81/19	81/19	79/21	79/21	79/21	80/20	79/21	79/21	80/20	80/20
Mass [kg]	3.03	3.2	3.1	3.03	3.22	3.08	5.05	5.15	2.62	2.62
Temp [K]	3063	3063	3023	3025	3018	3105	3088	3023	3023	3023
Brake Disk	no	no	yes	no	no	no	no	no	no	no
Coolant:Water										
Mass [kg]	7.1	7.7	7.7	7.7	34.2	36.3	34.1	34.1	34.1	34.1
Depth [m]	1.08	1.08	1.08	1.08	1.1	1.14	1.1	1.1	1.1	1.1
Temp [C]	78	25	90	21	23	96	17	18	17	17
Press [bar]	1	1	1	1	1	1	1	1	2	3.6
Ves'l ID [mm]	95	95	95	95	200	200	200	200	200	200
Trigger Press [MPa]	--	--	13	13	13	14.5	15.5	15	14.5	15.2
Trigger Time [msec]	--	--	980	990	977	1305	1020	1620	1090	1100
RESULTS										
Avg. Jet Velocity [m/s]	--	--	--	--	6.7	4.4	6.1	6.7	2.7	3.0
Melt Jet Penetration	T5	T4	---	T5	T4	T6	T3	T4	T5	T4
Max. Level Swell [mm]	--	--	--	--	300	>500	>500	>500	156	169
Mixing Press. Inc. [bar]	2.3	1.4	1.7	1.3	0.6	1.8	0.7	0.8	0.3	0.6
Steam Explosion	no	no	no	FCI	no	no	yes	FCI	yes	yes
Max. Press. [MPa]	--	--	--	--	--	--	20	16	17	35
Prop. Speed [m/s]	--	--	--	--	--	--	373	<200	321	454
Conv. Ratio [%]	--	--	--	--	--	--	0.04	0.01	0.02	0.05
Total Debris [kg]	2.6	2.8	1.42	2.8	2.9	2.8	5.0	5.15	2.43	---
Mass Mean Diam [mm]	2.0	3.0	3.0	1.1	1.4	1.7	0.5	1.22	1.0	0.55
Debris<0.1 mm [%]	1.0	1.4	1.4	9.0	1.0	2	24	7.0	14.	22.

NOTES: Jet Diam.[mm] = 30; Fall Ht. [m] = 0.44; Free Vol. [cu.m] = 0.23 Trigger Vol.[cc] = 15

Table 2.9: Summary of KROTOS Experiments with Corium

Table 2.10: Summary of the FARO Experiments

Test Facility & Run No.	Fuel/Coolant Fuel	$T_f/\Delta T_{sub}$ °C	M_f/M_c kg	Test-section H_c cm	D_{po} cm	P_a MPa	Results L.S.[10] m	α %	Remarks
FARO									
L-06	UO_2+ZrO_2[11]	2923/0	18/120	87	10	5.0	0.13	0.13	NE
L-08	UO_2+ZrO_2	3023/0	44/255	100	10	5.0	0.41	0.29	NE
L-14	UO_2+ZrO_2	3073/0	125/623	205	10	5.0	0.60	0.23	NE
L-11	UO_2+ZrO_2+Zr[12]	2823/0	151/608	200	10	5.0	0.80	0.29	NE

[10]Level Swell
[11]80 w/o UO_2, 20 w/o ZrO_2
[12]76 w/o UO_2, 19.2 w/o, ZrO_2, 4.1 w/o Zr

Table 2.11: Simulant Fuels and Coolant used in FCI Studies

Properties	$UO_2/ZrO_2/SS$	Fe/Al_2O_3	U_xAl_y	Al_2O_3	Al	Pb	Sn	H_2O
$T_{f,ref}$, K	2800	2800	1000	2800	1000	1000	1273	300
T_{mlt}, K	1700-2700	1700-2300	905-1230	2313	933	600	505	-
w/o[13], %	75/12/13	55/45	30/70	100	100	100	100	100
m/o[14], %	51/17/32	69/31	5/95	100	100	100	100	100
ρ_f, kg/m^3	7660	3830	3620	3400	2690	10000	6507	997
c_{pf}, kJ/kg K	0.526	1.06	0.86	1.4	1.16	0.15	0.257	4.179
$\rho_f c_{pf}$, MJ/m^3 K	3.997	4.06	3.113	4.76	3.12	1.50	1.672	4.166
k_f, W/m K	8.5	16.5	150	8	230	15	32	0.613
μ_f, mPa/s	5	5	3	3.9	2	2	0.87	0.855
σ_f, N/m	0.5-1.5	0.5-2	1.0	0.5	0.9	0.5	0.53	0.072
i_{fus}, kJ/kg	323	600	318	1000	396	25	59.5	-
β[15]	3.4	4	12.5	3.86	26	2.8	4.58	1
i_{rc}, kcal/g-mol fuel	13.4	5.3	92	-	90	>0	>0	-
E_{sp}[16], MJ/kg	1.65	3.28	0.95	4.50	1.24	0.134	0.310	-
E_{vol}[17], GJ/m^3	12.6	12.5	4.3	15.3	3.33	1.34	2.01	-

[13]Weight Fraction
[14]Mole Fraction
[15]Constant, $(k_f \rho_f c_{pf} / k_c \rho_c c_{pc})^{0.5}$
[16]Total Energy per Mass
[17]Total Energy per Volume

Table 2.12: Large Scale Experiments with Tin (Part I)

Test Facility & Run No.	Fuel/Coolant $T_f/\Delta T_{sub}$ °C	M_f/M_c kg	Test-section H_c cm	D_{po} cm	Trigger Type	MPa	Results Exp. Type	P_{pk} MPa	V_p m/s	CR %	Remarks
Hall [60], Tube Geometry											
2	750/5-15	0.5/0.523	85		DT[18]	-	TE	0.5	300-600	0.13-0.22[19]	Strong Tube
4	660/5-15	0.5/0.523	85		IST[20]	-	TE	0.45	300-600	0.15-0.24	Strong Tube
5	720/5-15	1.2/0.523	85		IST	-	TE	2.4	300-600	0.06-0.09	Strong Tube
7	720/5-15	1.2/0.35-0.4	85		IST	-	TE	16.5	300-600	0.06-0.09	Glass Tube
8	6205-15/	1.2/0.35-0.4	85		IST	-	TE	6	300-600	0.06-0.1	Glass Tube
THERMIR by Briggs [61]											
008	597/93	2.0/20-60[21]	35		-	-	NE	0.2	-		Local Interactions
009	602/90	2.0/20-60	20		-	-	NE	0.2	-		Local Interactions
010	605/91	2.0/20-60	35		-	-	NE	0.2	-		Local Interactions
044	503/88	20.0/20-60	20		-	-	NE	-	-		Local Interactions with Frag'ed Debris
045	797/87	20.0/20-60	20		-	-	NE	0.05	-		Mild Interaction
THERMIR by Fry *et al.* [31]											
061	786/56	-/-	20		MB[22]	-	TE	0.37	35		Open Rect.Vessel
062	786/41	16/-	20		MB	-	SE	0.90	47		Open Rect.Vessel
096	800/24	-/-	45		-	-	SE	1.05	109		Narrow Vessel
107	800/15	6/-	45		DT	-	TE	1.70	81		Narrow Vessel
109	800/14	6/-	45		DT	-	TE	3.40	120		Narrow Vessel
084	300/3	Coherent Interaction, M_f : 5 kg									
087	306/2	Coherent Interaction, V_c/V_f : 4									
095	302/4	Triggered Coherent Interaction, V_c/V_f : 4									
097	300/4	Incoherent Interaction, V_c/V_f : 4									
100	302/5	Incoherent Interaction, V_c/V_f : 4									

[18]Detonator, approximately 0.1 g of PETN

[19]Conversion ratios were calculated by the ratio of the observed impulse (150 - 250 J) to the internal thermal energy of the fuel

[20]Induced spontaneous triggering due to 20 °C of water at the bottom of the test section

[21]These numbers were roughly estimated by the sizes of the test section.

[22]Mechanical blow

Table 2.13: Large Scale Experiments with Tin (Part II)

Test Facility & Run No.	Fuel/Coolant $T_f/\Delta T_{sub}$ °C	M_f/M_c kg	Test-section H_c cm	D_{po} cm	Trigger Type	Trigger MPa	Results Exp. Type	P_{pk} MPa	V_p m/s	α %	CR %	Remarks
Baines [62]	Tube Geometry, Dim : 1m H x 2.95cm ID and 3m H of Expansion Tube											
CT04	670/10	-	100[23]		IST	-	TE	6.0	400[24]			No constraint
CT05	700/21	-	100		IST	-	SE	4.0	1600			No constraint
CT06	730/16	-	100		IST	-	SE	3.3	200			No constraint
CT07	820/7	-	100		IST	-	TE	3.0	110	21	0.39	No constraint
CT08	790/7	0.53/0.87[25]	100		IST	-	TE	9.0	240	23	0.63	Partial Constraint
CT09	840/8	0.53/0.87	100		IST	-	SE	4.0	240	19	0.41	Partial Constraint
CT10	830/7	0.46/0.87	100		IST	-	TE	3.5	140	17	0.49	Partial Constraint
CT11	830/6	0.62/0.87	100		IST	-	TE	3.0	160	30		Partial Constraint
CT12	820/6	0.46/0.87	100		IST	-	TE	-	130		0.19	Full Constraint
CT13	820/10	0.66/0.87	100		IST	-	TE	4.0	120		0.32	Full Constraint
CT14	800/6	0.57/0.87	100		IST	-	TE	3.3	70	20	0.18	Full Constraint
CT15	800/11	0.78/0.87	100		IST	-	TE	3.8	150	10	0.21	Full Constraint
CT16	830/15	0.82/0.87	100		IST	-	TE	3.5	180	10	0.38	Full Constraint
KROTOS	Tube Geometry, M_c/M_f: 1.04 (0.77 assuming 20 % void fraction)											
K-21	1080/13	6.5/6.75	110	>5	Gas	12	TE	6.5	270	20-50	0.054	

[23]Assumed from the length of test section

[24]Choosed largest velocity for propagation speed from the paper reported by Baines

[25]Calculated based on the test section volume

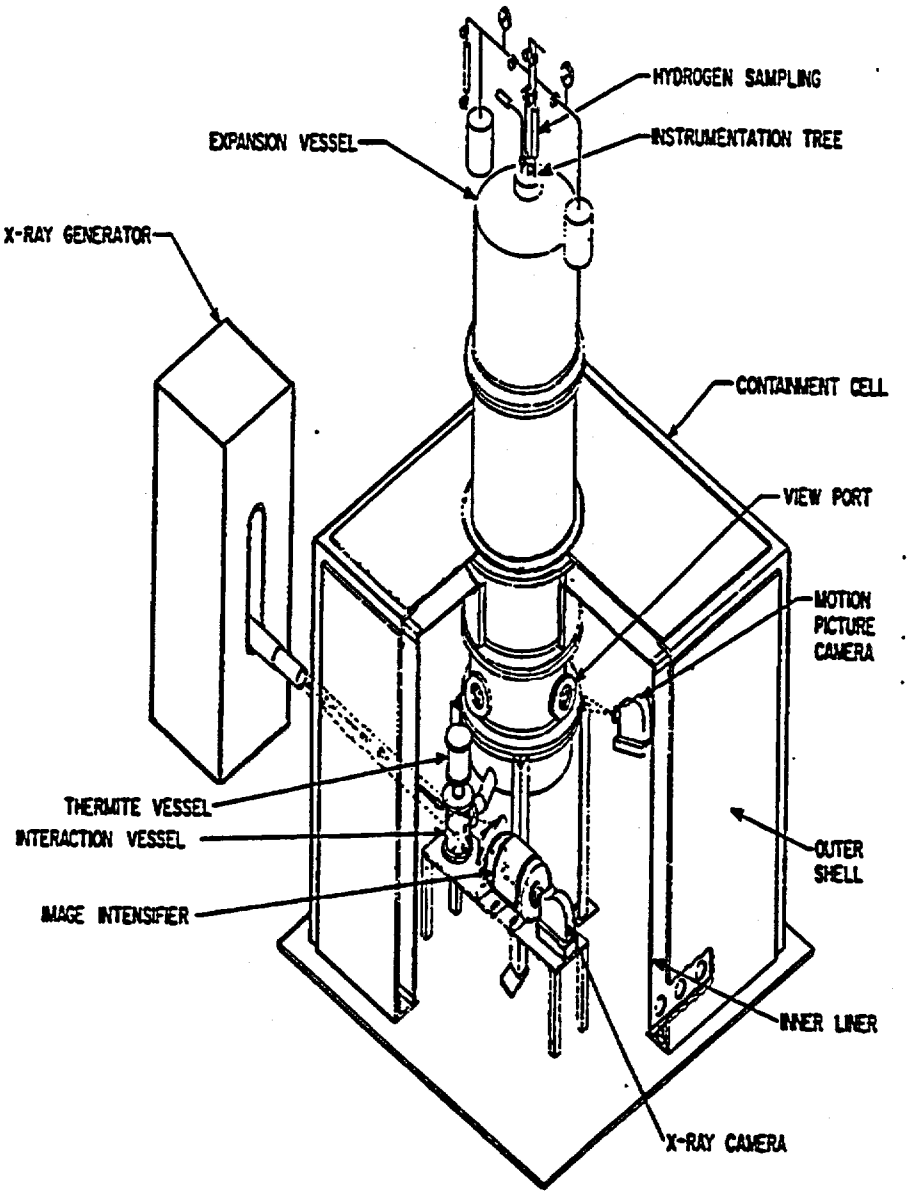

Figure 2.1: Schematic Illustration of the COREXIT Facility [28]

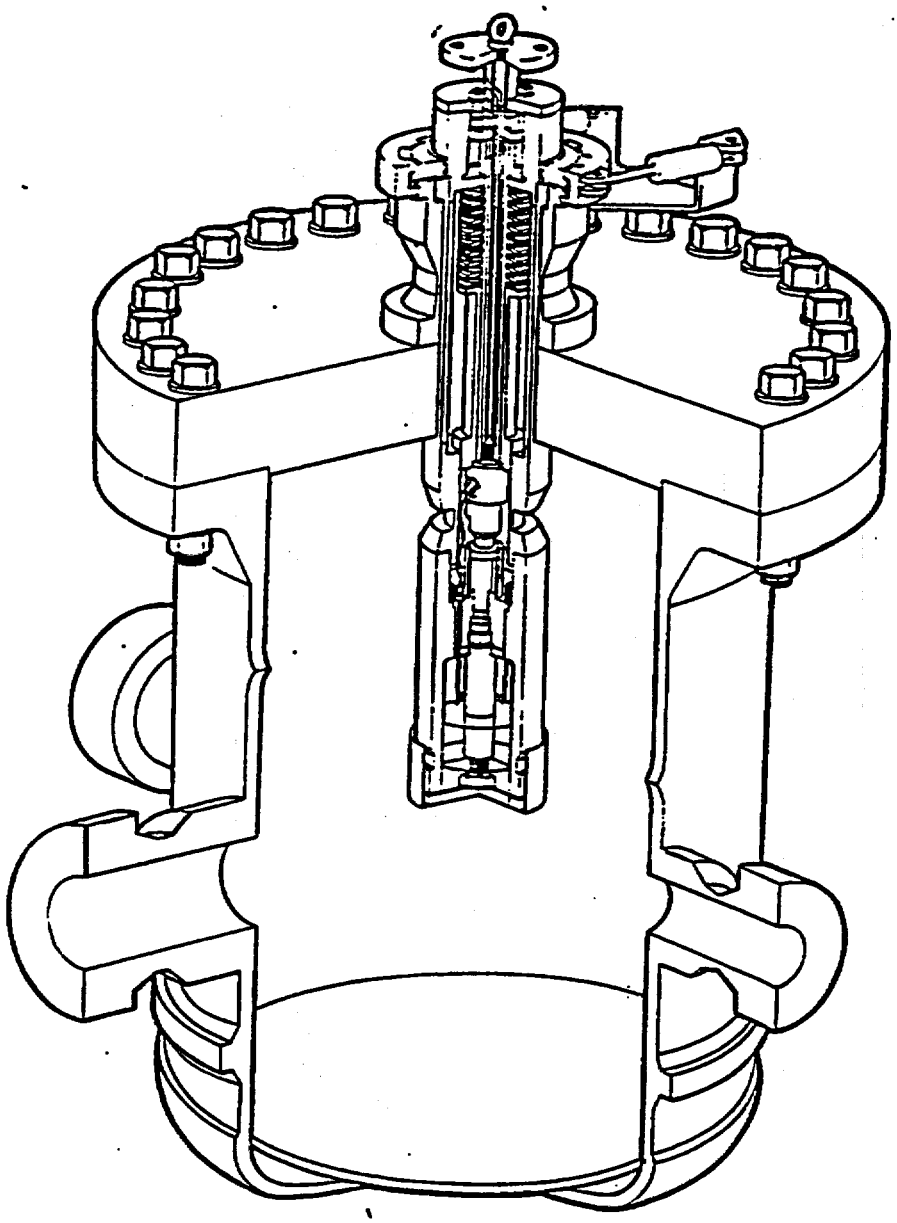

Figure 2.2: Schematic Illustration of the MFTF Facility

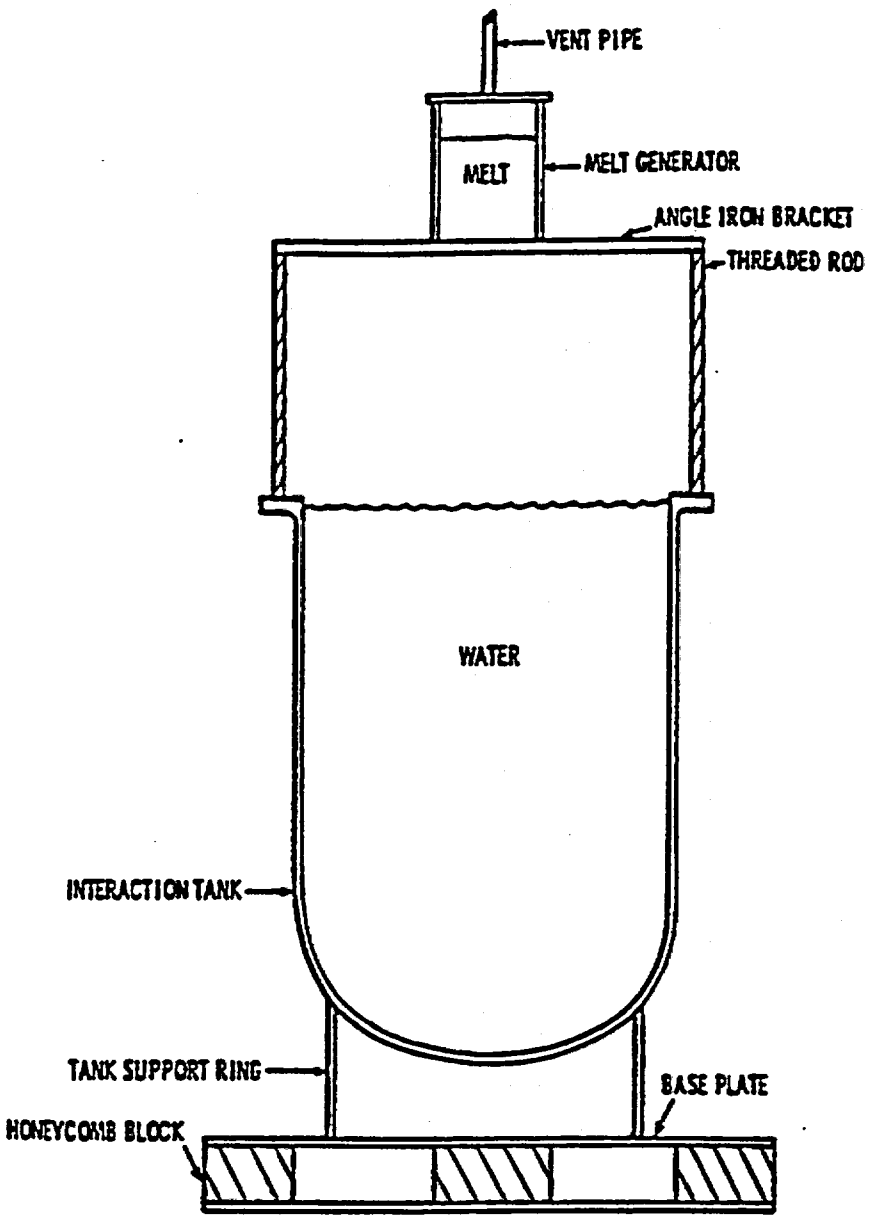

Figure 2.3: Schematic Illustration of the Open Geometry Facility [40]

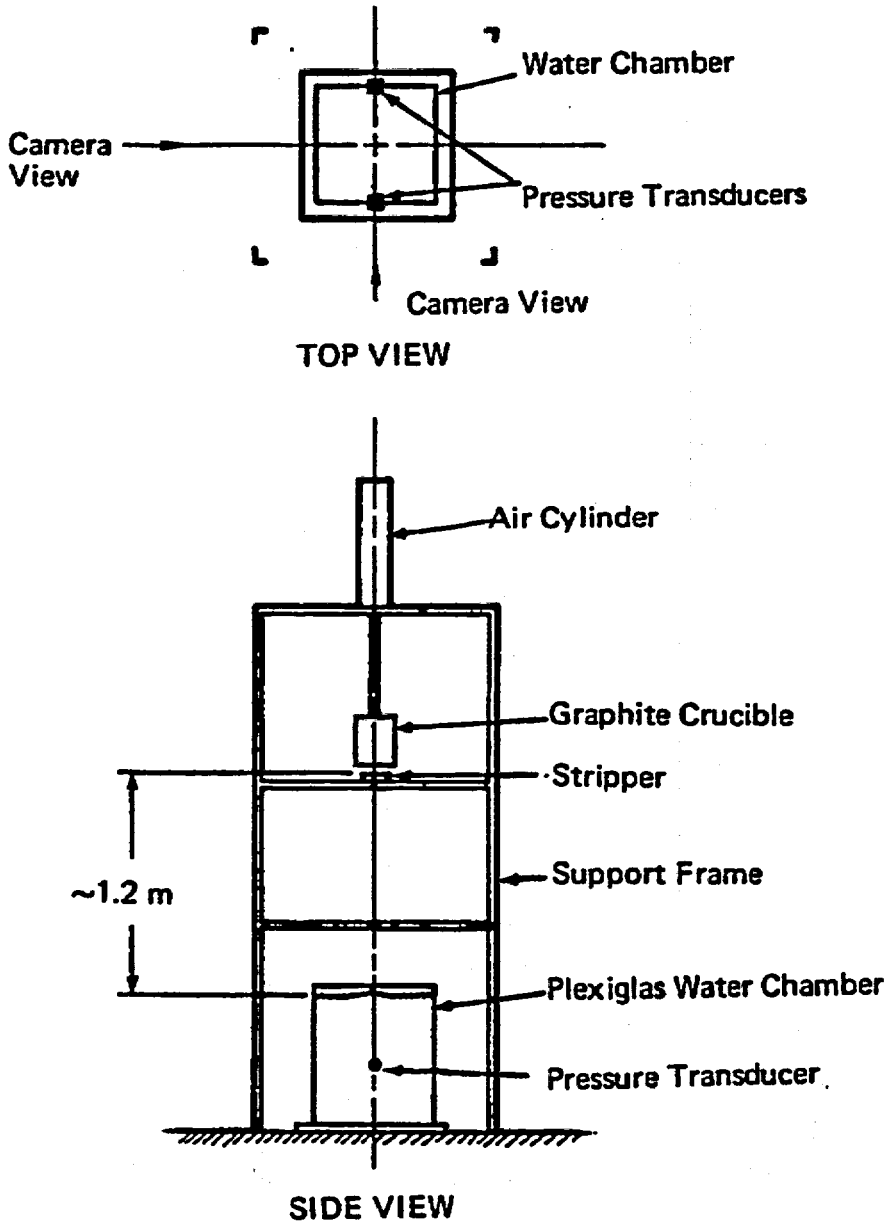

Figure 2.4: Schematic Illustration of the EXO-FITS Facility [40]

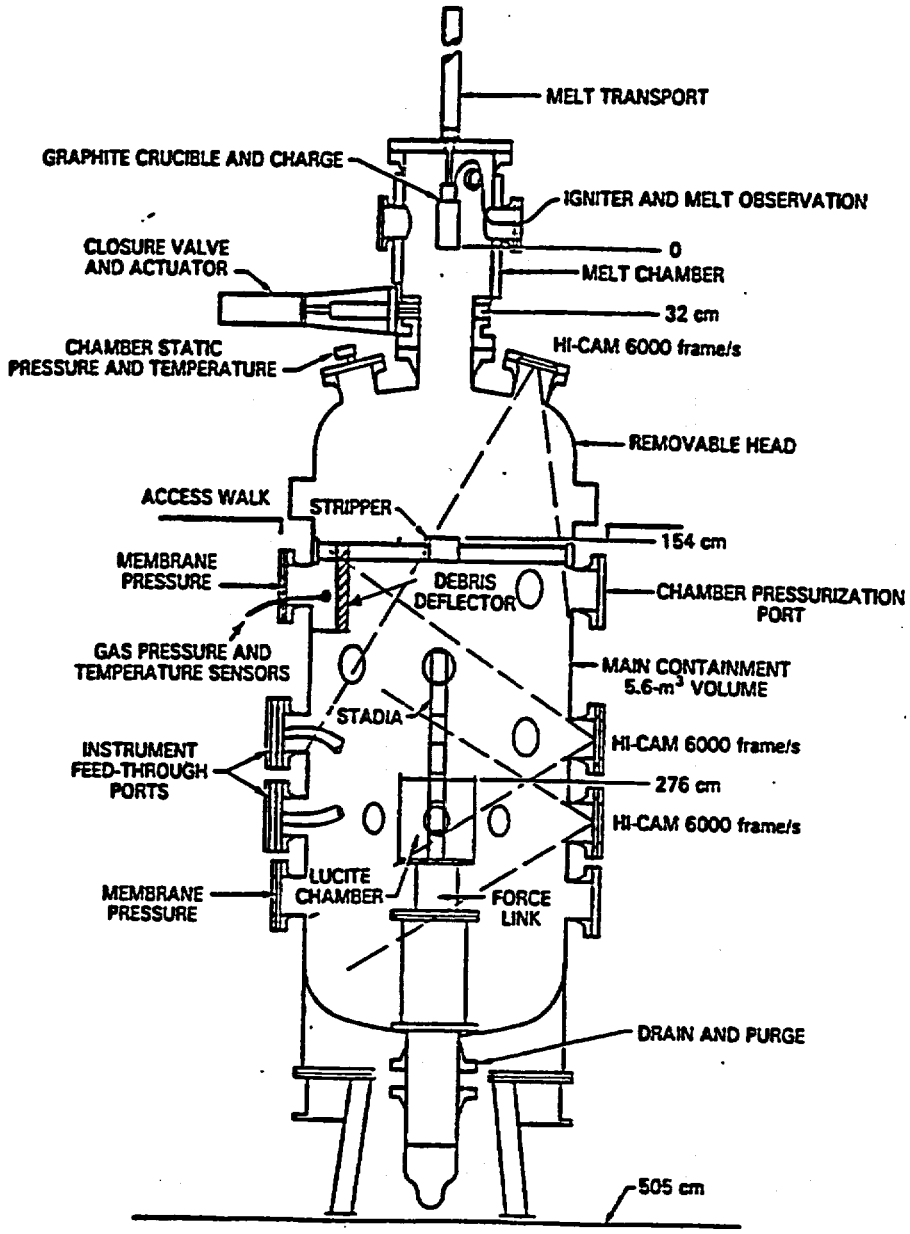

Figure 2.5: Schematic Illustration of the FITS Facility [40]

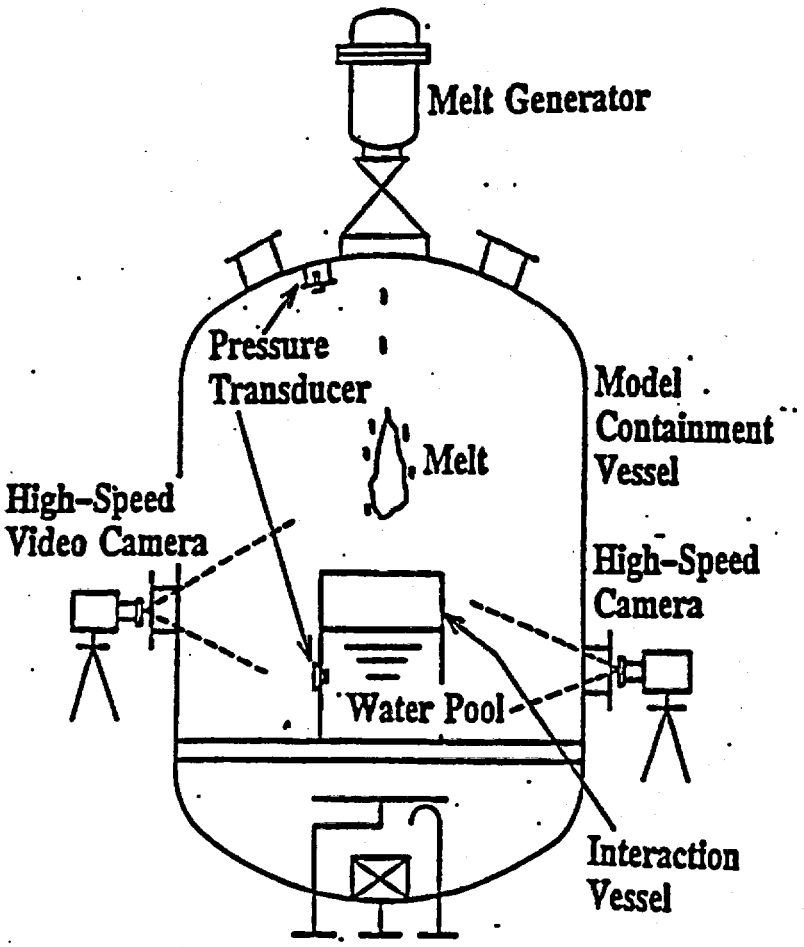

Figure 2.6: Schematic Illustration of the ALPHA Facility [43,44,45]

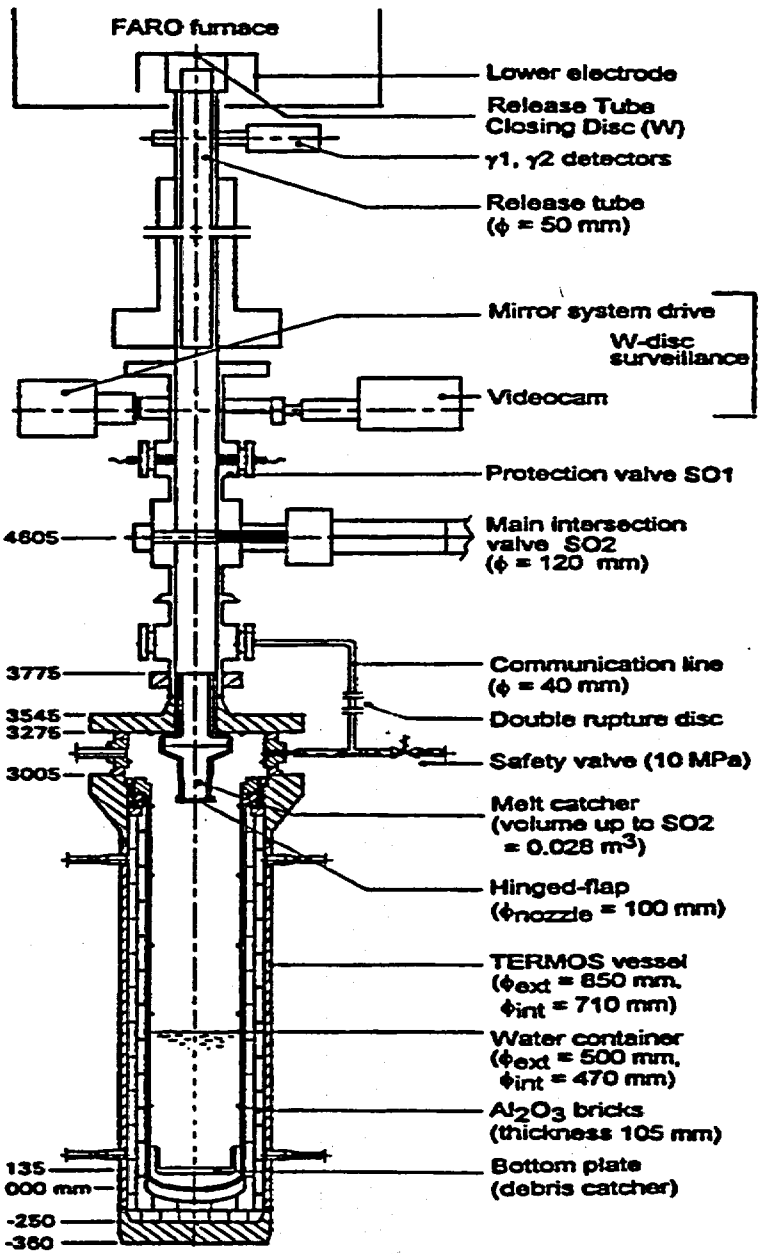

Figure 2.7: Schematic Illustration of the FARO Facility [48,49]

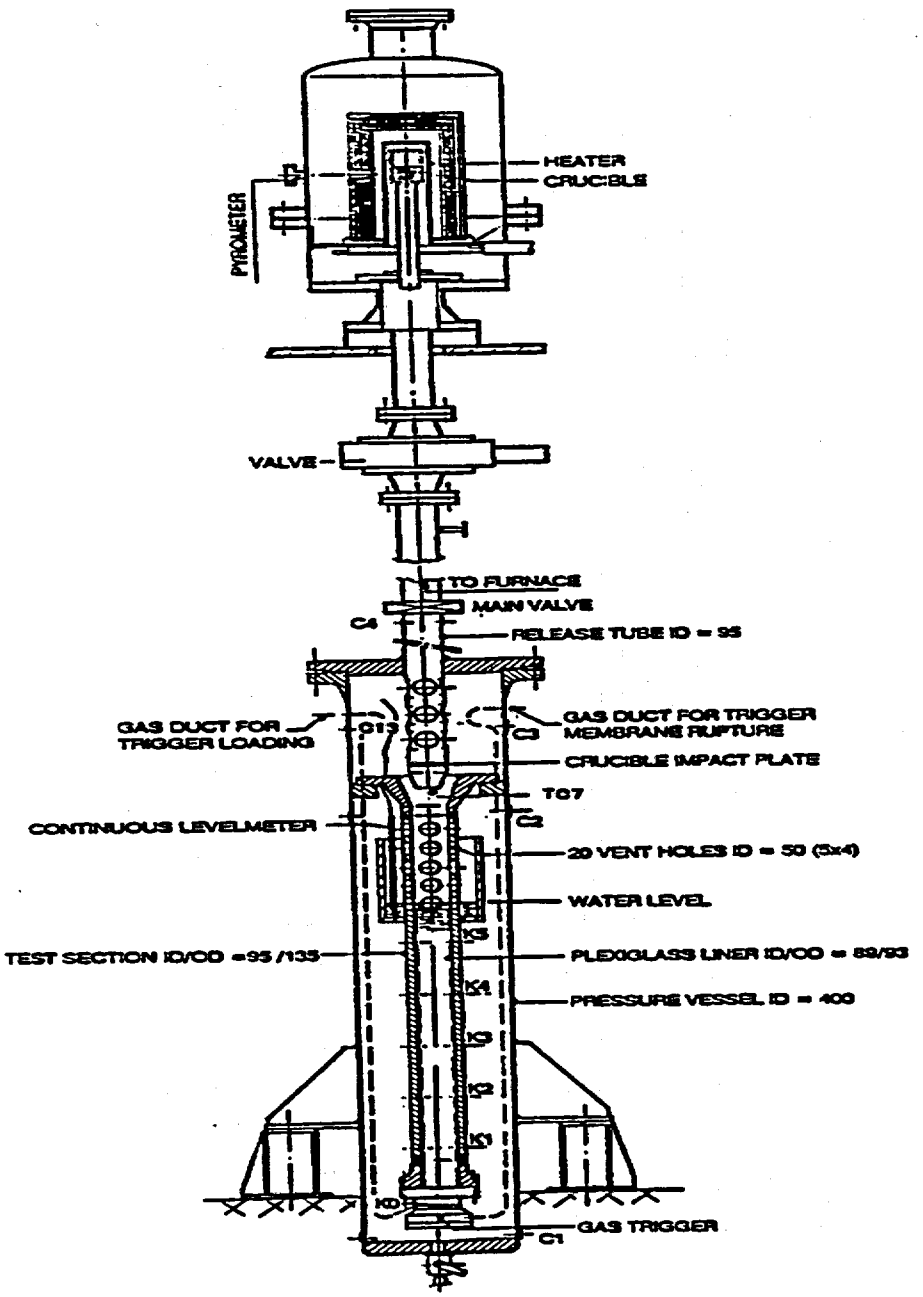

Figure 2.8: Schematic Illustration of the KROTOS Facility [47,48,63]

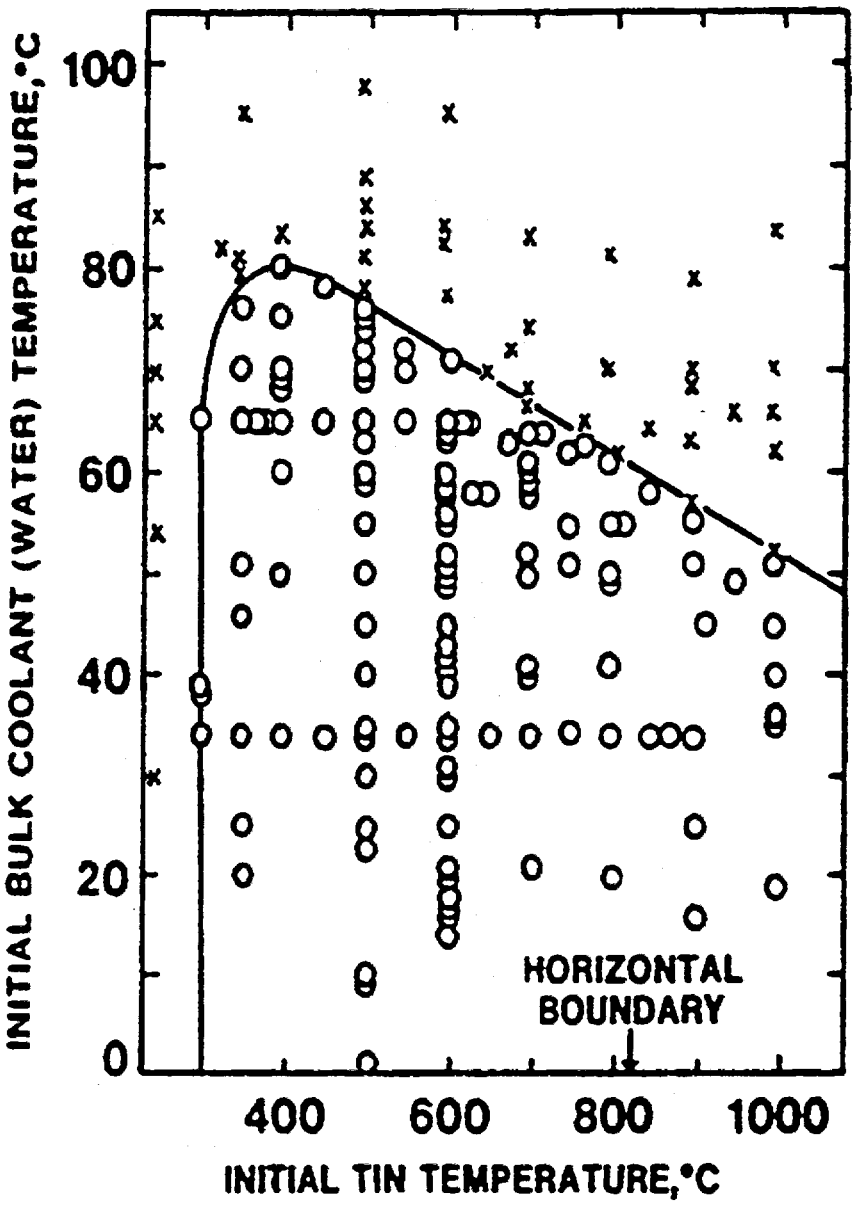

Figure 2.9: Temperature Interaction Zone for 12 g of tin dropped through 3 cm into boiled distilled water: 0 indicates an interaction: X indicates no interaction [52]

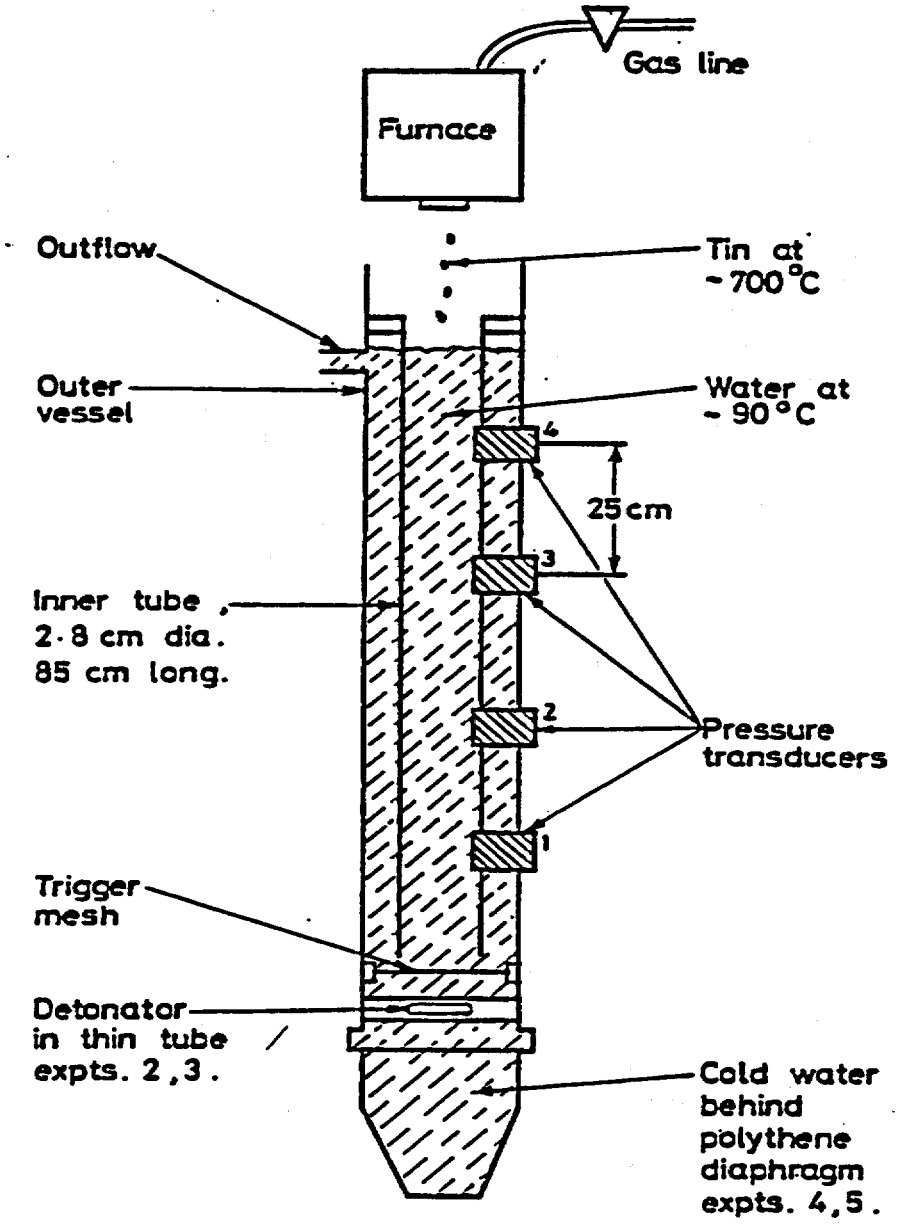

Figure 2.10: Schematic Illustration of the Hall's Facility [60]

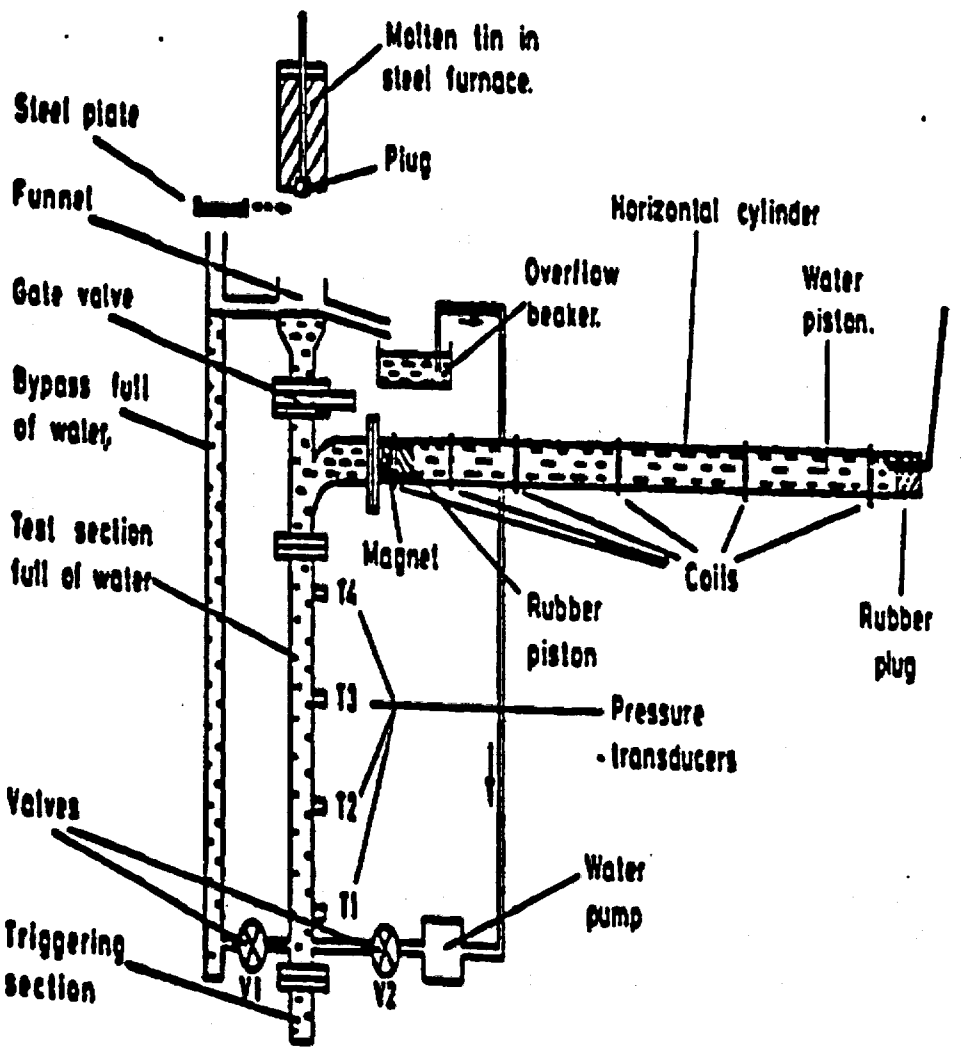

Figure 2.11: Schematic Illustration of the Baines' Facility [62]

Chapter 3

Experimental Description

3.1 Introduction

The Wisconsin Fuel-Coolant Interaction Facility (WFCI) has been constructed at the University of Wisconsin to support FCI research as originally sponsored by the US Nuclear Regulatory Commission (NRC), in particular to perform fundamental experiments in energetic fuel-coolant interactions. The facility was designed with insights and improvements from past experimental facilities of Baines [62] at CEGB and Hohmann [128] at JRC Ispra in which controlled vapor explosion tests were conducted. The experimental test chamber was designed as an approximate one-dimensional geometry (L/D>10). It allows for controlled initial and boundary conditions and for measurements of fuel-coolant mixing and explosion propagation/escalation data such as mixture level swell, spatial and temporal shock pressure histories, explosion propagation velocities, expansion work and fragmented fuel debris distributions.

3.2 Experimental Apparatus

The WFCI facility was originally housed on campus in a below-ground bunker, outside the Engineering Research Building. The roof of this bunker was protected by heavy steel grates that allow for pressure relief, yet provide a barrier to the environment. At this site initial tests were performed including the WFCI-A series. Subsequently, the apparatus was moved to the larger remote laboratory, which was the Physical Science Laboratory Tantalus building, about fifteen miles south at the University of Wisconsin Kegonsa Research Campus. The building is a below-ground vault with concrete walls, floor and ceiling. While the ambient conditions for the experiments at the previous site were difficult to maintain for consistency, the new site provided constant temperature and humidity. The general experimental arrangement is given with side views in Figure 3.1, with the major components identified. Figure 3.2 provides a three dimensional view. The facility includes the furnace, transfer vessel, upper funnel test section and slide gate, explosion test tubes and quench tank and trigger. Figure 3.3 is a front view of the facility which helps to better identify the water loop and bypass loop.

3.2.1 Heating and Transport System

Furnace

The furnace as shown in Figure 3.2 consists of a cylindrical Kanthal Al filament heater embedded in a low "K" factor vacuum cast ceramic fiber insulator. The insulator provides minimum heat loss, high temperature capability and rigid structure. This tube furnace is then encased in a steel outer jacket with support brackets for mounting at a particular location with the ability to rotate or move in place. The furnace is mounted in a vertical position but can be rotated by a motor (Masterflex variable-speed pump motor, Model 7018) with its own solid-state controller through remote operation to a nearly horizontal position. The bottom end section is closed with a round alumina plate insulator and the retort for the fuel fits through the top end section. The overall dimensions of the furnace are: outer diameter of 0.41 m; inner diameter of 0.15 m; length of 0.56 m; heating volume of about 8.3 liters. The temperature rating of the furnace is 1200°C with a heated length of 0.46 m. The single-phase electric power supply consumes 7.4 kW at 208 V. A melt crucible (retort) is placed in the furnace to hold the fuel during the melting process as shown in Figure 3.4. This crucible is made of a ceramic tube (I-MUL900) housed in a stainless steel tube. The stainless tube is supported from below by an alumina brick and from above by a steel ring attached to a pouring tube which transfers the melt to the transfer vessel. At the top of the stainless steel tube is attached a round ceramic collar to reduce the heat loss which results from direct metal-to-metal contact. The furnace is heated in an inert argon atmosphere with temperatures being monitored by a K-type thermocouple; the temperature is controlled by a Single Zone Temperature Control System (ATS series 3821).

For the iron-oxide experiments in the final test series, this furnace could not be used. Rather a furnace with a higher operating temperature (>1600 °C) was needed. We designed and fabricated the furnace box and control system with assistance from regional manufacturers. To accomplish this, a resistance heater fabricated from molybdenum-silicon-carbide was employed with an operating temperature up to 1800 °C. The insulation material was similar to that used in the current furnace; *i.e.*alumina and silica preformed sheets and cylindrical walls. Finally, to hold and deliver the molten iron-oxide, the crucible and retort was fabricated from solid blocks of boron nitride. Although this was an expensive approach, it provided the most reliable containment of this highly corrosive melt. The final result was a furnace with a similar design to our tubular furnace, but with a discharge hole in the retort. The detailed design of the furnace and its operating characteristics and difficulties are described in the Appendices.

Water Loop

To achieve the desired temperature, the water is heated in a boiler and then circulated by a

pump (Grundfos Model UP15-42SF) through the bypass loop as shown in Figure 3.3. The boiler consists of a 60 liter capacity aluminum tank and four 0.8 kW rod heaters. To control the water temperature, one thermocouple is installed in the middle of the water loop. An automatic temperature controller (Omega Model CN9000A) is used for maintaining the water temperature at a preset temperature.

Transfer Vessel

Because of the furnace construction, the tin furnace required a vessel to receive the molten tin and transport it to the WFCI chamber. The oxide furnace was equipped with a blast shield and required no transfer vessel. Once the tin melt is at the desired temperature the furnace is tilted to a horizontal position and the molten tin pours into the transfer vessel. This transfer vessel is then transported to the test section as shown in Figure 3.2. Figure 3.5 shows the transfer vessel and the spring-loaded bottom plug. The transfer vessel is made of alumina (I-COR909) with a spring-loaded stainless steel plug at its bottom. It contains a thermocouple for the measurement of the melt temperature. Fine ceramic powders are introduced for preventing molten fuel leakage from the gap between the transfer vessel bottom hole and the bottom plug. An alumina paper (Zircar-APA-2), with a thickness of 1.3 mm, is also attached to the inside wall of the transfer vessel to prevent crack development from sudden thermal shock between the hot molten fuel and cold ceramic vessel wall while molten fuel is pouring from the furnace into the transfer vessel and being transferred from the furnace to the test section. This paper maintains its rigidity by an alumina hardener (Zircar-A17401) and sustains up to 1650 °C. The transfer vessel can be moved by a motor on a transport rail system to a position over the funnel above the test chamber. At the appropriate moment, a pin holding the spring loaded bottom plug is removed by a pneumatic piston, the plug falls away and a melt jet pours into the test chamber.

3.2.2 Test Section

Funnel

The funnel as shown in Figure 3.2, is a stainless-steel type 304 schedule 160 with an outer diameter of 0.32 m, an expanded section of the test chamber. The funnel can hold a volume of about 0.038 m^3 of water. As the melt pours into the test section any water displaced from the test tube, due to the fuel or vapor production, is collected in this funnel and the level swell meter (discussed in next section) records the overall water level swell.

Slide Gate

The slide gate system is composed of a top and bottom stainless steel 304 flange, 25.4 mm thick and 0.38 m long stainless steel 304 plate with an 87 mm diameter hole and an air

cylinder to pull the slide gate plate. The schematic of this system is shown in Figure 3.6. Teflon dry lubricant is applied on the entire surface of the slide gate to allow the slide gate plate to move smoothly and prevent the surface of the slide gate from scratching. After a designated time to allow the fuel and coolant to mix, the stainless steel slide gate separating the explosion tube and the funnel is closed, isolating the mixture from the environment: at this time the fuel-coolant mixture is isolated and resides in the explosion tube.

Test Tube System

The test tube system shown in Figure 3.2 is composed of two tubes; one is a stainless steel cylinder Type 304, 101.6 mm NPS, Schedule 160 (called the I-tube) with an outer diameter of 114 mm, an inner diameter of 87 mm, and a height of 914 mm, and has a volume of 0.055 m^3. The other is a stainless steel tube (called the T-tube) with the same material and dimensions except a different height of 546 mm, which contains a water volume of 0.033 m^3. The total volume of the test tube system is 0.087 m^3. Along the test tube are mounting locations for high-range quartz pressure transducers. Near the bottom of the I-tube, a stainless steel bypass pipe, shown in Figure 3.3, is also provided to allow for heating of the water in the explosion tube and bypass of water flow as fuel-coolant mixing occurs. This bypass piping, if open during testing, can also provide for the water coolant to flow out of the mixing region as the fuel enters the chamber. This creates an additional path for coolant up and around the fuel-coolant mixing region during the FCI and before the vapor explosion.

Trigger Device

The trigger device shown in Figure 3.7 is a movable piston located in the lower explosion tube end plate. The sudden motion of this piston generates a shock wave (up to ~4 MPa for 170μs) in the water which then propagates into the fuel-coolant mixture to trigger the explosion. The piston is set into motion by the mechanical impact of an electromagnetic hammer from below. Initially the trigger system is prepared by charging a capacitor bank (0~500 VDC) at a preset voltage. If an external trigger signal is provided at a preset time, a sudden discharge of the capacitor bank initiates. This sudden discharge generates the electromagnetic force that causes the hammer movement. The trigger circuitry as shown in Figure 3.8 is used to provide the fast switching of high voltage and current from the capacitor bank. The capacitor discharge voltage, the hammer geometry, and the spacing between the piston and the hammer can be varied to tailor the initial pressure shock wave pulse height and width.

The pressure shock generated by the trigger device is produced by applying a mechanical impact to the trigger piston using an electromagnetic force generated by the sudden discharge from the capacitor bank. The sudden motion of the electromagnet produces an impact to the trigger device via a stainless steel rod which is directly attached to the

trigger piston disk. Motion of the magnet is actuated by an electrical circuit, shown in Figure 3.8, which consists of a variable DC power supply (0~500 VDC), a capacitor bank and a trigger circuit. In order to obtain a high current to the magnet, the capacitor bank is initially charged at a desired DC voltage and the fast switching to the magnet is made by a Silicon Controlled Rectifier (SCR) shown in Figure 3.8. The strength of the pressure shock is controlled by the applied DC voltage. The relationship between the charged voltage and corresponding pressure shocks will be discussed in a later section.

In order to measure temperatures in the test tubes and detect the melt during the mixing phase of the fuel-coolant interaction, a total of eight exposed K type thermocouples with 0.02 inch diameter stainless steel sheath are mounted on the test tubes. All eight thermocouples, as well as three for the transfer vessel, and those at the bottom of the test section and water loop are connected with the 16 Channel Thermocouple FET Multiflexer (HP E1353A) which has a scanning rate up to 13000 channel/s and a built-in thermister reference junction. The signals from the multiflexer are digitized by the Digital Multimeter (HP E1326B) with 14-bit resolution, a maximum 14 kHz scanning speed and 1 Mbyte non-volatile memory. All the temperature measurement systems are housed in the HP E1301A B-Size VXI Mainframe.

Expansion Tube

Once the explosion is triggered the subsequent expansion is directed down the stainless steel expansion tube which is composed of three identical tubes (one with a different flange) in series (Type 304, 4 inch NPS, Schedule 160, class 600 flange, class 1500 flange, 87 mm inner diameter, 1.22 m long), as shown in Figure 3.2. At the end of the expansion tube, a rupture disk (a 1 mil thick Kapton film which bursts at about 0.23 MPa differential pressure) is attached to hold the coolant in the system during the mixing phase. The rupture disk can be easily ruptured to release the expanded volume of coolant in the system for the expansion phase. A movable piston, which has a magnet at the center, is initially located in between the test tube and the expansion tubes. As the vapor explosion pushes the piston down the expansion tube, ten coils, wound outside the tube, sense the location of the piston as a function of time. The distance between the adjacent coils is evenly divided in 0.41 m segments. Water and/or lead blocks can be placed within the expansion tube to vary the inertial constraint of the system for the vapor explosion process. The explosion expansion products are captured in the downstream quench tank.

Larger Scale Test Section - WFCI-2

Two different test sections were used for the WFCI final test series (series K). The first test section is the same as that described above, referred to in this section as WFCI-1. The other test section is larger and has an inside diameter more than twice that of the smaller section. It will be referred to as WFCI-2 throughout this report. Both test sections are

rated to 3000 psig and are made of type 304 stainless steel pipe (NPS schedule 160). This larger test section was constructed to examine the effect of the lateral scale on the FCI, specifically with the iron-oxide melt.

The WFCI-2 test section is made of 8 inch NPS schedule 160 type 304 stainless steel pipe with inside diameter 6.82 in (173 mm) and wall thickness 0.91 in (23.1 mm). It is similar in geometry to the smaller diameter tube and is divided into two pieces, an I-Tube and a T-Tube, that are secured with NPS class 1500 type 304 stainless steel flanges. The I-Tube is 36.0 in (914 mm) tall and is the lower of the two pieces. It is mounted directly above the piston and base flange and also has a flanged opening near the bottom for the water return loop. The WFCI-2 I-Tube has a 21.5 L volume. Five pressure transducers (P1 through P5, numbered from bottom to top) are mounted along its length on the same side as the expansion tube opening. The T-Tube is 21.5 in (546 mm) in height, is mounted on top of the I-Tube, and facilitates the connection of the expansion tube. The WFCI-2 T-Tube has a 12.8 L volume. Three pressure transducers (P6 - P8) are mounted along its length on the side opposite the expansion tube opening.

3.3 Instrumentation and Data Acquisition

3.3.1 Instrumentation

The main physical parameters measured in the WFCI experiments are the transient pressures, temperatures and level swell histories as well as piston-slug displacement during the fuel-coolant interaction. Temperatures of the furnace, melt and water are monitored by K-type thermocouples located at the furnace, water loop, magnet trigger piston and test tubes. A video camera records the whole sequence of the experiment. Since the phenomena in this study are of a fast transient nature, a high speed, computer-based data acquisition system is used for digitizing and storing the analog signals. The following are details of the instrumentation and data acquisition system.

Transient Pressure and Temperature

The test section has been designed to accommodate up to eight high sensitivity piezoelectric pressure transducers (PCB series 112A03) for pressure signals during the explosion phase as well as the mixing phase. These are flush-mounted on the test tube. All locations and distances of transducers are shown in Figure 3.3. Each transducer is connected to a charge amplifier (PCB Model 462A) for converting electrostatic charge (1.0 pC/psi nominally) into a voltage output. The charge amplifier has multi-range (unit/volt) capability, thus a higher resolution can be obtained in the digitization by adjusting the full voltage scale. To attenuate high frequency noise (>180 kHz), each charge amplifier has a plug-in

filter (PCB Model 476A07). Low noise coaxial cables (PCB 003A35) are connected between the transducers and charge amplifiers. All pressure transducers have response frequencies greater than 10 kHz and the signals are recorded via a high speed A/D buffer interface (up to 1 MHz).

Several thermocouples (Type K) are used to monitor the melt temperatures in the furnace and transfer vessel, as well as the water temperature in the test tube. In addition, thermocouples are placed in the explosion tube at various heights to detect the leading edge of the fuel jet as it pours through the explosion tube and mixes with water. Thermocouples for detection of the fuel jet during the mixing phase are mounted on the test tube and are selected by response time. One of these thermocouples is used to control the water temperature in the test tube and connected to a temperature controller (Omega Model CN9000A) which maintains the water at a preset temperature.

Level Swell Meter

A level swell meter, shown in Figure 3.9, is used to measure the level swell in the funnel above the test section during the fuel-coolant mixing phase. The integral vapor volume fraction during mixing can be calculated from the signal measured from the level swell meter. The level swell meter is composed of two copper tubes with an outer diameter of 13 mm attached parallel to each other on the funnel side wall. The level swell with time is measured by the resistance changes between the two copper tubes. When the working voltage is supplied, however, the voltage generated by the level meter slowly decreases with time and also with the coolant temperature because of a slow degradation of the copper rod surface with time and temperature while electric power is supplied. The level swell, however, can be estimated by measuring the proportionality constant of the relationship between the water levels and the measured voltages from the initially known water level at the initial temperature and its corresponding voltages.

In the current test series the inductive level meter was not always utilized because weak explosions were triggered with residual tin melt at the water surface above the slide gate. This altered the signal and at times destroyed the metering system. When no energetics interactions occurred we were able to obtain data which will be subsequently discussed. To improve on its reliability and accuracy, the meter should be repositioned so it can be used in future tests. The level meter (OMEGA LD300-250) is intrinsically AC operating LVDT with ±10" linear stock, 0.25% full scale linearity and 2 ms frequency response. This meter incorporates an AC LVDT signal conditioner (OMEGA LDX-3) which provides ±5 VDC analog output.

Slug Displacement

The location of the piston as a function of time is measured by installing electrical coils

along the expansion tube that sense the magnetic core piston passing each coil location at a particular time as shown in Figure 3.10. This figure shows the series of signals generated when the piston passes through the series of coils. As the piston approaches the coil at point 1 as shown in Figure 3.10, the magnitude of the signal is positively increased. If the piston is just passing the location of the coil, the magnitude of the signal is rapidly falling down to zero as indicated at point 2. Finally as the piston begins passing away, point 3, the magnitude of the signal is rapidly increased in the negative value and then approaches zero asymptotically. Therefore, the exact time for the piston passing the coil is measured at point 2 as shown in Figure 3.10. From these data and the fact that all the explosion expansion products are directed through this tube, the explosion expansion work can be calculated.

3.3.2 Data Acquisition and Experimental Control

Figure 3.11 provides the overall facility layout and identifies the data acquisition systems and experimental control. A 486 PC based CAMAC system (LeCroy) is used for digitizing and storing the fast transient signals from the instruments. It includes four 12-bit digitizers (LeCroy 8200) with a 32 K memory module (LeCroy 8800A). Each digitizer has four input channels with 1 MHz maximum sampling rate per channel. The A/D system, T/C amplifiers, trigger control, pressure transducer amplifiers are located in the off-site control room and the signals are transferred to the off-site computer. In addition the computer and off-site timing control circuit are used to automatically control the operation of any test. Once the melt is remotely poured into the transfer vessel and the transfer vessel is remotely moved into position above the test section, the experiment enters an automatic sequence controlled by electronic timing circuitry as shown in Figure 3.12. As the melt pours into the funnel, the timing circuitry provides a sequence of events to close the slide gate, isolate the bypass loop, and initiate two simultaneous trigger pulses. One of the trigger pulses is for actuating the external trigger system; the other is for triggering the data acquisition system to begin recording the mixing process and the explosion event.

Timer

Two sets of timer blocks (called TA and TB) are connected between the power lines to actuate the specified automatic experimental sequence. Each set of timer blocks has two timers (called TA1, TA2, TB1 and TB2) as shown in Figure 3.12. The timers in the first block, TA1 and TB2, count a preset time (1 s) from reception of the arrival signal of the transfer vessel from the limit switch on top of the funnel. After one second, the bottom plug beneath the transfer vessel is opened by the TA1 which allows melts to be poured from the transfer vessel into the test tube. At the same time the second block of timers is triggered by the TA2. The first timer in the second block, TB1, starts counting the preset

time from reception of the TA2 signal and provides electric power to the slide gate system to be closed. Finally, the second timer, TB2, provides a signal to the external trigger and the data acquisition systems to be actuated. Each timer (335B Shawnee Timer) is a digital set and solid state timer with 10 ms resolution.

3.4 Initial and Boundary Conditions

Sixty experiments in separate test series have been conducted with tin as the simulant fuel material and water as a coolant to investigate the energetics of fuel-coolant interactions. In addition, we finished testing in the WFCI facility with a series using molten iron-oxide as the fuel. Each set or series of tests focused on particular initial or boundary effects on FCIs. The WFCI-A series tests were conducted for the repeatability of the WFCI facility with all conditions fixed. The WFCI-B series of tests were performed to investigate the spontaneous explosion conditions at the same experimental conditions as the WFCI-A series but without an external trigger. As one of the key boundary conditions, the effect of the external trigger strength on the energetics of FCIs was investigated in the WFCI-C series. The effect of a system constraint, another important boundary condition, was studied in the WFCI-D series. To study the effects of the initial conditions such as fuel temperature and coolant temperature, the WFCI-E and F series, respectively were conducted with varying temperatures. In the WFCI-G series, the effect of one coolant property, coolant viscosity, was investigated. For this test, water as a coolant was mixed with a certain amount of polymer to alter its viscosity. The WFCI-H series was performed by varying the mass of the fuel and other jet parameters to observe the effect of the fuel to coolant mass ratio on FCI energetics. Finally, we performed a series of twelve tests (WFCI-K series) with iron-oxide as the molten fuel. The purpose of these tests was to observe explosion energetics when a high temperature molten oxide is used at prototypic melt superheats. In the prepartion for this final test series a number of oxide melt delivery and melt preparation tests were conducted, but will not be reported in detail here.

3.5 General Experimental Procedures

3.5.1 WFCI-A, B, C, E, F Series

Every series of tests has the same procedure to investigate the fuel-coolant interaction phenomena with changing specific initial and boundary conditions. After the set-up of the WFCI facility, water is heated up to a preset temperature (typically 86 °C) in a boiler. The pump circulates the heated water from the boiler to the test section through the water

loop. About one hour before the actual test the entire system (including water and test tube) is heated up to a preset temperature (about 3 hours from starting circulation of the water), the furnace is turned on to start heating the melt (tin) up to a preset temperature (normally 1100 °C). The argon gas is supplied to the retort in the furnace before the furnace is turned on in order to produce an inert environment. It takes about 1 hour to achieve 1100 °C for the molten tin. While the water and tin are heating, all instruments are prepared in stand-by condition. After all the instruments are set in stand-by and the preset temperatures of water and fuel are achieved, the video camera recorder is turned on to film the whole sequence of the experiment. First, the furnace is turned to pour the molten fuel into the transfer vessel via manual operation from the remote site control area. The complete furnace tilting process is indicated by a signal from the furnace limit switch located above the furnace. When completion of the furnace tilting process is assured, the transport process starts with the turning of another manual switch in the remote site control area. At the top of the funnel is another limit switch which indicates the arrival of the transfer vessel in the proper position. When the limit switch is activated by the arrival of the transfer vessel, the rest of the experimental sequence (including opening of the transfer vessel to pour the transported molten fuel, closing of the slide gate, closing of the bypass valve, triggering the external trigger system and the D/A systems) are governed by the timers described in the previous section.

For all series of tests, the experimental procedures are similar but preparations are a little different for specific tests due to the different purposes of the experiments. In particular the following three series of tests, the WFCI-D, G and H will be discussed in more detail.

3.5.2 WFCI-D Series

The system constraint for a typical series of tests is provided by filling up the expansion tube with water. The degree of the system constraint or slug mass is defined by the initial total mass in this tube. Since the vapor expands due to the explosion in the expansion tube, it is expected that the mass of the slug in the expansion tube would affect the explosive interaction. To adjust this degree of system constraint in the D test series, two different methods are introduced to vary the total mass of the slug: the first is to change the mass of water, installing the rupture disk in conjunction with the test tube and the expansion tube. This method provides the minimum degree of system constraint in this series of tests. The second is to add lead slugs with a diameter of 73 mm and a length of 100 mm in the expansion tube, as a more massive slug for the explosion with the slug length being maintained.

3.5.3 WFCI-G Series

Based on previous studies [69], Polyethylene-oxide (PEO) with an average molecular weight of $4x10^6$, was selected as the polymeric additive in this study. Polymeric solutions with polymer concentrations of 400, 600, and 800 wppm are prepared by slowly adding the polymer in the form of a powder into distilled water while the water was stirred using a motor-driven stirrer. The stirring continues for another 16 hours at slower speed until the polymer dissolves completely. The viscosity of the solution is measured with a size 50 Cannon-Fenske type capillary viscometer. The viscosity ratios, η_r, of resulting solutions are shown in Figure 3.13 as a function of polymer concentration at 25 °C. Also in this figure, computed values using an empirical equation [129] are compared with the measured data. For each experiment, about 12 liters of polymeric solution is prepared for the desired concentration at room temperature. The polymer solution is poured into and stored in the test section at a temperature of 24 °C.

Table 4.1 indicates that two different molten tin masses of 2.4 and 5 kg were used to examine the effect of mass scaling on the FCI suppression by polymeric solution. An external trigger of magnitude 3 MPa was provided only in the WFCI-G-02 test to examine the effect of an external trigger on the FCI with polymeric additives. Two tests with pure water were conducted as a control to compare the effects of polymeric additives.

3.5.4 WFCI-H Series

In this series of tests, to control the amount of the fuel mass mixed with the coolant during the mixing phase, four different methods are possible: change the fuel pouring time, control the bypass valve opening during the mixing phase, change the pouring diameter or change the inner diameter of the test section. Among these, the first three methods were initially employed. In the final test series (K series), we constructed the WFCI-2 explosion tube and thus, the inner diameter of the test section was also varied.

The first method was introduced in the WFCI-H-02 and H-03 tests. In these tests, the pouring time is defined by the time period between the time of the bottom plug opening and that of the slide gate closing. The pouring time was increased from 1.5 sec to 1.9 sec in this test series. In the WFCI-H-04 test and most of the subsequent tests, the bypass valve was opened to allow more molten fuel to be mixed with water during the mixing phase of the vapor explosion. The bypass valve was then closed when the slide gate was closed. This would occur since the water would have an alternate flowpath in addition to counterflow upward through the fuel-coolant mixture. Finally, the fuel jet pour diameter was varied from 20 to 45 mm over these tests to produce a wider range of fuel pour rates.

3.5.5 WFCI-K Series

The general procedure for experimental preparation was similar for these molten oxide experiments as in the case of the molten tin experiments. However, certain aspects of the melt preparation are distinctly different and need to be briefly explained. Up to the point of iron-oxide melting the process is quite similar. Approximately 1 hour into the water heating, the furnace was readied for operation. Pneumatic cylinders were activated that hold a safety catcher pan in place underneath the furnace and a radiation shield closed at the bottom to prevent heat loss. The power circuit was activated, and the power level was manually controlled to prevent large current changes through the elements. The power was ramped up to maintain a 120 amp current at all times. It took approximately 2 hours to reach 1700 °C. During this waiting period, the areas around the test section were covered with fiberglass cloth to protect from damage that could be caused by high temperature ejected molten debris. Two video cameras were positioned to tape record the experiment, and the data acquisition system was tested to insure all the desired data would be captured at the right time.

When the melt was close to the desired temperature, the trigger capacitor bank was charged and the water heating circuit (if loop heating was used) was deactivated by shutting off the pumps and the heaters. Then the water level in the test section was lowered to a point near the bottom of the funnel. This was done to limit the amount of water the fuel jet must travel through to penetrate the test section, and it allowed for greater water level swell without overflowing. Then the rod that held the slug in place was removed, and when the furnace temperature reached 1700 °C, the test area near the test section was evacuated. The furnace catcher pan and shield were controlled remotely, and moved out of the way. Then the timing circuit was activated, and the test was initiated. Immediately after the test, the water was drained out of the test section and kept for processing. Then the test section and furnace were completely disassembled for cleaning and repair. The collected water was filtered through a 25 micron sieve to capture as much of the small debris as possible. Other remnants of iron oxide were removed from the bottom of the test section and scraped off the internal surfaces of the test section. All the debris was consolidated based on the location it was recovered from and weighed.

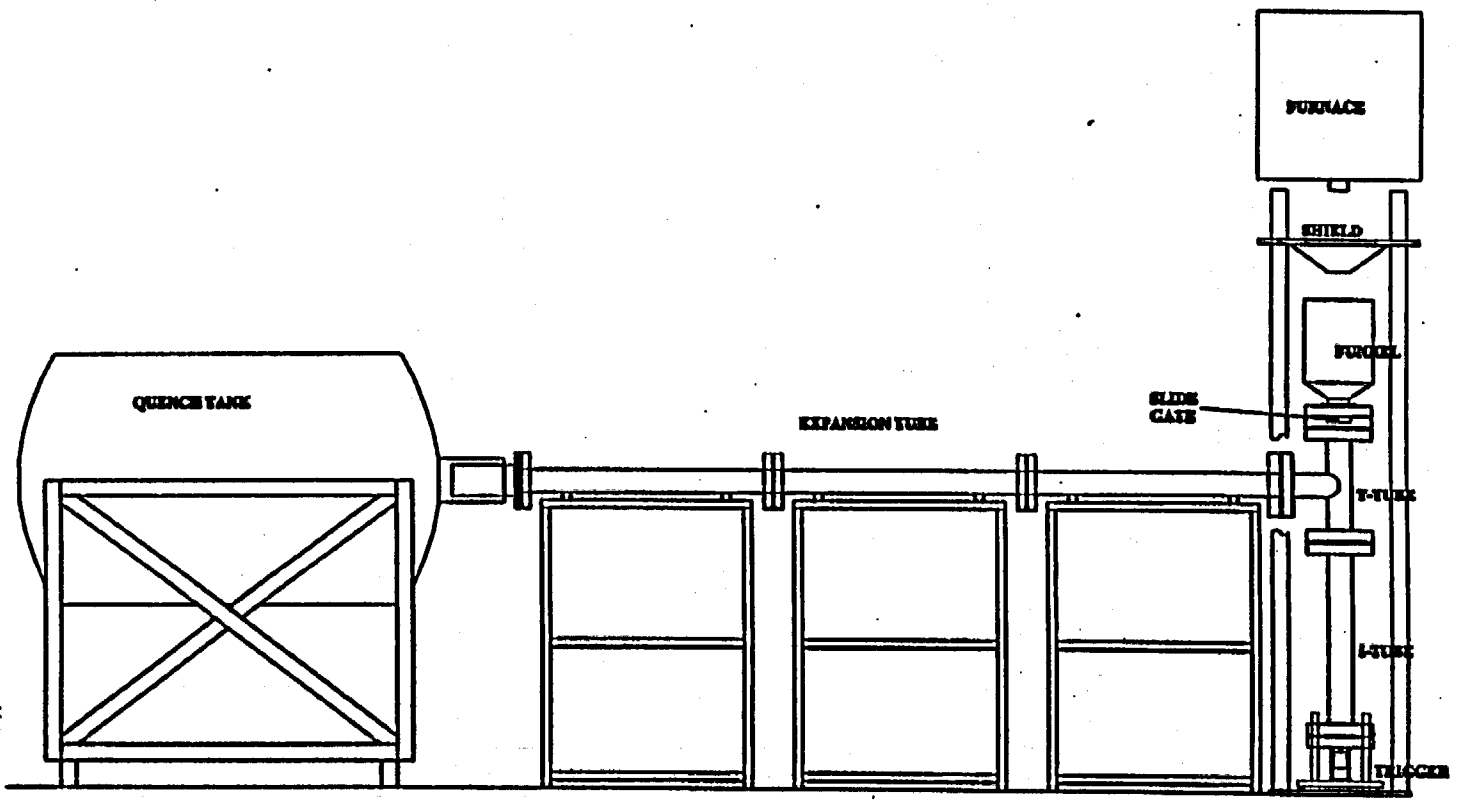

Figure 3.1: Overall Side View of the WFCI Facility

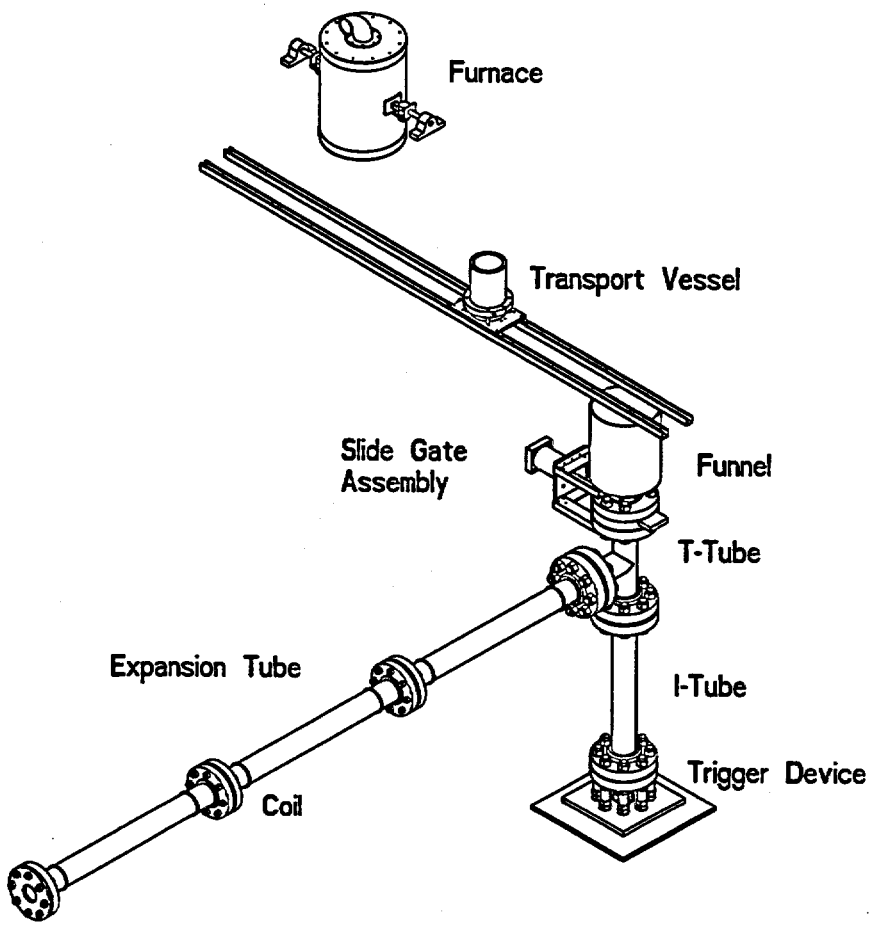

Figure 3.2: Overall Three Dimensional View of the WFCI Facility

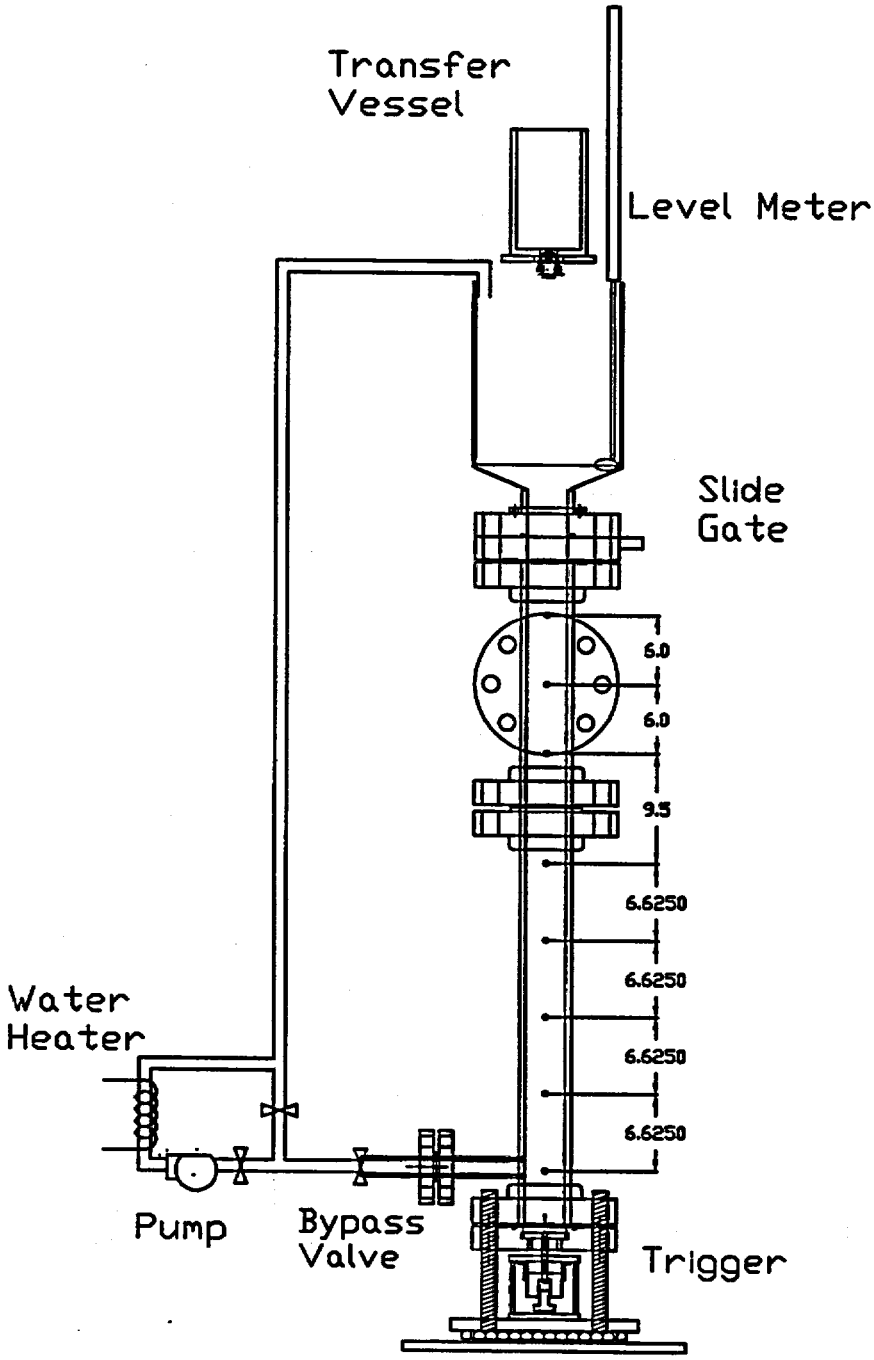

Figure 3.3: Schematic Illustration of the Front View of the WFCI Facility Including the Simplified Waterloop and the Location of the Pressure Transducer (Unit:Inch)

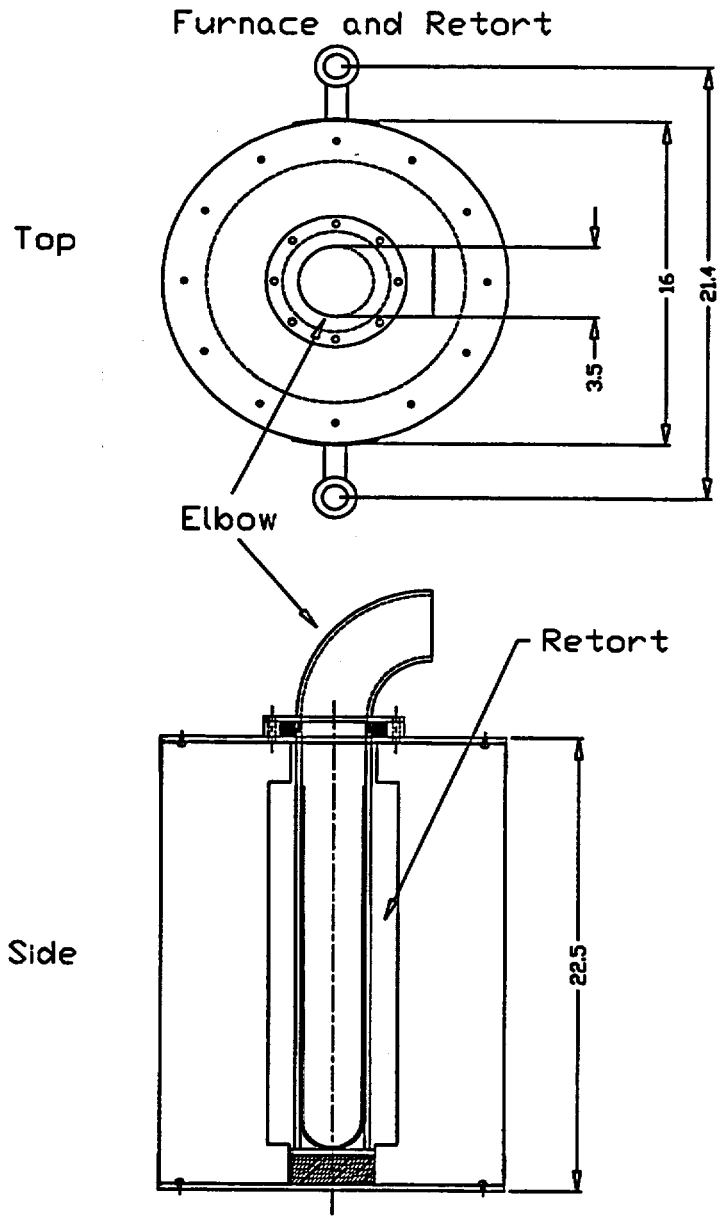

Figure 3.4: Schematic Illustration of the Furnace (Unit: Inch)

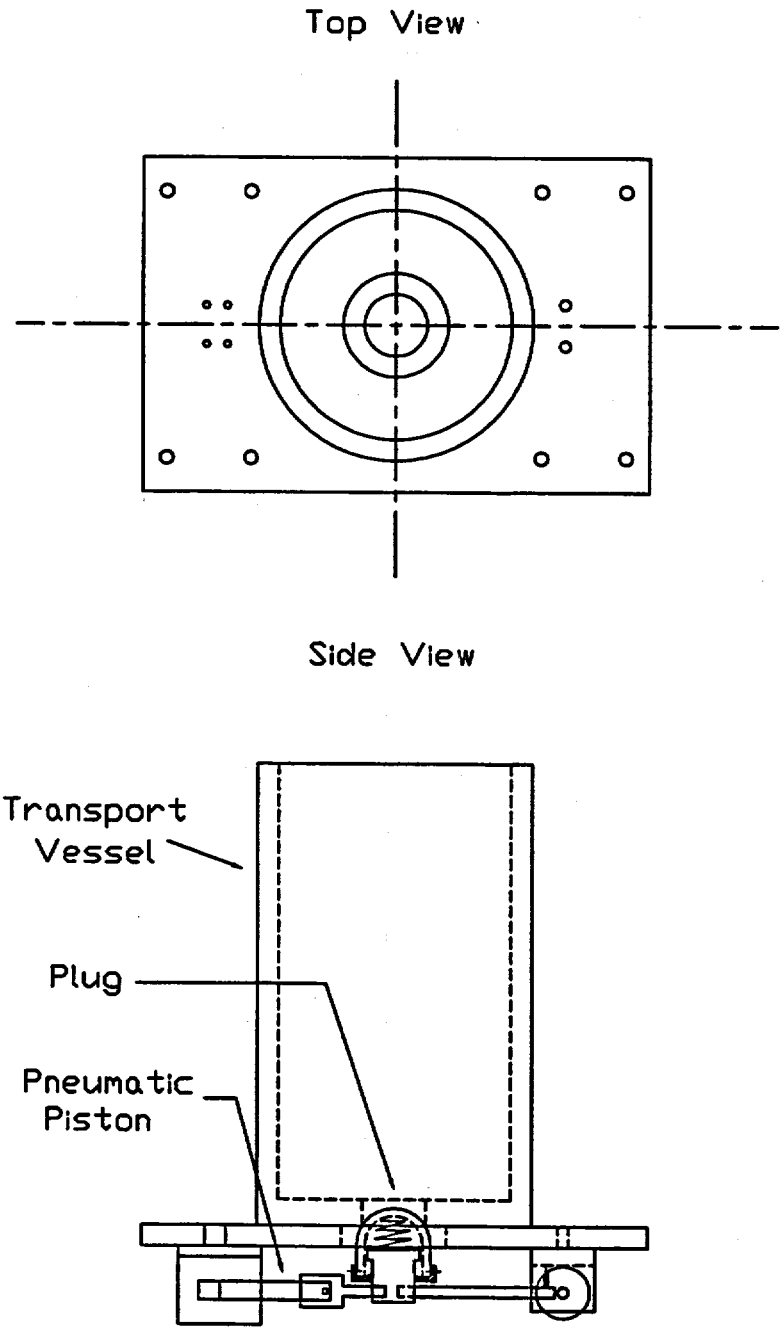

Figure 3.5: Schematic Illustration of the Transport System

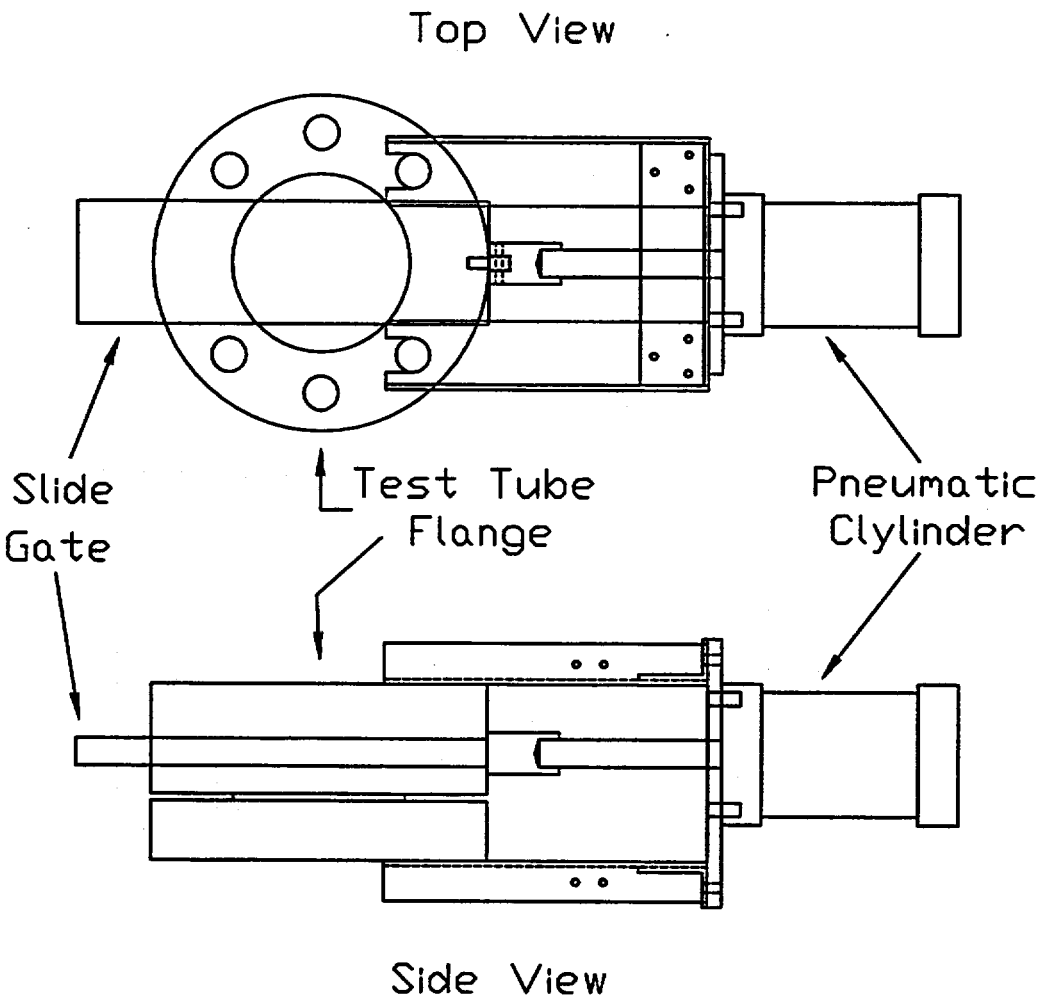

Figure 3.6: Schematic Illustration of the Slide Gate and Supporting Structure

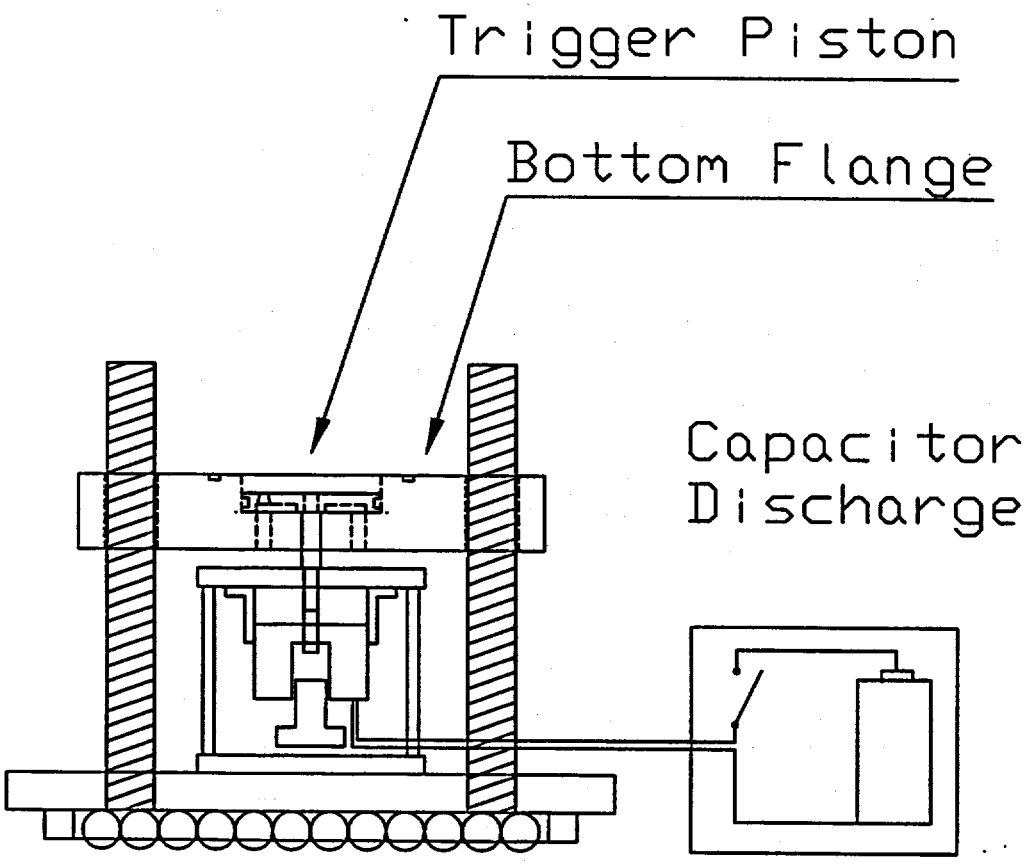

Figure 3.7: Schematic Illustration of the Magnet Trigger System

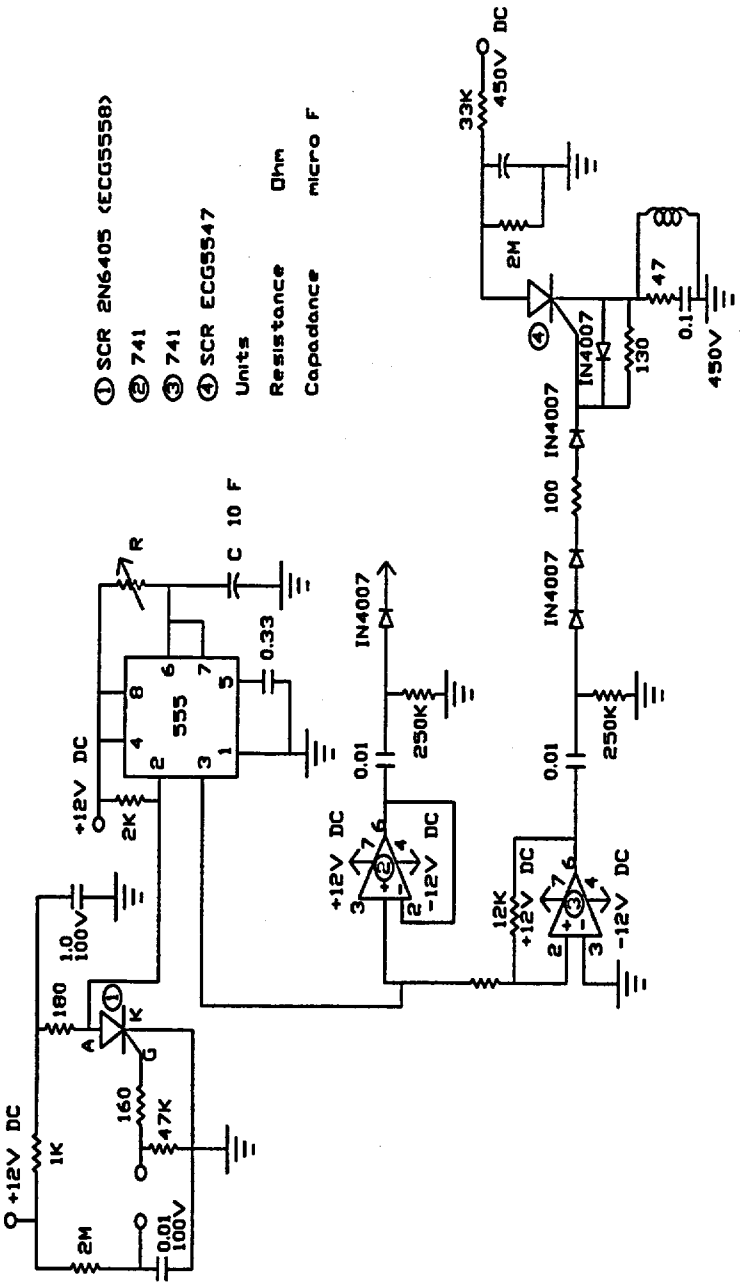

Figure 3.8: Schematic Illustration of the Trigger System Circuitry

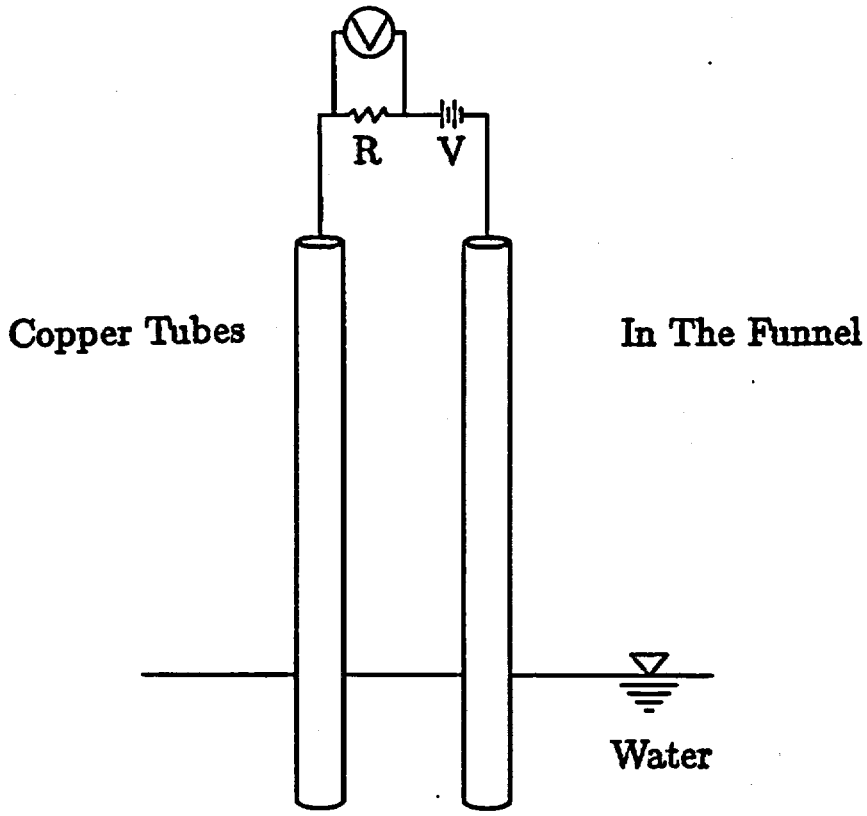

Figure 3.9: Schematic Illustration of the Level Swell Meter

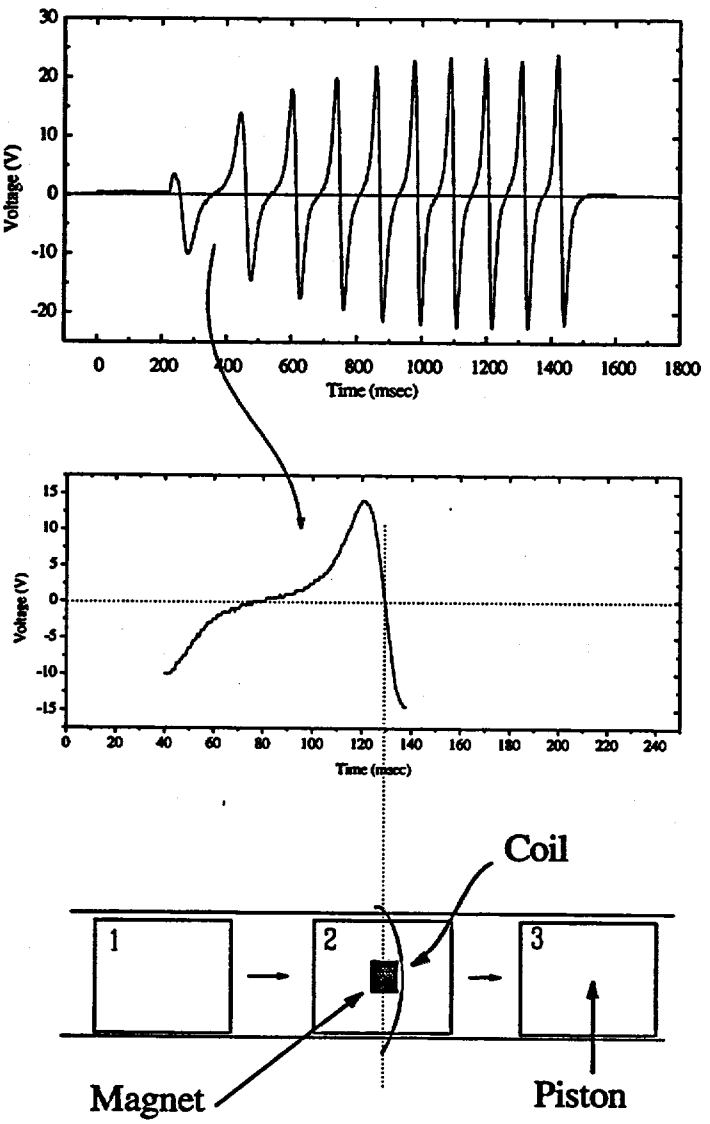

Figure 3.10: Typical Piston Signal Measured in the Expansion Tube

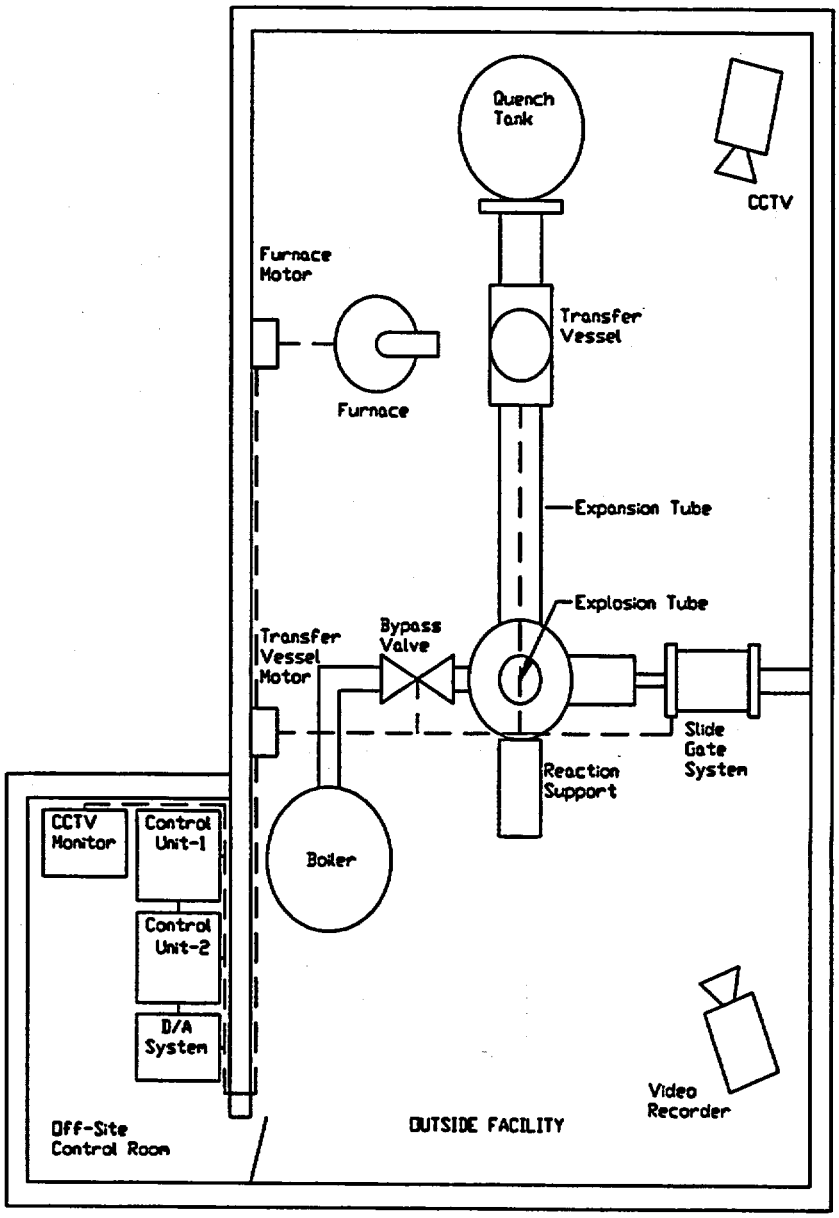

Figure 3.11: Overall Layout of the WFCI Facility in a Top View

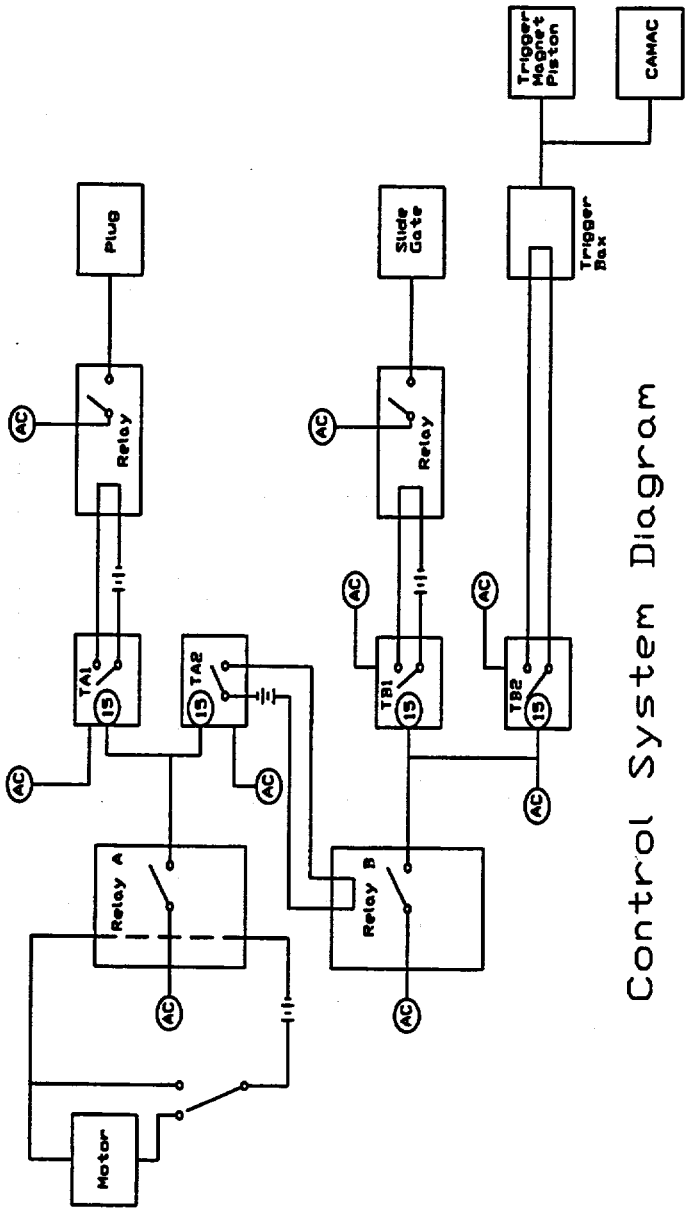

Figure 3.12: Schematic Diagram of the Control System

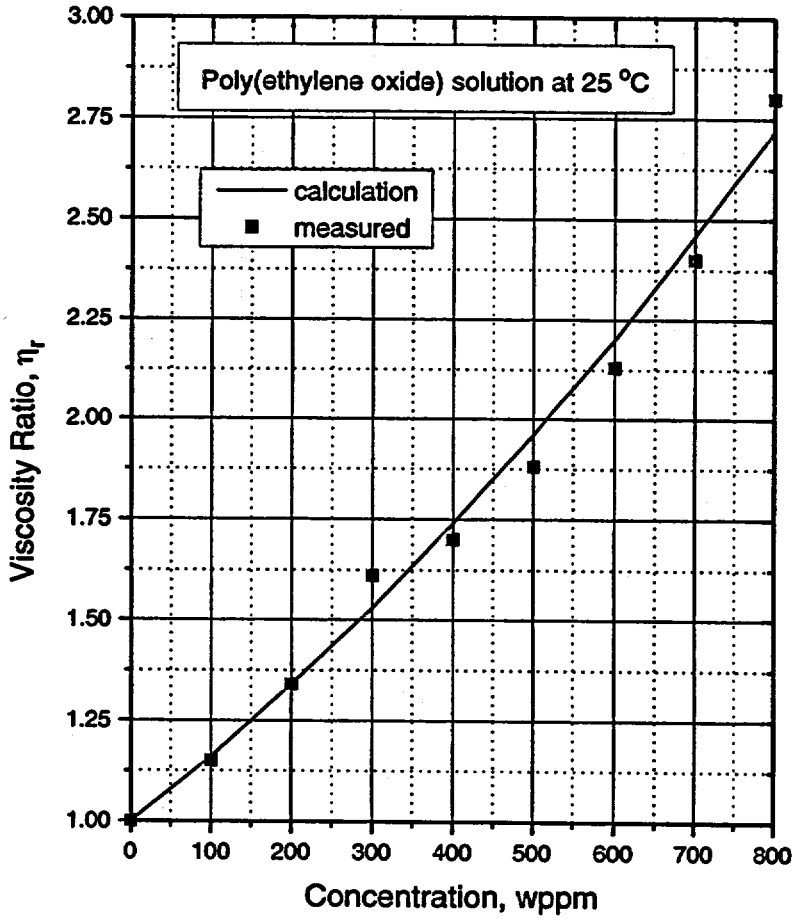

Figure 3.13: Viscosity Ratio with respect to the Polymer Concentration

Chapter 4

Experimental Results and Discussion

4.1 Introduction

The WFCI experiments involved several test series ; trigger characterization and series A to H and K. The first three series of tests, *i.e.*, triggering and series A and B, were performed as reference experiments. Among them, the triggering experiments were conducted to characterize the external trigger by varying the voltage charge to the capacitor in the external trigger system. The strength of the external trigger is determined by the amount of this voltage as well as pulse shape. The WFCI-A series was performed to verify the reproducibility of the WFCI facility by repeating a group of tests with the same initial conditions. Those initial conditions were intentionally similar to those of the KROTOS-21 experiment [63]. To obtain well controlled experimental data, it was also necessary to verify the possibility of spontaneous explosions under similar initial conditions. For this purpose, the WFCI-B series was conducted at the same initial conditions without the external trigger to examine the possibility of the spontaneous explosion.

The WFCI-C series was designed to determine the effect of trigger pulse strength on the vapor explosion behavior. In the WFCI-D series, the effect of the axial constraint on the vapor explosion was examined by varying the system constraint mass. The effects of fuel and coolant temperatures were investigated in the WFCI-E and WFCI-F test series, respectively. The WFCI-H series was conducted to examine the effects of the coolant to fuel mass ratio. To vary this coolant to fuel mass ratio, the molten fuel mass and jet diameter as well as its pouring time were varied. In addition, the test section bypass valve was opened to allow more fuel-coolant mixing during the fuel pour into the test-section. In contrast to the above experiments, the WFCI-G series of tests was conducted to investigate the possibility of vapor explosion suppression in a large scale geometry by changing a particular property of the coolant with an additive.

Finally, the WFCI-K series was performed with a different molten fuel composition, molten iron-oxide. The reason for this change is directly related to material scaling issues for these tests. Molten tin was known to produce vapor explosions when poured into water. Thus, the intent of the experiments using this fuel was to provide benchmark data to characterize explosion energetics under well-controlled conditions. However, it was recognized that the use of molten tin as a fuel simulant for the prototypic fuel melt in a severe accident had

limitations; *e.g.*low internal energy, high melt superheat and metallic fuel properties. Our material scaling considerations suggested that a molten oxide with modest superheat and similar properties to corium would be a better simulant. Thus, WFCI-K series was designed to deliver a similar volume of fuel as in the previous tests to the WFCI test section but with molten iron-oxide as the fuel simulant.

Initial and boundary conditions for all of the test series are shown in Table 4.1. A typical event timing is shown in Figure 4.1. In most experiments the slide gate was closed 1.5 s after the molten fuel pour began, then the trigger was activated less than 0.5 sec after slide gate actuation. However, this time sequence was slightly altered, if needed, in each experiment; for instance, WFCI-A-01 test and WFCI-H series as shown in Figures 4.2 and 4.3, respectively. Time zero is defined as the time when the control system simultaneously activates the trigger device and the data acquisition system. The pressure history plot is composed of eight different plots representing the pressure from the bottom to the top of the test section.

4.2 Trigger Characterization Experiments

To examine the characteristics of trigger pressure pulse, a large number of trigger pulse tests were performed. The external trigger system, composed of the capacitor bank, the mechanical hammer device and the piston in the test chamber, provided the external perturbation to the fuel-coolant mixture resulting from the sudden discharge of the capacitor bank. Various strengths of the external trigger are achieved by varying the supplied voltage of the capacitor bank; *i.e.*, 100 to 400 V. All experiments were conducted in the test section filled with water at 15 to 20°C.

Figure 4.4 shows the relationship between the trigger pressure at different locations and the supplied voltage. The peak pressures are in a range of 2.0 to 4.0 MPa with respect to the supplied voltages of 100 to 400 V. The attenuation of the peak pressure is fairly linear up to 0.8 m from the bottom of the test section.

Figure 4.5 shows typical trigger pressure histories for capacitor charge-up voltages of 200 DCV. The first pressure transducer, located 0.12 m above the bottom of the test section, detected the peak pressures of 3.2 MPa. The rise time of the trigger pressure is usually less than 100 μs and the full width at half maximum of the pressure is approximately 100 μs. The fast Fourier transform analysis of these pressure signals shows that the dominant frequencies range from 0.2 to 0.4 kHz and harmonic behaviors were clearly observed resulting from the reflection of the pressure waves against the rigid boundaries. The reflection waves generate several "wiggles" after the primary peak pressure propagation. These trigger pulses can be easily distinguished from the explosion pulses which have wider pulse

width, slower pulse rise time and more noise resulting from the wave reflection.

The appearance of peak pressures at the first pressure transducer are delayed approximately from 6 to 14 ms due to the supplied voltage after the external trigger system is triggered as shown in the Figure 4.6. The propagation speed of the trigger pulse is about 1500 m/s which corresponds to the sound speed of water. This speed is weakly dependent on the supplied voltage as expected.

The impulses of the trigger pressure measured at the first pressure transducer range from 0.8 to 1.6 kPa-s. The impulses do not vary with the supplied voltages because most trigger pressures have characteristics similar to each other except for the magnitude of the peak pressures. Instead of characterizing the trigger pulses with their impulses, the product of the peak pressure and impulse may provide a more reasonable indicator for the strength of the external trigger, as noted by Berman *et al.* [1], because this product represents the energy density of the external trigger pulse. Figure 4.7 shows that the product of the peak trigger pressure and its impulse ranges from 3 to 6 MPa kPa-s. This energy density is equivalent to 2 to 4 Joules per liter of water and is negligible compared to the energy density of the molten tin fuel simulant; *i.e.*, 2 MJ per liter. Also note that this figure of merit increases with the increase of the supplied voltage up to 250 V and increases more slowly as the voltage increases to 400 V.

4.3 Conversion Ratio

The conversion ratio has widely been used as a prime measure for the energetics of a fuel-coolant interaction. We discuss its general concepts here, since it can be directly determined from the data, and is integral to our understanding of the FCI. It is defined by the ratio of the work done by the fuel-coolant mixture, W, to the initial total fuel thermal energy, E_f ; given by

$$CR = \frac{W}{E_{f,i}} \tag{4.1}$$

The initial total fuel thermal energy E_f is usually given as

$$E_{f,i} = m_f \left\{ c_{p,liq} \left(T_{f,i} - T_{mp} \right) + c_{p,sol} \left(T_{mp} - T_c \right) + i_{fus} \right\} \tag{4.2}$$

where m_f is the total fuel mass, c_p is the specific heat of molten material involved in the explosion, $T_{f,i}$ is the initial molten fuel temperature, T_c is the coolant temperature, T_{mp} is the melting temperature of the fuel and i_{fus} is the specific latent heat of fusion of the

molten material. If the fuel can undergo chemical reaction (fuel oxidation), then there would be an appropriate term added for $E_{f,i}$.

In order to determine the value of CR, it is necessary to estimate how much work has been done by the fuel-coolant mixture. Several experimental methods have been introduced to estimate the work output from the fuel-coolant interaction. In single drop or small scale experiments, the fuel-coolant mixture expansion during the explosive interaction was observed by high speed cinematography and the work was estimated by graphically integrating the pressure and bubble volume traces. In this case, the work for the expansion of the fuel-coolant mixture can be calculated by

$$W = \int PdV \tag{4.3}$$

assuming that the expansion process is reversible.

For large scale tests, however, it is very difficult to visualize the total fuel-coolant mixture expansion. Some of the EXO-FITS tests performed at SNL determined the work output using the expansion velocity of the fuel-coolant mixture from the analysis of high speed film data. Because of large uncertainties in the analysis of the film data, the work outputs obtained by this method gave only rough estimates. In the OG (Open-Geometry) series of tests as one of the experiments performed at SNL, crushable aluminum honeycomb block was placed underneath the interaction chamber. The work output was estimated by the degree of deformation of the honeycomb when the interaction energy was driven downward by the explosion. In the FITS series of tests, the work output was estimated by the chamber pressurization using equation 4.3. However, since the estimation was largely varied with the assumption of the relationship between the pressure and volume and the expansion process [133], this also provided only a rough estimate.

In this work, the work output is more directly determined by measuring the expansion speed through the expansion tube during the explosion. Figure 4.8 shows the schematic diagram for measuring work done by energetic FCIs in an interaction volume on the slug in the expansion tube. The slug as shown in Figure 4.8, is defined by the entire water in the expansion tube including the magnet embedded piston. When the interaction volume starts to increase due to FCIs, the piston moves and a part of the initial slug escapes from the expansion tube. Therefore, the slug mass, $m_s(t)$, in the slug control volume decreases. The position of the slug as a function of time in the expansion tube is provided by measuring a signal of the piston as the piston passes each of the ten electrical coils wound outside the tube. The first coil is located at the initial position of the piston to detect the initial time of the piston movement and the rest of 9 coils are located at the expansion tube. These ten data points are fitted to a polynomial function, $x_s(t)$, and the slug acceleration, $a_s(t)$,

as a function of time is obtained by differentiating $x_s(t)$ twice with respect to time. From this position of the slug, the mass of the slug, $m_s(t)$ is also determined as illustrated in Figure 4.8. Hence, the work done on the slug at any time t after the slug starts to move, is given by the following equation,

$$W_s(t) = \int_0^t F_s(t')v(t')dt' = \int_0^t m_s(t')v(t')a_s(t')dt' \tag{4.4}$$

where $F_s(t)$ is a net force acting on the slug. The maximum work done on the slug is obtained by calculating the above equation until $t = t_{max}$ when the acceleration of the piston reaches zero. Therefore, the conversion ratio is obtained by the following equation using the measured maximum work done on slug as the work output, neglecting work losses by friction and drag,

$$CR = \frac{W}{E_f} \simeq \frac{W_s}{E_{f,i}} \tag{4.5}$$

4.4 Reproducibility Tests: WFCI-A Series

The WFCI-A test series was performed to investigate the reproducibility of vapor explosion under nearly identical initial conditions in the WFCI facility. The initial conditions chosen are quite similar to those of the KROTOS-21 test. The reason for this choice is to obtain a comparison between similar experimental facilities, with similar fuel and coolant conditions to determine if the explosion is reproducible and to understand any observed differences. The tests involved an initial molten fuel mass of five kilograms at a temperature of 1120 to 1300 K poured into the test section filled with distilled water through a 38 mm orifice. The actual mass of the fuel below the slide gate in the test tube was found to be an average of 3.5 kg after the experiments. The water in the test section had a mass of 8.6 kg and a temperature of 358 to 360 K with a depth of 1.48 m below the slide gate. An additional water mass of 23.4 kg as an inertial constraint was provided in the expansion tube and separated from the explosion tube by the plug. In all the tests, the bypass loop was closed just before triggering while the slide gate was closed 1.5 s after the fuel pour began.

Table 4.1 shows that both spontaneous and triggered vapor explosions were produced in this series of tests even though experimental conditions of all experiments were initially set to be equal. Some of tests in this series were performed outside the building at temperatures below 20 °C as shown in Table 4.1. This cold weather caused some variability in the experimental conditions and may have contributed to experimental scatter. The coolant temperature varied only one degree and the fuel temperature at melt delivery varied about one hundred degrees. This latter variation may have contributed to the spontaneous trigger delay; *i.e.*, spontaneous versus triggered explosions. Another inconsistency was caused by

the location of the measurement of the coolant temperature just above the piston trigger. The thermocouple was positioned below the recirculation line inlet to the test tube and thus, may be at a lower temperature than the rest of the test tube due to temperature stratification. The inside coolant temperature was assumed to be equal to the temperature measured at the outlet of the water circulation loop. Thus, in the case of the spontaneous explosions, the coolant temperature may have been lower than the reported temperature, since the melt may have penetrated below the recirculation line (about 120 mm from the bottom). Even though spontaneous explosions occurred, the slide gate did close completely in all tests and isolated the explosion from the environment, allowing the explosion to propagate through the explosion and expansion tubes.

In all experiments, most explosion characteristics were similar to each other. First, a double explosion was observed; *i.e.*, the explosion was triggered at the bottom of the mixture and then a second explosion propagation wave moved downward growing in strength through the mixture as the fuel-coolant mixture began to expand. Additional propagations may have been present, but could not be distinguished from the pressure data. This observation should not be that surprising since the explosion is not just constrained by the mixture constituents as in all past FCI tests; *i.e.*, the fuel-coolant mixture expansion is controlled by the slug constraint which can be independent of the coolant depth. The phenomenon is considered a double explosion, since the explosion continued to escalate in strength as it propagated up the explosion tube and back down from the upper slide gate.

This explosion escalation is similar to observations for the KROTOS-21 test (shown in Figure 4.9) as were the overall transient pressure histories. The results from both spontaneous and triggered explosions indicated that measured peak pressures range from 2 to 8 MPa, but the pressure plateaus (analogous to a Chapman-Jouguet (C-J) pressure) observed after the explosion peak are always in a similar range of 2$\sim$3 MPa. These magnitudes of the quasi-steady pressures are very similar to those measured in the KROTOS-21 test. The explosion propagation velocities of about 200 m/s are also quite similar to each other. The conversion ratios for the WFCI-A series of tests are in the range of 0.2 to 0.7%. These results are also comparable to the KROTOS-21 test with a low conversion ratio of less than 0.2%

In the WFCI-A-01 test, the slide gate was closed 1.5 s after the melt pour began, then the trigger was actuated 0.5 s after slide gate actuation, while in subsequent tests this latter time was reduced to 0.4 s to assure explosion triggering before any spontaneous trigger may have occurred (Figures 4.1, 4.2). In these experiments it was found that the explosion was quite sensitive to the timing of the external trigger. In all these tests the external trigger produced a pressure pulse of about 3 MPa over a time span of 0.1$\sim$0.2 ms. In the first test the time delay was 500 ms after the closure of the slide gate which isolated the explosion chamber from the environment. This allowed a spontaneous explosion to occur about 80 ms before the trigger was provided, as shown in Figure 4.10. In this case, the explosion

occurred near the PT3 transducer, about 0.45 m above the bottom of the test section. The pressure wave propagated upward and downward simultaneously. In the upward direction the wave has an average propagation velocity of 250 m/s. The downward propagating explosion occurred at the top of the test section with a peak pressure of 4.2 MPa at t =-78 ms and proceeded downward.

In all subsequent tests the time delay was 400 ms and this successfully allowed for external triggering; *e.g.*, as in the WFCI-A-02 test as shown in Figure 4.11. As a typical case of a triggered explosion, the explosion in the WFCI-A-02 shown in Figure 4.11 is induced by the external trigger shown at the PT1 with about 2.9 MPa at t =7.9 ms. The actual explosion due to the external trigger occurred at PT3 and escalated with peak pressures of 2.5 MPa to 3.9 MPa and velocity of 333 m/s. After about a 10 ms delay a downward propagating explosion occurred and propagated from the PT7 to PT1 with an average propagation velocity of 180 m/s. This explosion shown in this test is stronger than the first propagation. This might be explained considering that a more appropriate mixing condition for the onset of the second explosion is achieved by the first explosion. This will be discussed in further detail in a later chapter.

In the WFCI-A-03 test the vapor explosion occurred just before the trigger and may have been caused by the slide gate impact upon closure, triggering the explosion about 50 ms after the slide gate closed. The pressure signal was not properly measured in this test but available information suggests the same trend of an upward and then downward propagation occurred. In the WFCI-A-04 test, as shown in Figure 4.12, the vapor explosion was triggered spontaneously at about 100 ms. Such a delayed spontaneous explosion was caused by the failure of the external trigger which was identified by the pressure signal recorded at the first pressure transducer. There was no trigger pressure-like signal in the pressure transducer of PT1. However, the first spontaneous explosion occurred at the bottom of the test section. The pressure traces also clearly show the same explosion behavior.

In the WFCI-A-06 test, eight pressure transducers were mounted in the test section and provided a much better spatial resolution of the explosion pressure behavior as shown in Figure 4.13. The traces show more clearly the explosion behavior; *i.e.*, upward and then downward propagation. The first explosion occurred at about 0.8 m above the test section and propagated in both directions. The second explosion propagated from the top to bottom of the test section escalating its strength.

Our goal was to produce energetic FCI events under controlled conditions for this first set of experiments. The results indicate qualitative and quantitative agreement with the one published KROTOS experiment using molten tin, KROTOS-21. In addition, the explosion behavior is consistent between the six experiments whether spontaneous or externally triggered. The WFCI-B test series further examines spontaneous explosions and the observation of multiple propagation events.

4.5 Spontaneous Explosion Tests: WFCI-B Series

To further characterize the spontaneous explosions observed in WFCI-A, additional experiments in the WFCI-B series were performed without any external trigger under the same initial and boundary conditions as the WFCI-A series. In the first experiment of the WFCI-B series, the spontaneous explosion occurred about 1200 ms after the D/A system was triggered. Even though the pressure signal could not be recorded because of an overflow of the of D/A data storage, the movement of the magnet piston in the expansion tube was measured and provided an estimate of the explosion timing. The average slug expansion speed was about 10 m/s which was a lower speed than any observed in the previous WFCI-A series. After the first experiment, it was decided to decrease the sampling rate in the D/A system in order to catch the pressure signal while measuring a wider time range. The disadvantage of this choice is a loss in the time resolution. In the second experiment of WFCI-B series, explosion pressures were successfully measured. A spontaneous explosion occurred about 660 ms after the D/A system was triggered, which was earlier than in the WFCI-B-01 test.

Figure 4.14 illustrates the characteristics of WFCI-B-02 pressure signals. Once again an upward explosion propagation and then a downward explosion propagation is observed. In Figure 4.14, the first peak appears about 663 ms after the D/A system is triggered at PT1 transducer. Considering a falling speed of the molten fuel estimated from the WFCI-A-06 test, the leading edge of the fuel had already reached the bottom of the test section and started to accumulate on the chamber base. This pressure peak propagated through the test tube up to the top transducer with an average velocity of 216 m/s. Following this relatively mild explosion (~2 MPa), another larger explosion (~5.7 MPa) occurred at the top of the test section, and then propagated down with an average velocity of 94 m/s. This second explosion occurred in the same manner as in the previously discussed WFCI-A series. The pressure histories show that the magnitudes of the peak pressures at the top and bottom are much larger than those at the tube mid-section. This may be explained by the fact that a larger amount of vapor was present in the middle of the test section due to the fuel-coolant mixing and the upward propagation. Therefore, the pressure wave propagating downward from the top was attenuated to some extent.

In the WFCI-B-03 test, shown in Figure 4.15, (equipped with eight pressure transducers in the test section) an explosion occurred spontaneously near the location of the PT3 transducer. The pressure wave travelled with propagation velocities of approximately 660 m/s and 156 m/s in the upward and downward directions, respectively. In this test the behavior of the pressure was very similar to those in the WFCI-A tests and WFCI-B-02 test even though the exact time of the spontaneous explosion was different. In these three experiments, the average expansion velocities were measured as 10.2, 12.1 and 17.6 m/s respectively.

In the WFCI-B tests, the kinetic energies of the spontaneous explosions were somewhat smaller than in the other tests (shown in Table 4.1), even though similar quantities of fuel were initially used in each test. The conversion ratios ranged from about 0.15 to 0.45 percent. These explosions from these spontaneous events occurred relatively late; usually later than 0.5 s after the time of external trigger is normally applied in other series of tests. Since the external trigger was not used in this test series, the fuel cooled for a longer period of time than in other experiments, causing the fuel temperature to be lower at the time of the explosion. If the WFCI-A and WFCI-B test series are taken together we have a data set in which qualitatively similar behavior is exhibited under spontaneous and externally triggered circumstances.

4.6 Effect of External Trigger: WFCI-C Series

To examine the fuel-coolant interaction phenomena, a controllable trigger was used to synchronize the interaction and aid in reproducility. Also, since the external trigger pressure is an important initial condition to the energetic FCI, it is important to investigate its effect on the vapor explosion. A total of six experiments were performed with different magnitudes of trigger DC voltages of 100, 200, 300, 400 and 450 V which corresponded to trigger pressures of about 1.3, 2.4, 3.2, 4.0 and 4.3 MPa, respectively.

First, the WFCI-C-01 test was conducted with a supplied voltage of 200 V in the trigger system, equivalent to about 2.4~3.0 MPa of trigger pressure. The initial conditions for this test were the same as the WFCI-A series, and it also showed the similar double explosion behavior. The first pressure peak propagated upward with an average velocity of 210 m/s and the average expansion velocity was measured at about 15.8 m/s which was comparable with the results of the WFCI-A series. WFCI-C-02 was similar to WFCI-C-01 from inspection of pressure histories, however, all of the expansion data was lost due to a malfunction of that data signal.

The WFCI-C-03 experiment shown in Figure 4.16 was performed with a charge voltage of 400 V. The clear difference in this experiment to the previous five externally triggered tests was that one single explosion occurred propagating upward through the fuel-coolant mixture. One can detect a pressure signal propagating downward from the slide gate, but in this case it is not growing in strength and quickly diminishes and disappears. Also, the energetics from this single upwardly propagating explosion is similar in magnitude to the cumulative energetics from the double explosions in these past triggered events. Note that the external trigger pressure appeared at t =5.8 ms with a peak pressure of 4 MPa. This pressure trace shows that the leading edge of the molten fuel had not reached this region. However, the pressure trace from the PT3 transducer indicates that the explosion had been induced by the external trigger pulse near this location. The data from the

propagation velocity between PT1 and PT3 pressure transducers show that the average velocity was 224 m/s. This average velocity also indicated the occurrence of an explosion between those transducers. The explosion propagated with escalating magnitude of the propagation velocity and the pressure peak in an upward direction up to the location of the PT5 transducer. In the upper region of the test section, however, the propagation velocity decreased noticeably. This test gave the first indication that the presence of the double explosion is a strong function of the initial trigger strength.

The WFCI-C-04 test was conducted with a supplied voltage of 450 V. In addition, four additional pressure transducers were installed to provide better spatial resolution to pressure histories. The WFCI-C-04 experiment also resulted in a single explosion. The pressure histories are shown in Figure 4.17. The first and second pressure signals show that the leading edge of the melt had not reached the second transducer, PT2. The external trigger pressure pulse propagated upward with a velocity of about 1400 m/s (approximately equal to the sonic velocity of single phase water) and a peak pressure of 4.3 MPa. An explosion then occurred near the location of the PT3 transducer. The explosion pressure was small at this location, similar to the previous experiment. Post-test debris suggested that the leading edge of the melt stream had mostly solidified and a small part of the melt was finely fragmented. This indicates that the small peak in the explosion pressure at this location resulted from a small amount of fuel participation and the relatively low fuel temperature of 880 °C.

Although the external trigger pulse had already diminished at this location, this small local explosion provided a sufficient trigger to the upper mixture. The magnitude of the explosion increased in the upper region and the propagation velocity of the explosion in the test section was 210 m/s. In this test, the explosion behavior at the slide gate was more clearly recorded by additional pressure transducers installed at this location. The peak explosion pressure occurred near this location at 17 MPa. The reason for this can be understood by the observation of the distribution of the fuel debris after the experiment. Approximately 30 to 50 % of the fuel debris was found in the T-tube with a shape of packed "sand" just below the slide gate. This suggests that the fuel-coolant mixture was located at this position or had moved to this position together and became packed in this region during the explosion expansion. Thus, the relatively 'rich' fuel-coolant mixture contributed to the larger pressurization at this particular location.

The WFCI-C-06 test was performed with a supplied voltage of 300 V to find the transition from single to double explosions. Figure 4.18 shows that the pressure traces of the explosion had characteristics of a single explosion with a pressure reflection. The trigger pressure at the bottom is similar as in previous tests and propagates with a velocity of 1300 m/s. The explosion was induced at the second pressure transducer, however, a little earlier than in the WFCI-C-04 test. A sharp pressure wave with rise times of 20 to 40 μs propagated with an average speed of 240 m/s. Compared to past double explosion cases, the second

peak in this test appeared as a wide and low pressure pulse. It did not have any explosion characteristics and is interpreted as a reflected wave from the initial explosion at the top of the test tube. This reflected wave had an average propagation velocity of 68 m/s. The empirical conclusion is that external triggers near this value result in an upward propagating single explosion.

The WFCI-C-05 test was repeated with the same conditions as the WFCI-C-02 test, in which the supplied voltage was 100 V, however, the piston signal in the expansion tube was not measured. Figure 4.19 shows the pressure traces induced by the weakest trigger in this series of tests. The explosion occurred near the PT3 transducer, propagated with a velocity of 190 m/s and peak pressure of more than 17 MPa. As expected, a downward explosion propagation also occurred at the top of the test section. The weak trigger pulse provides an initial behavior similar to that of the WFCI-C-06 test, in which the second explosion propagated and induced a stronger explosion. The detailed analyses on this subject are discussed in the next section.

In the WFCI-C series of tests, the conversion ratio was in the range from 0.25 to 0.38 percent, as shown in Table 4.1. These are similar to the conversion ratios obtained from the WFCI-A series. Figure 4.20 shows the relationship between the trigger pressures and the measured conversion ratios. In this figure, the pressure signals at the PT1 transducer were taken as the peak trigger pressure since the molten fuel had not reached that location when the external trigger was actuated. In this figure, the WFCI-A-02, WFCI-A-05, and all WFCI-C series of tests were included because their mixing conditions were similar to each other and all tests produced triggered explosions. The remaining WFCI-A and WFCI-B explosions were spontaneous. The figure shows that the conversion ratio tends to increase when the peak trigger pressure increases from 1.75 to 2.36 MPa. However, the conversion ratio decreases with peak pressures increasing from 2.36 to 4.24 MPa. The maximum conversion ratio was observed at the peak trigger pressure of 2.3 MPa. Because the data base is sparse, it is not our intent to draw any major conclusions from the work. However, we must emphasize that energetics of spontaneous explosions and weak externally triggered explosions can be affected by the trigger magnitude. At some point for any fuel-coolant combination the explosion energetics would become independent of the trigger and this is the region where we need to operate for our experiments. The presence of the double explosion is another issue the trigger affects and which we must also consider.

In these tests, the presence of double shock wave propagations through an axial interaction zone with the presence of the rigid slide gate at the top of the test section was observed. It is interesting to note that, in the KROTOS tests, similar multiple wave propagations have also been observed even without a solid boundary at the top of the test section. Post-test analyses of the KROTOS tests show that about fifteen percent of the total debris was packed in a region near the top of the fuel-coolant mixture, presumably caused by the mixing during fuel pouring and subsequent freezing during the FCI. Thus, one can consider

the fuel in this region to act as a "porous plug" of melt providing a "semi-rigid" boundary at the top of the mixture. This boundary not only can dissipate the explosion impulse and expansion, but also acts as a point of shock reflection for downward FCI propagation.

The WFCI-C experiments confirm that the characteristics of the explosion are strongly affected by the external trigger. If the external trigger pressure is weak or absent, in the case of spontaneous events, the fuel jet may not be sufficiently fragmented by a single propagation event through the mixture. A more energetic explosion would be expected by any subsequent pressure reflection back into the fuel-coolant mixture, if a proper combination exists of unfragmented molten fuel, mixture void fraction and relative mixture length scales, such as the fuel mixing diameter. From the dozen experiments which exhibited this behavior in these three test series, it is not possible to ascertain what is the precise combination of conditions, but it clearly exists. If the trigger pressure is sufficiently strong, the initial explosion propagation event causes sufficient fuel fragmentation in the mixture to allow the pressure to grow to a level that fragments enough fuel and creates mixture conditions where no subsequent propagation is possible. From an energetics standpoint, it is important to also note that the explosion energetics is not noticeably different for explosions with single or double propagation events. The source of any pressure reflection in a fuel-coolant interaction has been addressed above and is not relevant to our main point here.

In subsequent tests the trigger pressure is planned to be set at about 3 MPa to minimize the chance of multiple propagations. This trigger level also addresses the independence of the trigger from any subsequently observed energetics. The presence of these double explosions only emphasizes the fact that the fuel-coolant mixture is metastable and potentially capable of sustaining subsequent explosive propagations, even after the first explosion propagation, if the conditions are conducive for them to occur. This has never been clearly documented from past FCI data.

4.7 Effect of System Constraint: WFCI-D Series

In the WFCI-D test series, the explosion expansion was channeled through a lateral expansion path just below the closed slide gate. This geometry is similar to the design used in the past by Baines to establish a system constraint to measure energetics. This constraint is easily controlled and allows one to vary the constraint independently of the fuel and coolant masses in the mixing region. In the stratified tests performed by Bang [3], it was noted that the expansion of fuel-coolant mixture was controlled by the constraint of the slug mass and by the coolant depth.

During an energetic FCI the explosion impulse and the mechanical work potential depend on

the system constraint. Hydrodynamically, the constraint was classified by Cho *et al.* [130] as acoustic or inertial. The system constraint was considered in developing their parametric models for an acoustic or inertial system, based on two different timescales for potential mechanical work output. The first timescale is the time for relief of a shock wave in the system. During this time interval (so called the "acoustic unloading time") a shock wave propagates within the fuel-coolant mixture in the explosion chamber. This represents the time for the shock pressure front to travel through the mixture and system constraint above it to the nearest free surface and reflect as a rarefaction wave travelling back to the interaction zone. This time is approximately equal to $2l/c$, where l is the distance from the interaction zone to the nearest free surface and c is the velocity of sound in the media. The second timescale is the time for the inertial expansion of the fuel-coolant mixture. In this period, the mass of the liquid column and the fuel-coolant mixture itself is accelerated upwards by vapor pressure in the expanding mixture.

From a thermal point of view the timescale for explosion expansion, as related to the system constraint, could be divided into two time periods. The first period is for heat transfer between rapidly fragmenting fuel and the local coolant causing vapor production. The second period involves heat transfer from the vapor to the surrounding coolant liquid without significant vapor production, either because fuel fragmentation has ceased or from fuel quenching. These periods are not as separable as the hydrodynamic time periods. These two time periods are conceptually plotted with the mechanical timescales in Figure 4.26. During the first time period, since the vapor production rate is directly proportional to the fuel fragmentation rate, more energetic FCIs may be expected as the time increases. This is because as more time is made available, larger vapor pressures driving the explosion can result, with minimal slug expansion. This phenomenon was observed in stratified geometry experiments [131]. In that test, slug masses of 1 and 4 kg were used as the lower and upper limits, respectively. The results showed that the maximum mechanical energies of the explosion for the upper limit case was twice as large as in the lower limit case. If the time continues to increase into the second period, however, less energetic interactions are anticipated. Under these circumstances the vapor production could significantly diminish or revert into vapor condensation as the fuel quenches, as the slug expansion becomes appreciable and the coolant bulk heating begins to dominate. The system constraint directly affects these timescales since it controls both the acoustic and inertial timescales and thus affects these thermal time periods for fuel-coolant energy exchange.

Figure 4.27 shows the pressure history for the WFCI-D-04 test as an example of this concept. This data illustrates the typical pressure history of the WFCI-D experiments. The plot presents the pressure histories measured with eight pressure transducers from the bottom to the top of the test section. It clearly shows pressure propagation and escalation from the bottom of the test section. The bottom two figures show the typical pressure history of the external trigger. The external trigger provided a pressure of about 3 MPa

with a pulse width of about 0.1 to 0.2 ms at its half height to all WFCI-D series experiment. The trigger shock traveled with a speed of 1530 m/s from the first transducer to the second one. However, the shock speed dropped to about 290 m/s and the shape of the shock was changed at the third transducer location. This indicates that no melt had reached the location of the second transducer and the leading edge of the fuel melt was located between the second and the third pressure transducers about 1.1 m below the slide gate. After that point, the shock generated by the explosive interaction with less than 0.1 ms peak rising time traveled with a speed ranging from 290 m/s down to 80 m/s. These speeds can be explained by the condition of the mixture; *i.e.*, high vapor void fractions as one moves up the explosion tube.

To gain an understanding on the effect of the axial constraint on energetics the six WFCI-D tests along with selected tests from WFCI-A, B and C series are compared. The degree of axial constraint for fuel-coolant interactions is characterized by the total initial mass of the slug which can be made up of water or water interspersed with high density lead slugs (73 mm diameter and 100 mm long each) in the expansion tube. The degree of an axial constraint is represented by a dimensionless parameter, $< m >$, defined by the following expression,

$$< m >= \frac{m_{s,i}}{m_{c,i}} \tag{4.6}$$

where $m_{s,i}$ is the total initial mass of the slug in the expansion tube as shown in Figure 4.8 and $m_{c,i}$ is the total initial mass of water in the interaction zone. In this experiment, $< m >$ ranges from approximately 0 to 8. The experimental conditions of the WFCI-D series and other series in the WFCI experiments are summarized in Table 4.1.

The WFCI-B series tests are included even though no external trigger was provided since spontaneous explosions also occurred over a wide range of mixing times and these data illustrate the effect of the fuel quenching time on the FCI energetics.

Specific comparison to past data [60, 62, 63] was chosen because of their similarity in geometry, materials, and experimental conditions as well as their completeness in data measurement. For the KROTOS-21 test [63], since the facility is not equipped with a system for direct measurement of work output, the conversion ratio for the KROTOS-21 test is estimated from the TEXAS simulation [117], which produced the maximum work output of 1.1 kJ. The total fuel mass of 5.4 kg measured after the experiment and called '*the probable-mixed mass*' was used for the estimation of the total thermal energy.

The conversion ratio for Hall's tests [60] was determined from the measured impulses of the explosion pressures which ranged from 150 to 250 J. These corresponds to the estimated conversion ratios ranging from 0.06 to 0.25 %. In the Baines' tests [62] the estimated conversion ratios were ranging from 0.18 to 0.38 %.

For Hall and KROTOS experiments, their axial constraints, $< m >$, are assumed to be zero to be consistent with the definition applied in the WFCI test; *i.e.*, the slug mass is defined as the slug mass above the actual fuel-coolant mixture. For Baines's experiments, however, $< m >$ is obtained by the total initial mass of water as a slug in his expansion tube divided by the total initial mass of water in the interaction tube. Table 4.4 summarizes the ranges of their experimental conditions.

The conversion ratios of this series of experiments are plotted in Figure 4.5 with respect to the dimensionless parameter, $< m >$ as an indicator of the axial constraint, including previous other test results [63, 60, 62] for comparison. In this figure, the duration time of the piston movement, Δt_s, in the expansion tube is plotted with respect to the axial constraint, $< m >$, as well. The data of the duration time, Δt_s, shown in Table 4.6 are linearly fitted with their standard deviation of about 50 ms. It indicates that the average slug velocity in the expansion tube linearly decreases as the axial constraint increases.

All data for the conversion ratio are fitted to the second order polynomial function and show that the conversion ratio increases with an increase of the axial constraint up to $< m >$ of approximately 5, then decreases, although Δt_s keeps increasing with $< m >$.

Figure 4.29 shows the relationship between the peak pressure of vapor explosions and the axial constraint comparing with the conversion ratio. Note that peak pressures obtained from the WFCI-A, B and C-01 are not used in this figure because the location of the pressure transducers for obtaining maximum pressures and preset maximum ranges of the transducers are quite different from the WFCI-D series. The figure shows that the peak pressures increase up to approximately $< m >$ of 3.5 and decrease with the axial constraint increase. The maximum peak pressure occurs at a slightly lower axial constraint than the maximum conversion ratio. However, the general trend of the peak pressure with respect to the axial constraint is almost identical to that of the conversion ratio. It clearly indicates that the peak pressure of vapor explosions is closely related to the energetic of vapor explosions (*i.e.*, conversion ratio).

A possible reason for the effect of axial constraint can be linked to the two thermal time periods previously discussed. Those two time periods related to the axial constraint are a time period for heat transfer between the fragmented fuel and the adjacent coolant causing rapid vapor production, and a time period for heat transfer between the fuel-vapor mixture to the bulk coolant causing vapor condensation and fuel quenching (especially in highly subcooled coolant) without significant vapor production. Those time periods were conceptually plotted for comparison with the mechanical time scales suggested by Cho *et al.*, in Figure 4.26, and were previously discussed.

In general, the axial constraint directly affects these time scales since it controls both the acoustic and inertial time scales through its variation and its effect on fuel-coolant energy

exchange. If the axial constraint increases, both acoustic and inertial times will increase, leading to an increase of the time duration of the slug movement. It provides more time for fuel-coolant mixture energy exchange and increases the FCI energetics. However, as the time duration increases further, vapor condensation and fuel quenching play more significant roles and result in the conversion ratio decrease.

In this experiment, the turning point occurs within a range of 500 msec for Δt_s. Because of low subcooling of the bulk coolant in this series of tests, the vapor condensation may play a less important role than fragmented fuel quenching on conversion ratio decrease. One should note that qualitatively, such behavior would always be expected but it would occur at quantitatively different values for different fuel compositions.

Figure 4.30 shows the maximum conversion ratios calculated by the UWFCI code [105] with respect to the degree of the axial constraint, $< m >$. This calculation was done, not to validate the code as much as to demonstrate that this qualitative effect should be demonstrable in a straightforward manner. The computer model calculation shows fairly similar qualitative trends of the axial constraint effect. In this figure, calculated conversion ratios for the axial constraint are maximized at $< m >$ of about 10, which are larger than that observed in the experiments; *i.e.*, $< m >$ of about 5. The maximum conversion ratio decreases from 2 to 1 % as the volume ratio of the vapor to water in the mixing zone increases from 20 to 50 %. It shows that the conversion ratio is strongly affected by the initial mixing conditions, *i.e.*, void fraction, decreasing with the void fraction increase. Although the conversion ratios calculated are about an order of magnitude higher than those obtained, the general trend with respect to the axial constraint is nearly identical to the experimental results.

The time histories of the conversion ratios and system pressures for $< m >$ of 3.3, 11.2 and 44.4 are shown in Figure 4.31. The figure shows that the conversion ratio starts to increase earlier as the axial constraint is smaller. It is because the conversion ratio is calculated by the slug movement as in the experiments. The higher the axial constraint, the later the slug starts to move. It also illustrates that the maximum conversion ratio varies with the axial constraint and does pass through a maximum value. The system pressure, however, increases with the increase of the axial constraint without exhibiting any maximum as in the experiments.

The completion of the WFCI-D test series represents the final test series which examines the boundary conditions of the FCI on its energetics. We have seen that the trigger (or lack of it) and the system constraint do have a marked effect on the explosion propagation and energetics. We next examine how the fuel and coolant initial conditions affect the explosion process.

4.8 Temperature Effects of the Fuel and the Coolant: WFCI-E and F Series

To investigate the temperature effects on the vapor explosion, two series of tests were performed, the WFCI-E and WFCI-F for fuel and coolant temperatures, respectively. The test conditions for these experiments are shown in Table 4.1. The test series are similar to what have been reported in the past for other fuel-coolant pairs. Also similar to past data, once the intial conditions have been found that produce the explosion, the effect of the absolute temperature variation on energetics is not large. Note that the fuel in all of these cases had significant superheat. In these tests, the general behavior was that explosions were observed for most of the test conditions, with the most notable change being that spontaneous explosions became more frequent and unpredictable. As the temperature of fuel or coolant decreased, further explosions became more incoherent; *i.e.*, vapor film stability required for fuel-coolant mixing would not be satisfied.

In the WFCI-E tests, the fuel temperatures were varied from 490 to 790 °C, with all other conditions similar to the previous WFCI-A series of tests. There are two tests that are of particular note. The WFCI-E-02 test, as shown in Figure 4.21, had an initial fuel temperature of 790 °C and produced a triggered double explosion. In this case though the second explosion, with a wide pulse width, can be identified as the combination of two pressure pulses; one is a typical downward propagation and the other is a reflected wave from the bottom of the test section superimposed on it. This reflected wave propagates upward with a sonic velocity of single phase water but diminishes near the PT5 transducer. Once again we would expect that the largest local void fraction in the mixture would occur near this point. In the WFCI-E-03 test (Figure 4.22), a spontaneous explosion occurred about one second before the system was to be triggered near the top of the test section. It was the first explosion that occurred before the slide gate was closed. No damage was noted because it happened near the top of the test section where there was minimal liquid constraint before the explosion vented to the ambient. The likely reason for this explosion was that fuel entrapped water between the structure and funnel. Both steel frames were bent up to 45° by the impact. The work done by this structure against the steel frame was estimated as at least 2 kJ, based on the frame deflection analysis. This demonstrates that the damage resulting from an impact of a missile generated by an explosion is more severe than that due to the explosion expansion in the ambient air without missile generation.

In the WFCI-F series of tests, a total of three tests were conducted to investigate the coolant subcooling effects on the vapor explosion, varying the coolant temperatures from 27 to 72 °C. All other conditions were the same as in the WFCI-A series. In all tests, spontaneous explosions occurred before the slide gate closed. Small amounts of molten fuel penetrated below the slide gate because of these early FCIs, as shown in Table 4.1. The WFCI-F-02 test was performed with a coolant subcooling of 73 °C. As shown in Figure 4.23, several pressure spikes with relatively small magnitudes appeared near the top of the test

section about 1.25 s before the system was triggered. Such early FCIs probably occurred since the vapor films around the fuel could not maintain their stability at these fuel-coolant conditions. These events occurred near the top of the test section preventing pouring of the molten fuel into the test section. Only about 1 kg of fuel was collected in the test section. As the coolant subcooling decreased (higher water temperatures), the pressure signals changed from incoherent spikes to an explosive behavior as shown in Figures 4.24 and 4.25.

4.9 Coolant Additives: WFCI-G Series

A group of experiments were conducted to investigate the ability of a polymeric solution to suppress vapor explosions. This series of tests was denoted as the WFCI-G series. Five experiments were conducted with polymer solutions of concentration from 400 to 800 wppm. The viscosity ratios measured just before the experiments with polymeric concentrations of 400, 600, and 800 wppm were 1.5, 2.0, and 2.5 respectively. Two other experiments were performed with pure distilled water at the temperature of 24 °C to provide reference cases of explosions in the polymer solution. In the two cases of pure water experiments, *i.e.*, the WFCI-G-05 and WFCI-F-02, spontaneous interactions occurred as the melt entered the water, as shown in Figure 4.32. The early local explosions in this highly subcooled water limited the amount of melt entering the explosion tube and subsequent energetics.

In the cases of polymer solutions, however, none of the five tests showed initial eruptions or energetic spontaneous explosions as shown in Figure 4.33. This figure shows that multiple pressure "spikes" with magnitudes of several hundreds kilopascals occurred during the pouring period of the molten tin into the water. It is believed that these spikes result from the vapor film collapse around the melt drops. But it was shown that such vapor film collapse in polymer solutions did not initiate coherent vapor film collapse of adjacent melts and eventually the energetic events were suppressed. In the single drop tests, the same order of magnitude of pressure spikes was treated as the explosion. Even if these spikes are pressures resulting from the explosion, one may say that explosions are suppressed since there was no escalation and propagation of the explosion.

Such suppression of the FCIs due to the coolant viscosity increase can be explained by two possible effects. First, the fragmentation mechanism during the melt and water contact is altered. In general, one possible melt fragmentation mechanism has been described by the Taylor instability between the vapor and water interface. When the melt contacts with the water, the melt is surrounded and stabilized by the vapor film. The vapor film, however, becomes unstable due to the Taylor instability of the interface between the vapor and water. Taylor fingers develop and water jets penetrate through the vapor film to the molten fuel surface [14], [57]. If the viscosity of the coolant is high enough, however, the

instability may not grow sufficiently fast to break up the melt.

Second, the boiling heat transfer characteristics are also changed. As mentioned previously, the polymer solution shifts the boiling curve, for example, increasing the nucleate boiling heat flux in general. Recently, Bang [132] investigated the boiling heat transfer characteristics of a highly subcooled polymeric solution (PEO and water). He used a heated stainless steel ball with a diameter of 22 mm. He observed that the film boiling over the sphere in the polymer solution at 30 °C sustained for a period of time relatively longer than in pure water. The minimum film boiling temperature rapidly decreased increased polymer concentration up to 300 wppm, and did not change from this value when the concentration was further increased. Bang also observed from the temperature-time trace at the center of the sphere and synchronized visual observation that the stable vapor film was sustained even after the temperature of the sphere surface reached the solidification temperature of tin. From this observation the tendency of no energetic event in the WFCI-G series experiments with polymer solutions may be explained; the surfaces of melt jets with stable vapor films were solidified and then quenched before the vapor films were destabilize enough to cause energetic interactions. Either of these effects of weaker hydrodynamic instability development or more stable film boiling, may be the root cause of the suppression of the energetic FCI.

In order to investigate the stability of vapor film in polymer solutions under an external disturbance, WFCI-G-02, identical to the WFCI-G-01 test but with an external trigger, was conducted. An external trigger with a magnitude of 3 MPa peak pressure was applied. No explosion was observed in this case. It is noted that in the cases of pure water at 85 °C, the molten tin exploded without the external trigger or with a trigger of a magnitude from 3 to 4.5 MPa [65], [78]. Since the vapor films around the melt are stable in the polymer solutions, there may be a potential for the melt to explode energetically if the external trigger is strong enough.

In this series of experiments, the concentration of polymer was changed from 400 to 800 wppm, corresponding to viscosity ratios of 1.5 and 2.5. For small scale experiments [69], at a viscosity ratio of 2 the explosion was completely suppressed. Based on this empirical information, the viscosity ratio was reduced to 1.5. Even at this ratio (WFCI-G-04) no explosions occurred. This confirms the belief that small scale single droplet results cannot be directly extrapolated to these larger scale tests. In order to examine the mass scale effect (WFCI-G-06), the molten tin mass was increased to twice the previous value. This test with tin mass of 5 kg and polymer concentration of 800 wppm also showed no explosion. For this test series, the debris analysis provides some unique insights. Thus, this debris

analysis is presented here with comparisons to these other results.

WFCI-G Debris Analysis

The post-test debris analysis showed that in the polymer solutions, the melt was broken into nearly spherical particles ranging from a few tenths micrometers to centimeters as shown in Figure 4.34. The shape of the melt fragments in this series of tests was closer to spherical than those observed in Dowling's single drop tests. In the case of pure water, however, the debris appeared to be larger and more arbitrarily shaped, indicating some fine fragmentation at the time of the FCI as shown in Figure 4.35. Table 4.5 shows that about 70% of the molten tin entered the test section with no explosion. However, in the cases with spontaneous explosions, only 20 to 35% of the molten tin had entered. Some sort of surface eruption at the early stage of the mixing phase in two spontaneous explosion cases limited the amount of molten tin entering the test section.

Figures 4.36 and 4.37 show that debris mass less than 0.5 mm in size in a spontaneous explosion case (WFCI-G-05 test) is much larger than those in other tests (WFCI-G-01 and G-04) because of the explosion and its associated fine fragmentation. The debris masses of the non-explosion cases are bounded by the highest polymer concentration case (WFCI-G-01) and the lowest polymer concentration case (WFCI-G-04).

Figure 4.38 shows the relationship between the Sauter mean diameter and the viscosity ratios of the polymer solutions in this series of experiments. The Sauter mean diameter, D_{sm}, [88], is defined in general as follows:

$$D_{sm} = \frac{\int_0^{D_{max}} D^3 p(D) dD}{\int_0^{D_{max}} D^2 p(D) dD} \tag{4.7}$$

where $p(D)$ is the probability of a debris particle having diameter between D and $D + dD$. Since the different sizes of debris have been separated by a set of sieve bins with mesh sizes ranging from 25 to 8000 μm, the above equation was modified to the following by assuming that all debris particles in a certain sieve bin, i, have a perfectly spherical shape with only one average diameter, D_i:

$$D_{sm} \simeq \frac{\sum_{i \leq N_s} D_i^3 p(D_i) \Delta D_i}{\sum_{i \leq N_s} D_i^2 p(D_i) \Delta D_i} \tag{4.8}$$

where N_s is the total number of sieve bins used in the process, and ΔD_i is the mesh size difference between the sieve bin numbers of i and $i+1$. The debris particle probability, $p(D_i)$, was calculated from the mass of the debris at the sieve bin number i divided by the total mass of the debris. As indicated in equation (4.7), the Sauter mean diameter, SMD, is proportional to the ratio of the volume to surface area of the debris particle. Therefore, it represents a characteristic diameter of particles with the proper surface area to volume for heat and mass transfer. One should note that because of the method of averaging, the SMD tends to be larger than the mean diameter based on particle number or particle surface area. SMD values are biased by the large particles in the fuel debris. Figure 4.38 shows the SMD in these entire tests with respect to the viscosity ratios. At the viscosity ratio of one, the SMD for two tests conducted at the pure water are almost identical, having diameters of about 3 mm. Compared with other tests performed in dilute polymer solutions, these diameters are approximately four times smaller. In fact, the SMD values for pure water tests will be somewhat smaller than the values shown in this figure because this value was calculated by assuming all debris having a spherical shape. These small SMDs for the pure water tests are indicative of the explosive heat transfer between molten fuel and water due to vapor explosions and its fine fragmentation.

This figure also shows that the Sauter mean diameters at higher viscosity ratios seem to be independent of the viscosity ratios ranging up to 2.5. The SMD of WFCI-G-02 conducted with an external trigger of 3 MPa was also similar to that of non-triggered tests. It indicates that there was no fine fragmentation of molten fuel due to the external trigger. The trigger was not strong enough to initiate the explosive interactions between molten fuel and solutions. For the WFCI-G-06 test with a doubled mass of molten fuel, its Sauter mean diameter was also similar to those of other tests.

These debris size distributions are indicators that identify the characteristics of vapor explosions (*e.g.*, its energetics). Therefore it is valuable to know the debris size distribution at the mixing phase since this provides the initial mixing conditions of the fuel-coolant mixture and eventually determines FCI energetics. However, most debris data were obtained after explosions. Therefore, it is almost impossible to predict the debris size distribution for the mixing phase from these data. It is our hypothesis that the non-exploded debris size distributions obtained in dilute polymer solutions such as Figure 4.36 and 4.37 may provide a possible fragment size distribution of the molten jet of fuel in the mixing phase of the FCI phenomena. Hence, these debris data may be useful to predict the size of the jet breakup in the mixing phase of an FCI.

4.10 Mass Ratio Effect: WFCI-H Series

The WFCI-H series was designed for investigating the effect of mass on the vapor explosion, by varying the coolant to fuel mass ratio. Also, during this series, our level swell meter was tested and verified by visual observation and filmed by a video camera. Different methods to control the mass ratio were introduced; variation of the fuel pouring time and a change in the fuel pouring diameter. We also controlled the position of the explosion tube bypass valve to affect the mixing process.

During the WFCI-H tests, the pouring time was varied from 1.5 to 2.0 s, to allow the trigger to be actuated 0.1 s after the slide gate closed, as shown in Figure 4.3. The explosion then occurred at a lower axial position, near the second pressure transducer instead of the third transducer as shown in the WFCI-A series. Different fuel masses can be introduced into the test section by variation in the pouring time. Finally, it was known that in our test section at low water subcooling and long pour times (large fuel mass) one could develop conditions in which fuel penetration would be hampered by vapor production. Under these conditions we would open the bypass valve to allow for faster penetration of the fuel jet into the water pool, enhancing mixing and changing the fuel-coolant mixture volume.

In this test series, the level swell meter described in chapter three was installed and verified by visual observation in the WFCI-H-03 and H-05 tests. The original level swell meter signals are shown in Figure 4.41. The voltage signal decreases with coolant level increase, due to the variation of the electric resistance between two copper rods. About 1.6 s before the trigger, the signal from the level swell meter indicates the increase of the water level resulting from the coolant splashing when the fuel jet initially contacts the surface of the water. Such transient surface movements of the coolant are restabilized about t =-1 s, the voltage decreased gradually while approaching asymptotic levels.

In the WFCI-H-03 test, violent oscillations of the level swell signal as shown in Figure 4.41 after the onset of external trigger resulted from the spontaneous explosion occurring above the slide gate. The difference between the initial voltage signals resulted from the operation time of the level swell meter. However, both signals show very similar behavior while maintaining a constant voltage difference.

Figure 4.42 is a plot of integrated average void fractions converted from the voltage signals, and from the images captured with the video camera. The upper and lower limits for the level swell signals represent the error range of the signal interpretation with a maximum range of $\pm$ 13 %. The lower limit for the level swell was calculated by assuming that the vapor was distributed only within the range of the test tube diameter, from the bottom of the test section to the surface of the water. However, the upper limit case was estimated by assuming uniform distribution of the vapor in the test section and funnel.

The signals agree well with the visual observation until t =-0.8 s; at later times values from the level meter gradually increase while the visual observation indicates that the level remains constant at a void fraction of about 25 %. The constant water level measured from the visual observation is due to the slide gate closing about 400 ms before the trigger. The reason for the asymptotic increase of the level swell meter signal is the resistance change due to the suspension of molten fuel debris in the coolant. After the slide gate is closed, the signal tends to remain constant but indicates higher void fractions than from the visual observation. From the level meter results, the average void fraction for the typical WFCI tests is in the range of 20 to 30 %.

As the fuel is poured into the coolant chamber and subsequently mixes with the water, a certain coolant to fuel mass ratio is established in the mixture. This ratio determines the local vapor production rate and can have a significant effect on the void fraction in the fuel-coolant mixture and the subsequent explosion escalation and propagation. From an experimental viewpoint, this ratio is indicative of the integral quantities because it only determines the integral quantity of fuel and coolant in the test section and not the local mixture concentrations of fuel and vapor volume fractions in the liquid.

Thermodynamic analyses [95, 134] show that, theoretically, the volume ratio which maximizes the work output from an explosion, is near one. For the case of tin as a fuel, this volume ratio corresponds to a mass ratio of approximately 1/7. If the mass ratio is smaller than this, the conversion ratio decreases with increasing mass ratio. This happens because the mixture is 'coolant lean' with too little coolant available as the working fluid for heat transfer from the fuel. In contrast, as the mass ratio increases beyond the maximum point, the conversion ratio tends to decrease, because the mixture is 'fuel lean', due to the relatively large amount of coolant liquid which quenches vapor production. It is interesting to note that the observed effects for axial constraint and time scales for heat transfer represent dynamic analogues to this thermodynamic explanation.

The experimental results as shown in Figure 4.43 indicate that the conversion ratios increase with increasing mass ratio in the range from 0.2 to 1.0. This corresponds to a mixture volume to fuel volume ratio of 1.5 to 7.0. A broad maximum of the conversion ratio of less than 1.0 % appears at a mass ratio of about 1 to 3 (mixture volume to fuel volume ratio of about 7 to 20). Finally, the conversion ratio is seen to decrease when the mass ratio (or volume ratio) increases further. These experimental results show that the optimal point for the mass ratio was shifted from the theoretical point of 1/7 to an actual value of 1. This might be expected because the kinetics of the mixing process would increase to large values of this ratio to accommodate the fuel jet penetration into the coolant along with vapor production and coolant liquid outflow. These results include other tests similar to the WFCI tests; *i.e.*, tests conducted by Baines [62] and Hall *et al.*[60]. These tests were chosen because of their similar geometry and experimental conditions as discussed previously in the WFCI-D series.

In Figure 4.43, the conversion ratio for the WFCI series and the above two experiments can also be compared with the Hicks-Menzies' thermodynamic model [95] and Board-Hall's detonation model [134]. The interesting point to note is that all the data is far below the thermodynamic values expected for the tin-water FCI pair. The Hicks-Menzies and the Board-Hall models both indicate theoretical conversion ratios of about 30 percent. This point will be revisited in the experimental analysis as to the implication of these data.

4.11 Iron-Oxide Fuel Composition: WFCI-K Series

A group of experiments were conducted in the K-series with iron-oxide as the fuel simulant. The purpose was to investigate the likelihood of an energetic FCI with a fuel simulant that is more prototypic of molten fuel materials; *i.e.*, molten urania, zirconia and zirconium with modest superheats. The initial conditions were similar in all tests to the past WFCI tests, except for the change in fuel composition and the use of a larger test section in the last two tests. Table 4.2 summarizes the experimental results for all series K iron-oxide experiments. The trigger strength varied from the original WFCI test section (designated WFCI-1) to the larger test section (designated WFCI-2), only because of specific mechanical limitations. The larger piston trigger assembly in WFCI-2 was not able to generate the same trigger peak as in the smaller one, because the same solenoid was used for both designs. Thus, even though the capacitance of the trigger charging circuit was doubled for the WFCI-2 tests, the actual acceleration of the larger piston was smaller. This resulted in a delivered trigger impulse of 8.5 millinewton-sec compared to 14 millinewton-sec in WFCI-1. In addition to these WFCI-K experiments, melt generation and delivery development tests were performed. Smaller masses of melt were dropped into a pit of sand to test the reliablility of the delivery method and repeatability of the melt jet geometry. These tests are not reported in this topical report (Series I and J). Two other tests in the series were excluded because of equipment malfunctions. In test K-06, the melt was not successfully delivered to the test section due to a failure to remove the catcher pan from beneath the furnace. Test K-11 was successful, but the data acquisition system failed to record any data. Since the rupture disk did not break and the slug did not move, there is no way to tell if an explosion occurred.

Since the trigger signal is an integral part of every experiment, it is important to understand its characteristics, specifically with test section size. Past data suggest changes in the magnitude and duration of the trigger signal may affect the experimental results, so care was taken to limit the variation in trigger input. There was some variation between the triggers for tests with WFCI-1 and WFCI-2, and this will be illustrated. It was desired that all the triggers be of the same amplitude and duration for every experiment to eliminate its effect as an experimental variable on the explosivity for the oxide fuel.

Figure 4.44 shows a typical set of pressure peaks generated by the trigger for WFCI-1, and Figure 4.45 shows the same for WFCI-2. The WFCI-1 trigger clearly shows a sharper and more defined peak. This is due to the fact that the WFCI-1 piston is smaller and has a larger travel distance, so it can reach a higher velocity when struck from below, and hence a larger peak (as mentioned above), even with a lower charging voltage. All WFCI-1 triggers were charged to 200 V with two capacitors, while the WFCI-2 triggers were charged to 400 V with four capacitors. The magnitude of the peak pressure and the width of the peak are measured directly from the data. Summation of the pressure values generates the area under the peak, which when multiplied by the surface area of the transducer (= 0.236 cm2), has units of N-s as the impulse. The WFCI-1 trigger has a peak amplitude of around 3.0 MPa, a peak width of 150 microseconds, and an impulse of 0.008 N-s. The WFCI-2 trigger has a peak of near 1.5 MPa, a similar pulse width and impulse of 0.005 mN-s. Though the peak characteristics differ, the propagation speeds of these pulses are similar, as expected. The data for shock arrivals at various positions are plotted in Figures 4.46 and 4.47. The propagation speeds are 1441 and 1431 m/s, respectively, and constant along its length.

The pressure data taken during each experiment provides information about the pressure at eight points along the test section tube. Table 4.2 gives the maximum pressures, the peak impulses, and propagation speeds for the pressure data taken in all experiments and two trigger runs, and Figures 4.48 to 4.56 show the transient histories for each experiment. It was from this data that information about the peak pressure, impulse, and propagation speed was determined.

Peak pressures give a fairly qualitative measure of interaction strength. Impulses are calculated using an integration technique where the pressure values are added over a given time span, and are dependent upon the choice of integration region. The time period is constant for all of our comparisons. The propagation speed is estimated by determining the time that a given peak arrives, which is characterized by the pressure value attaining a certain level above the background noise level (chosen to be 0.5 MPa). These values are only used for rough comparisons between experiments. For experiments K-02 to K-08, the pressure histories are quite similar. In all cases, the trigger peak can be seen from the P1 trace, while the P2 shows a lower value, and P3 through P8 show no pressure signals at all. The traces for test K-10 are similar to those for tests K-02 through K-08, where the trigger can be seen, and the amplitude markedly decreases as the pressure pulse propagates. Some evidence of the trigger can be seen up to P5. The pressure data for experiments K-01 and K-09 show the peak pressures propagating upwards and gaining in amplitude, while the propagation speeds and the associated impulses decrease. In addition, the peaks tend to become wider at the top of the test section, and peaks can be seen apparently coming down from the top in traces P7 and P6.

The amplitudes of the pressure peaks are tabulated in Table 4.2 and give some insight into the strength of the interactions that occurred. In tests K-03 and K-05, the pressure

peak amplitudes of 5.25 MPa and 5.02 MPa at the P1 transducer are larger than the known trigger amplitude for WFCI-1 of 3.0 MPa, which would indicate a weak interaction occurring there. Tests K-02, -04, -07, and -08 all have maximum pressures less than the trigger pressure, which indicates that there was no interaction. Experiments K-01 and K-09 yielded the largest maximum pressures: 6.53 MPa for K-01 and 9.70 MPa for K-09, with these occurring near the top of the test section. Test K-10 had a maximum pressure of 4.36 MPa at transducer P1, and the pulse tapered off as it traveled upwards. The impulses of the pressure peaks can also give some insight into the energy released during the interactions (or explosions). For a given timespan encompassing the FCI, data are numerically integrated resulting in a number that is multiplied by the surface area of the transducer face ($0.236cm^2$). This number is only used as a guide to indicate which interactions were stronger relative to others in this test series. The impulses are the largest for tests K-01 and K-09 with values of 0.73 N-s and 0.16 N-s, respectively.

A closer examination of tests K-01 and K-09 will now be made, since there are multiple peaks on the pressure plots, and the impulses given in Table 4.3 do not differentiate between the different peaks. Table 4.3 gives detailed impulse calculation information for each peak. In experiment K-01, the impulse is fairly constant for the first four transducers, and the fifth loses its signal after peak arrival. Transducers P6 and P7 show peaks traveling upwards, and peaks traveling downwards. The impulse of the upward peaks are 0.03 N-s and 0.024 N-s, for P6 and P7, respectively. For its downward propagation, they are 0.03 N-s and 0.015 N-s, for P7 and P6, respectively. There was no data collected for transducer P8. For test K-09, the impulses are very small to begin with, then get large very quickly from P4 to the top. The largest occurs at P7 traveling upwards, and has an impulse of 0.13 N-s. Traveling downwards, the peaks at P6 and P5 have a 0.1 N-s and 0.075 N-s impulses, respectively, then the impulses get smaller after that. The propagation speeds are calculated by noting the time of the initial rise of each pulse, and performing a simple linear slope calculation between each transducer. In tests K-01 peaks, so the position of each transducer is plotted as a function of the time that the peak arrives (Figures 4.57 and 4.58). The slope of this curve is the peak propagation speed. Both K-01 and K-09 show that the initial peak propagation speed is 509 m/s, and the speed drops off as the peak rises to a minimum of 94 m/s for K-01 and 27 m/s for K-09 (both at transducer P7). In addition, in test K-01, it is estimated that the pressure peak was traveling upwards from P7 to the slide gate and back down at a rate of 168.9 m/s, then had a speed of 183.6 m/s downward to P6. The propagation speeds of the downward moving peaks in experiment K-09 are difficult to measure due to the number of peaks present in P6.

The conversion ratio is the parameter used to represent the work done by the fuel-coolant interaction. As noted previously, test K-05 was the only test in which the slug moved from the interaction, and the resulting conversion ratio was determined to be 0.058 percent . Clearly, the energetics from the FCIs with iron-oxide are quite weak compared to the

molten tin tests, even though the available thermal energy is much larger. Let us consider a few visual observations before we address the actual existence of explosions for the WFCI-K series in the next section.

Consider several visual clues that aided in the determination of whether or not an explosion occurred, and where it occurred. A visual record of each experiment was taken with two different video cameras, and from these it was noted if there was a visible interaction in the funnel. This would indicate the occurrence of a delayed spontaneous explosion or interaction. In addition, the rupture disk at the end of the expansion tube can be used to determine if an interaction occurred inside the test section that caused an increase in pressure. On several occasions the rupture disk did break, and corresponding pressure peaks were noted, but the explosion (or interaction) was not strong enough to move the slug down the tube. From this information, it was determined that in tests K-05, K-09, and K-10, there were fuel-coolant interactions strong enough to break the rupture disk, and in tests K-04, K-05, and K-09, there were delayed spontaneous explosions that occurred in the funnel after the slide gate closed (Table 4.2).

Table 1: WFCI Series A - H Experimental Initial Conditions and Results											
Initial Conditions								Results			
Experiment Number	Melt Mass	Melt Temp	Coolant Temp	Ambient Temp	Viscosity Ratio	Trigger Voltage	Slug Mass	Internal Energy	Work	CR	Interaction Type
	(kg)	(C)	(C)	(C)		(V)	(kg)	(kJ)	(kJ)	(%)	
A-01	3.45	940	85.0	25.0	1	200	23.4	963.36	2.49	0.258	ESE
A-02	3.73	980	85.0	3.0	1	200	23.4	1079.89	2.05	0.190	TE
A-03	3.45	940	85.0	13.5	1	200	23.4	963.36	6.75	0.701	ESE
A-04	3.30	955	85.0	15.0	1	200	23.4	934.2	4.22	0.452	DSE
A-05	3.58	940	85.0	23.0	1	200	23.4	999.66	3.25	0.325	TE
A-06	3.50	850	84.5	24.0	1	200	23.4	896.82	3.15	0.351	ESE
B-01	3.87	975	85.0	23.0	1	0	23.4	1115.45	1.73	0.155	DSE
B-02	2.87	969	85.0	23.0	1	0	23.4	822.79	2.49	0.303	DSE
B-03	3.84	970	83.0	15.0	1	0	23.4	1103.84	5.04	0.457	ESE
C-01	3.31	978	85.0	24.0	1	200	23.4	956.59	3.66	0.383	TE
C-02	3.20	937	85.0	24.0	1	100	23.4	921.72	—	—	SE
C-03	3.48	983	85.0	24.0	1	400	23.4	1010.2	2.60	0.257	TE
C-04	3.57	881	83.0	10.0	1	450	23.4	944.57	2.48	0.263	TE
C-05	3.09	913	84.0	13.0	1	100	23.4	842.19	2.67	0.317	TE
C-06	3.19	923	86.5	24.0	1	300	23.4	875.59	2.43	0.278	TE
D-01	3.19	901	84.3	24.0	1	200	0.53	859.36	0.83	0.097	TE
D-02	3.31	911	84.6	24.0	1	200	42.2	899.94	3.78	0.420	TE
D-03	3.51	877	84.1	24.0	1	200	42.2	924.1	4.90	0.530	TE
D-04	3.19	901	86.6	24.0	1	200	58.8	857.47	—	—	TE
D-05	2.91	819	82.9	24.0	1	200	71.2	723.65	2.50	0.345	ESE
D-06	3.01	889	83.6	24.0	1	200	71.2	802.13	2.40	0.299	TE
E-01	3.85	680	87.0	24.0	1	200	23.4	815.82	3.44	0.422	ESE
E-02	3.66	790	88.0	24.0	1	200	23.4	879.96	2.65	0.301	TE
E-03	0.72	491	93.0	24.0	1	200	23.4	—	—	—	ESE
F-02	0.99	782	27.0	24.0	1	0	23.4	—	—	—	ESE
F-03	1.52	850	62.5	24.0	1	200	23.4	—	—	—	ESE
F-04	1.23	871	72.0	24.0	1	200	23.4	—	—	—	ESE
G-01	1.62	584	25.0	24.0	2.5	0	23.4	454.03	—	—	NE
G-02	1.66	820	25.0	24.0	2.5	200	23.4	437.93	—	—	NE
G-03	1.70	875	33.0	24.0	2.0	0	23.4	469.02	—	—	NE
G-04	1.70	853	28.0	24.0	1.5	0	23.4	461.59	—	—	NE
G-05	0.82	850	27.5	24.0	1	0	23.4	—	—	—	ESE
G-06	3.67	860	27.5	24.0	2.5	0	23.4	1003.57	—	—	NE
H-01	1.01	855	82.0	24.0	1	200	23.4	—	—	—	ESE
H-02	3.54	855	87.5	24.0	1	200	23.4	908.89	—	—	TE
H-03	4.24	920	88.0	24.0	1	200	23.4	1161.07	4.83	0.416	TE
H-04	4.48	920	86.0	24.0	1	200	23.4	1228.79	2.69	0.219	TE

ESE = Early Spontaneous Explosion
DSE = Delayed Spontateous Explosion
TE = Triggered Explosion
NE = No Explosion

Table 4.1: WFCI series A-H experimental initial conditions and results

Table 4-2: Pressure Peak Propagation Speeds and Impulses for WFCI Experiments												
		WFCI-1 Trig	WFCI-2 Trig	K-01	K-02	K-03	K-04	K-05	K-07	K-08	K-09	K-10
P1	Peak Pressure (MPa)	2.5	1.7	2.4	1.3	5.3	3.0	5.0	2.4	2.0	9.7	4.4
	Impulse (mN-s)	8.1	4.6	55.6	19.5	9.7	22.6	30.4	25.6	16.5	141.6	66.6
	Speed (m/s)	---	---	---	---	---	---	---	---	---	---	---
P2	Peak Pressure (MPa)	2.5	1.6	1.5	0.4	---	---	---	1.3	0.4	1.2	1.6
	Impulse (mN-s)	7.6	4.4	45.1	22.6	2.4	16.1	26.2	11.7	10.9	107.7	45.1
	Speed (m/s)	1402.3	1435.7	509.6	736.1	254.8	236.6	473.23	552.1	225.5	509.6	565.2
P3	Peak Pressure (MPa)	2.6	1.2	2	---	---	---	---	---	---	0.7	1.1
	Impulse (mN-s)	7.6	4.4	57.7	11.7	0.5	5.4	23.1	9.4	8.0	26	45.2
	Speed (m/s)	1402.3	1423.3	179.1	---	---	---	---	---	---	44.5	560.3
P4	Peak Pressure (MPa)	2.2	1.4	2.8	---	---	---	---	---	---	3.3	1.0
	Impulse (mN-s)	6.8	4.4	34.6	15.3	0.4	4.6	20.9	8.8	8.1	59.1	42.4
	Speed (m/s)	1402.3	1331.5	114.2	---	---	---	---	---	---	70.5	---
P5	Peak Pressure (MPa)	2.3	1.5	1.2	---	---	---	---	---	---	9.1	---
	Impulse (mN-s)	7.8	4.4	6.4	10.5	0.0	4.8	16.3	7.7	8.6	146.7	33.6
	Speed (m/s)	1529.8	1641.4	132.5	---	---	---	---	---	---	50.2	---
P6	Peak Pressure (MPa)	2.5	1.4	4.7	---	---	---	---	---	---	6	---
	Impulse (mN-s)	7.3	4.4	61.6	14.2	0.0	5.3	14.7	8.8	8.6	149.	27.6
	Speed (m/s)	1526.0	1346.6	126.6	---	---	---	---	---	---	45.6	---
P7	Peak Pressure (MPa)	2.2	1.3	6.5	---	---	---	---	---	---	3.8	---
	Impulse (mN-s)	3.1	4.0	73.2	14.7	0.0	4.3	24.5	8.4	8.6	160.4	34.5
	Speed (m/s)	1385.5	1419.8	93.8	---	---	---	---	---	---	28.6	---
P8	Peak Pressure (MPa)	1.9	1.3	---	---	---	---	---	---	---	8.3	---
	Impulse (mN-s)	2.9	3.9	---	11.9	0.0	3.6	24.8	8.4	8.4	114.9	14.5
	Speed (m/s)	1270.0	1567.7	---	---	---	---	---	---	---	105.3	---

Table 4-2: WFCI series K pressure peak propagation speed and impulse data.

Table 4-3: Impulse Data for Tests K-01 and K-09			
		K-01	*K-09*
P1 - up	*Impulse (mN-s)*	27.9	5.4
	Time Range (ms)	18 - 21	17 - 21
P2 - up	*Impulse (mN-s)*	25.8	6.2
	Time Range (ms)	18 - 21	17 - 21
P3 - up	*Impulse (mN-s)*	30.8	0.0
	Time Range (ms)	18 - 21	17 - 21
P4 - up	*Impulse (mN-s)*	27.2	18.5
	Time Range (ms)	18.5 - 20.5	19 - 23
P5 - up	*Impulse (mN-s)*	2.0	35.4
	Time Range (ms)	19 - 21	21 - 25
P6 - up	*Impulse (mN-s)*	30.8	35.9
	Time Range (ms)	20 - 22	23 - 27
P7 - up	*Impulse (mN-s)*	22.4	130.2
	Time Range (ms)	20 - 22	25 - 31
P8	*Impulse (mN-s)*	—	103.6
	Time Range (ms)	—	25 - 31
P7 - down	*Impulse (mN-s)*	31.4	—
	Time Range (ms)	24 - 26	—
P6 - down	*Impulse (mN-s)*	14.7	103.1
	Time Range (ms)	24 - 26	27 - 31
P5 - down	*Impulse (mN-s)*	—	71.5
	Time Range (ms)	—	29 - 33
P4 - down	*Impulse (mN-s)*	—	0.0
	Time Range (ms)	—	29 - 33

Table 4.4: Experimental Conditions of Experiments in Comparison

	Hall	K-21	Baines	WFCI
H_{ts} (m)	0.85	1.1	1	1.5
H_{ep} (m)	0	0	3	3.9
D (mm)	28	95	30	87
T_c (°C)	85 ~ 95	85	90	83 ~ 87
T_f (°C)	600 ~ 750	1080	800	819 ~ 911
m_f (kg)	0.5 ~ 1.2	6.5	0.5 ~ 0.8	3 ~ 3.5
m_s (kg)	0	0	2.4	0.5 ~ 71
$< m >$	0	0	3.4	0.06 ~ 8

Table 4.5: Debris Masses Collected from the WFCI-G Series Tests

WFCI Series	M_o (kg)	M_{it}[1] (kg)	M_{ot}[2] (kg)	M_t[3] (Kg)	Remarks
G-01	2.4	1.60	0.52	2.12	NE[4]
G-02	2.4	1.66	0.70	2.36	NE
G-03	2.4	1.70	0.57	2.27	NE
G-04	2.4	1.70	0.62	2.32	NE
G-05	2.4	0.82	1.35	2.17	SE[5]
G-06	5.0	3.67	1.21	4.88	NE
F-02	5.0	0.99	3.79	4.78	SE

[1]Collected mass in the test-section tube
[2]Collected mass outside of the test-section tube
[3]Total recovered mass
[4]No Explosion
[5]Spontaneous Explosion

Table 4.6: Experimental Results of the WFCI-A, B, C and D Experiments

Test Series	CR	P_{pk}	$\bar{u}_{prop}$	t_{exp}	Δt_s	Remark
	%	MPa	m/s	ms	ms	
D-01	0.068	9.4	203	9.66	107.1	TE
D-02	0.365	16.6	217	9.01	416.1	TE
D-03	0.442	>17.0[a]	271	8.21	376.1	TE
D-04	n/a	8.8	203	8.58	n/a	TE
D-05	0.317	n/a	n/a	-307.7	622.2	ESE
D-06	0.274	10.0	203	8.58	636.1	TE
A-02	0.184	> 7.0[a]	282	8.21	358.0	TE
A-05	0.324	> 5.1[a]	222	12.04	283.6	TE
B-01	0.153	n/a	n/a	1189.2	392.4	DSE
B-02	0.297	5.7[b]	216	663.4	332.0	DSE
B-03	0.453[c]	> 4.0[b]	157	-67.8	228.8	ESE
C-01	0.384	> 3.8[b]	210	9.31	260.0	TE
C-05	0.309	>17.0[a]	190	13.97	319.5	TE

[a] peak pressure was exceeded the maximum range of pressure transducer
[b] four pressure transducers (instead of eight in present study) were installed
[c] estimated by the incompletely collected debris due to the early spontaneous explosion

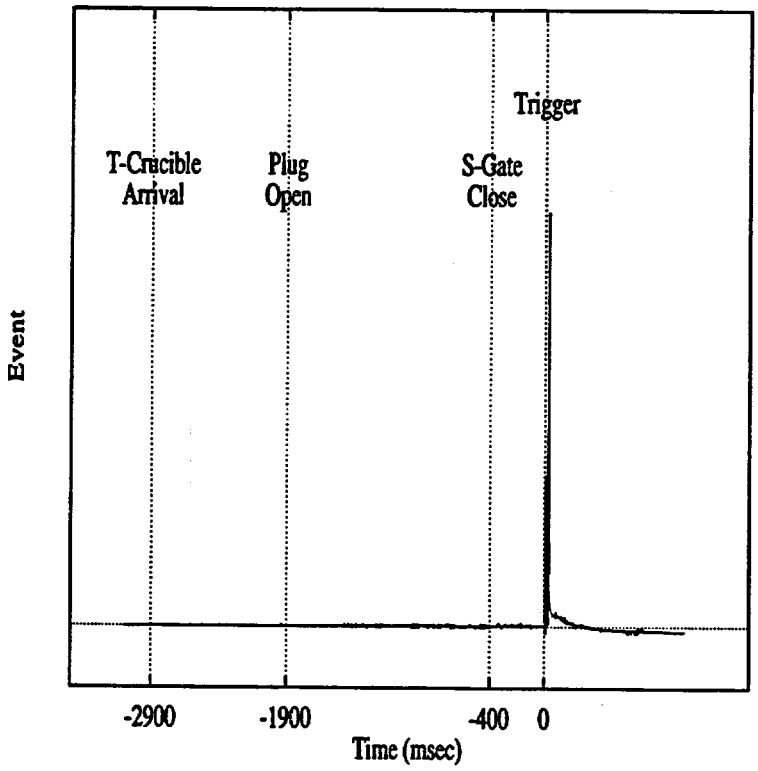

Figure 4.1: Sequential Events of the Typical WFCI Tests

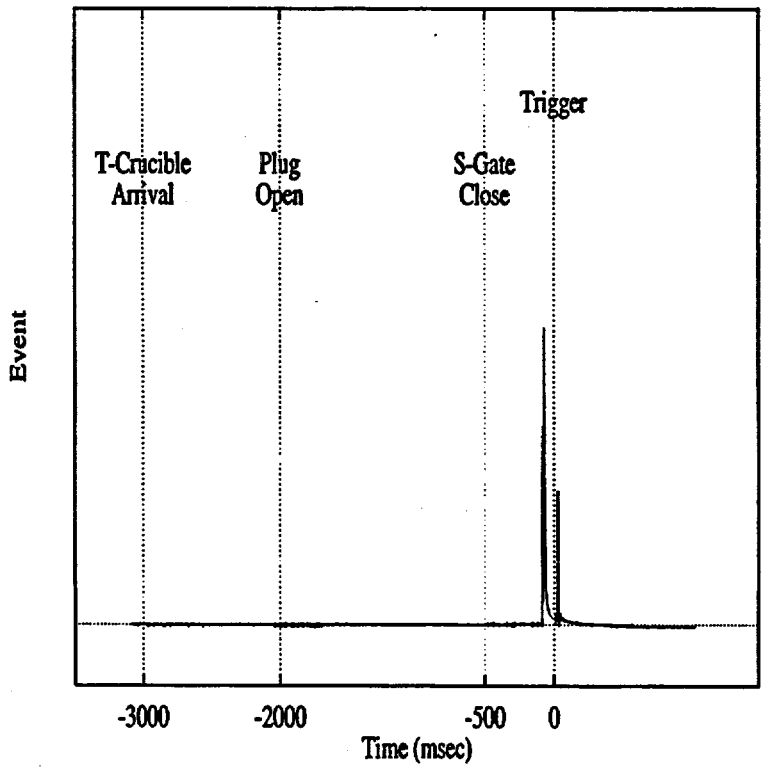

Figure 4.2: Sequential Events of the WFCI-A-01 Test

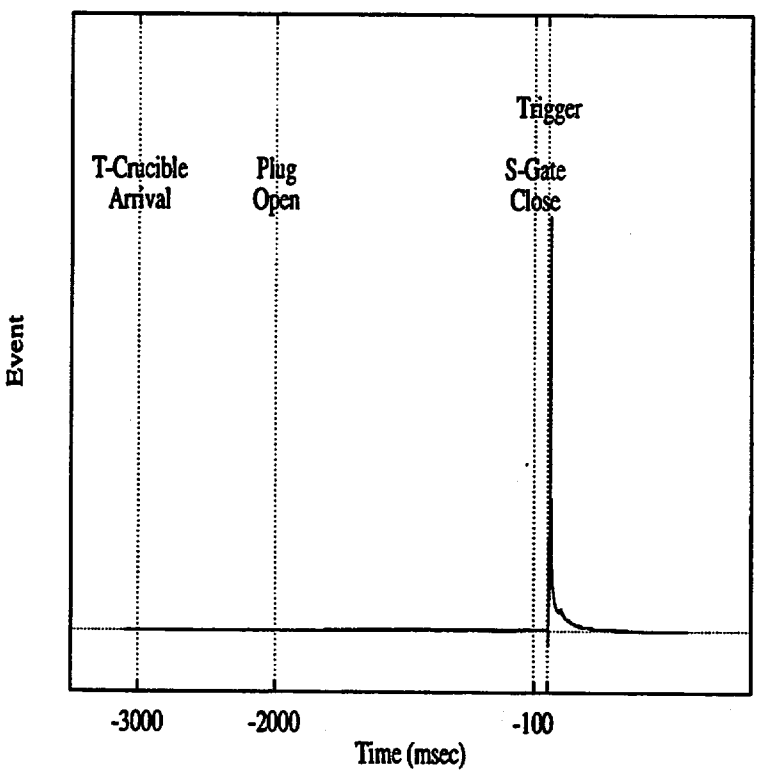

Figure 4.3: Sequential Events of the WFCI-H Series Tests

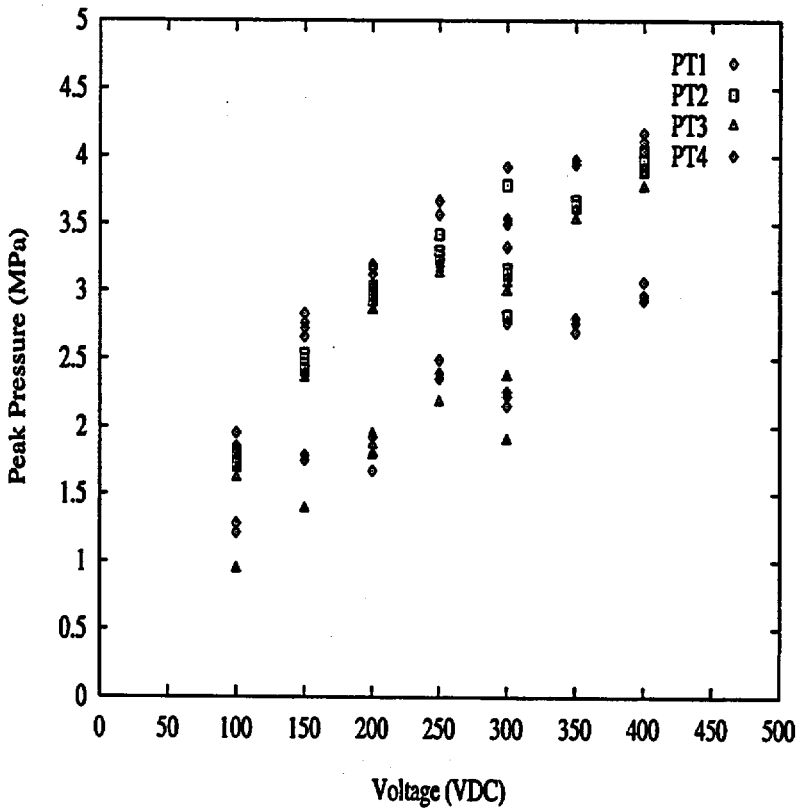

Figure 4.4: Peak Trigger Pressures vs. Supplied Voltages

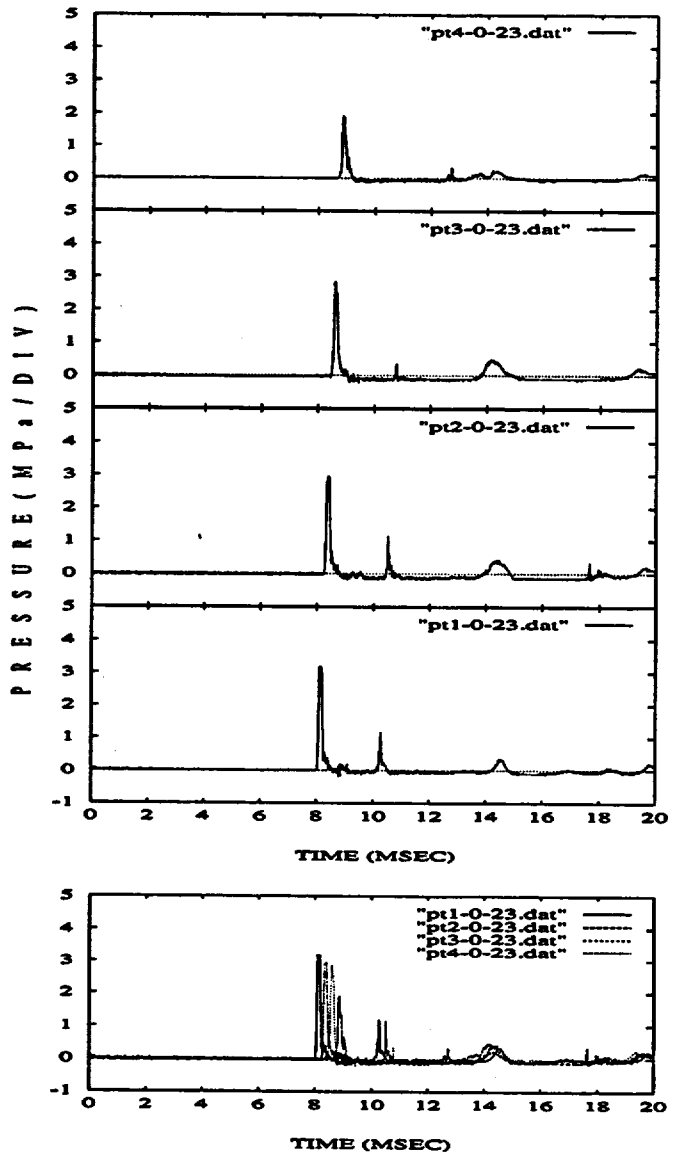

Figure 4.5: External Trigger Pressures Generated by a Supplied Voltage of 200 V

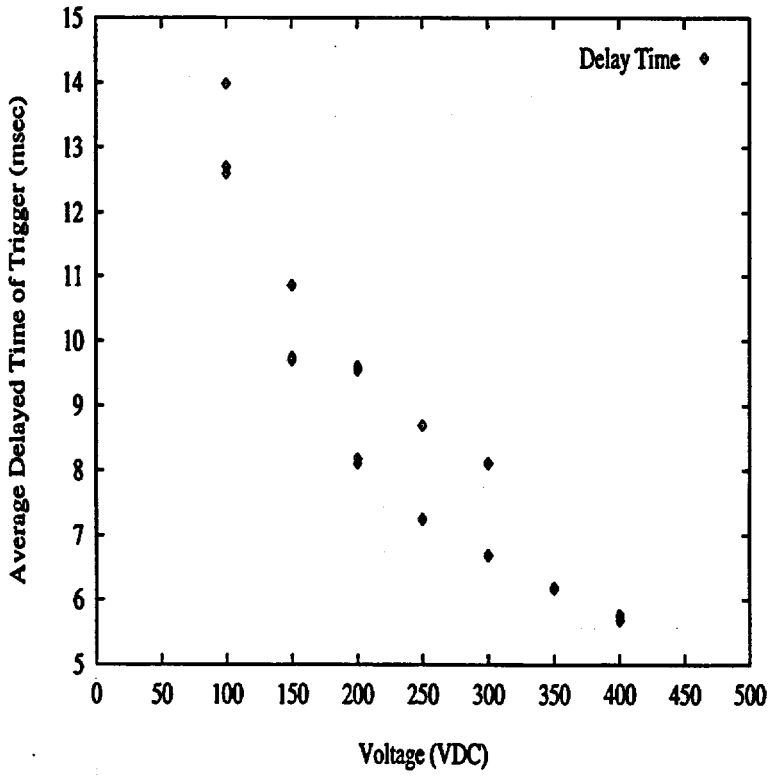

Figure 4.6: Average Time Delay of the External Trigger vs. Supplied Voltages

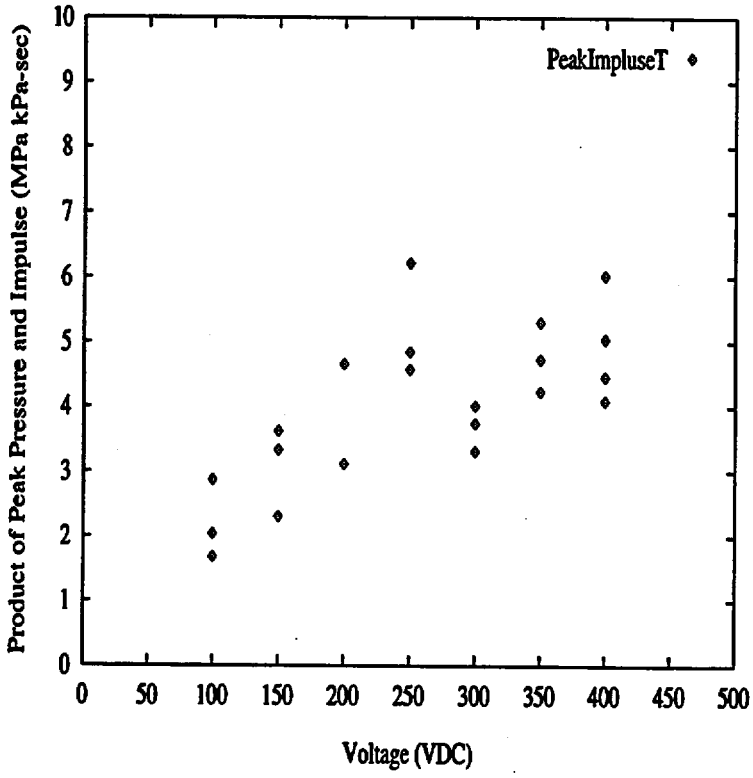

Figure 4.7: Product of the Peak Pressure and Impulse at the First Pressure Transducer with respect to Supplied Voltages

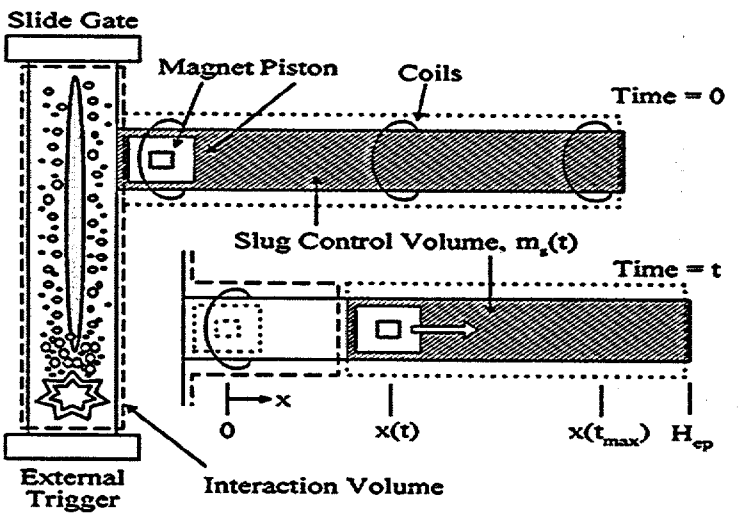

Figure 4.8: Measurement of the Work done by Energetic FCIs on the Slug in WFCI Facility

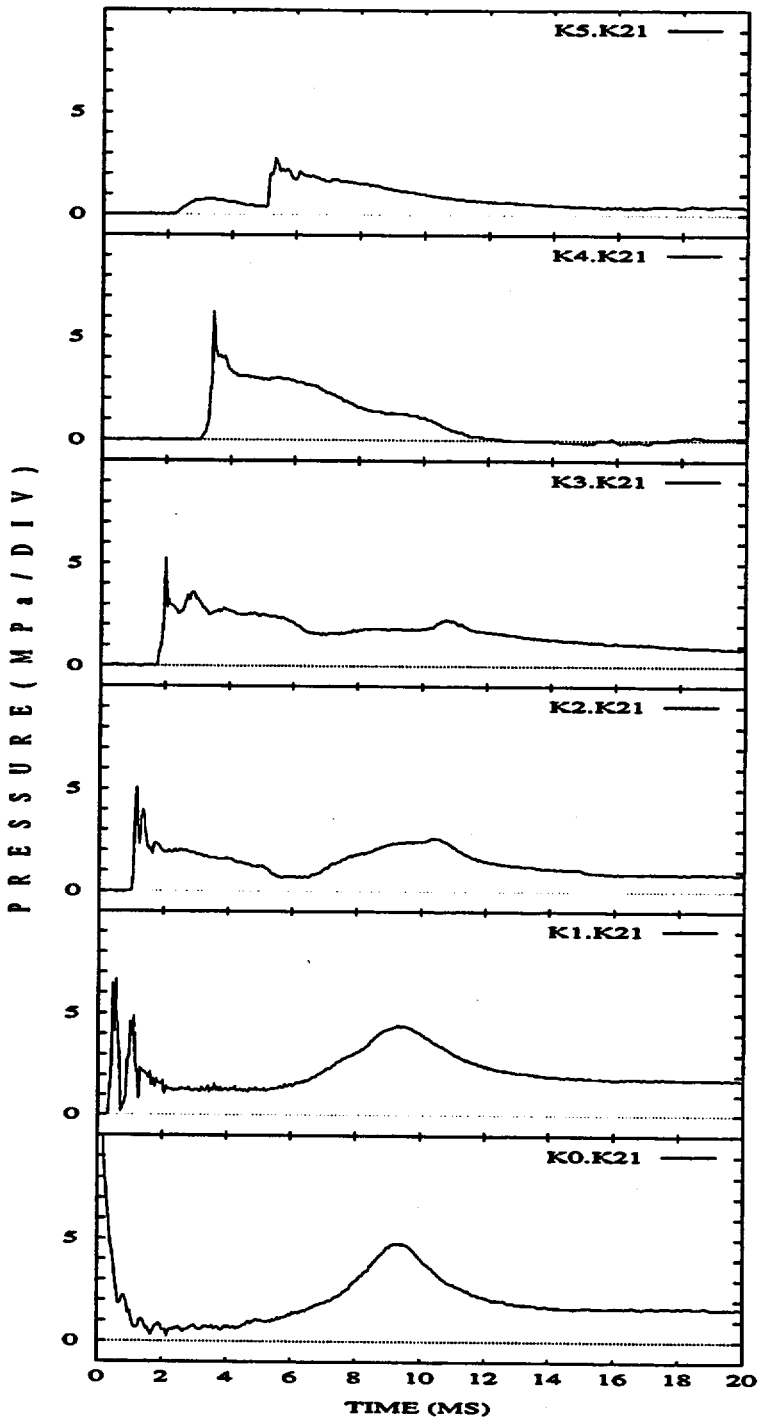

Figure 4.9: Pressure Traces of the KROTOS-21 Test [66]

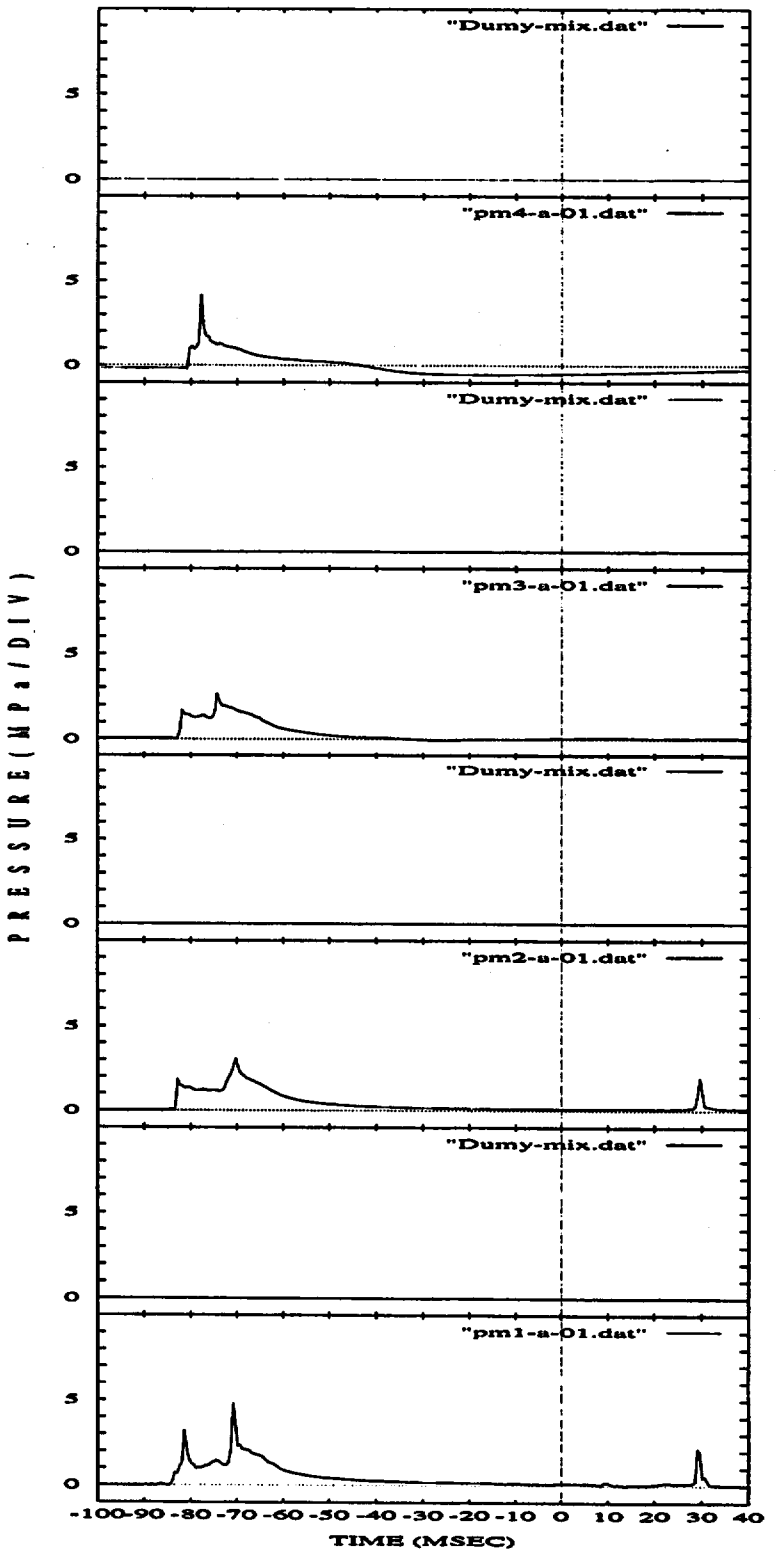

Figure 4.10: Pressure Traces of the WFCI-A-01 Test

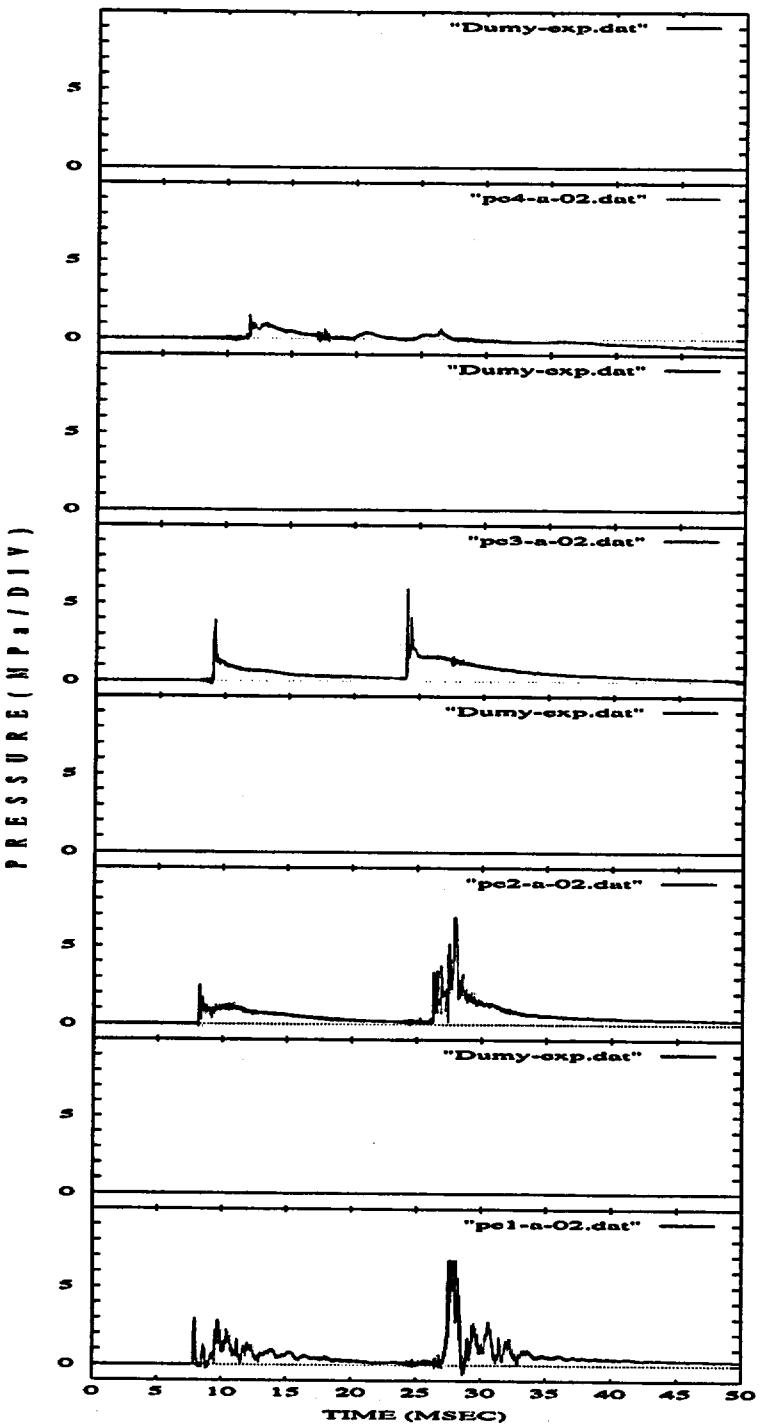

Figure 4.11: Pressure Traces of the WFCI-A-02 Test

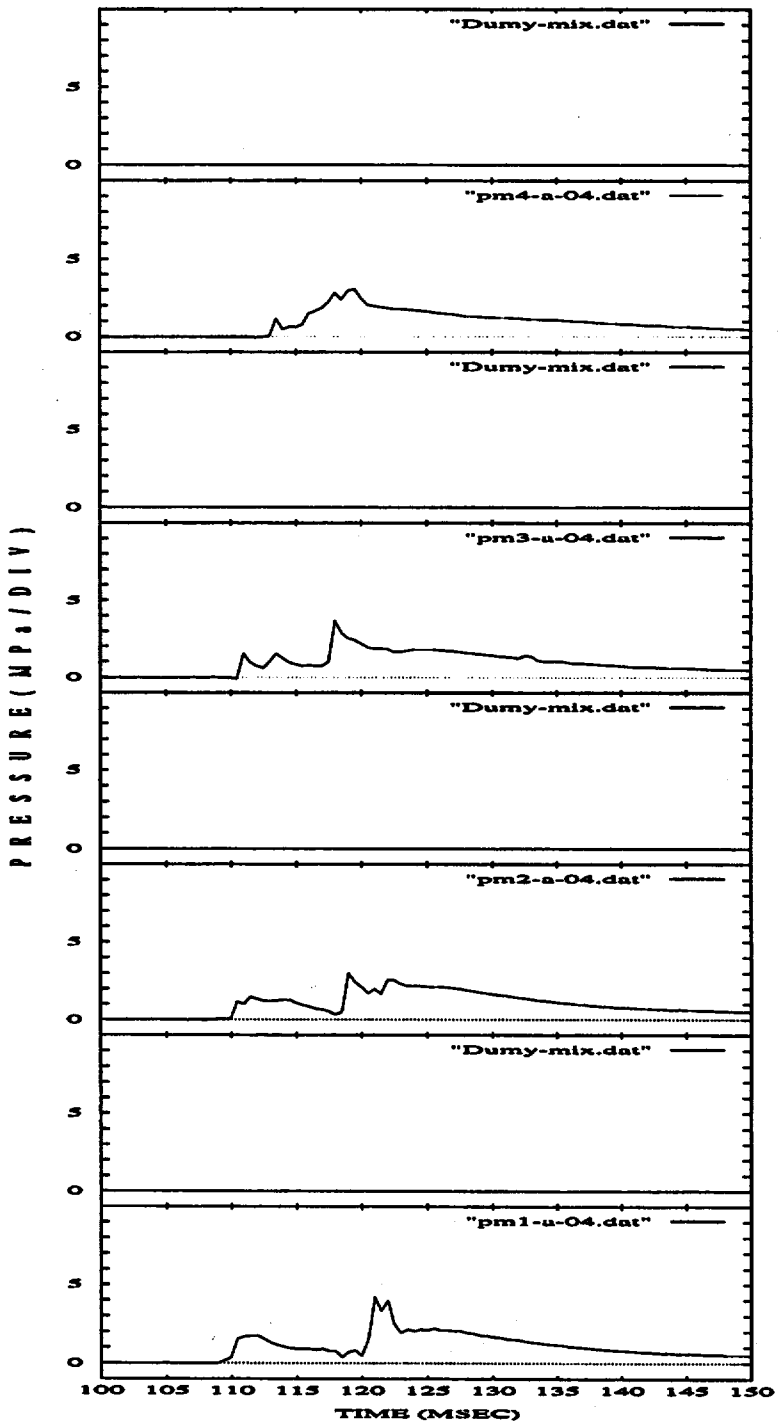

Figure 4.12: Pressure Traces of the WFCI-A-04 Test

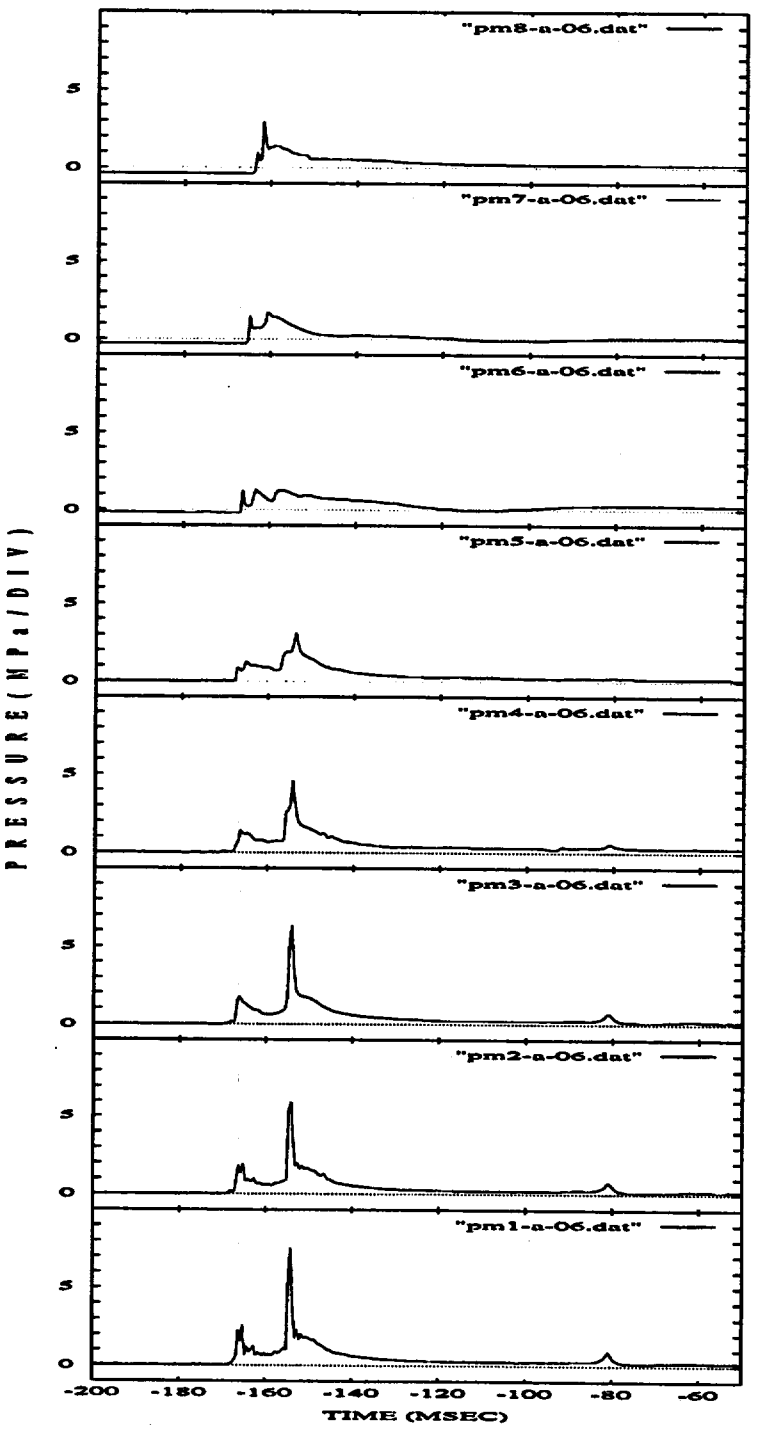

Figure 4.13: Pressure Traces of the WFCI-A-06 Test

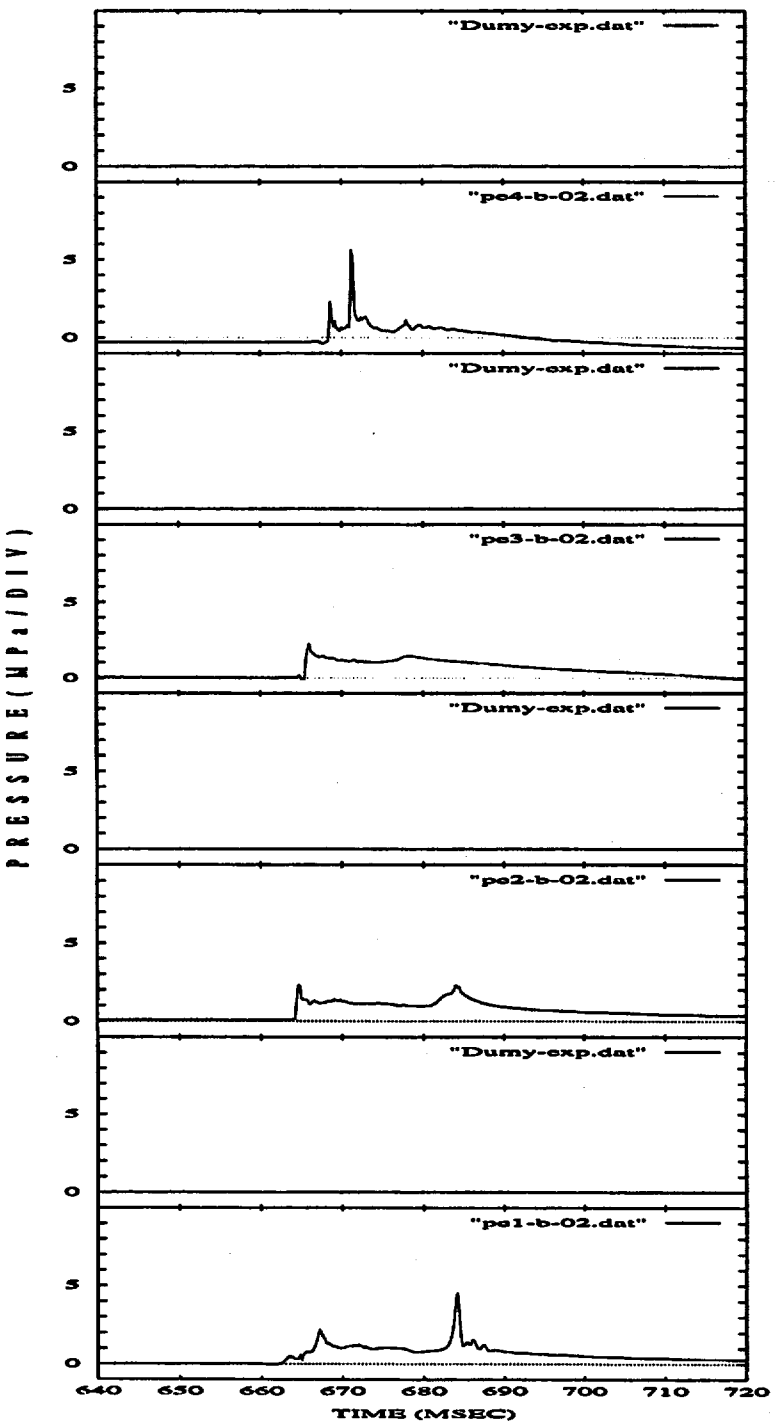

Figure 4.14: Pressure Traces of the WFCI-B-02 Test

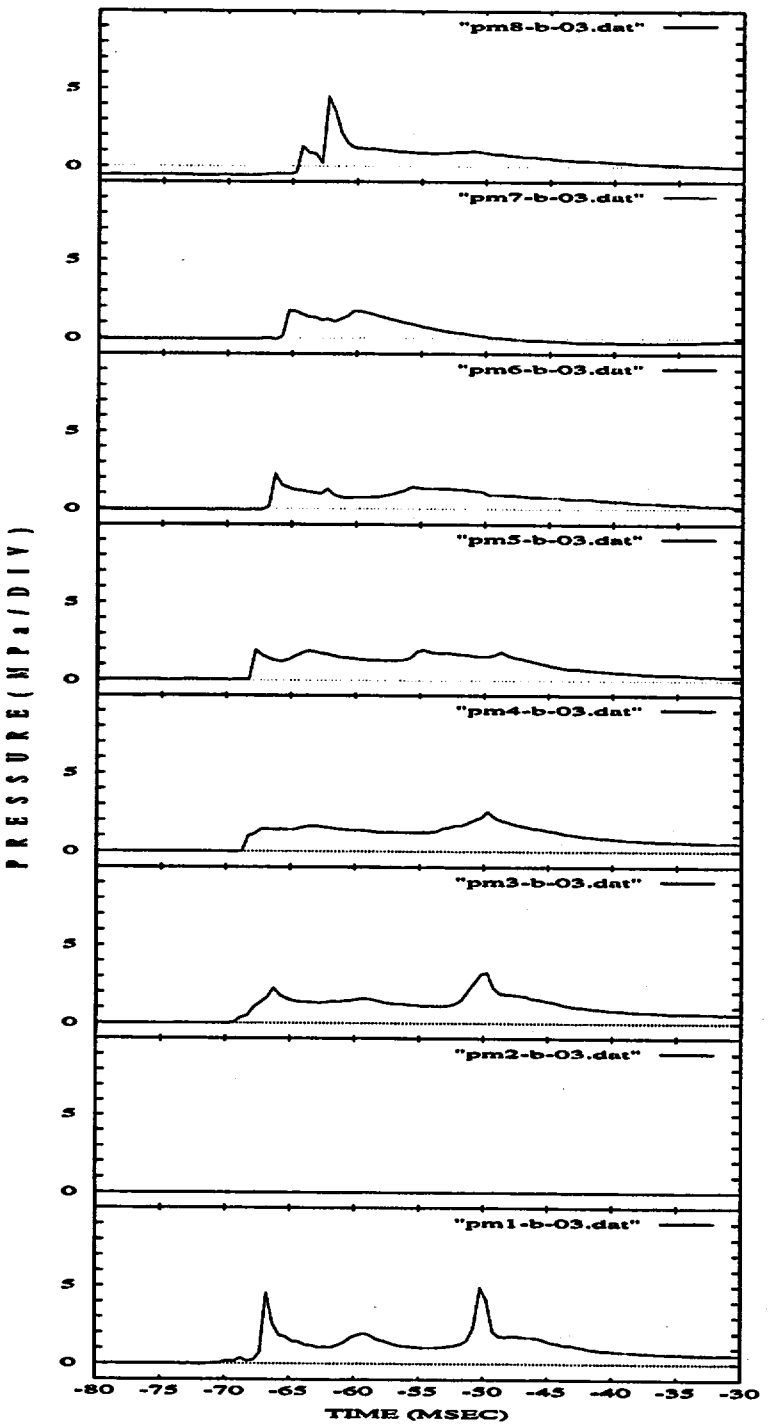

Figure 4.15: Pressure Traces of the WFCI-B-03 Tests

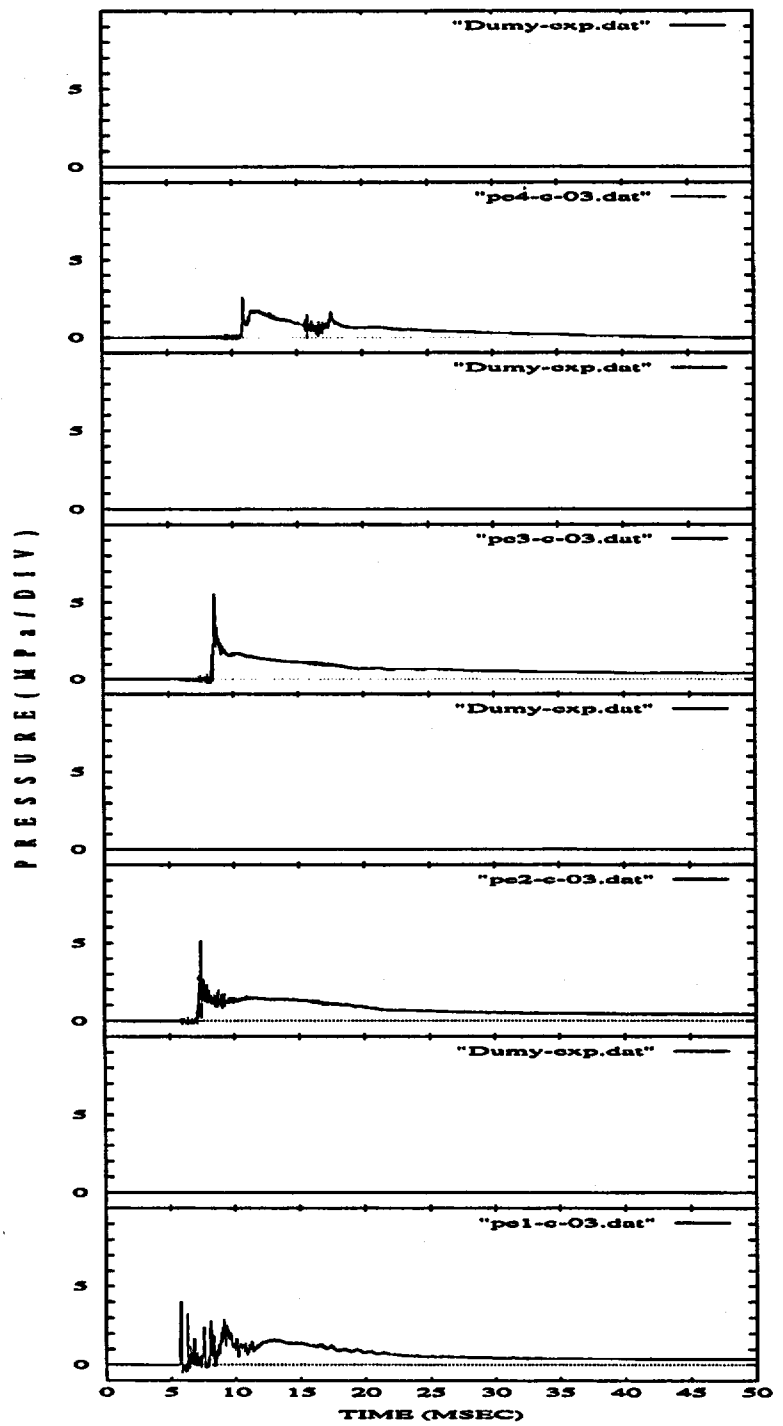

Figure 4.16: Pressure Traces of the WFCI-C-03 Test with a Supplied Voltage for the External Trigger of 400 V

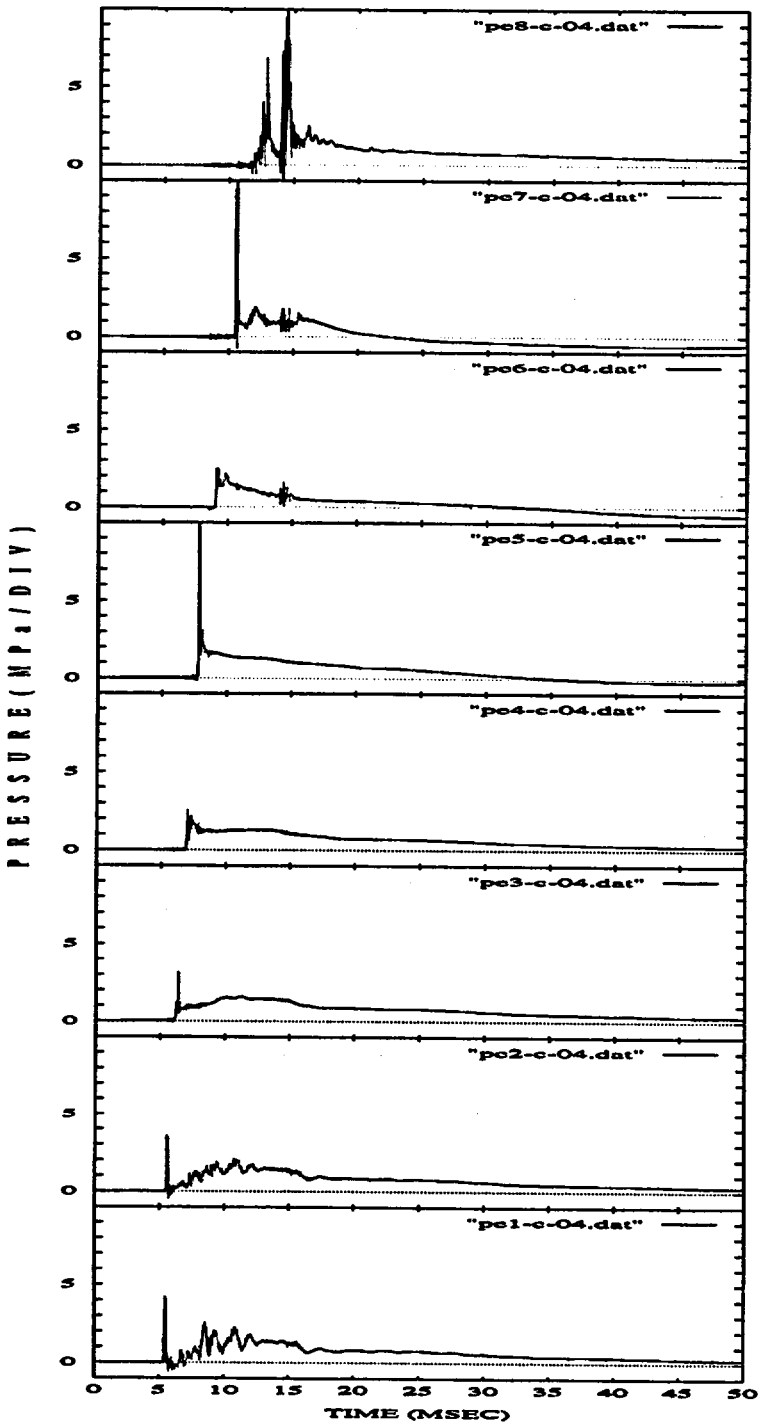

Figure 4.17: Pressure Traces of the WFCI-C-04 Test with a Supplied Voltage for the External Trigger of 450 V

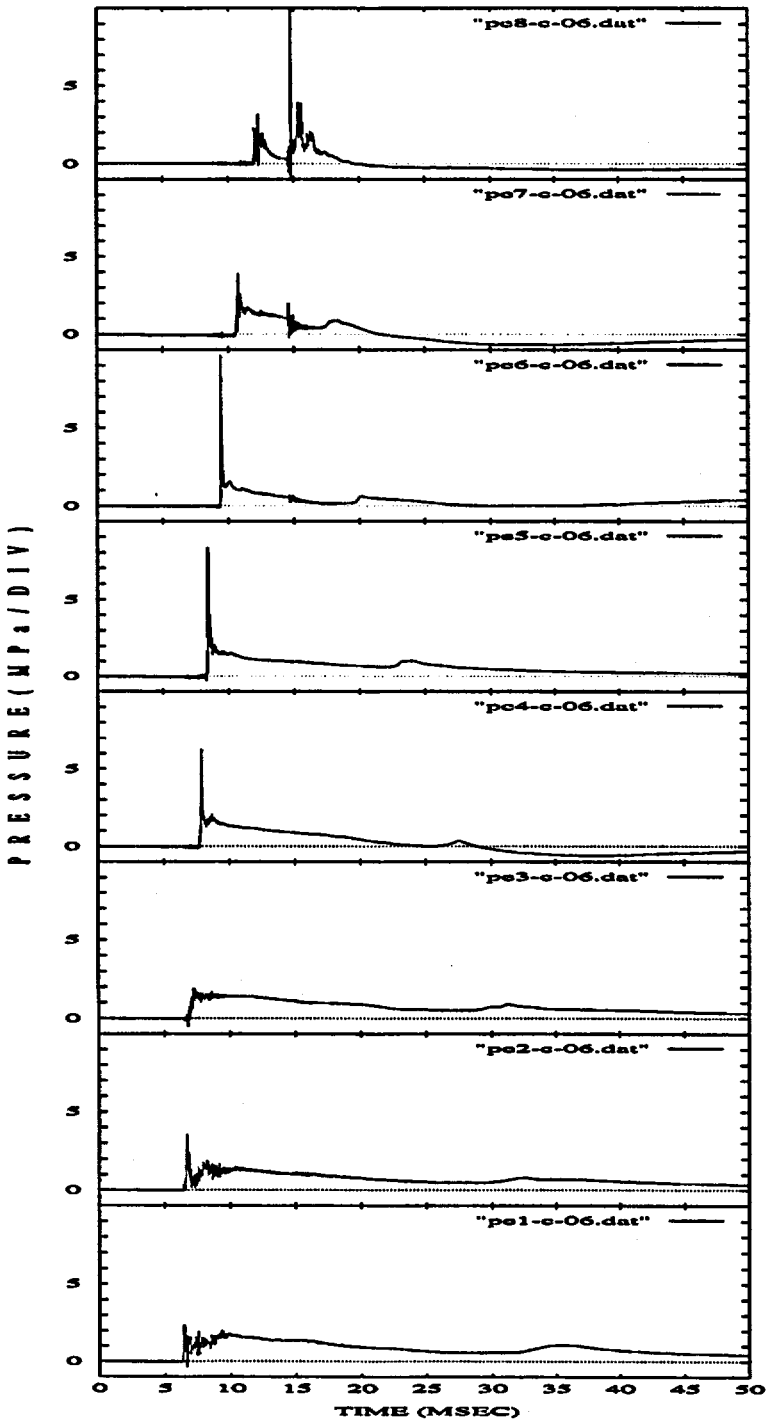

Figure 4.18: Pressure Traces of the WFCI-C-06 Test with a Supplied Voltage for the External Trigger of 300 V

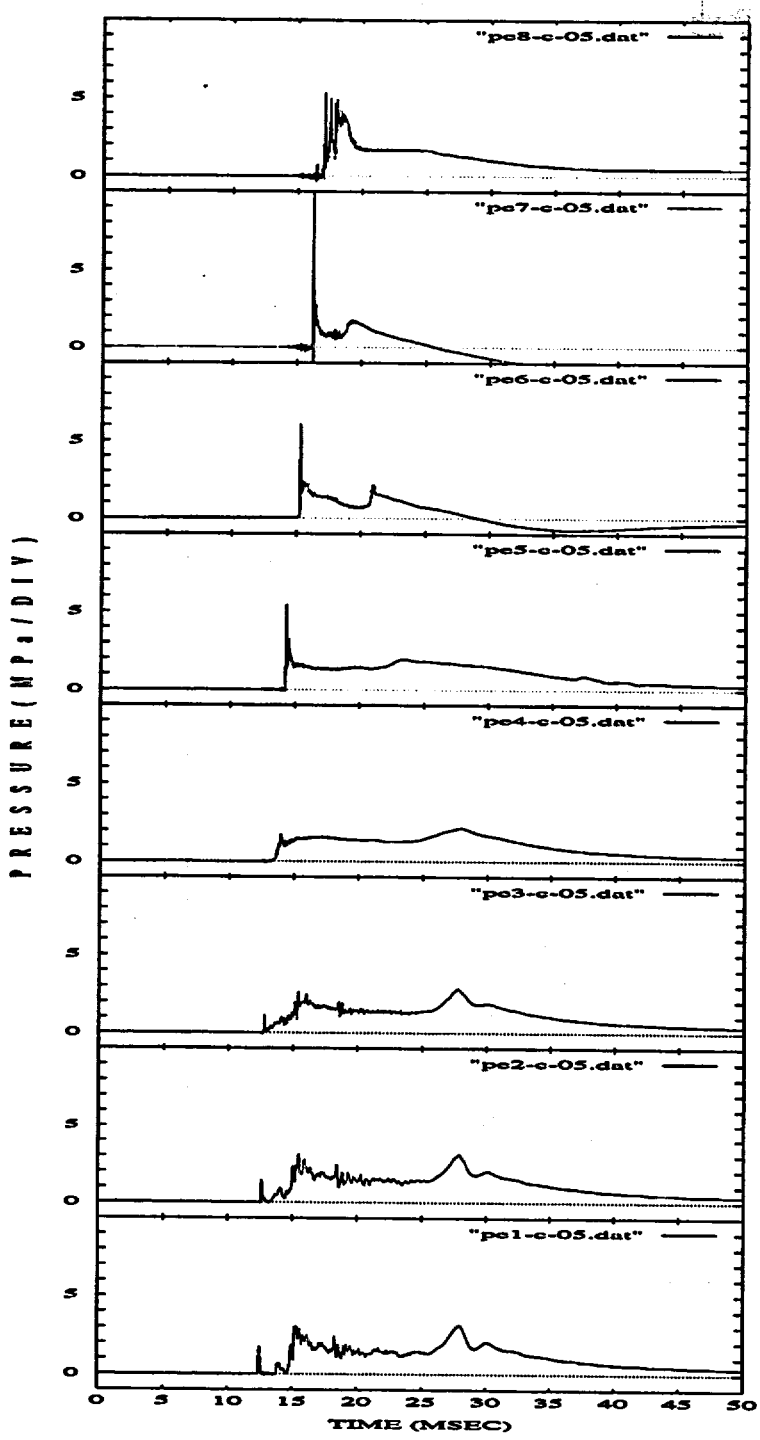

Figure 4.19: Pressure Traces of the WFCI-C-05 Test with a Supplied Voltage for the External Trigger of 100 V

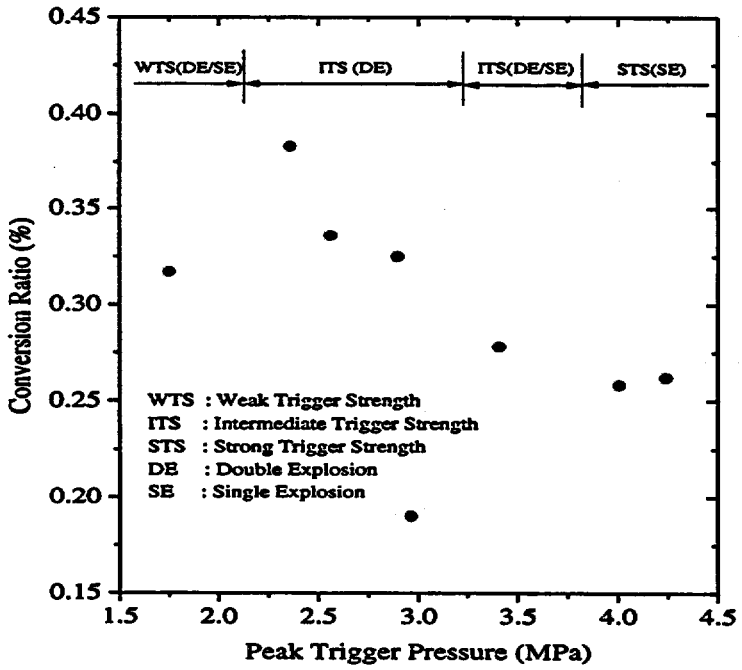

Figure 4.20: Conversion Ratios with respect to the Peak External Trigger Pressures

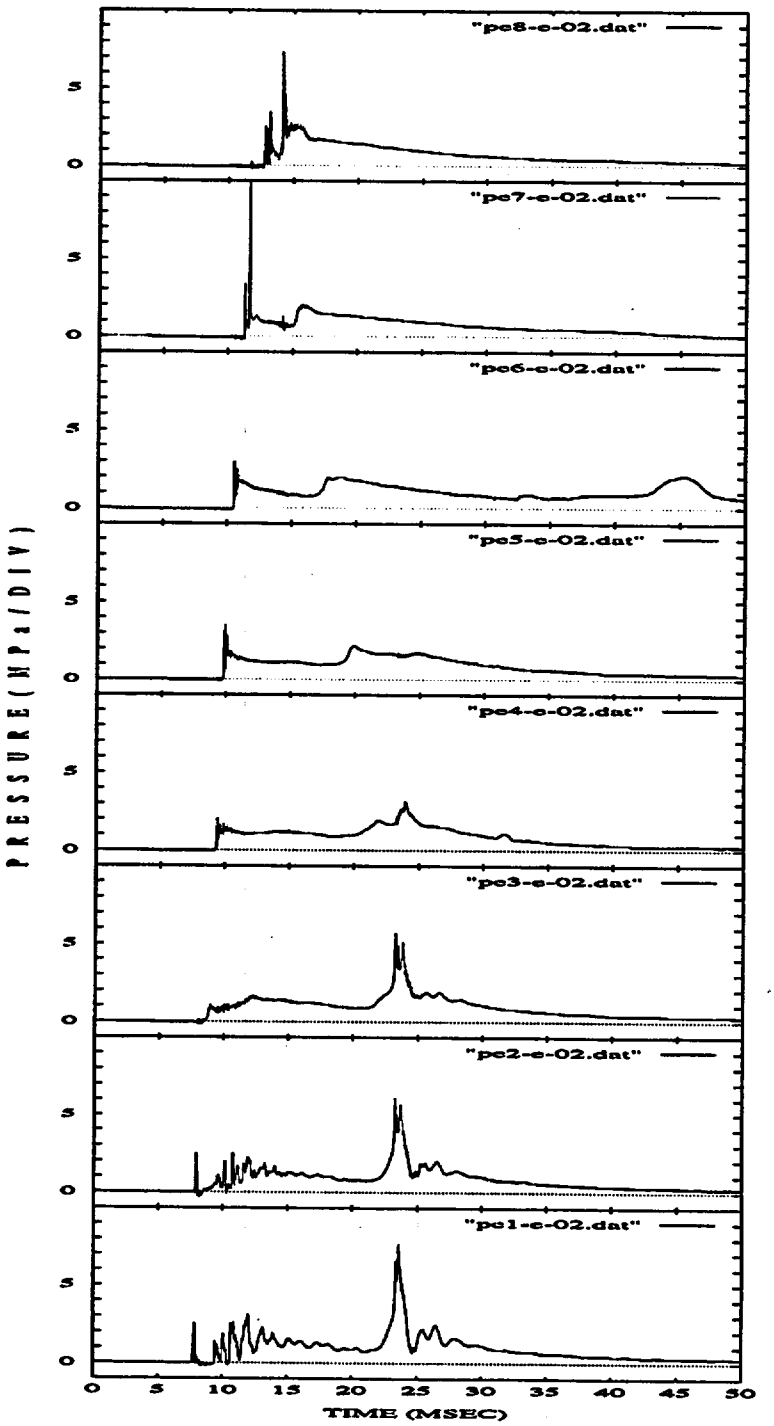

Figure 4.21: Pressure Traces of the WFCI-E-02 Test with the Fuel and Coolant Temperatures of 790 and 86 °C, respectively

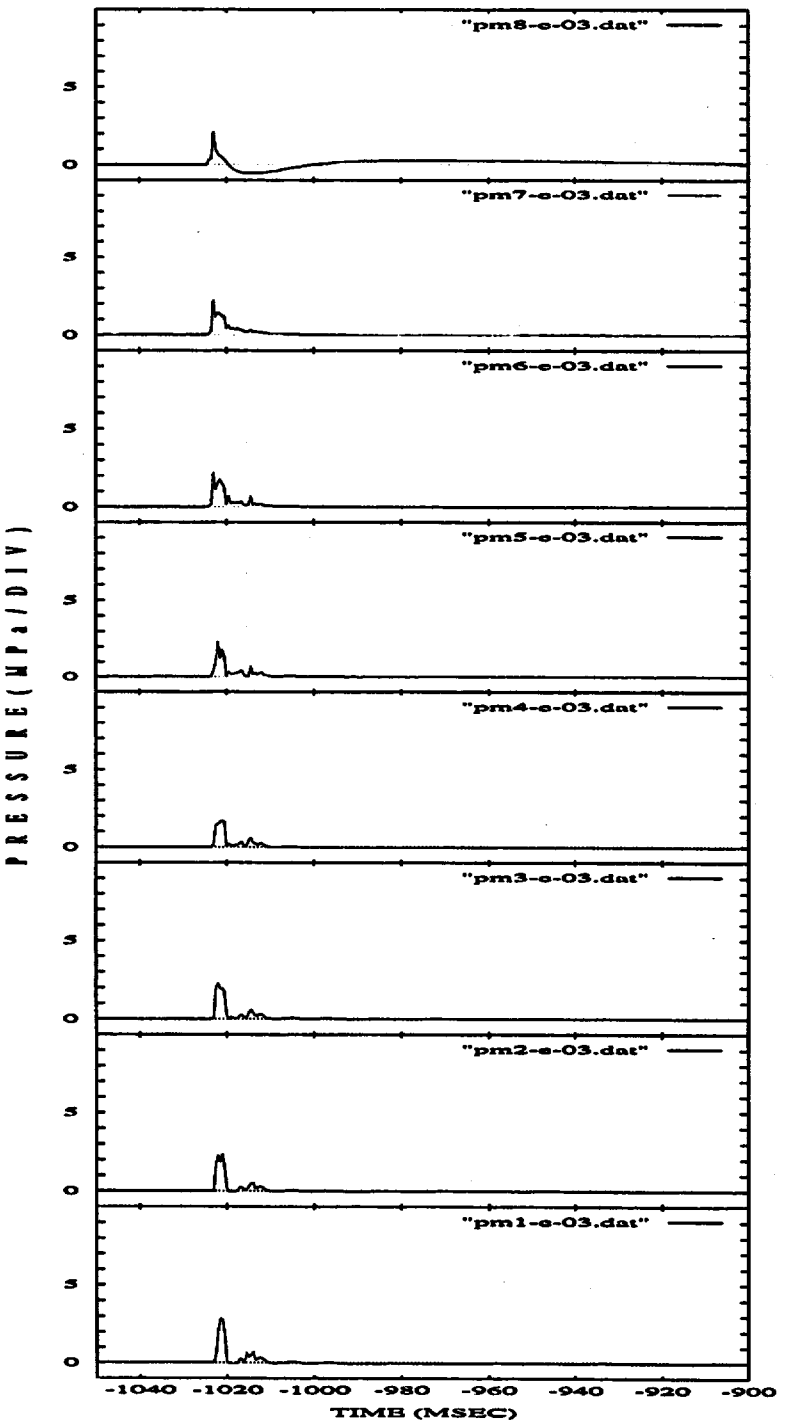

Figure 4.22: Pressure Traces of the WFCI-E-03 Test with the Fuel and Coolant Temperatures of 491 and 93 °C, respectively

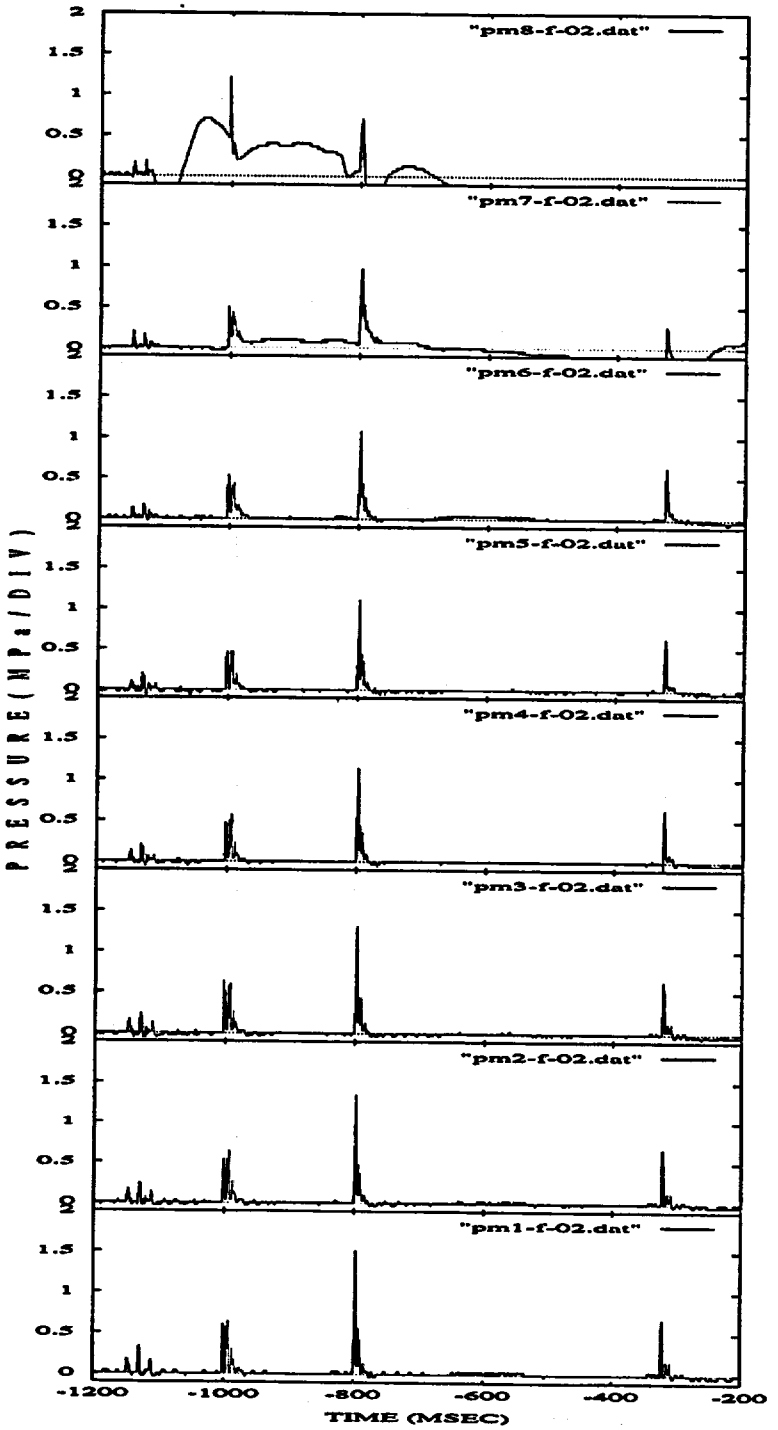

Figure 4.23: Pressure Traces of the WFCI-F-02 Test with the Fuel and Coolant Temperatures of 782 and 27 °C, respectively

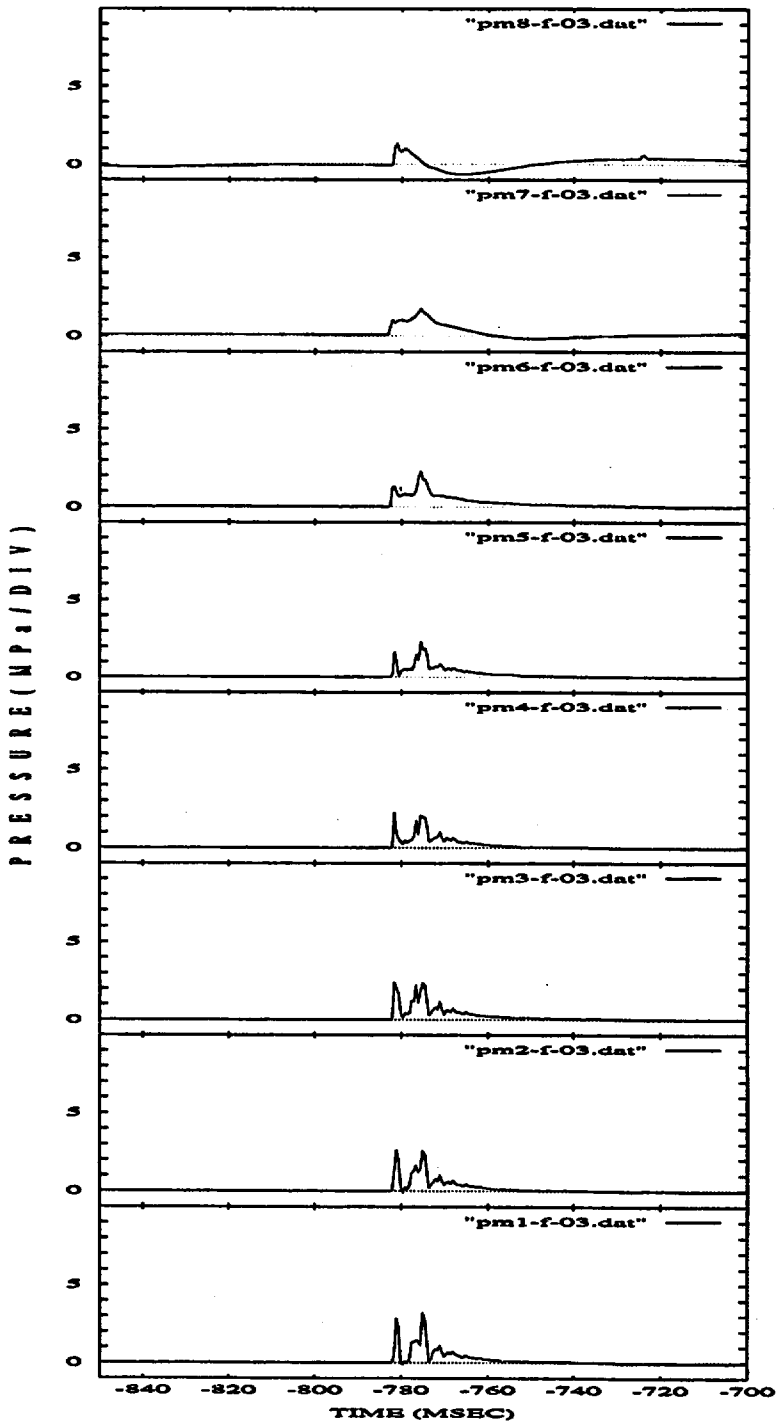

Figure 4.24: Pressure Traces of the WFCI-F-03 Test with the Fuel and Coolant Temperatures of 850 and 62.5 °C, respectively

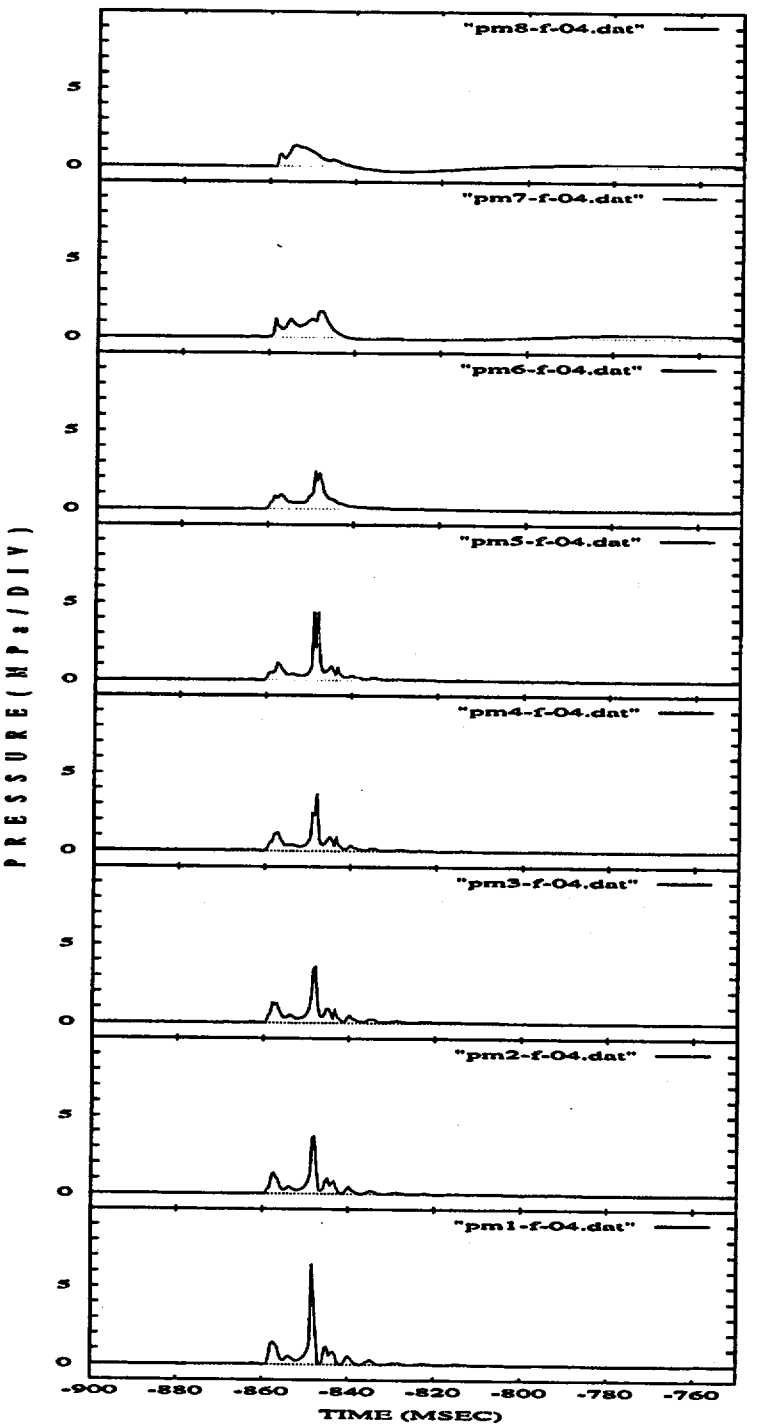

Figure 4.25: Pressure Traces of the WFCI-F-04 Test with the Fuel and Coolant Temperatures of 871 and 72 °C, respectively

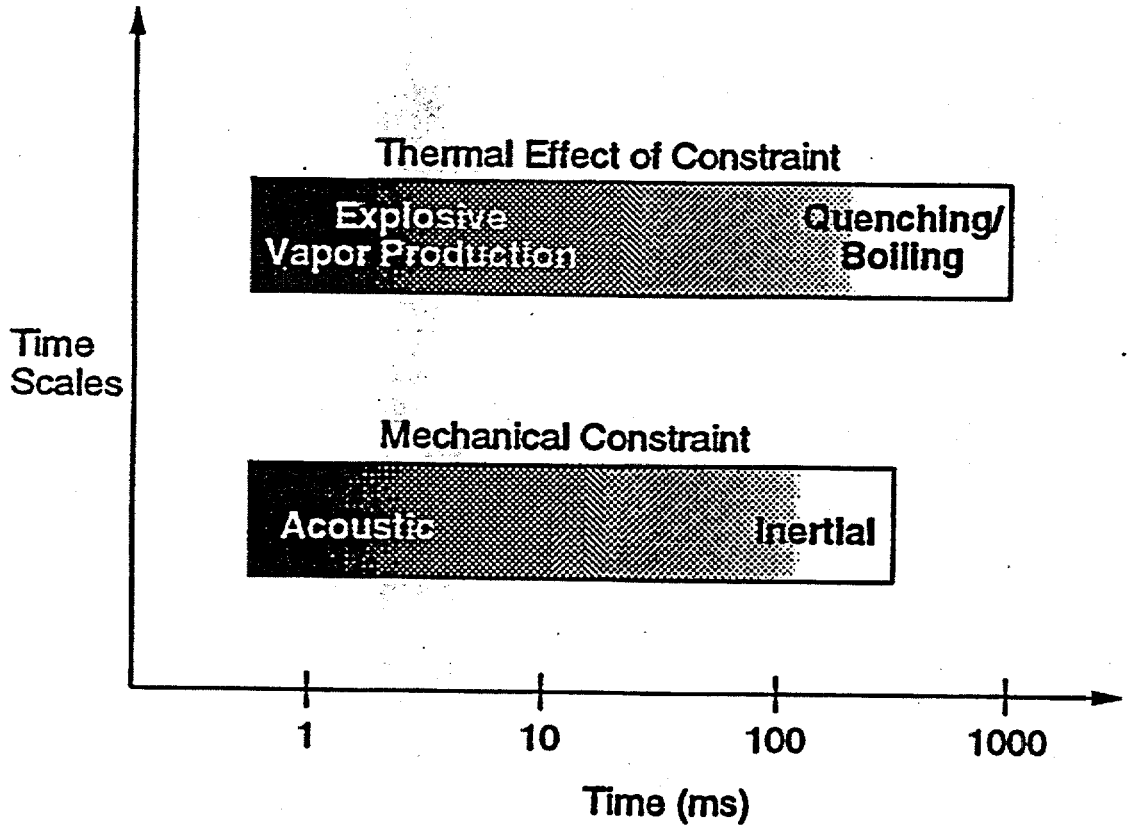

Figure 4.26: Time Scales with respect to the System Constraint

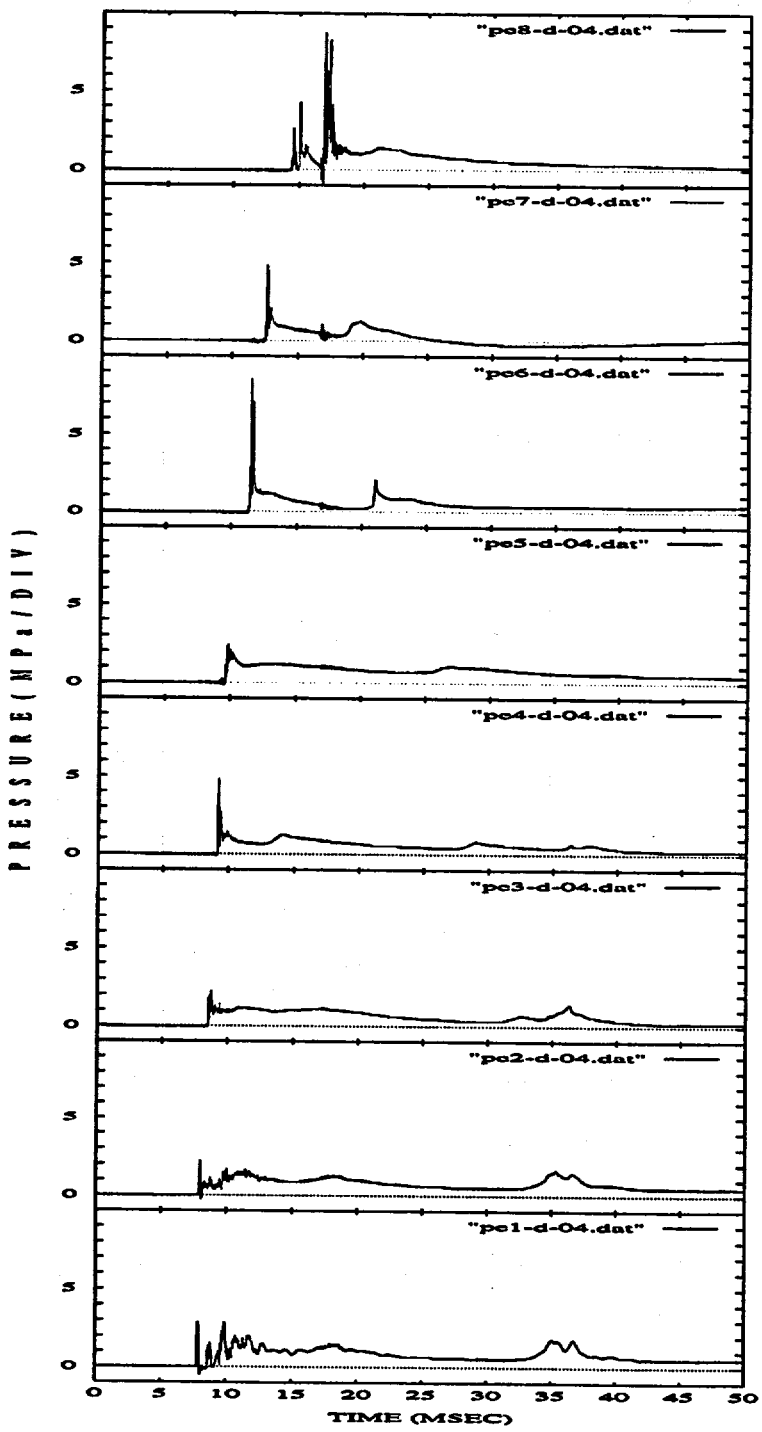

Figure 4.27: Pressure Traces of the WFCI-D-04 Test with a Total Constraint Mass of 56.8 kg, $< m >$=6.38

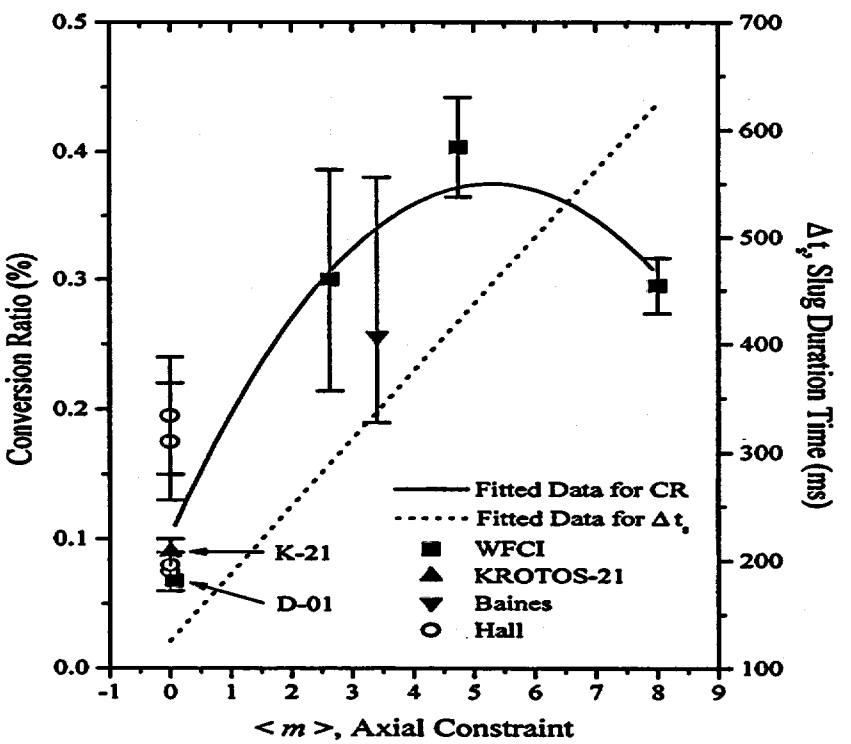

Figure 4.28: Conversion Ratios and Δt_{slug} with respect to Axial Constraint

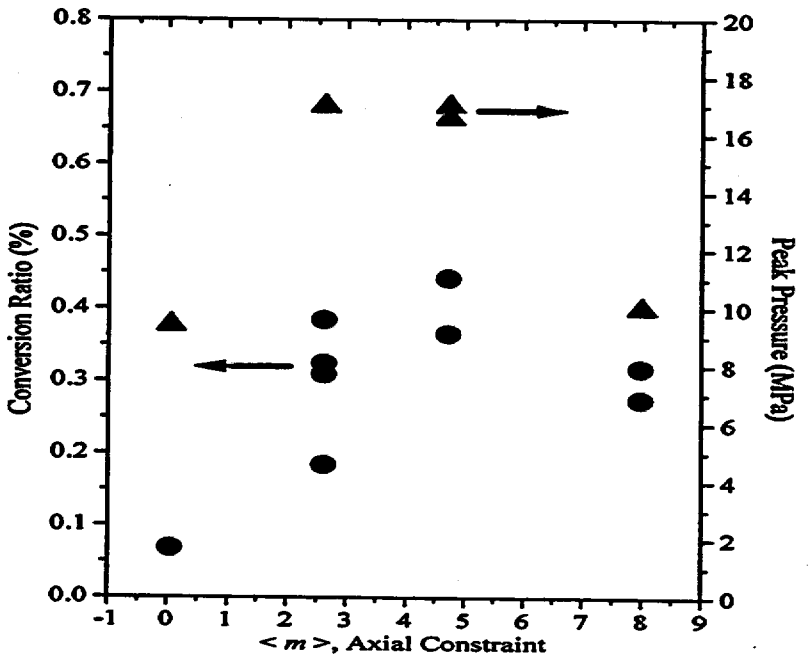

Figure 4.29: Conversion Ratios and Peak Pressures with respect to Axial Constraint

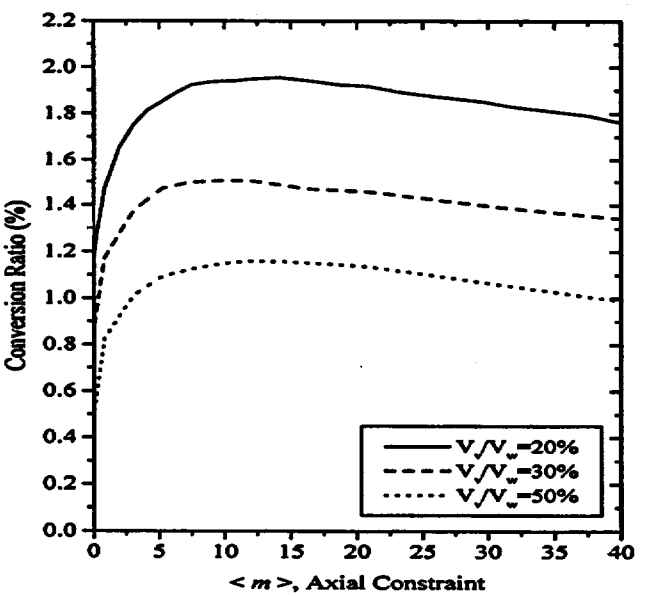

Figure 4.30: Conversion Ratios with respect to the System Constraint calculated by the Parametric Model (UWFCI Code)

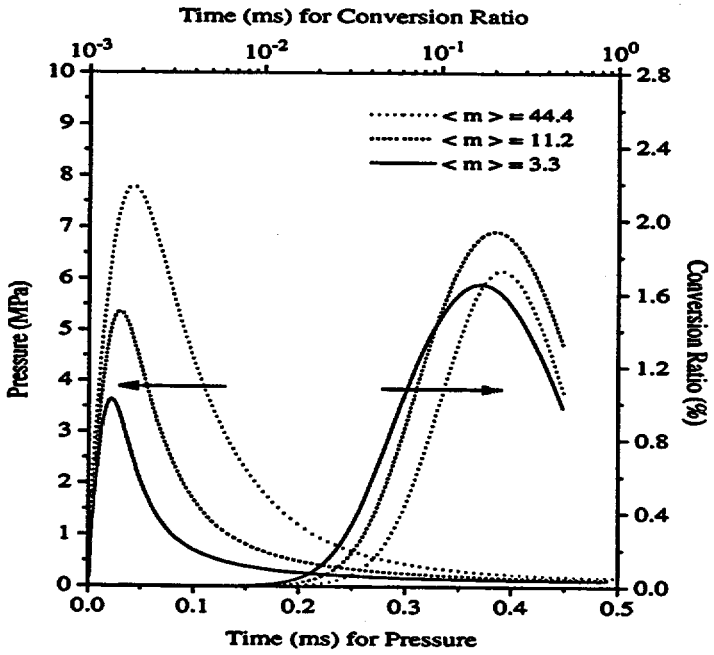

Figure 4.31: Conversion Ratios and Pressure Histories calculated by the Parametric Model (UWFCI Code) with respect to $< m >$ of 3.3, 11.2 and 44.4

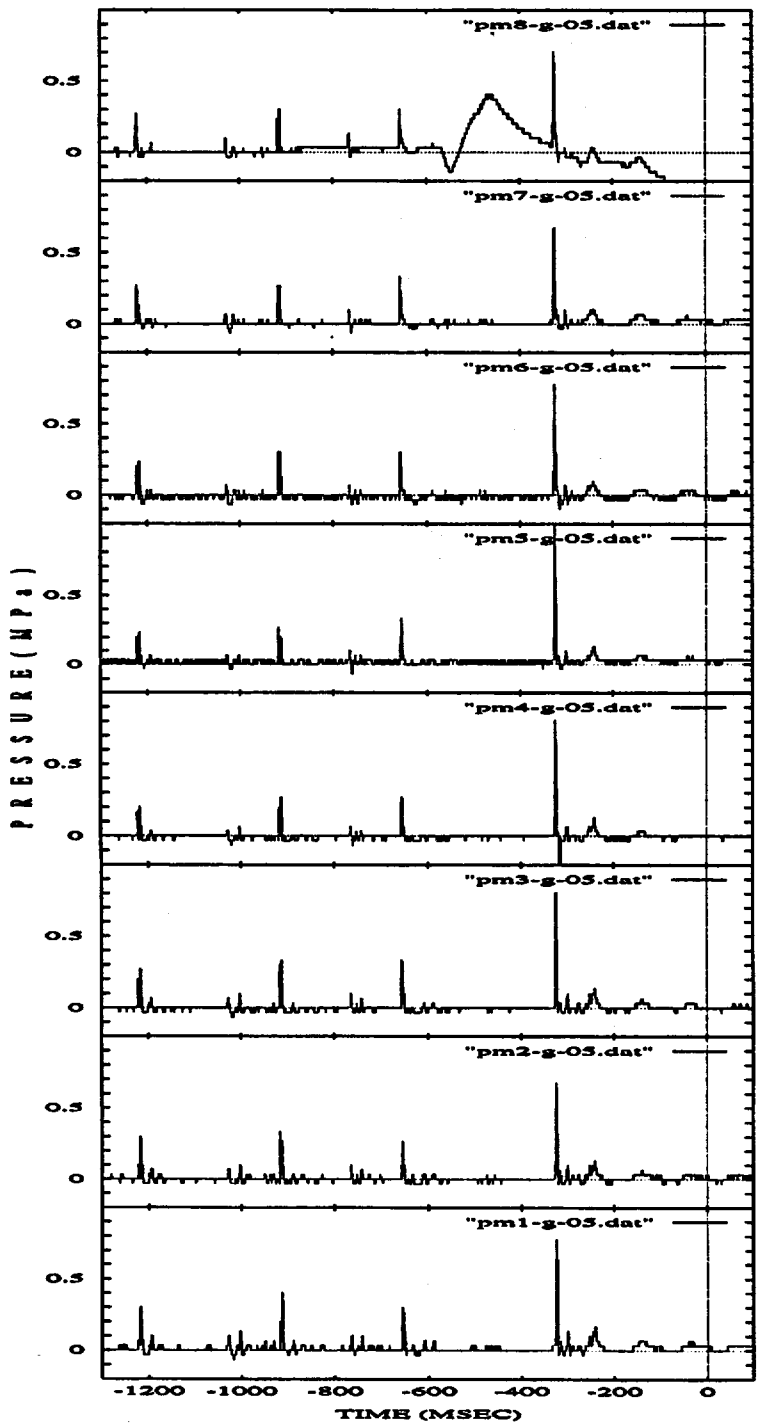

Figure 4.32: Typical Pressure Traces in Pure Water (WFCI-G-05)

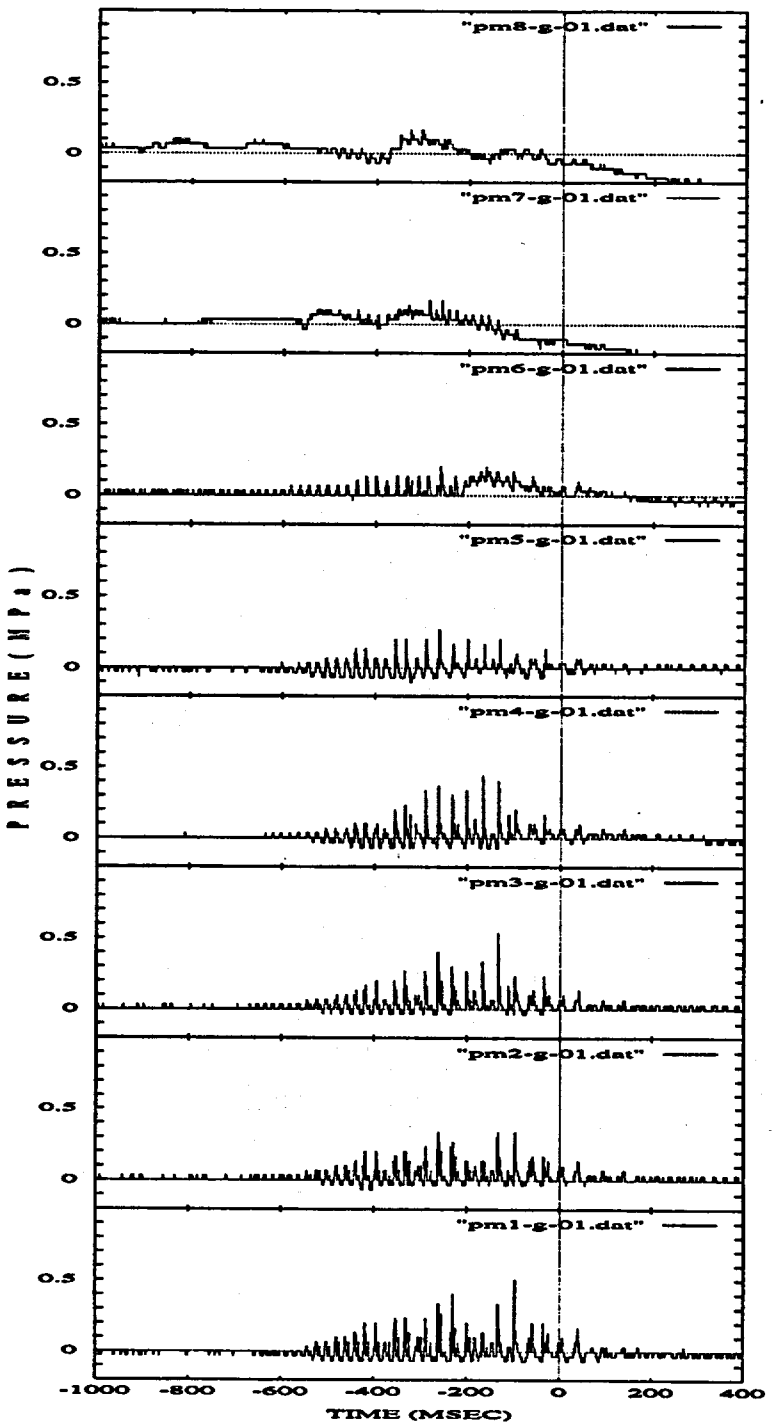

Figure 4.33: Typical Pressure Traces in Polymer Solution (WFCI-G-01)

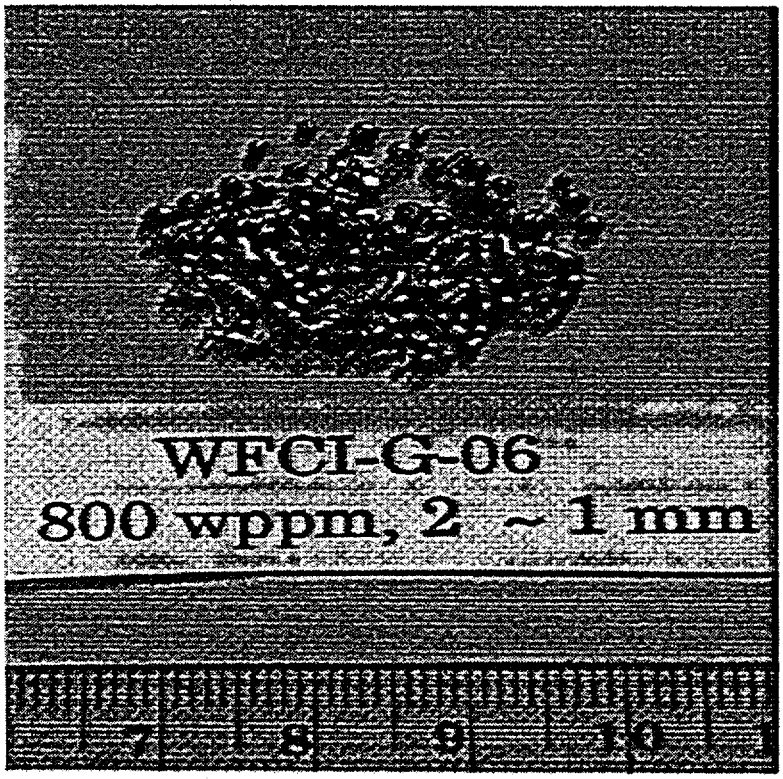

Figure 4.34: Debris Shape of the WFCI-G-06 Test in Size between 1 to 2 mm

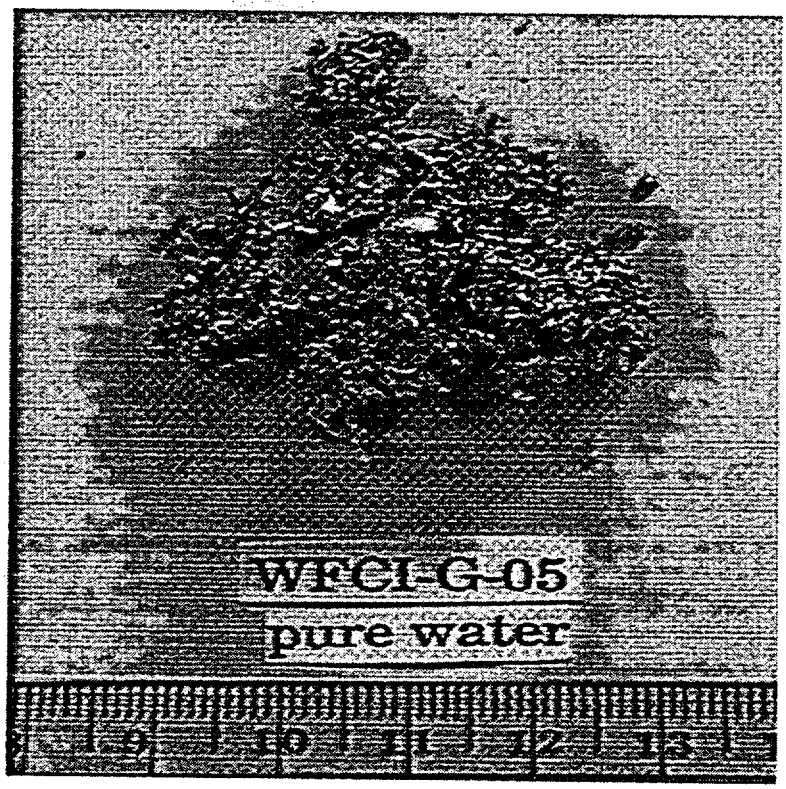

Figure 4.35: Debris Shape of the Pure Water Test (WFCI-G-05)

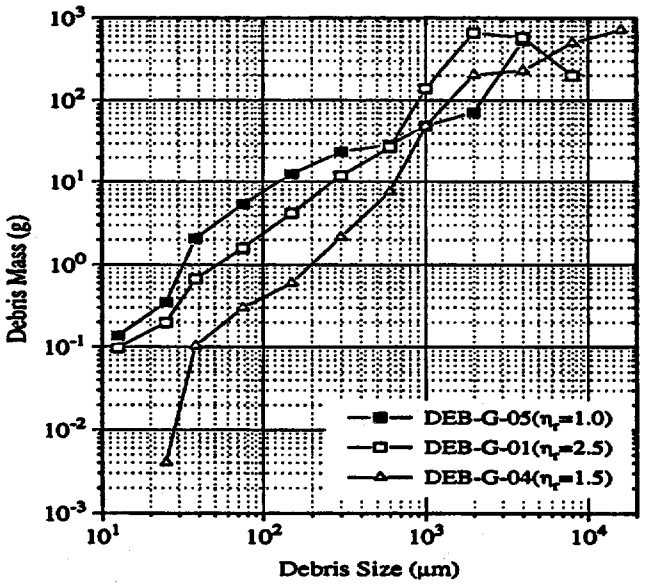

Figure 4.36: Distribution of the Debris Mass by Comparison with the Tests of Pure Water (WFCI-G-05) and Polymer Solutions (WFCI-G-01 and G-04)

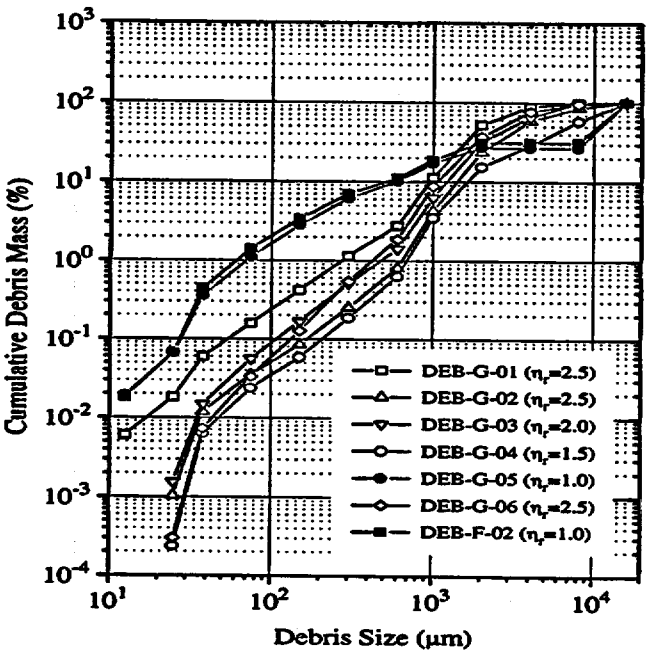

Figure 4.37: Distribution of the Cumulative Debris Mass Fraction

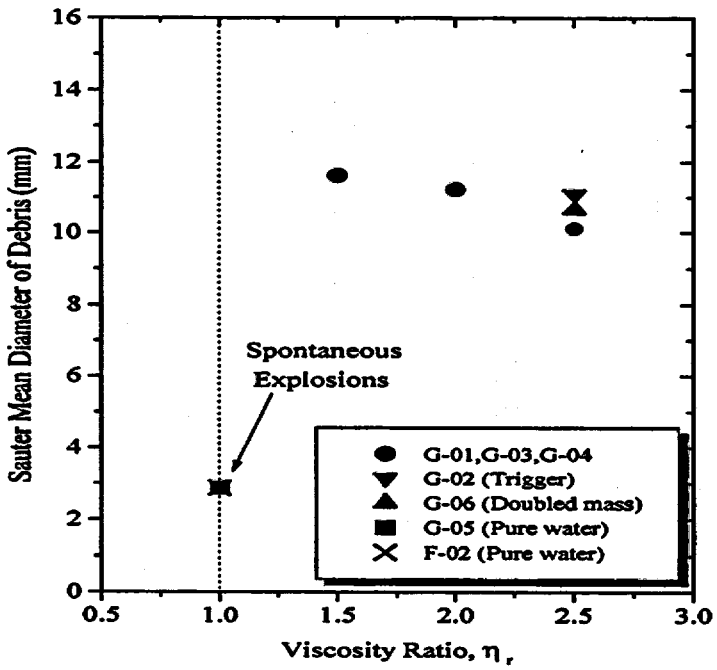

Figure 4.38: Sauter Mean Diameters of Collected Debries in the WFCI-G and F Series Tests

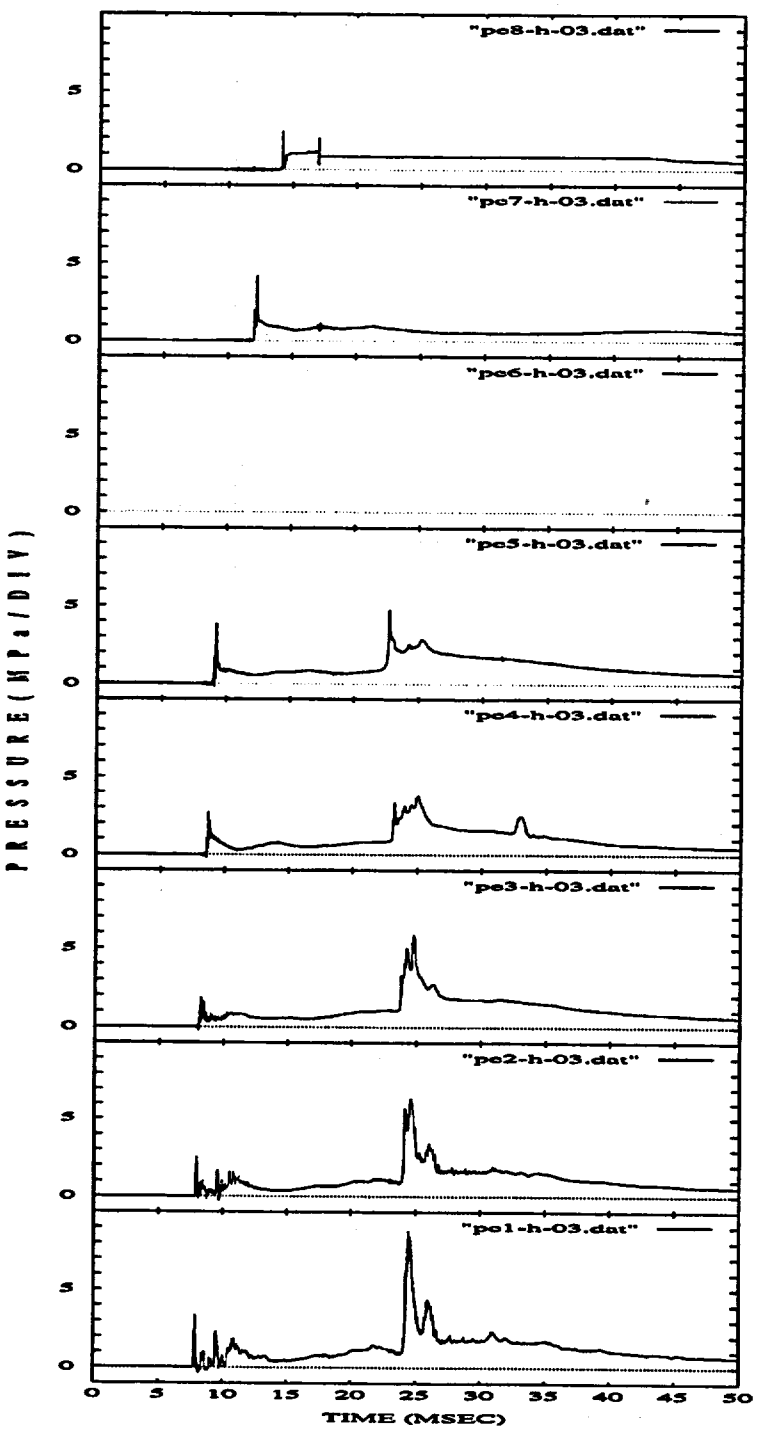

Figure 4.39: Pressure Traces of the WFCI-H-03 Test

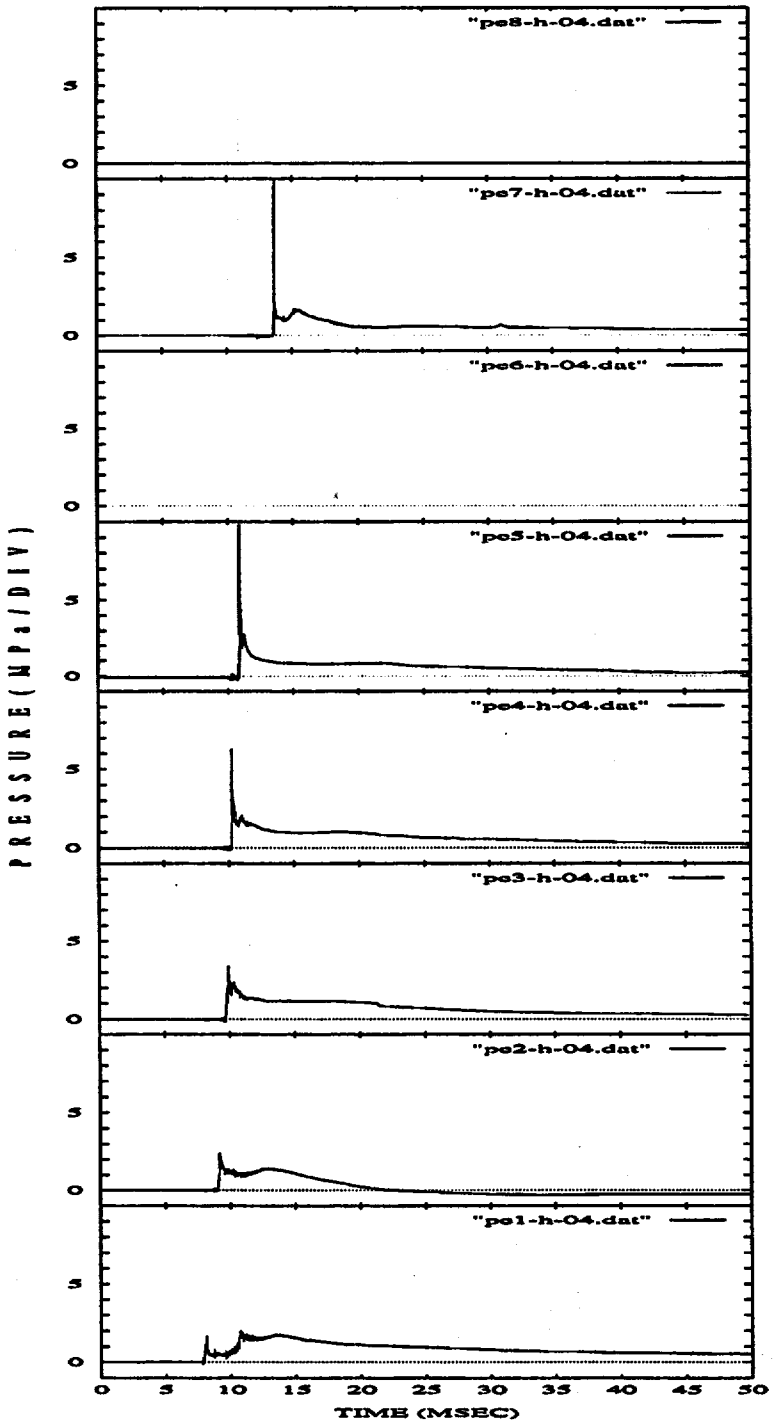

Figure 4.40: Pressure Traces of the WFCI-H-04 Test

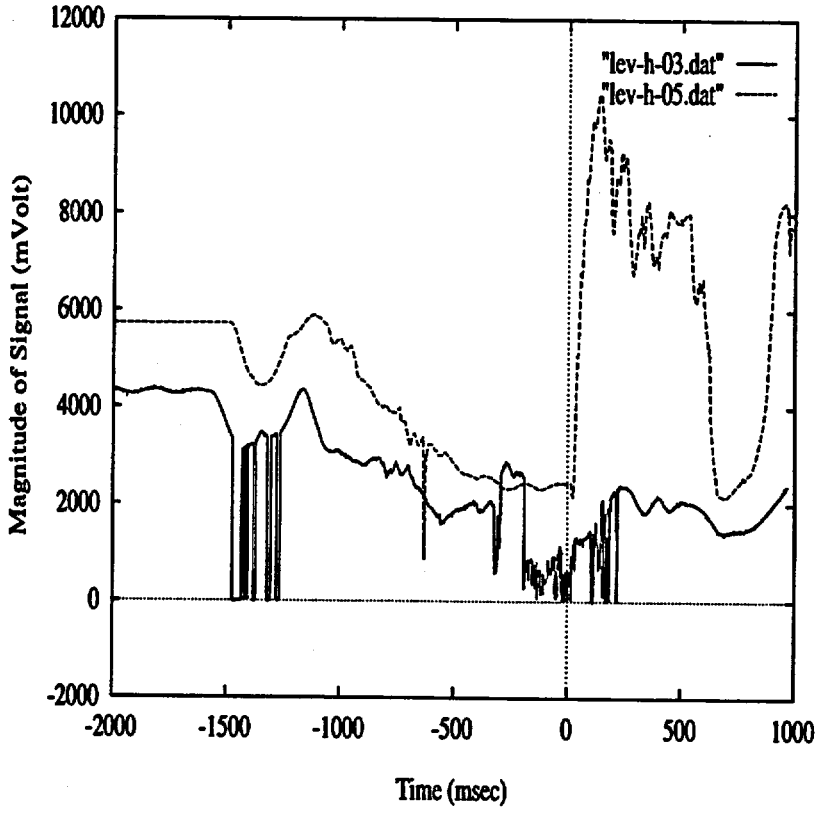

Figure 4.41: Level Swells of the WFCI-H-03 and H-05 Tests

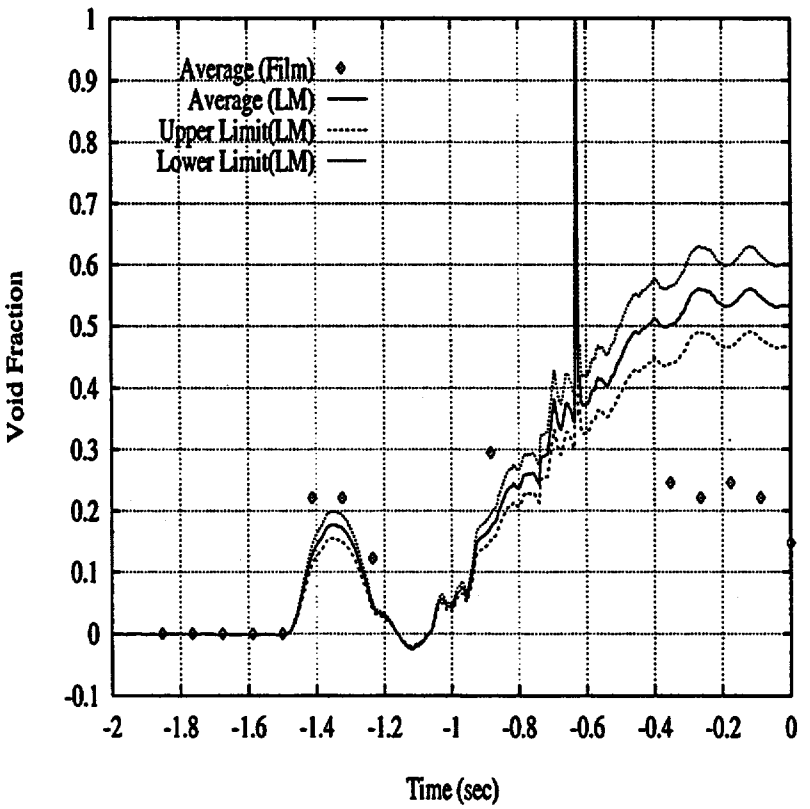

Figure 4.42: Void Fractions of the WFCI-H-05 Test Comparing with the Visual Observation

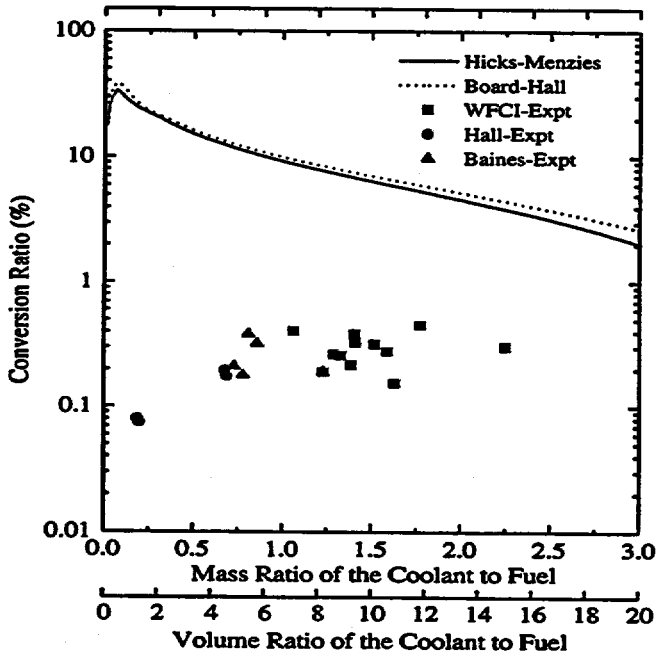

Figure 4.43: Conversion Ratios with respect to the Coolant to Fuel Mass Ratio Compared to Thermodynamic Models

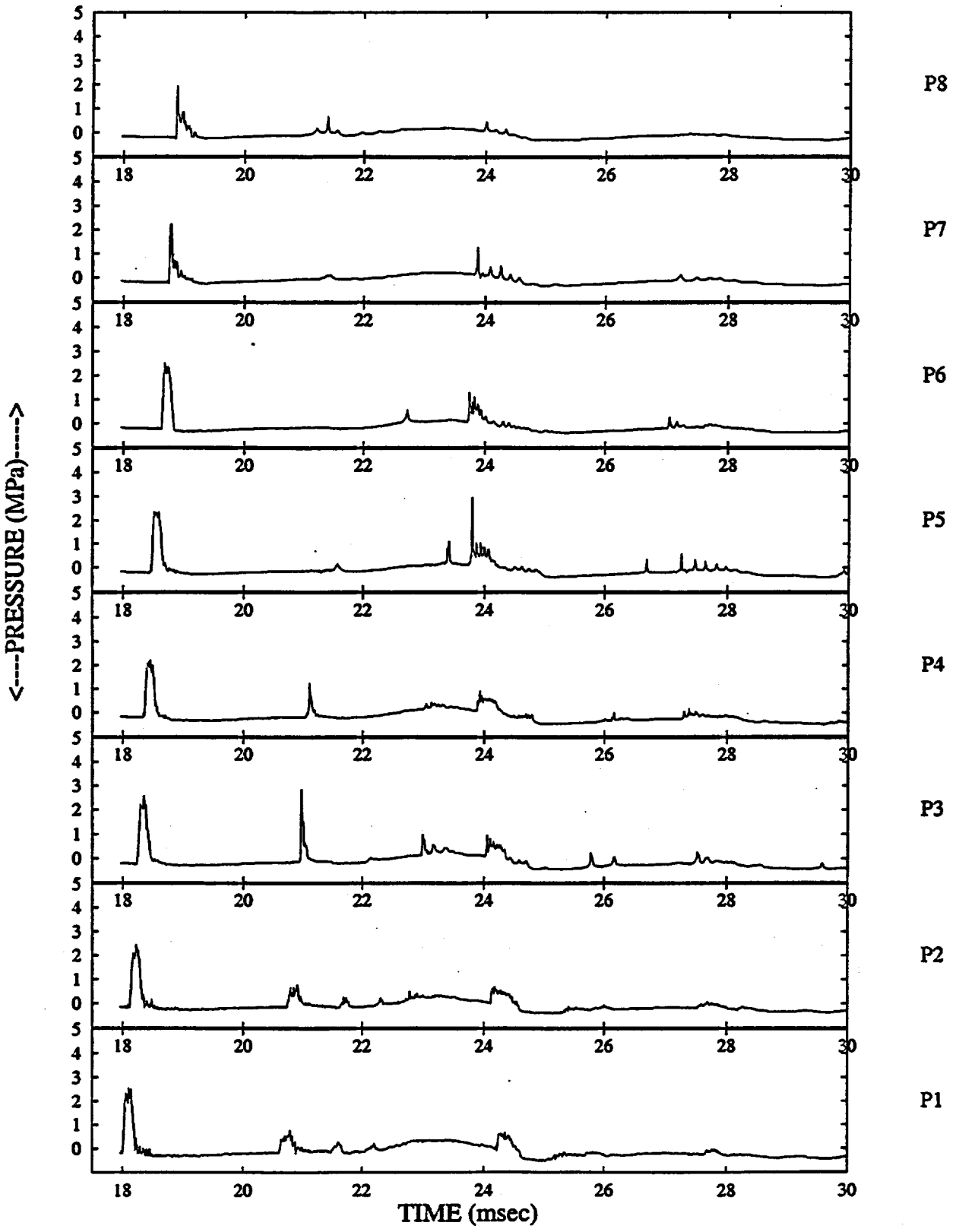

Figure 44: Trigger pressure histories for WFCI-1 apparatus charged to 200 V

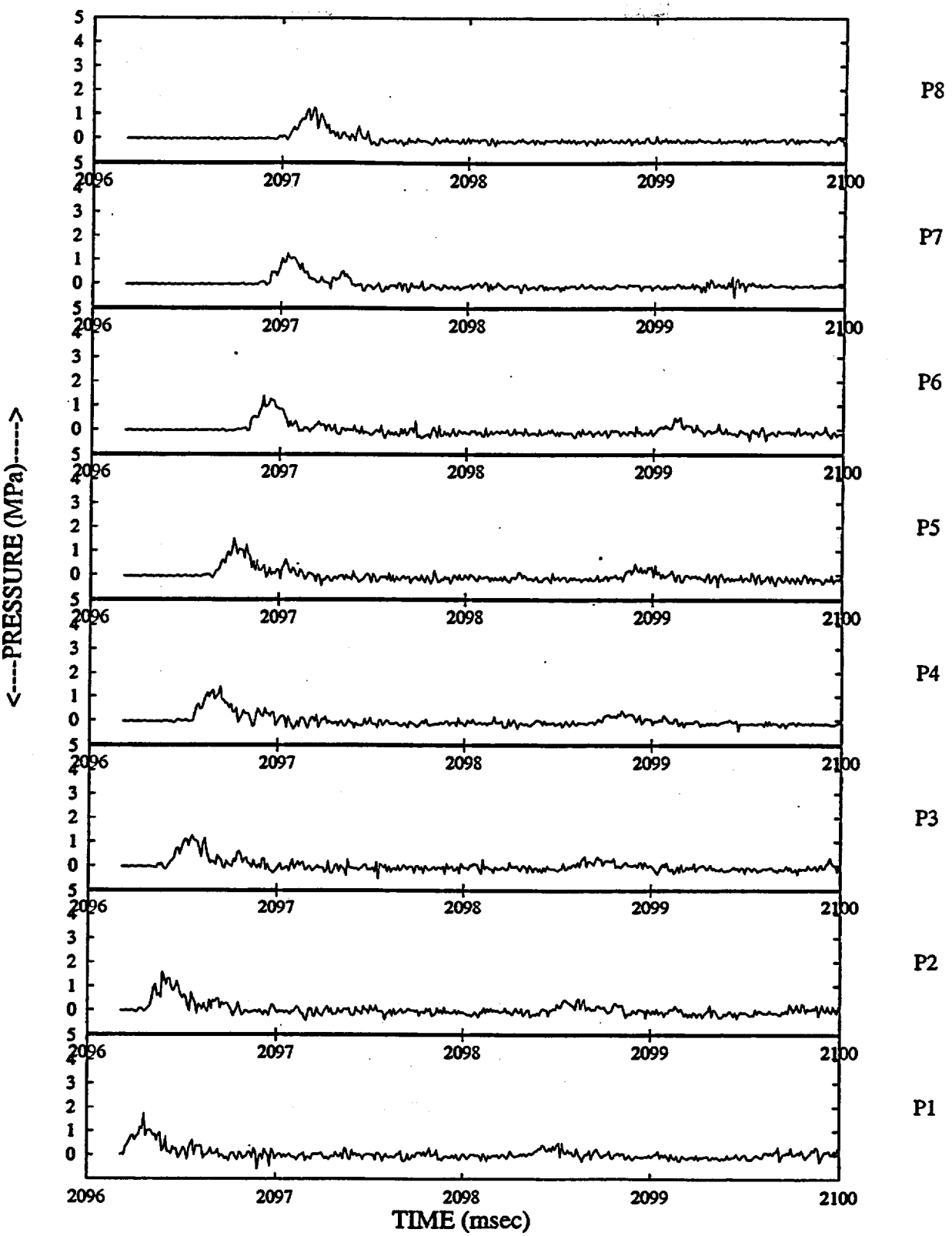

Figure 45: Trigger pressure histories for WFCI-1 apparatus charged to 400 V

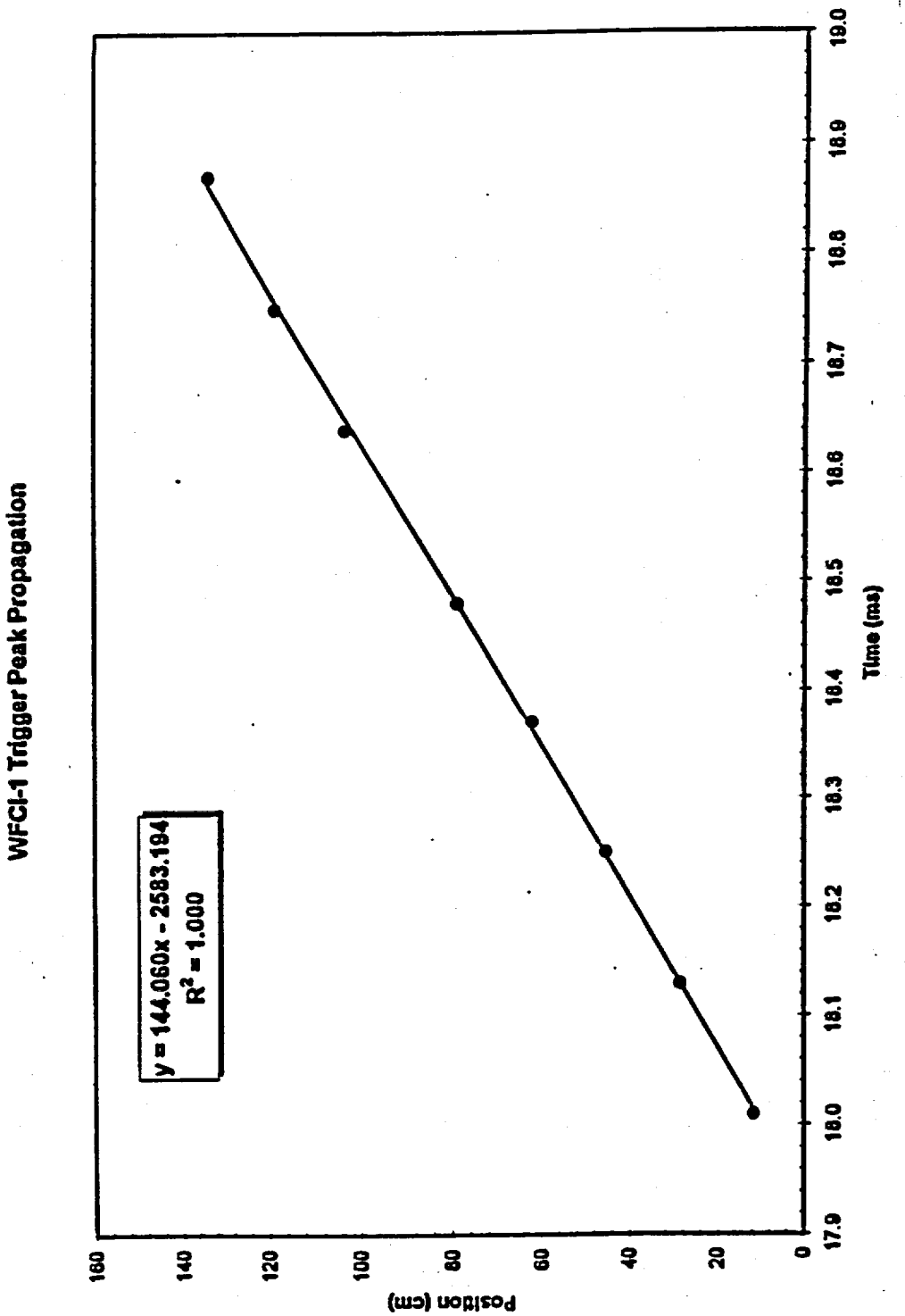

Figure 4.46: WFCI-1 trigger peak propagation curve

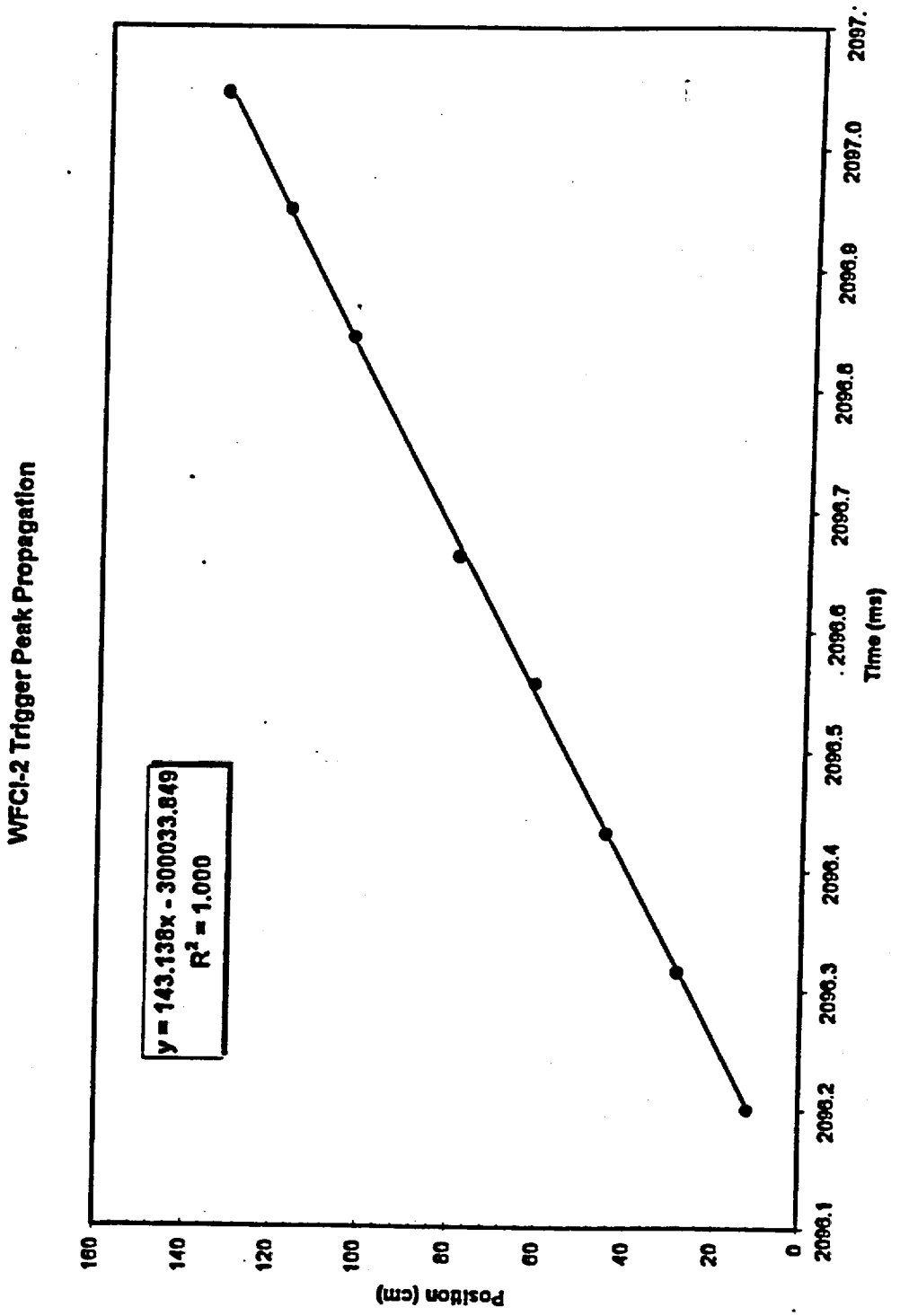

Figure 4.47: WFCI-2 trigger peak propagation curve

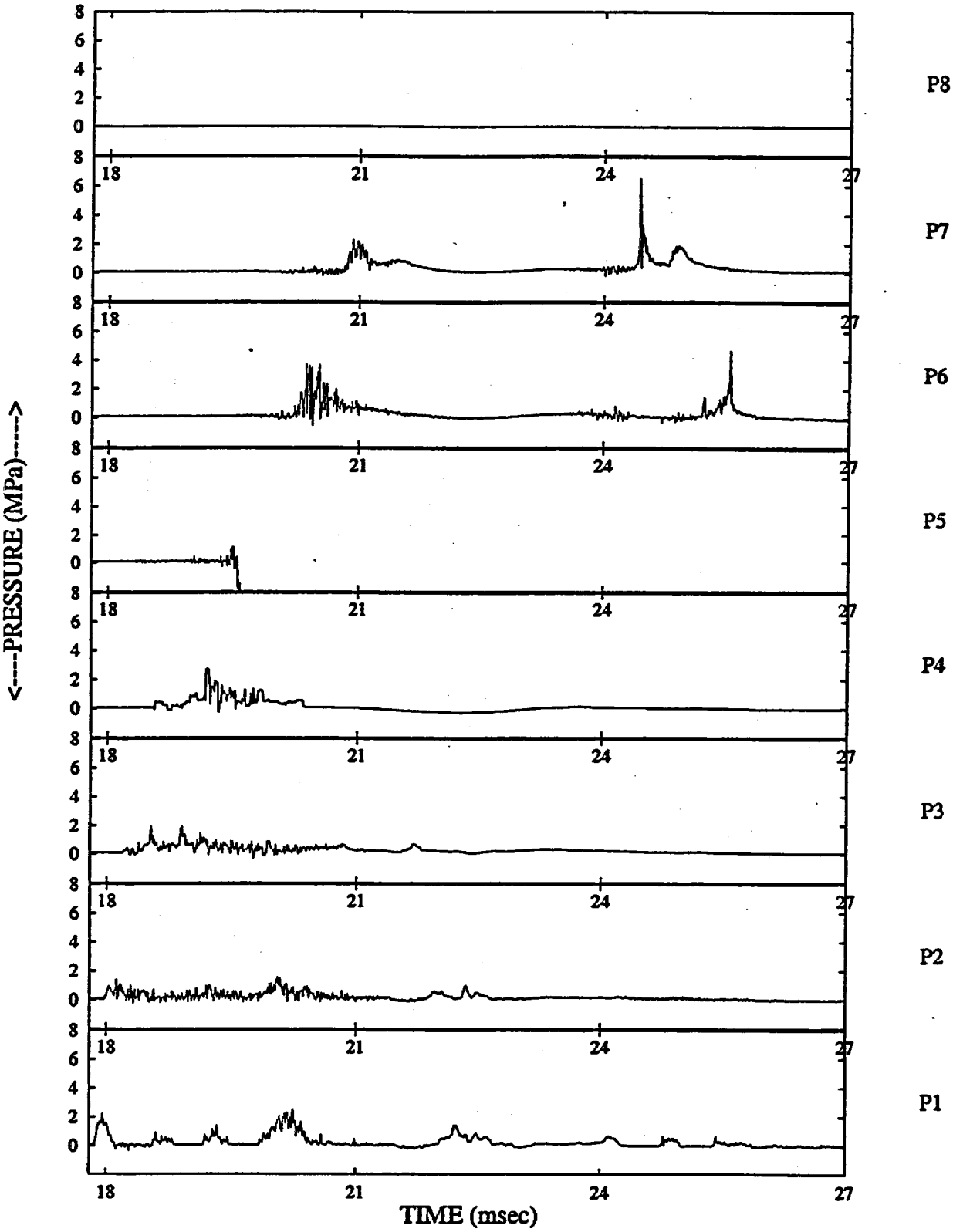

Figure 48: WFCI-K-01 transient pressure histories

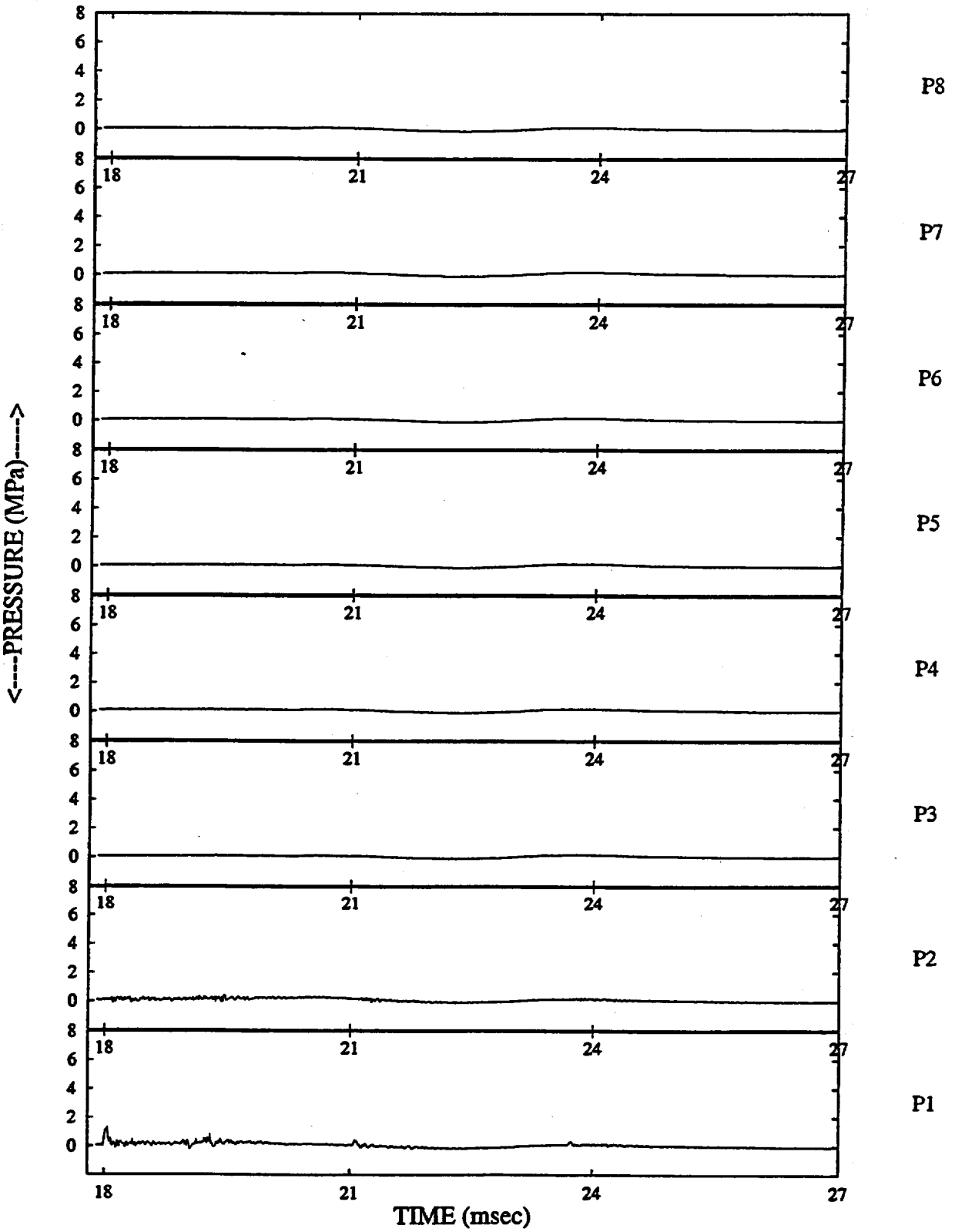

Figure 49: WFCI-K-02 transient pressure histories

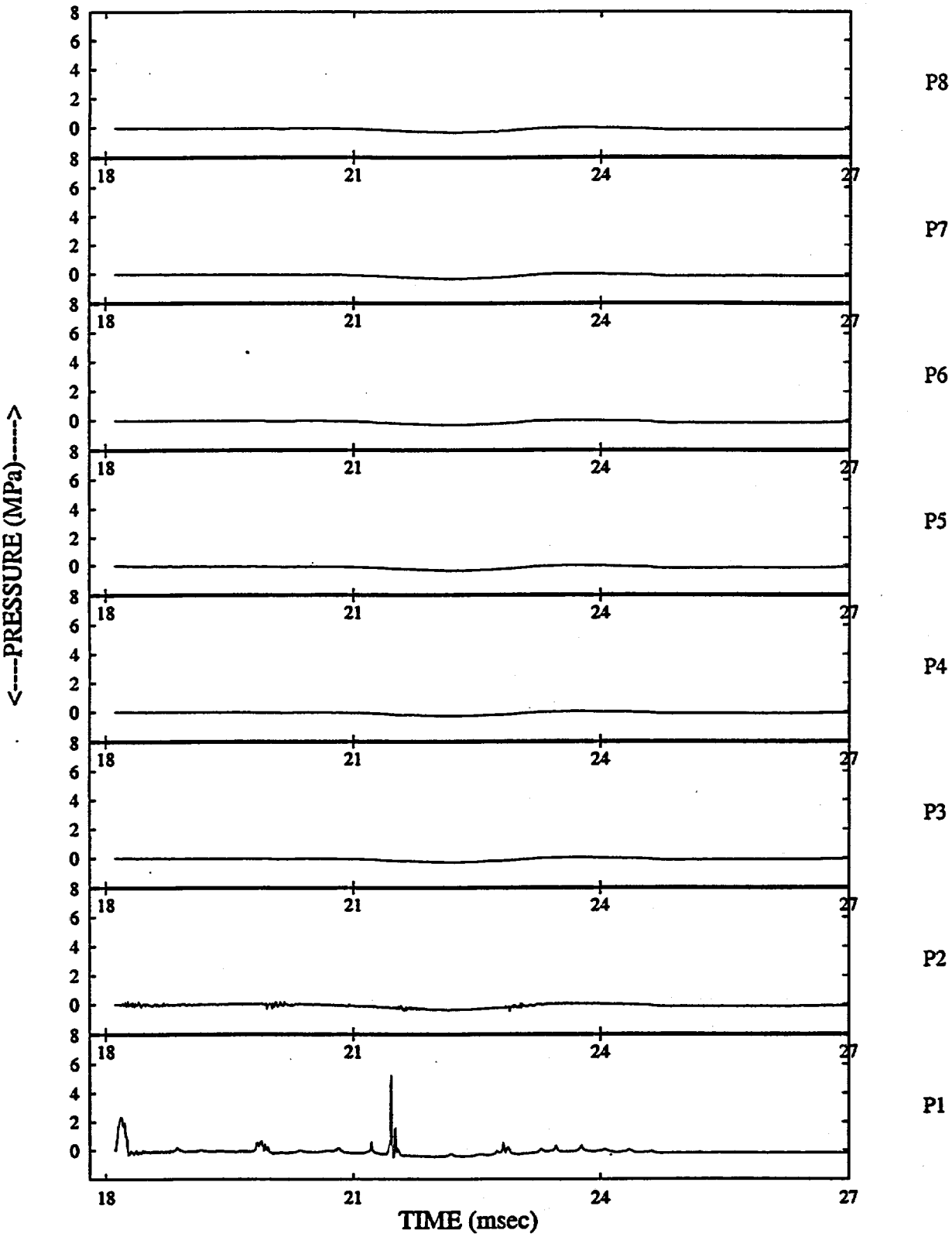

Figure 50: WFCI-K-03 transient pressure histories

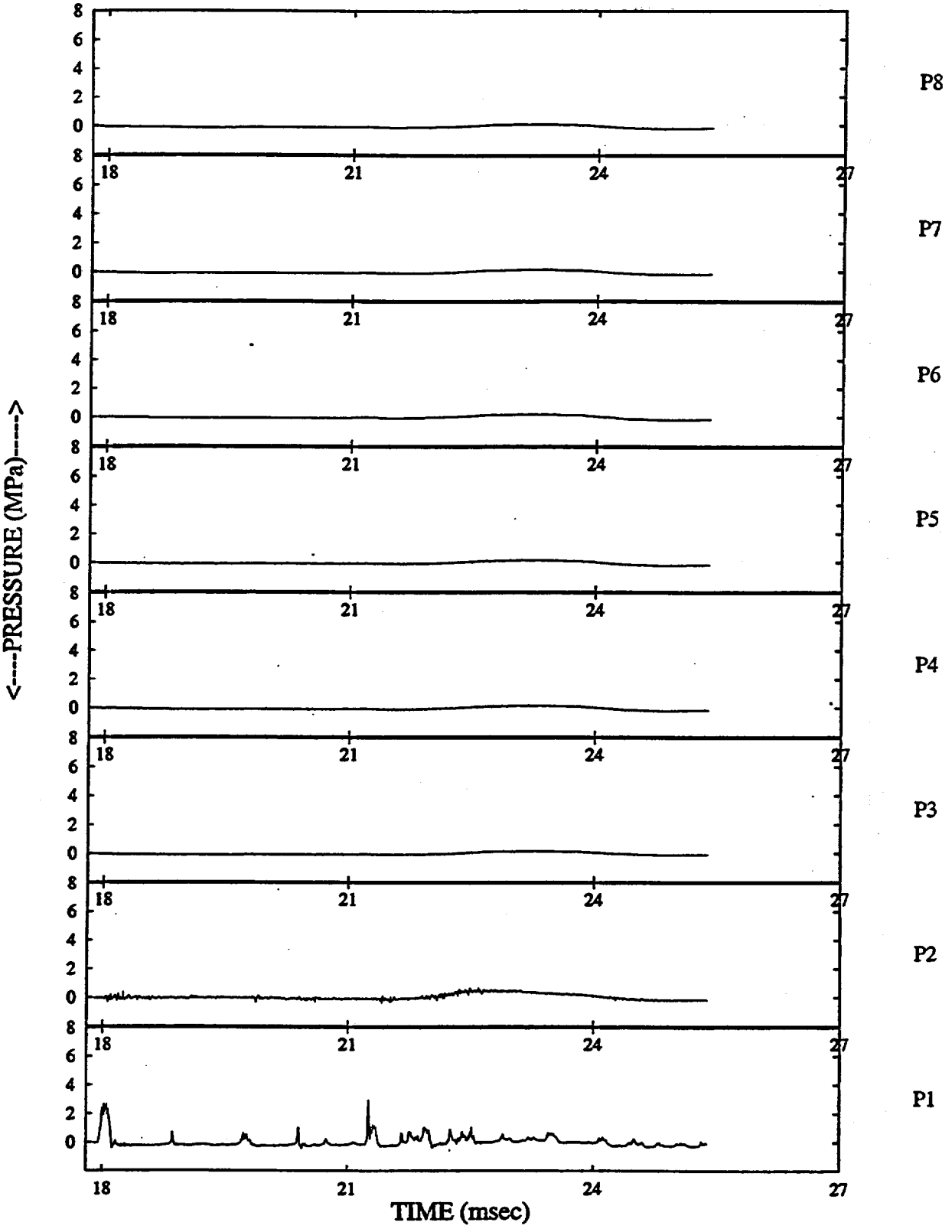

Figure 51: WFCI-K-04 transient pressure histories

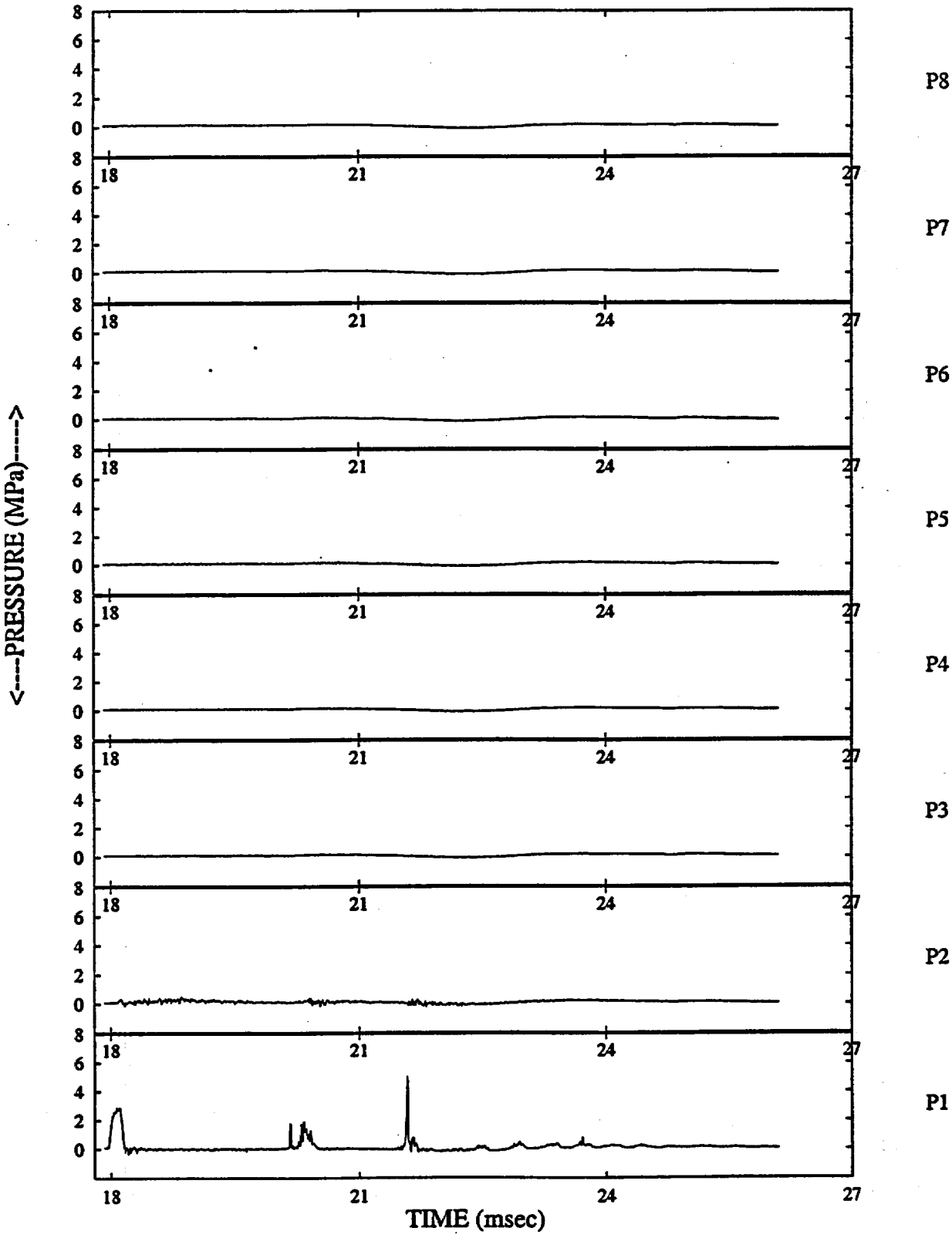

Figure 52: WFCI-K-05 transient pressure histories

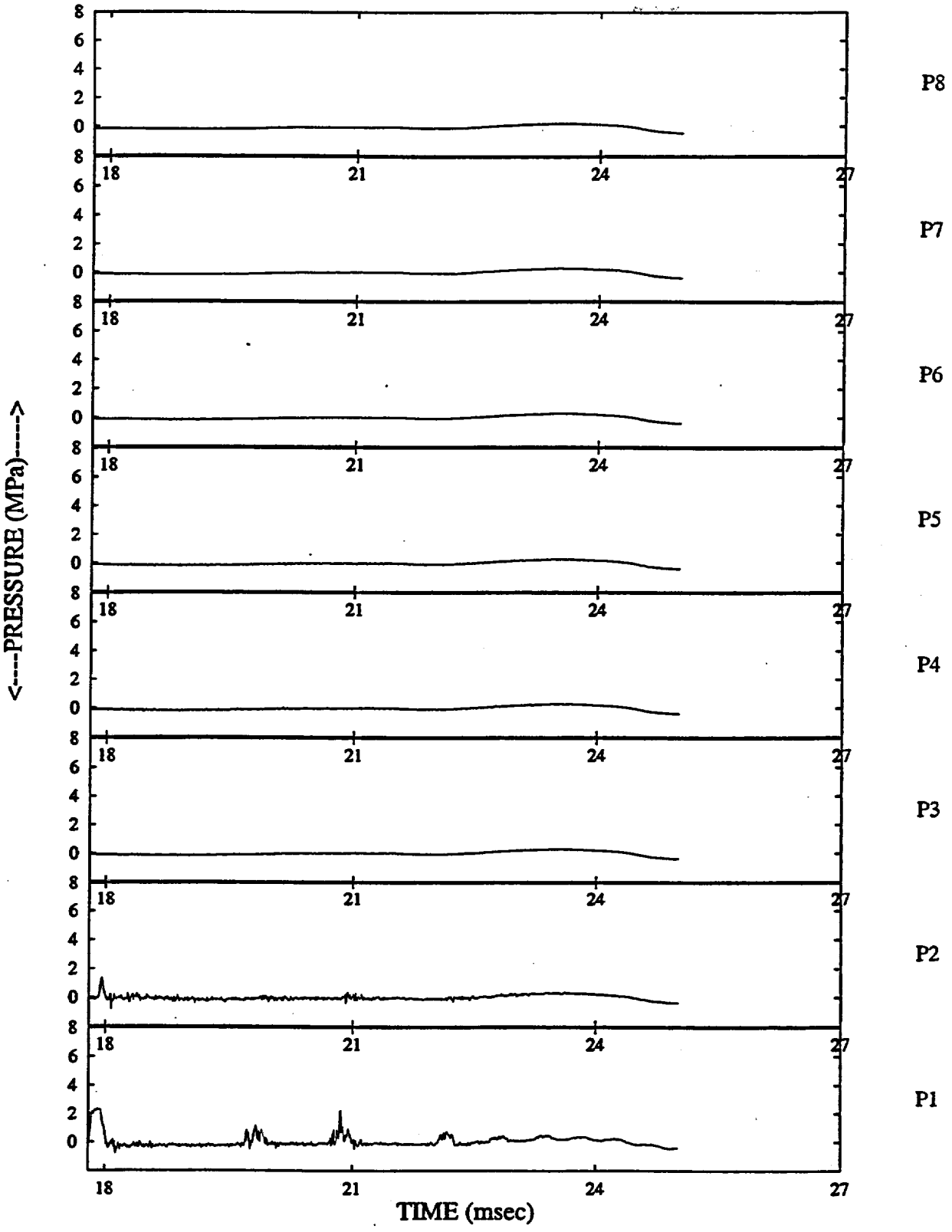

Figure 4.53: WFCI-K-07 transient pressure histories

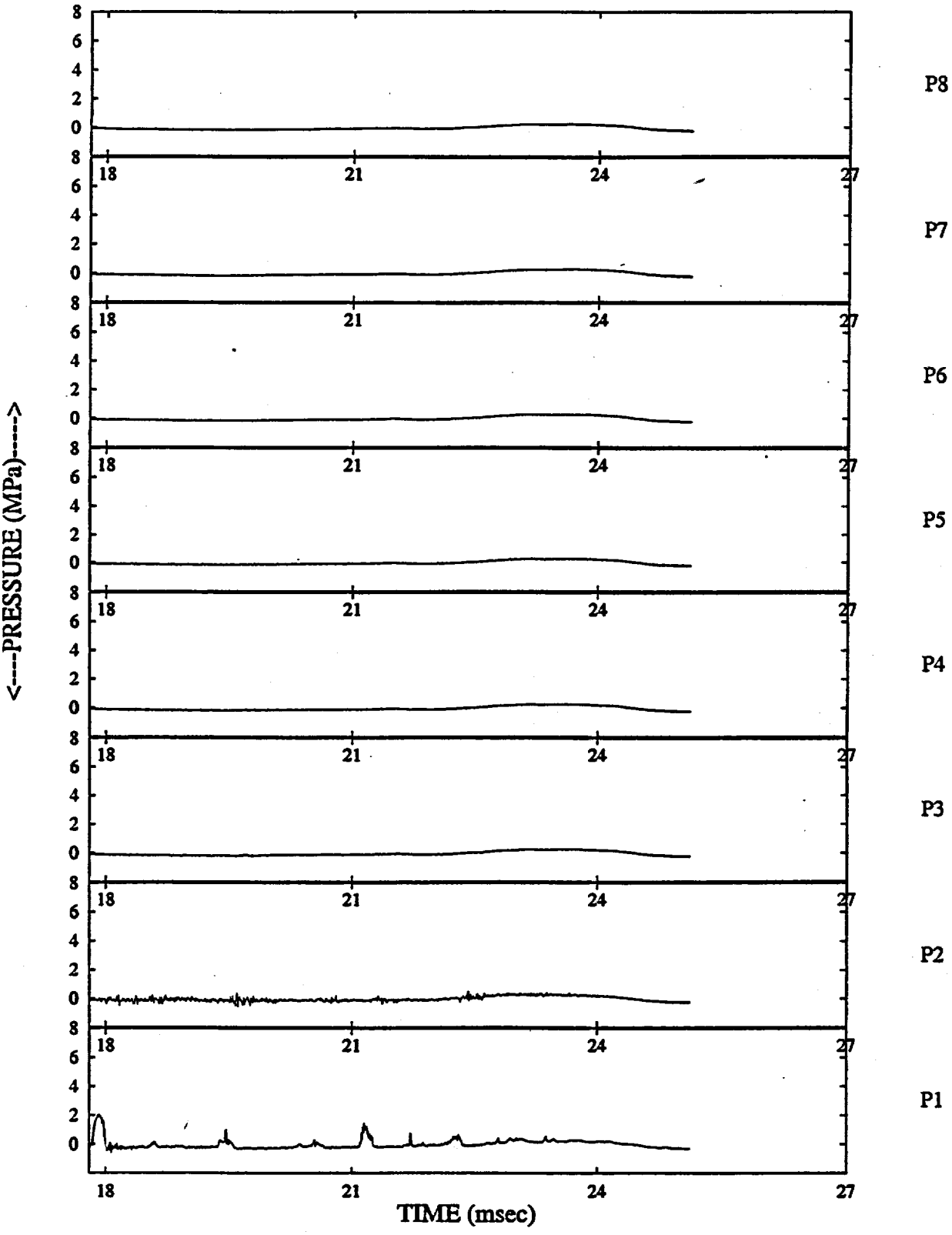

Figure 4.54: WFCI-K-08 transient pressure histories

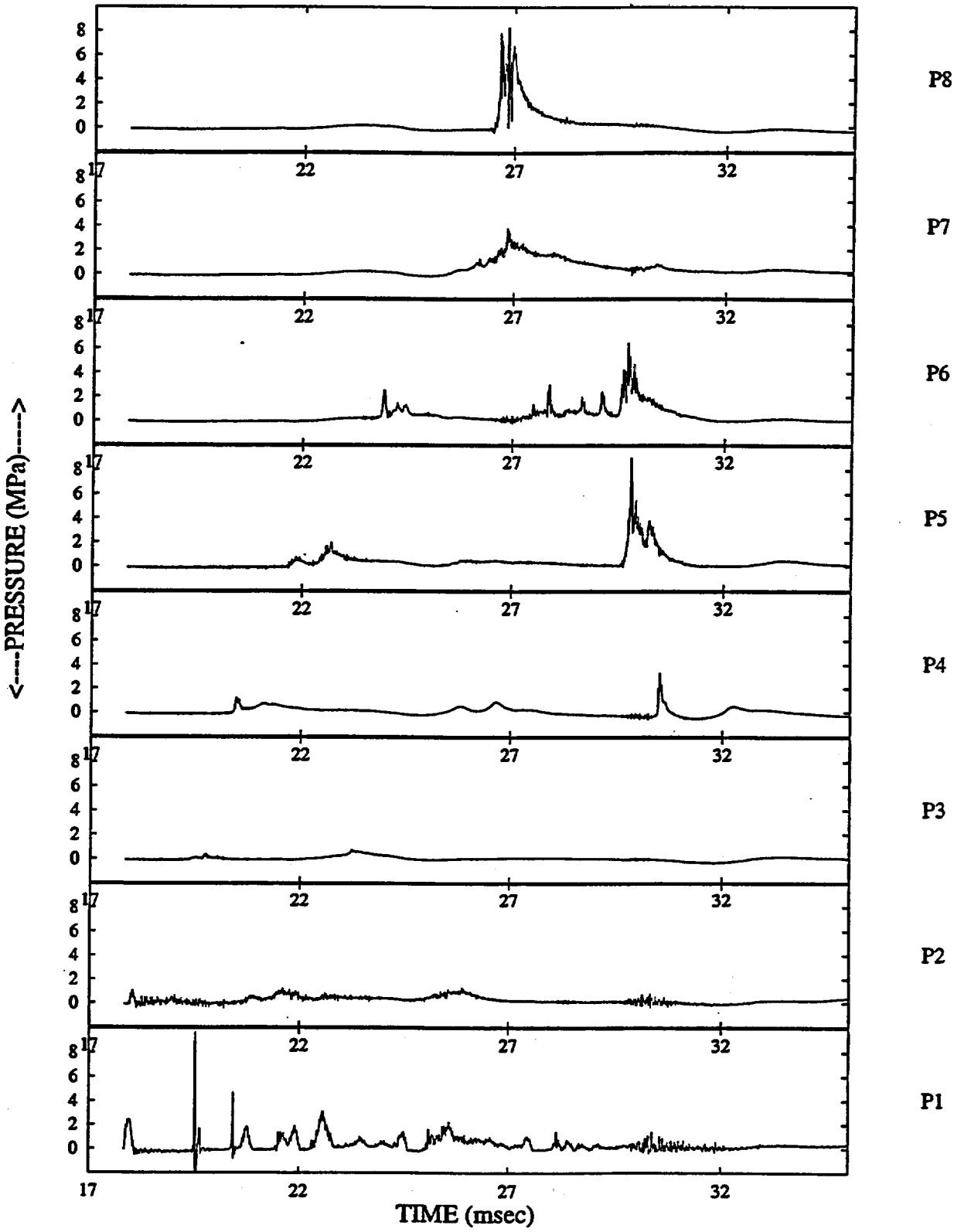

Figure 4.55: WFCI-K-09 transient pressure histories

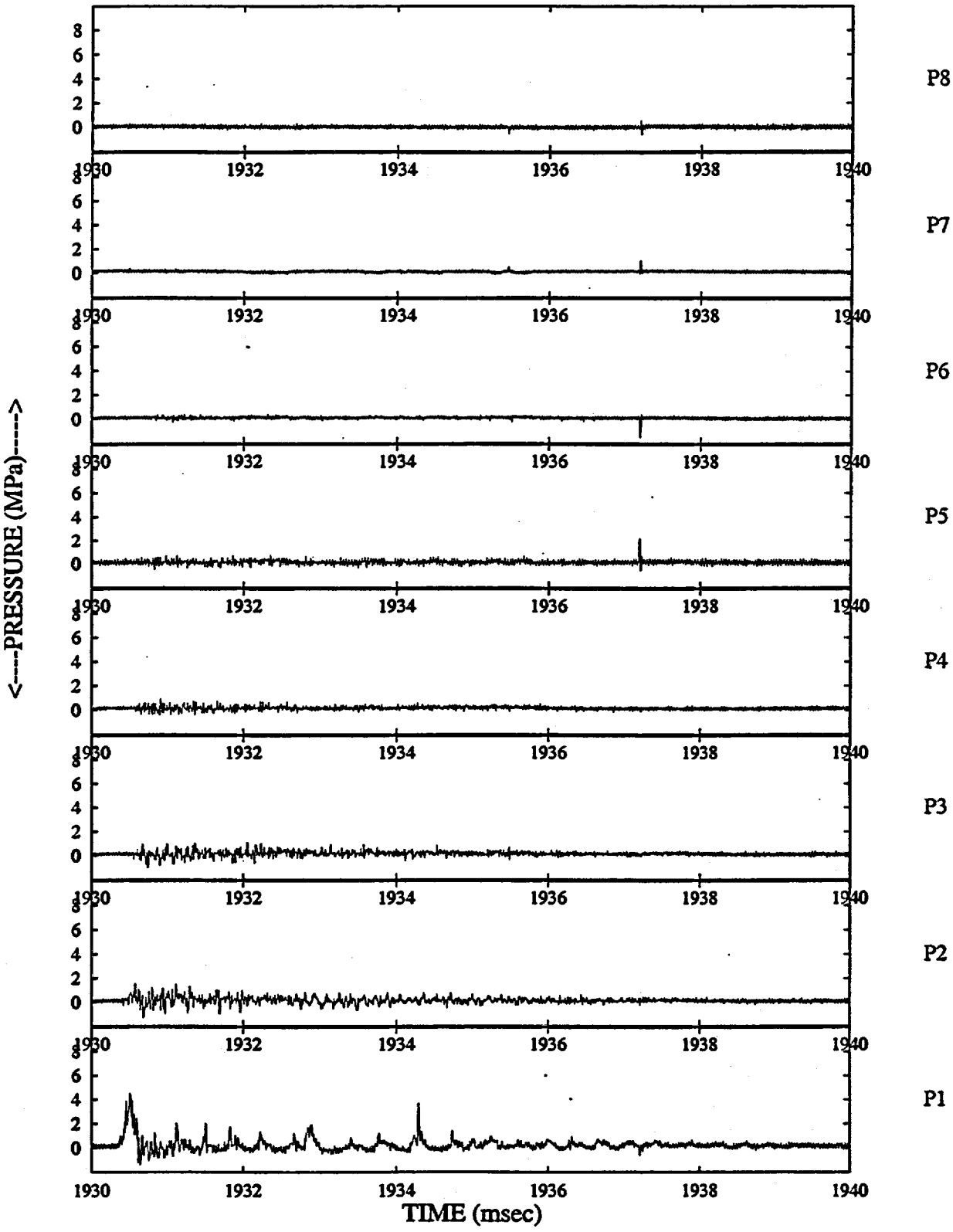

Figure 4.56: WFCI-K-10 transient pressure histories

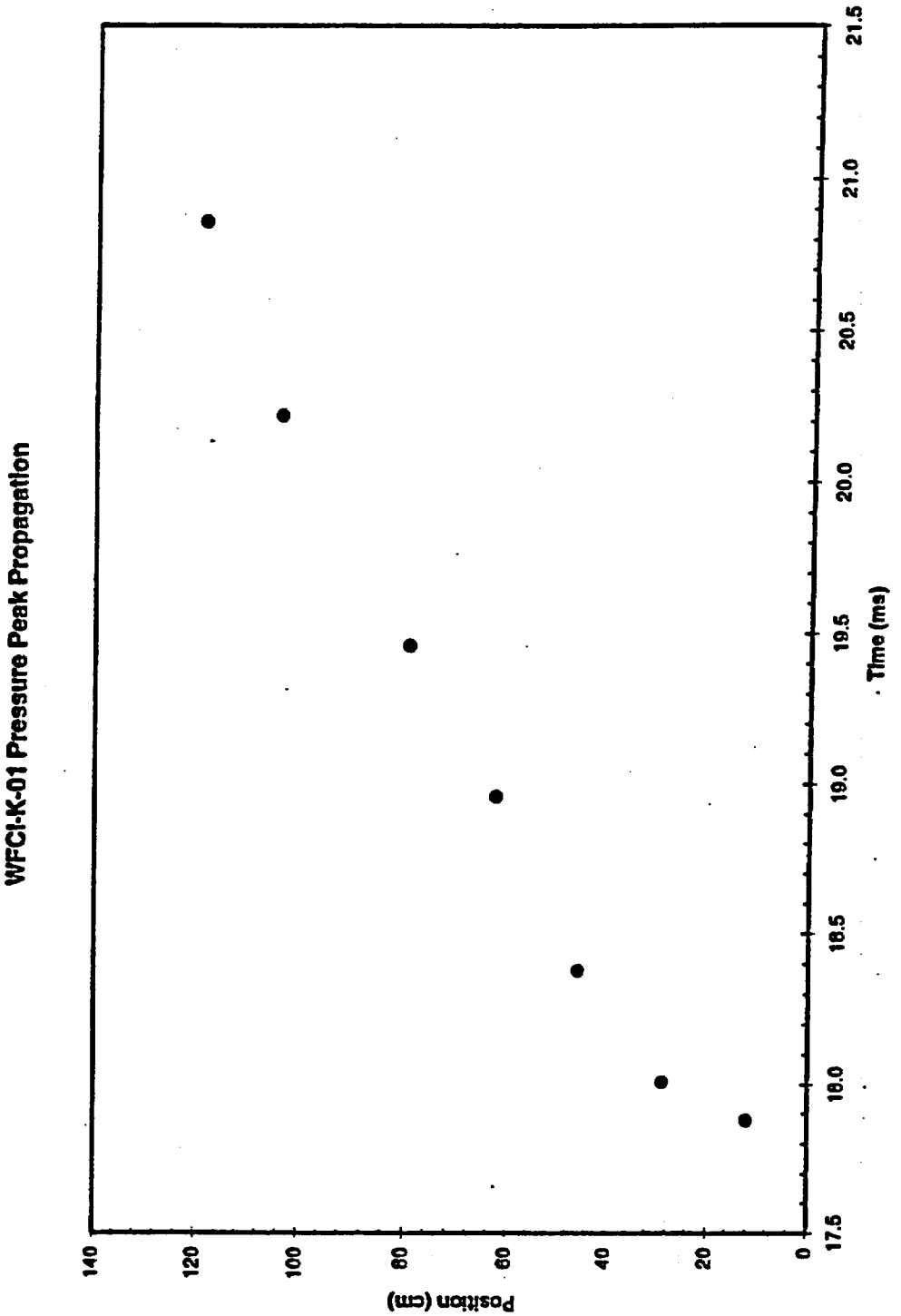

Figure 4.57: WFCI-K-01 pressure peak propagation curve

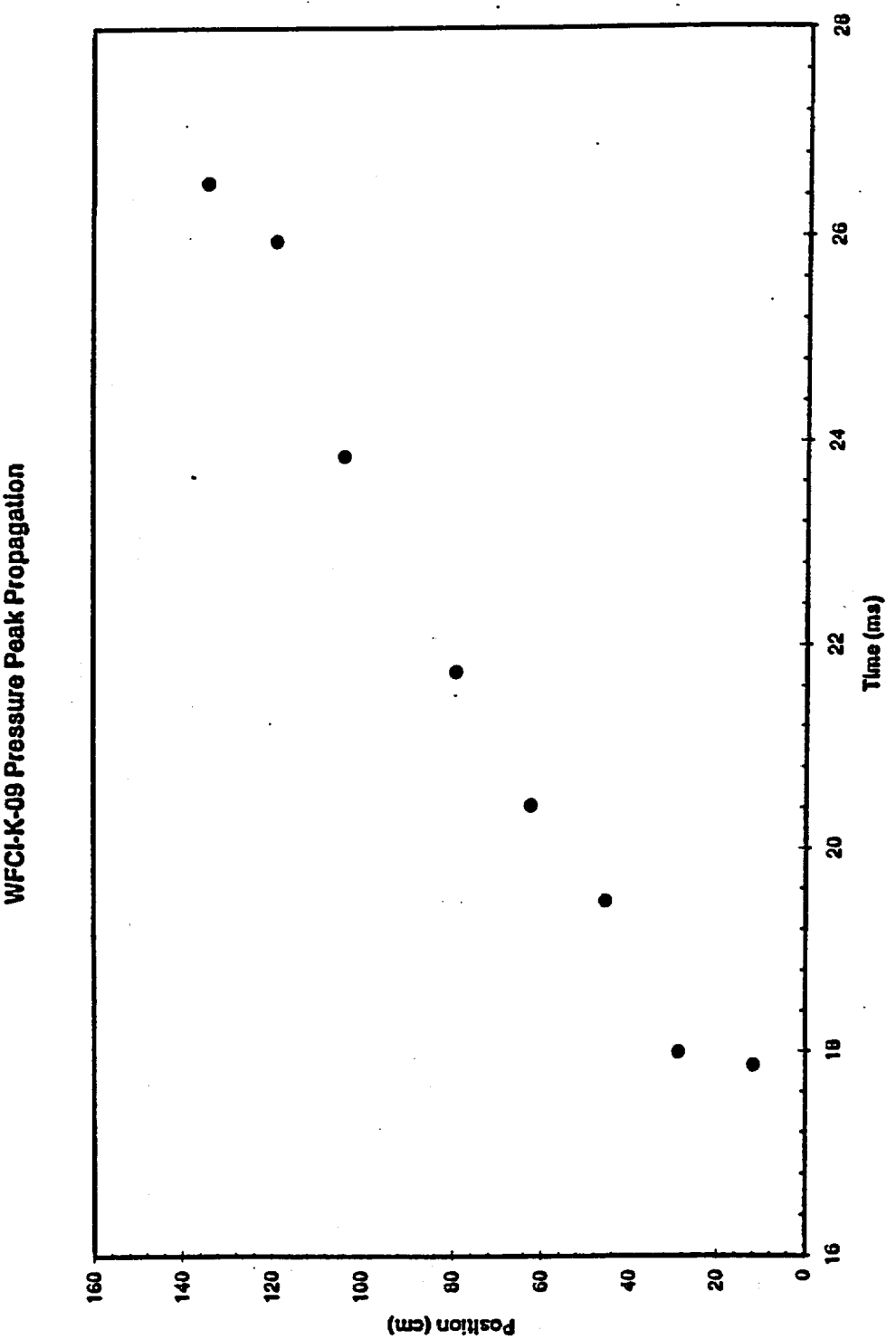

Figure 4.58: WFCI-K-09 pressure peak propagation curve

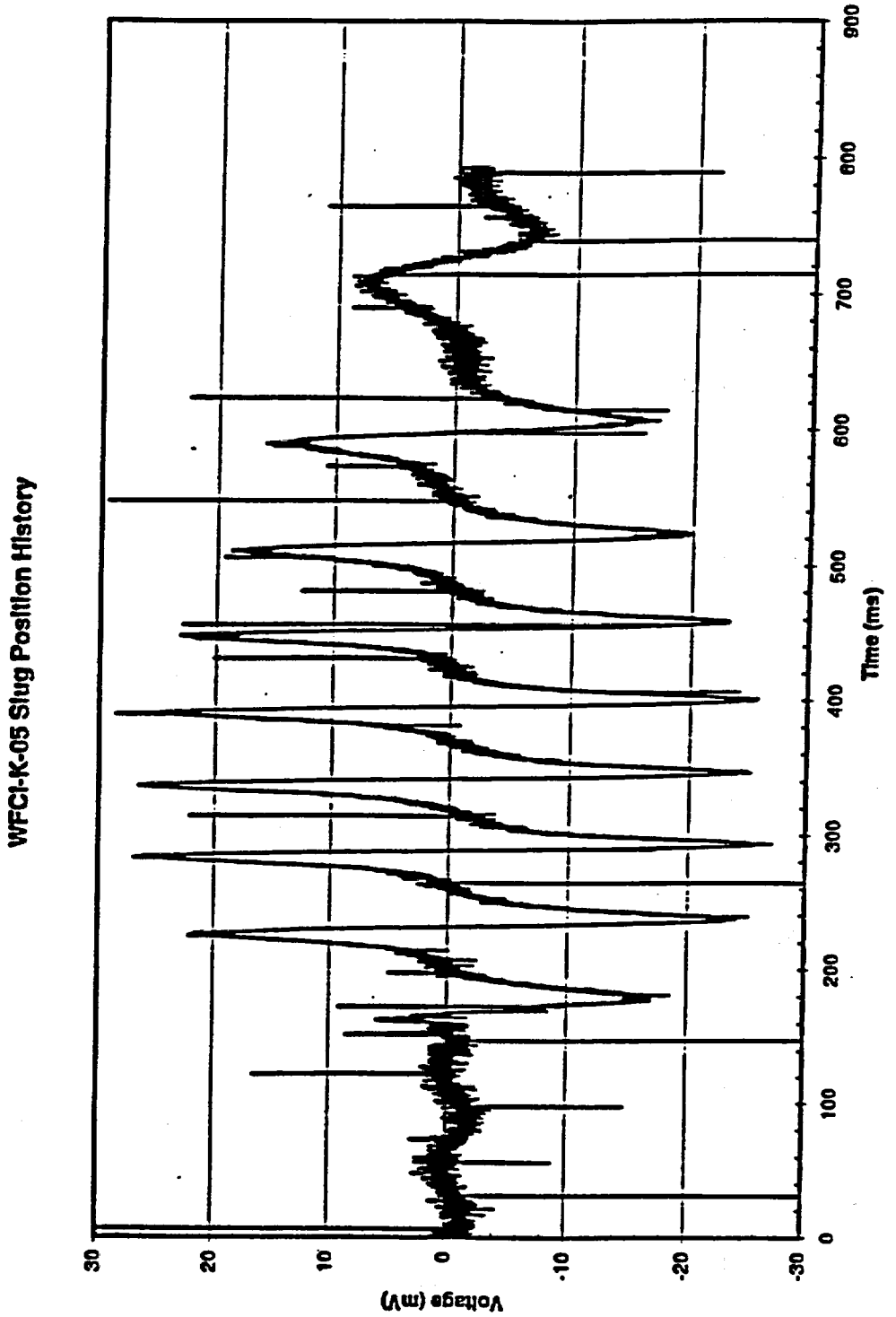

Figure 4.59: WFCI-K-05 slug position signal

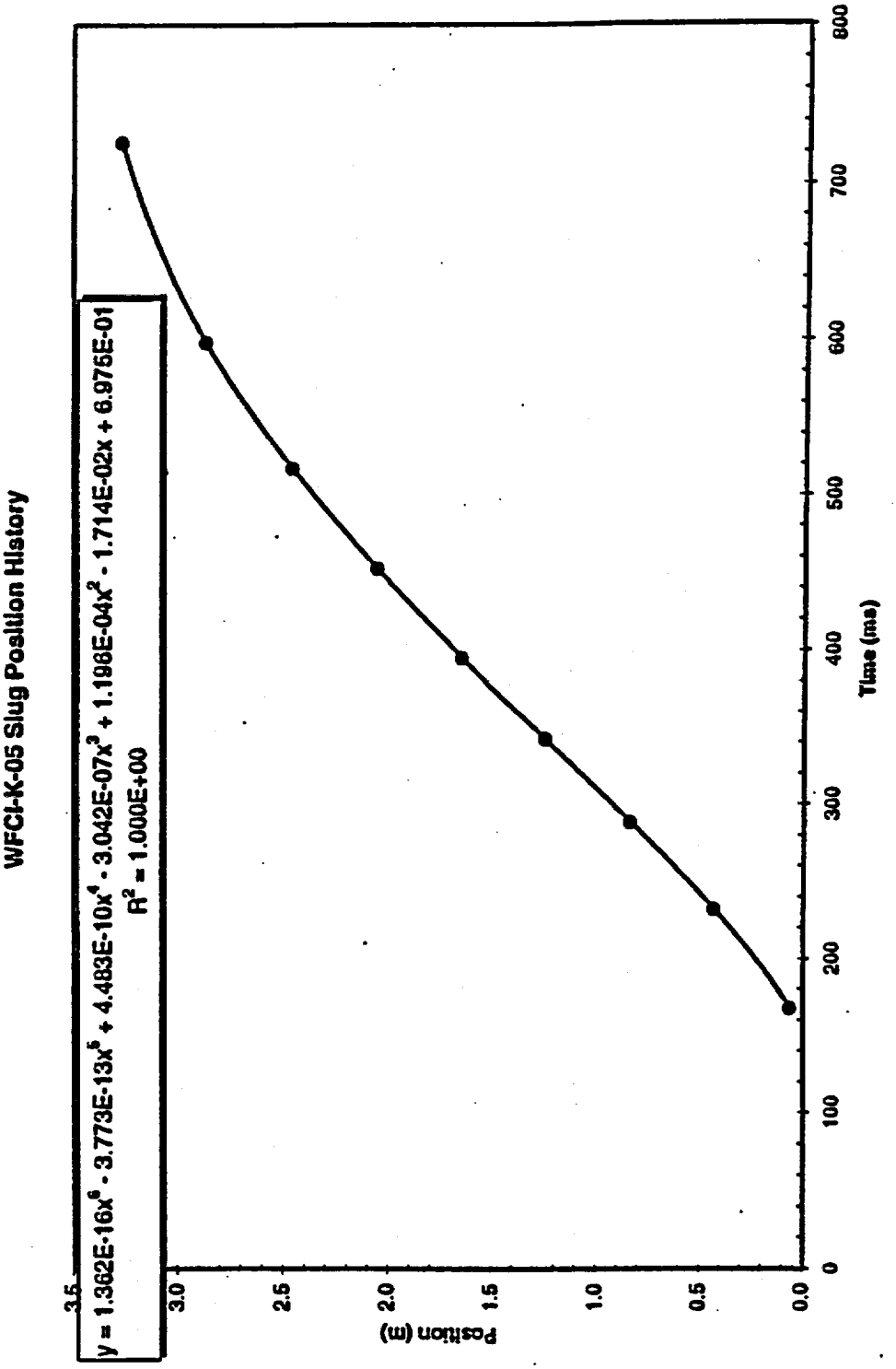

Figure 4.60: WFCI-K-05 slug position as a function of time with polynomial curve fit

Chapter 5

Analysis of Experimental Results

5.1 Temperature Effects

The initial temperatures of the fuel and coolant may have a noticeable affect on the mixing phase of the FCI through the coolant vaporization during mixing and the mixture void fraction. This in turn can affect the ability to trigger the FCI event. Based on the results from the WFCI-A, B, C, E, F and H series, the relationship between temperature and the likelihood of spontaneous explosions was investigated and shown in Figure 5.1. In this figure, other available experimental data with tin, [60, 62, 63] which have similar geometrical scales are also included and compared with the temperature cut-off line of the single drop tests [53].

Note that temperature effects on the vapor explosion are dependent on the fuel mass involved in an experiment. As shown in Figure 5.1, the cut-off temperature for a spontaneous explosion in the large scale tests is higher than in smaller scale tests. The spontaneous explosions in large scale tests occurred at coolant temperatures more than 20 °C higher than that in the single drop tests. Such a scale dependency may be explained by considering that in large scale tests, fuel in greater quantities, can have a range of diameters and length scales during mixing. Because of the natural oscillations occurring during film boiling around the fuel surface and considering the wide array of fuel diameters in the mixture, an FCI can be easily triggered by any perturbation, whether it be an external pressure source or some relative velocity or pressure fluctuation.

Second, the effect of coolant subcooling on the FCI is more profound than the effect of the fuel temperature. Note that this observation for tin is predicated on the fact that the fuel superheat is quite large, >500 degrees.This is because the net vapor produced and vapor film stability strongly depend on the net energy transfer at the coolant vapor-liquid interface. As the coolant bulk liquid temperature decreases (subcooling increases) the net amount of vapor produced during the mixing phase is significantly reduced, due to the large temperature gradients near the vapor-liquid interface which promote rapid vapor condensation. This in turn causes the vapor film surrounding the fuel particles to be relatively thin and more easily destabilized due the fluctuations encountered in the large scale boiling processes. Thus, an increase in subcooling would promote spontaneous interactions. As shown in Figure 5.1, fuel temperatures above 800 °C have little effect on the

likelihood of spontaneous explosion. However, modest changes in the coolant temperature can induce early FCIs and spontaneous explosions.

Finally, we note in Figure 5.2, the relationship between the explosion conversion ratio and different fuel thermal energies. The figure shows that conversion ratios of 0.2 to 0.7 % are not dependent on fuel energy within the variation of the fuel thermal energy from 0.8 to 1.25 MJ for a tin simulant. Thus, for a particular fuel simulant, once the temperature is above some threshold which satisfies the criterion for molten fuel and the ability to mix with the coolant without early spontaneous FCIs, variation in the fuel thermal energy does not have a first-order effect on energetics. This threshold is related to some minimum amount of melt superheat. In contrast, a different fuel simulant with sufficient superheat, but larger thermal energy per unit volume, would be expected to produce a vapor explosion with a a larger conversion ratio. Figure 5.3 illustrates this point for molten alumina melt compared to tin. We will revisit this later when we investigate the question of scaling.

5.2 Propagation Speed Characteristics

The propagation velocity is measured using the pressure traces from the eight axially distributed pressure transducers. For most of the WFCI tests, the propagation behavior of the explosion pressures is shown in Figure 5.4. In this figure, the positive value of the propagation speeds represent the upward propagation from the bottom to the top of the test section. The negative values represent the reflected explosion wave propagation from the top to bottom of the test section. In the explosions observed in most of the WFCI tests, average propagation speeds ranging from 800 to 1600 m/s were measured at 0.2 m above the bottom of the test section. This shows that the leading edge of the fuel had not reached this position during the mixing period. The trigger pressure wave propagated through single phase water with near sonic velocity. However, the propagation speed quickly drops to about 200 to 400 m/s as the wave encounters the mixture of fuel and coolant liquid/vapor. The explosion first occurred at or near the leading edge in a location between 0.3 to 0.7 m from the bottom and escalated upwards even where the local void fraction was high; *i.e.*, more than 25 % . Possibly because of this high void fraction near the top of the test section, the explosion pressure peak propagates with a velocity of about 100 m/s. In some of the double explosion cases, the second explosion occurs near the upper rigid boundary and propagates downward to the lower rigid boundary. The propagation velocity for the second explosion ranges from about 100 m/s or less at the top to about 600 m/s at the bottom. As a typical case for a double explosion, propagation speeds for WFCI-C-06 test are plotted with a solid line in Figure 5.4.

In particular, the WFCI-H-04 test shows no indication of single phase sonic velocity behavior at the bottom of the test section. This indicates that the leading edge of the molten fuel

had already reached the bottom and generated some amount of vapor. This was expected because the pouring time was increased by 400 ms and the bypass valve was opened in this test. Due to the external trigger, the explosion occurred at the bottom and escalated upward. The maximum escalation speed was reached relatively early, as compared with other experiments. Comparing this with the WFCI-H-03 test, in which only the pouring time was increased, the fluid near the bottom of the test section remains as pure water during the interaction. This clearly shows that fuel penetration was hindered by vapor upflow.

Based on Park *et al.*'s analysis [87], the void fraction at the flooding region is given by following equations,

$$\alpha_v = \frac{1}{C_0 + a} \tag{5.1}$$

where,

$$a = 1.7 \left[\frac{\sigma_c \rho_v^2}{\rho_c^2 g D_h^2 (\rho_c - \rho_v)} \right]^{\frac{1}{4}} \tag{5.2}$$

In this model, the coolant hydraulic diameter, D_h is given by

$$D_h = \frac{4\left(A_{ch} - \frac{m_f}{\rho_f H_{mix}}\right)}{P_w + \frac{4m_f}{\rho_f H_{mix} D_f}} \tag{5.3}$$

where P_w is the chamber perimeter, H_{mix} is the depth of the pool and m_f is the fuel mass mixed in the pool. For the WFCI-H-02 test conditions, D_h is about 60 mm. If the drift flux coefficient is 1.4, a void fraction at the flooding conditions in the present facility would be about 66 percent. The average vapor velocity, U_v^*, at the flooding condition can be calculated using Wallis' flooding criterion [88] given by

$$j^* = j_v = \alpha_v U_v^* = \sqrt{\frac{\rho_v}{g D_h (\rho_c - \rho_v)}} \tag{5.4}$$

This equation gives an average flooding vapor velocity of greater than 20 m/s. For our conditions this limit would not be reached but the mixing process was still hindered by the vapor upflow.

5.3 Qualitative Debris Analysis

The post-test debris collected after an FCI is another observable used to characterize vapor explosion energetics. Whether the explosion occurred or not, debris size distribution is also of importance in other aspects of FCI analysis. The debris distribution is generated

by fragmentation processes during two different time scales in the fuel-coolant interaction, the mixing phase, and the explosion phase. In the mixing phase, the characteristic size of the debris is governed by hydrodynamics related to phase relative velocities. The WFCI-G series of tests showed that the shape of the debris resembled a sphere with a Sauter mean diameter on the order of a few millimeters. However, in the explosion phase, fine fuel fragments may also be produced by other fragmentation processes in sub-millisecond times. The characteristic size of the debris in the explosion phase is much finer than in the mixing phase such as sub-millimeter sizes. The shape of the debris may also be very arbitrary.

The debris from the explosions are collected within the test tube, the expansion tube and the quench tank. Less than a fifth of the initial fuel mass charge for our tests remains as a crust within the furnace, transfer crucible and the upper portion of the test tube above the slide gate. In many tests spontaneous explosions occurred in the funnel above the slide gate, but this FCI did not directly affect the interaction below as long as the gate is closed. Thus, this debris was not collected and analyzed. The explosion debris had general characteristics similar to all past molten tin tests [63, 62]: *i.e.*, porous tin "plugs". They were found at various locations within the explosion tube with fine fragments intermingled and fused with the coarser porous plugs. In addition, discrete particles of fine tin fragments were swept down the expansion tube with the steam/water mixture, eventually settling in the quench tank. Different shapes of debris were found in different locations. In most tests, one piece of a long, round, porous plug was found in the I-Tube. The I-Tube debris was fused together and seemed to have resolidified after the explosion. The tin debris which was presumably near the leading edge of the fuel jet did not exhibit as many fine particles within its porous plug or as separate debris. This may be interpreted as being caused by some partial solidification as it cooled and penetrated the water pool. One can hypothesize that although this was probably the sight for the FCI triggering, a smaller portion of the tin melt at this location underwent rapid fragmentation during the explosion. In the T-tube, however, the shape of the debris resembled densely packed "sand." This may be more indicative of finely fragmented debris which participated in the explosion. In all tests the debris were removed from the tube and separately collected, weighed and measured.

These "plugs" seem to be remnants of the initial fuel jet which entered the water, spread radially and mixed with the water, and then broke into these plugs as the explosion propagated through the mixture and expanded, thereby, fragmenting portions of the fuel mixture. The fuel locations of these plugs seem to have no relationship to where they were formed since the multiphase explosion expansion would transport them to various locations where they are eventually quenched and become lodged in the test section. However, it is again important to note here that the plugs in the T-tube are just below the slide gate and would act a point of shock reflection for the upward propagating shock wave from the escalating explosion. Such plugs were also noted in the KROTOS tin tests and seem to have

contributed to the observed behavior of shock reflection in KROTOS.

The quantitative debris analysis of all the loose debris (no "plugs") was performed with mechanical sieves down to 25 μm . All of the debris distributions for this work are listed in the Appendix. As one can see, only a small fraction of the debris is at sizes which could be interpreted to be small enough to rapidly quench in an explosion timescale of a couple of milliseconds; *i.e.*, less than 5 % below 150 μm. Even accounting for the fact that some of these particles were trapped within the porous "plugs" leaves one with the qualitative conclusion that only a small fraction of the fuel rapidly fragmented in the propagation process which initially drives the explosion. This is consistent with the analysis of TEXAS for the tin test KROTOS-21 [117], which indicated that a fuel mass less than 0.1 kg was needed to drive the explosion. This is also consistent with the concept that the explosion is actually more efficient when one considers the smaller masses that may be actually involved.

5.4 Thermodynamic Analysis

In thermodynamic analyses, it has been historically assumed that all of the fuel and coolant are ideally mixed together and participate in the FCI. This is one of the key reasons for the large pressure and work output estimated by such models. However, it is possible to re-examine this assumption by using these experimental results. In this section, the experimental results obtained in the present work are analyzed to predict the minimum amount of fuel participation during the vapor explosion. This is done by using a thermal detonation model which employs the explosion pressures and propagation velocities obtained from the experiments to predict the mixture conditions which produced them.

The thermal detonation model proposed by Board and Hall [11] has the advantage that the explosion propagation behavior is obtained without knowing any detailed rate processes. In their model, a shock wave is generated by the vapor explosion in an one-dimensional geometry and propagate as a "quasi-steady" state through uniformly mixed fuel and coolant as designated '1'. At the downstream point, '2', the interaction between the fuel and coolant occurs and the fuel and coolant reach thermal and mechanical equilibrium. This satisfies the one-dimensional steady-state conservation balance of mass, momentum and energy. The mass, momentum, and energy balance across the shock front is shown with subscript 1 denoting upstream conditions,and 2 denoting quasi-steady interaction conditions;

mass balance:

$$\rho_1 u_1 = \rho_2 u_2 \tag{5.5}$$

momentum balance:

$$P_1 + \rho_1 u_1^2 = P_2 + \rho_2 u_2^2 \tag{5.6}$$

energy balance:

$$i_1 + \frac{u_1^2}{2} = i_2 + \frac{u_2^2}{2} \tag{5.7}$$

For a homogeneous mixture, the properties are obtained by the mass averaging, as follows:

$$v = \sum_i x_i v_i \tag{5.8}$$

$$i = \sum_i x_i i_i \tag{5.9}$$

where at state 1 the fuel, coolant, and vapor are at different temperatures and at state 2, the fragmented fuel, participating coolant and any remaining vapor are in thermodynamic equilibrium. Combining the above equations, the equilibrium Hugoniot condition for state 2 is derived for given initial conditions at state 1. The pressure and velocity at state 2 are given by

$$\frac{P_1 + P_2}{2}(v_2 - v_1) = e_1 - e_2 \tag{5.10}$$

$$u_2 = u_1\sqrt{\frac{P_2 - P_1}{v_1 - v_2}} \tag{5.11}$$

In this analysis, however, the initial mixing conditions were estimated by this model using experimentally measured explosion propagation behaviors such as the explosion pressure peak, P_{exp}, and the propagation velocity, u_s. The minimum mass of the fuel involved in the explosion is obtained by using the calculated initial conditions and measured explosion work output. The reader should note that this is an estimate based on the assumption of quasi-steady state behavior and that the C-J chemical dentonation analogy is applicable to the vapor explosion process.

Figure 5.5 and 5.6 are the C-J pressures and propagation speed calculated from the above equations with respect to the ranges of initial conditions, *i.e.*, the coolant to fuel mass ratios and void fraction which are representative of the WFCI experiments. For the current experimental conditions, the measured C-J pressure and propagation speed are equal to approximately 3 MPa and 200 to 300 m/s, respectively as shown in Table 4.1. From these data and two figures, the corresponding initial void fraction and the coolant to fuel mass ratio can be estimated to be about 20 % and 0.33, respectively. The measured work is in the range of 2 to 5 kJ and the calculated isentropic maximum work ranges from 40 to 60 kJ/kg. Thus, the minimum mass of fuel involved is calculated by the measured work divided by the calculated specific thermodynamic work. Corresponding fuel masses of 40 to 120 g are obtained from this estimate. These masses are about 1.0 to 3.6 % of the total fuel mass injected of 3 to 4 kg.

The large difference in the explosion energy conversion between actual measurements and ideal conditions might be explained by considering significant thermal dissipation of the fuel thermal energy during the expansion process. Using this hypothesis, one estimates that a large amount of vapor (more than 50 %) would be produced, while more fuel could participate in the interaction under such circumstances. Considering a propagation velocity of 200 to 300 m/s as observed in the experiments with a relatively high void fraction, say 60 %, one can estimate a mass ratio of 0.1 from Figure 5.6. However, under these conditions, the possible C-J pressure is near the critical pressure of the water coolant. Larger void fractions can be assumed to reduce this explosion pressure, but such volume fractions are unphysically high. This again suggests that a small fraction of fuel participating in the FCI seems to be more plausible than a large fraction of fuel participation with large void fraction. Most post-test debris analyses in the WFCI tests indicates that a large fraction of molten fuel in the I-tube did not take part in the interaction.

The fuel debris distribution for the WFCI-A and C test series have debris sizes of 60 to 660 μm. The associated mass to this size range corresponds to similar mass fractions of few percent. This result is also consistent with KROTOS-21 analysis [117] which indicated a fuel mass on the order of 100 g was needed to drive the explosion. It suggests that the explosion is actually more efficient with small fuel masses driving the interaction, and the remainder of the fuel and coolant may not participate over the explosion propagation time-scale. The same analysis has been also applied to recent KROTOS tests [135] for high temperature molten oxides and similar conclusions were reached.

5.5 Energetics of Iron-Oxide Melt

Most WFCI experiments (series A to H) used a molten fuel simulant, tin, which was known to easily produce energetic explosions. Our major contribution using this simulant was to demonstrate explosion reproducibility and provide an extensive data base on the effects of initial and boundary conditions on explosion energetics. Based on analysis we expect the insights gained are applicable to other molten fuel-coolant fluid pairs. In contrast to these past tests, the WFCI-K test series was focused on using a molten fuel simulant that was more prototypic of the high temperature molten oxide that would be present in a severe accident. Our choice of iron-oxide was based on proven energetics at small scales, the ability to melt and deliver kilogram quantities and the conclusion that it was a good simulant for reactor materials. This approach allows us to gain some understanding of FCIs with molten oxides at prototypic superheats as well as generate a more extensive data base on materials scaling. Note that no previous large scale experiments have been attempted with this fuel simulant.

The WFCI-K test series results were ambiguous as to whether an energetic explosion occurred. There are three pieces of data that give us information about whether an explosion occurs during any experiment. The first is the pressure data that is taken during the test. This provides detailed information about what occurred inside the test section during the interaction, and is examined in several ways to see if the interaction has explosive qualities. For example, sharp pressure peaks that escalate and propagate through the test section suggest an explosive interaction. The second indication is the breakage of the rupture diaphragm at the end of the expansion tube, due to the initial movement of the water slug as work is being done on the surroundings. The final evidence of an explosion is the acceleration of the slug down the expansion tube. Given a measureable slug velocity, this allows measurement of the slug kinetic energy and calculation of the conversion ratio. All three of these data indicators were always present for vapor explosions when tin was poured into water. For this series of experiments with iron-oxide, no single test had all three of the above characteristics, but several tests had at least two. This suggests that fuel-coolant interactions did occur in K-01, -05 and -09, but none were vapor explosions. Let us consider each source of data.

Pressure Histories and Impulses

The pressure histories give the most insight into the characteristics of each interaction, because these data are quantitative and recorded at a high sampling rate to capture explosive propagations. Seven of the ten series K experiments performed exhibited very similar pressure traces, with rather weak signals from the trigger occurring at transducer P1, and very weak or no signal for all others. It is most likely that the pressure signals are absent at higher levels in the test section due to a large increase in void from boiling during fuel-coolant mixing, which limits the pressure increase due to the compressibility of the vapor. Thus, in the absence of an FCI, the trigger pressure impulse is quickly dissipated in the multiphase medium. This effect is most prominent in tests with the WFCI-1 test section, which has a smaller inside diameter. There is less water per unit length of test section, and thus a greater likelihood of vapor production producing a larger local void fraction. In fact, since the iron-oxide (assuming a composition of Fe_3O_4) begins to solidify at 1556 °C, substantial boiling will occur even after the fuel has solidified. This effect seemed to be independent of water temperature with modest subcooling. Tests K-02, -03, -04, and -10 all had uniform water temperature (using loop heating) ranging from 70 to 85 °C. Tests K-05, -06, and -07 all had nonuniform temperature gradients set up with hot water in the funnel (80 °C) and cooler water at the bottom of the test section (25 - 47 °C). This was done in an attempt to reduce the void fraction inside the test section, thus allowing an interaction to occur, and to suppress an FCI in the funnel. All these cases exhibited a similar type of characteristic pressure traces. The magnitude of the peak pressures give

some indication of which tests had the strongest fuel-coolant interactions. Tests K-01 and K-09 had peak pressures of 6.53 and 9.70 MPa respectively. This suggests to us that the mass of melt required to generate an explosive pressure trace need not be very large, since test K-01 had about 15 % of the melt mass delivered to the test section.

The shock propagation speeds give some insight into whether an interaction is explosive. In most of the tests, shock propagations were only measured between P1 and P2, and the values were always much less than the sound speed in water, indicating that there is voiding in this region, but not necessarily an explosive interaction. Test K-01 also has a moderate propagation speed at the bottom (510 m/s) which quickly drops as the peaks propagate upwards to about 100 m/s between transducers P6 and P7. Subsequently, the speed increases, as the time for the first P7 peak to travel up to the slide gate and back down indicates a speed of 169 m/s. Then the speed increases further to 184 m/s from P7 to P6, which indicates that some sort of explosive interaction had occurred locally and was propagating downward. Test K-09 also exhibits similar characteristics, with a large speed a the bottom (510 m/s) which drops as it propagates upward (30 m/s from P6 to P7) then increases again at the top (105 m/s from P7 to P8). The difficulty in resolving any clear shock propagation behavior and the fact that the speeds were relatively low again suggest that local FCIs occurred, but give no clear indication of a propagating explosion.

The impulses tended to give results similar to the peak pressure data. Test K-10 has a moderately large impulse of 0.069 N-s, and this occurs at the bottom (P1). The two tests with the largest impulses are K-01 and K-09, with values of 0.073 N-s and 0.16 N-s respectively. These maximum impulses occur near the top of the test section (P7) in both cases. In addition, tests K-01 and K-09 exhibit some evidence of an increase in impulse in the upper portion of the test section. In test K-01, the impulse decreases slightly from around 0.03 N-s as the pressure peak propagates upward, to around 0.02 N-s when it reaches the top. Then as the peak travels back down, an impulse of 0.03 N-s is measured. There must have been additional energy release due to a fuel-coolant interaction, because if the peak simply reflected off the top surface (the slide gate) its impulse would be the same or slightly smaller. In the data for test K-09, there is also clear indication of an increase in impulse at the top. The impulses are very low at transducers P1 to P3, then they increase to around 0.035 N-s at transducers P4 and P5. Then the impulse jumps to 0.13 N-s at P7 and 0.1 N-s at P8. Traveling downward, the impulse is still 0.1 N-s at transducer P6. These impulses clearly indicate that an interaction occurred in this region with a rather large energy release compared to all other experiments.

Work Output and Efficiency

Experiment K-05 was the only test that provided a measurement of the conversion ratio,

0.056 percent. The slug was forced down the tube at a significantly rapid speed to have its position recorded by the instruments. Based on the available internal energy of the fuel, the conversion ratio is quite low, especially when compared to values attained for other materials such as tin or alumina (0.3 to 3.0 % for these simulants respectively). The data for the slug movement is typical of other slug movements with tin. The low conversion ratio can be interpreted not only because of a high internal energy of the fuel, but also because the fuel is at a low superheat (100 to 200 °C) when compared to other fuels (e.g. tin and alumina with superheats greater than 300 °C). This means that the fuel can solidify quickly, which can prevent any further fuel fragmentation, after longer mixing or upon pressure reflections in the chamber.

Another issue that needs to be considered is the effect of the contamination of the melt by the erosion of the boron nitride crucible. The Appendix discusses in some length the results of our debris analysis and the associated inspection of the boron nitride crucible, the delivery tube, and the test chamber region above the slide gate. Post-test debris analysis did not to provide much quantitative data into FCI energetics directly, but provides qualitative insights and detailed morphology of the melt composition. The most important conclusion from these analyses seems to point to the fact that as much as 10 percent of the non-oxidic melt by weight delivered to the test section is boron. This suggests that the melt upon delivery is iron-oxide with small amounts of boron-oxide intermixed. The net effect of this melt contamination by crucible material is that the liquidus temperature of the fuel is decreased. The exact amount of decrease is difficult to know, but an estimate can be given. Based on past work with iron-oxide, one can estimate the decrease in the melting temperature by the product of the percentage of the minority composition and the melt temperature difference. For iron-oxide and boron-oxide the maximum melt temperature difference is 1100 °C, and the minimum is about 950 °C, from liquidus to solidus for iron-oxide and assuming the boron-oxide has a discrete melting point (note: it has a 'softening point' of 450 °C). Thus, the depression in liquidus point of 1556 °C, would be at most about 100 °C, increasing the initial superheat to about 200 °C. This is not a substantial effect given the initial melt temperature and the rapid cooling that seems to take place during the mixing phase. In addition, the thermophysical properties of the melt would not be seriously affected by this minority melt component. It is still our view that the melt superheat is small enough to be the major reason for the limited energetics observed during the WFCI experiments.

5.6 Possible Explosion Mechanism

The results of the WFCI experiments seem consistent with the rapid fragmentation process resulting from the vapor film collapse process. Kim [14] proposed that the model for the fuel fragmentation is due to a jet impingement mechanism, in which the fuel outer

surface mixes with or entraps coolant below its surface. This local microscale mixing causes further pressurization and drives further fuel droplet fragmentation in the near vicinity. This process can be cyclic, with the fuel surface progressively fragmented by this collapse-jetting process. However, in a large scale explosion, such as that observed in these experiments, the collapse process would be operative for some time span after local film collapse. Following this time span local pressure differences caused by coolant vaporization and fuel fragmentation would equilibrate and only hydrodynamic fragmentation would take place.

Recent single droplet (or small scale) data by Ciccarelli *et al.* [56] seem to provide some visual confirmation of this process. They suggest that upon film collapse the molten fuel droplet expands into a "starfish" shape. This may be due to local coolant jets impacting and perhaps touching or penetrating the fuel surface at local spots. Because the liquids are essentially incompressible, this coolant jet impingement also expels fuel outward as "projections". In a large scale explosion these expelled fuel particles would be fragmented in the coolant and quickly quenched within it. This would generate vapor at the local pressures, sustaining and escalating the explosion event.

This conceptual picture is similar to Kim's in that each one views the explosion fuel fragmentation process as a surface phenomenon in which there is a time span over which it is operative. The explosion propagation leaves the fuel-coolant mixture partially "reacted or exploded." The local void of the fuel-coolant mixture determines the initial extent of film collapse and associated fuel-coolant contact. Fuel thermal energy and fuel droplet surface area determine the associated local pressurization as the surface of the fuel disintegrates due to this "microscale" fuel-coolant mixing, coolant vaporization and fuel quencing process. The local pressures and the induced particle velocities then transmit this event spatially through the fuel-coolant mixture and the escalation continues based on the volume fraction of the fuel-coolant mixture. Such an explanation would be consistent with the limited fine fragmentation energetics data taken from the experiments. Also large scale explosion mixture might be able to sustain multiple propagations through the mixture, provided it is held together by a sufficient inertial constraint and the associated vapor void behind each propagation is not too large to retard further shock propagation, vapor film collapse and heat transfer with the molten fuel particles remaining in the mixture. Thus, the extent of the fuel participation in an explosion is really controlled by the initial fuel-coolant mixing conditions, the inertial constraint and the fuel thermal energy. Scaling to reactor conditions implies one must primarily consider these conditions.

5.7 Vapor Explosion Scaling for Reactor Safety Issues

Most experimental investigations, including this work, have been performed with various simulants used for the actual molten reactor fuel material; *e.g.*, using less toxic or more readily available lower temperature metals or inert oxides in smaller geometries. In order to relate observed experimental behavior to postulated reactor scale behavior, it is necessary to establish appropriate scaling for the vapor explosion; *i.e.*, geometric as well as material scaling. In the first section of this work, we established the reactor safety issues for postulated in-vessel and ex-vessel conditions; *i.e.*, how to predict energetics, work output and dynamic pressures, under a variety of fuel-coolant contact conditions. From a theoretical point of view, direct use of governing equations to scale the phenomenon is not possible because the details of vapor explosion dynamics, involving mixing, fuel fragmentation and explosion propagation, still have key uncertainties. Rather, it would be useful to consider which initial and boundary conditions are of greatest importance to energetics and what would be a proper scaling approach. A complete discussion of this was presented at the 1997 CSNI workshop by one of the current authors (Appendix). Let us try to apply these principles to what has been observed in these experiments.

In this work, the following four different initial and boundary conditions were examined with consideration for the geometric, materials and thermodynamics aspects of the FCI phenomenon.

- The effect of the trigger;
- The system constraint specifically the degree of axial constraint;
- The effect of fuel temperature with substantial superheat and water subcooling;
- The effect of changing fuel composition to a molten oxide with limited superheat;
- The effect of the coolant to fuel mass ratio or volume ratio.

The effect of the trigger would be highly variable for fuel-coolant mixing and explosion propagation in a real situation. Our approach for the trigger effect in these experiments was to understand its effect for our test conditions, and then eliminate it from any energetics considerations. The first four WFCI experimental series characterized the trigger, showed reproducibility of energetics for spontaneous and externally triggered events and then found the external trigger range that could be used in subsequent tests for consistency of test results without further concern that the trigger affected the data. The WFCI test program was successful in these efforts. If FCI triggering was the main issue, it would be necessary to identify the cause of the trigger in a real situation, while investigating the trigger effect in a systematic manner for the actual materials. This was not our main objective.

The system constraints for the fuel-coolant mixture can be divided into two different constraints; radial and axial constraints. For the radial constraint, our previous discussions for WFCI-D test indicated that in small scale tests [77] the rigid radial boundary provided reproducible results for explosion propagation and escalation more easily. In contrast, under weak radial boundary conditions local interactions occurred incoherently without propagation. To achieve controllable experiments, one needs to use a rigid boundary for a given fuel-coolant mixture. This rigid boundary would allow experiments, large in scale but small in relation to the reactor scale, to behave in a manner similar to a "one-dimensional slice" of a larger fuel-coolant mixture. Because the reactor scale environment would exhibit some radial compressibility, a rigid radial boundary would tend to maximize energetics. For the axial constraint, as discussed in a previous section, the degree of constraint affected the energetics of the vapor explosion. As the degree of the acoustic constraint was increased, the energetics of the vapor explosion also increased. A further increase of the inertial constraint can maximize the explosion energetics due to a competition between vapor production and fuel quenching during the propagation-expansion. Therefore, it is necessary to scale the experiments with an axial constraint that mimics expected reactor scale conditions coupled with rigid radial boundaries.

The results of the WFCI-E and WFCI-F test series suggest a scaling process that is more qualitative than quantitative. Results indicate that once fuel and coolant temperatures are within an envelope of fuel-coolant mixture conditions where the fuel remains molten (sufficient superheat) and the vapor film boiling process is stable (proper subcooling), a vapor explosion can result and constituent temperatures have a second order effect on energetics. The implication from this experimental observation needs to be taken with the result that the molten iron-oxide tests were at modest superheats and did not result in vapor explosions. This leads one to conclude that experimental values of fuel superheat and coolant subcooling must also mimic reactor scale conditions to be scaled appropriately.

These conclusions require us to focus on material scaling and the issue of fuel composition. It should be recognized that it is almost simulate the thermal behavior of one fuel material composition with another. Thus, any simulant used for the actual fuel material introduces distortions in the materials scaling of the phenomenon, that must be understood to the extent that the mixing or energetics is affected. In fuel property table in chapter 2 we assumed that most fuels had a modest superheat above its melting point, as has been predicted from severe accident simulations. This is in accord with the scaling argument just made. The major exception are the low-melting-point liquid metals, which has been historically used at higher temperatures to compensate for their low energy content near their melting point. Inspection of the table indicates quite clearly that iron-oxide and the corium melts are quite analogous in their specific energy, energy density and latent heat. Also, alumina, a chemically inert fuel simulant, contains more specific energy per unit mass than any other fuel melts, while tin contains much less specific energy per unit mass. This

suggests that iron-oxide may be a good thermodynamic match for corium, while tin and alumina would bound its energetics.

The final condition to consider is the coolant to fuel ratio in the fuel-coolant mixture. The WFCI-H experimental series provides two important observations about this ratio. First, there appears to be a broad maximum in explosion energetics for a range of coolant to fuel mixture conditions. Thus, from a scaling perspective once other experimental conditions are specified a range of mixtures can be considered to produce similar energetics as long as 'fuel lean' or 'coolant lean' mixtures are avoided. The second observation is that the explosion conversion ratio is quite low for all the tests, far below calculated thermodynamic values. The reason for this observation is the limited amount of fuel participating, and it may be necessary to verify this observation at different geometric scales and material compositions. Note that alumina tests in the KROTOS facility corroborate this observation.

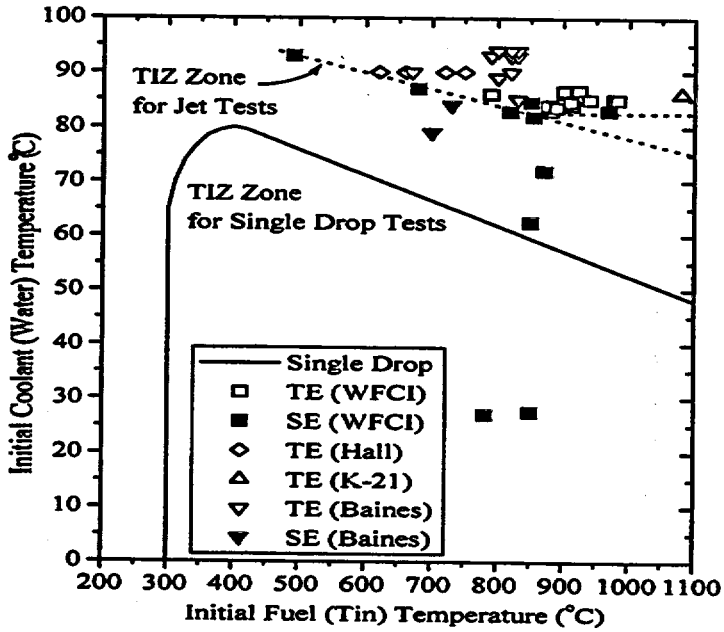

Figure 5.1: Temperature Interaction Zone in the Large Scale Tests

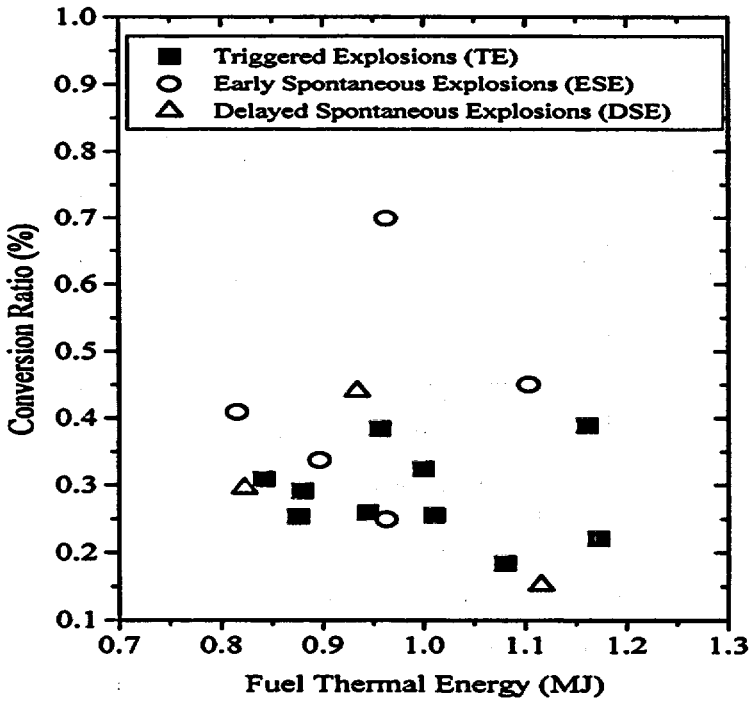

Figure 5.2: Conversion Ratios with respect to the Fuel Thermal Energies

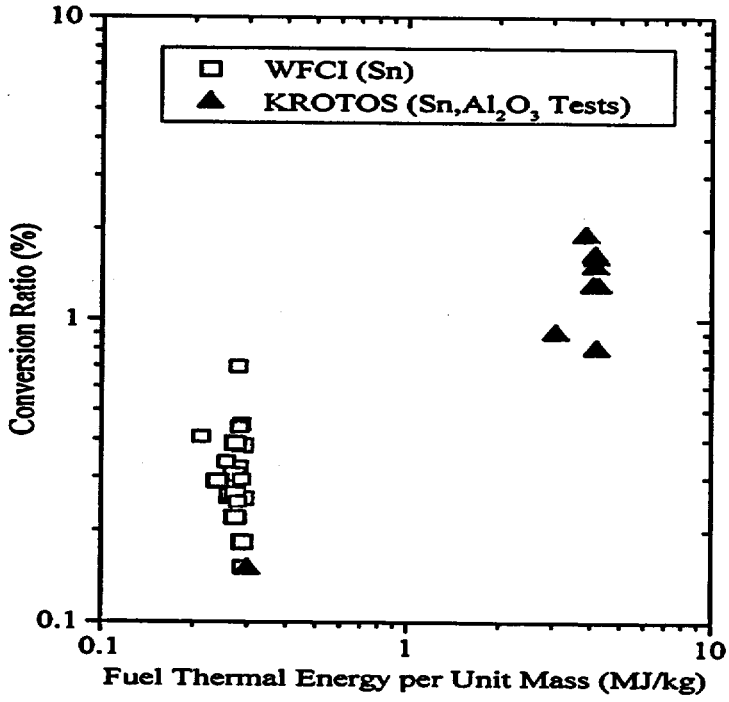

Figure 5.3: Conversion Ratios with respect to the Fuel Specific Thermal Energies

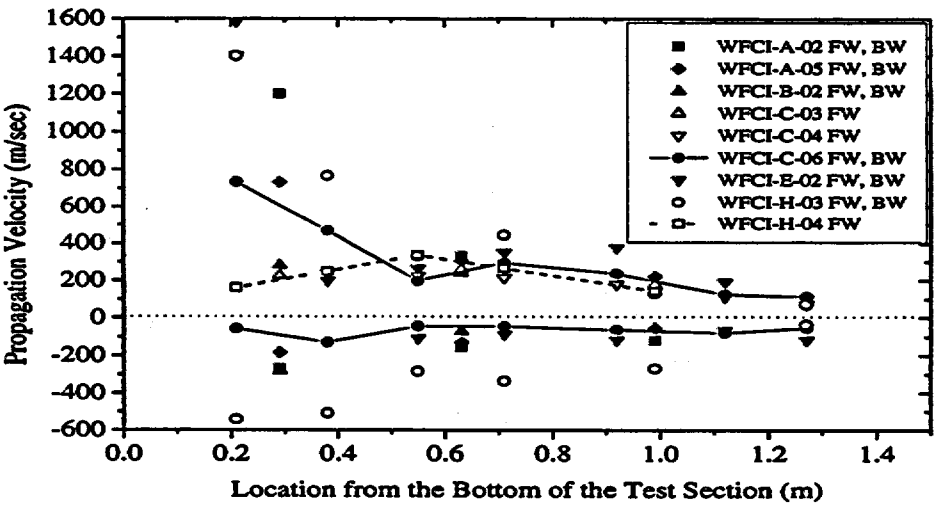

Figure 5.4: Propagation Speeds with respect to Locations of the Test Section

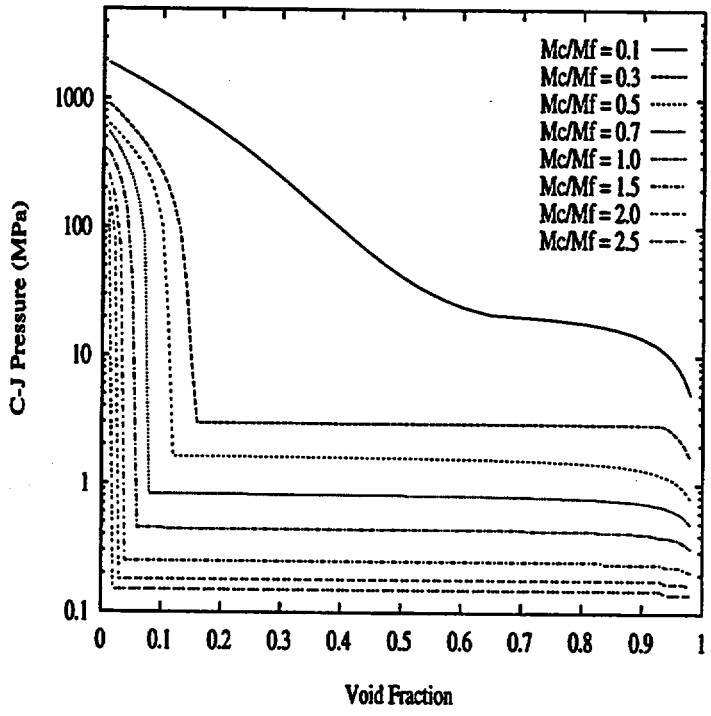

Figure 5.5: Variation of the Chapman-Jouguet Pressures associated with the Fuel-Coolant Mass Ratio in the Typical WFCI Experimental Conditions

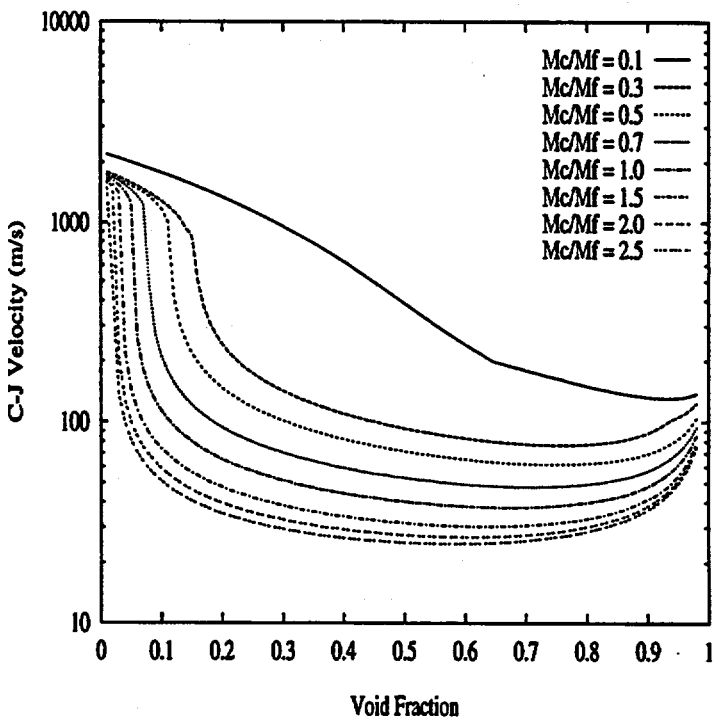

Figure 5.6: The Variation of the Chapman-Jouguet Velocities associated with the Fuel-Coolant Mass Ratio in the Typical WFCI Experimental Conditions

Chapter 6

Conclusions and Recommendations

Vapor explosions are a potential hazard in light water reactors after a prolonged lack of cooling allows reactor core materials to melt and contact residual water coolant within the reactor vessel or below in the containment reactor cavity. Past studies have demonstrated the explosive nature of certain liquid pairs, but have not systematically examined explosion energetics at larger scales as a function of controlled initial and boundary conditions. This has hampered basic understanding and has been a major deficiency in the database for modelling the vapor explosion.

Our objectives for this work were to obtain well-characterized data for the explosion propagation/escalation phases, while systematically investigating the effect of a comprehensive set of initial and boundary conditions on the explosion energetics:

- trigger strength,
- system constraint,
- fuel mass, composition and temperature, and
- coolant mass, viscosity and temperature.

This objective was subdivided into three specific tasks. First, a vapor explosion apparatus, WFCI, was designed and fabricated for well-characterized explosion data and demonstrated reproducible explosions, with tin as the simulant fuel. Second, the explosion energetics was examined as a function of varying initial and boundary conditions for this simulant fuel. Finally, the simulant fuel was changed to iron-oxide, a fuel that was more prototypic of actual fuel compositions and explosion energetics were reexamined.

The experimental investigation was subdivided into smaller test series to better understand specific vapor explosion mixing and propagation behavior. First, the WFCI-A test series was performed to demonstrate the reproducibility of the explosion phenomena. Initial conditions similar to KROTOS-21 were chosen as the nominal case for these tests, for comparison to independent data. The explosion behavior in the WFCI facility showed good reproducibility and agreement with KROTOS-21. Dynamic pressures had peak values as high as 10 MPa and quasi-steady values of 2-3 MPa, while explosion propagation

speeds were in the range of 200 m/s. The explosion conversion ratios were about 0.2 to 0.5 % for both spontaneous and for externally triggered explosions. The next test series, WFCI-B and C investigated the effect of the external trigger on the vapor explosion; i.e., spontaneous explosions compared to triggered explosions with specific impulse strengths. The tests showed that as the external trigger was reduced and then eliminated, multiple propagation events occurred during the explosion *i.e.*, double propagations first upward and then downward. The energetics of the complete interaction was relatively independent of trigger strength, but the detailed behavior of propagation process became more complex with spontaneous triggers. Once the trigger strength exceeded 3 MPa no multiple propagation events were observed and single propagation events of similar energetics were observed. Energetics for all of these vapor explosions were less than one percent .

The WFCI-D series investigated the effect of axial constraint. The WFCI facility was originally designed with a rigid radial constraint to maximize the energetics for any given set of mixing conditions, but the axial constraint could be varied. The axial constraint was varied by changing the slug mass in the horizontal expansion tube by an order of magnitude. Results indicated that there was an optimal degree of axial constraint to maximize explosion energetics. This could be explained by the competing effects of rapid vapor production during the propagation and vapor condensation and fuel quenching in surrounding coolant liquid as the explosion mixture expands. This effect suggests that the axial constraint needs to be similar in FCI tests when considering energetics for reactor safety issues.

The sixth and seventh test series, WFCI-E and F investigated the effect of the fuel and coolant temperatures on energetics. The results indicated that once the fuel temperature was above a threshold value its effect on energetics was of second-order importance. The same result was noted for a variation in the coolant temperature. This suggests that if the fuel and coolant temperature are large enough to satisfy the qualitative requirements of a molten fuel and stable film boiling at the time of triggering, then an energetic explosion can result, with temperature having a small quantitative effect within this envelope of conditions. This should be scale independent and KROTOS tests also suggest this based on the scale for KROTOS-21 and for compositions with alumina fuels.

The WFCI-G test series was performed to investigate the suppression effect of polymer additives by an increase in the coolant viscosity. Polymer additives suppressed spontaneous vapor explosions in this large scale geometry in qualitative agreement with past small scale tests. This was the first time that explosion suppression was demonstrated at a larger scale. Also, the post-test fuel debris generated in the absence of the explosion may be quite representative of the fuel debris during the mixing and fuel quenching process. Use of the polymeric solution should be considered as a technique for mixing studies.

In the WFCI-H series the fuel jet diameter and the timing of the external trigger were

altered to vary the ratio of coolant mass to fuel mass in the mixture at the time of the explosion. Varying this mass ratio of coolant to fuel indicated that the explosion conversion ratio exhibited a broad maximum in energy conversion. These values were more than an order of magnitude lower value than one predicts from ideal thermodynamic situations. Analysis again indicated that the broad maximum is created by competing effects related to the development of the fuel-coolant mixture prior to triggering. The location of this maximum relative to mass ratio is secondary to its qualitative existence. However, the value of this coolant to fuel ratio can be understood relative to mixing kinetics. The small energy conversion ratio can only be explained by the observation that only a few percent of the fuel mass fragments into small enough debris (<< 1mm) to directly participate in the explosion. This conclusion is applicable for all of our test data and seems to be scale independent and has important implications for reactor safety issues.

Finally, in the WFCI-K test series, the effect of changing the fuel composition from molten tin to more prototypic simulant (iron-oxide) was observed. These tests indicated that the triggering of energetic FCIs with more prototypic fuel materials and superheats was quite difficult. Fuel-coolant interactions were empirically observed in four of the twelve tests, but no propagating vapor explosions were observed. This observation is consistent with those of JRC staff and their corium tests in KROTOS at atmospheric pressures in which weak fuel-coolant interactions were observed. The reason for these weak FCIs seems to be that the melt superheat was low and mixing and quenching was efficient. This serves as validation of the temperature effects previously discussed.

With respect to reactor safety issues, this experimental work using fuel simulants has yielded a number of results that have potentially quite important safety implications. First, this work has provided clear evidence of the reproducibility of vapor explosion energetics for a controlled set of initial and boundary conditions. This suggests empirically that this phenomenon is predictable if one can establish and control the initial and boundary conditions. Second, the experiments demonstrate that geometric scaling can be properly specified; e.g., a rigid radial constraint for one-dimensional tests is conservative for energetics when compared to full-scale, while the axial constraint scale factor from test to prototype needs to be the unity to preserve energetics.

Finally and most importantly, the data suggests that once the fuel-coolant initial conditions are within an envelope for triggered events, the energetics is much less than thermodynamic due to the small amount of fuel that participates in an explosion time scale. And this envelope of triggerability is much smaller for a simulant molten oxide with low superheat, such as molten iron-oxide. This observation is somewhat of an enigma at the present time since iron-oxide and corium both exhibit 'weak vapor explosions' where the energetics is far below what was observed in WFCI for tin and in KROTOS for alumina. It is hypothesized that the mixing process for these fuels with modest superheat is efficient enough to cause the local void fraction in the mixture to be large and the fuel to be near solidification; *i.e.*, both

conditions hampering explosion triggering and propagation. This suggests that material scaling for reactor safety issues must preserve the same fuel composition and superheat from the test to the prototype.

The current work has limited data at larger scales with more prototypic molten oxides; i.e., larger fuel volumes than 0.5 liters, larger chamber geometries, prototypic molten oxide compositions and superheats. It is recommended that further tests could be carried out under these conditions to empirically verify our findings. Models developed from our analysis can also be used to analyze these experiments. Finally, it is known that the mixing conditions determine the envelope of explosivity for the vapor explosion. Thus, it is of fundamental interest to better measure the mixture local conditions just prior to the explosion to correlate with the explosion energetics; i.e., void fraction profiles, fuel volume fractions and mixing diameters. Our future work in vapor explosion research is specifically targeted toward this purpose.

Chapter 7

References

[1] Berman, M and Beck, D. F., "Steam Explosion Triggering and Propagation; Hypotheses and Evidence," *Proc. 3rd International Seminar on Containment of Nuclear Reactors*, University of Califonia, Los Angeles, CA, 10-11, (Aug. 1989), (Also available as *SAND89-1878C*).

[2] Condiff, D. W., "Thermal Detonation Modelling Analysis of FCI Vapor Explosions; A Critical Overview," *ANL/RAS 83-39*, Argonne National Laboratory, (Oct. 1983)

[3] Bang, K. H., "A Study of Stratified Vapor Explosions," Ph.D Thesis, Unversity of Wisconsin-Madison, Madison, Wisconsin, (1989).

[4] Nuclear Regulatory Commision, "Reactor Safety Study; An Assessment of Accident Risks in U.S. Commercial Nuclear Power Plants," *Report NUREG-75/0114 (WASH-1400)*, (Oct. 1975).

[5] Corradini, M. L., Kim , B. J. and Oh, M. D., "Vapor Explosions in Light Water Reactors; A Review of Theory and Modeling," *Progress in Nuclear Energy*, Vol. **22**, No. 1, pp 1~117, (1988).

[6] Reid, R. C., "Rapid Phase Transitions From Liquid to Vapor," *Adv. Chem. Eng.*, **12**, pp 105~208, (1983).

[7] Long, G., "Explosion of Molten Aluminum in Water - Cause and Prevention," *Metals Progress*, **71**, pp 107~112, (1957).

[8] Katz, L. D. and Sliepcevich, D. M., "LNG/Water Explosions; Cause and Effect," *Hydrocarbon Progressing*, pp 240~244, (1971).

[9] Grace, T. M., "Energetics of Smelt/Water Explosion," Project 3575, The Institute of Paper Chemistry, Appleton, Wisconsin (1985).

[10] Wohletz, K. H., "Explosive Hydrodynamic Volcanism," Ph.D Thesis, Arizona State University, (1980).

[11] Board, S. J. and Hall, R. W., "Recent Advances in Understanding Large-Scale Vapor Explosion," *The 3rd Specialist Meeting on Sodium Fuel Interactions*, Tokyo, PNC N251, 76-12, pp 249~283, (1976).

[12] Theofanous, T. G., Najafi, B. and Rumble, E., "An Assessment of Steam-Explosion-Induced Containment Failure, Part I: Probabilistic Aspects," *Nuclear Science and Engineering*, **97**, pp 259~281 (1987), *NUREG/CR-5030*, (1989).

[13] Corradini, M. L., "Vapor Explosions; An Experimental Review for Accident Analysis," *Journal of Nuclear Safety*, Vol *32*, No. 3, (1991).

[14] Kim, B. J., "Heat Transfer and Fluid Flow Aspects of Small-Scale Single Droplet Fuel-Coolant Interactions," Ph.D Thesis, Unversity of Wisconsin-Madison, Madison, Wisconsin, (1985).

[15] Board, S. J. and Hall, R. W., "Propagation of Thermal Explosions; Part 2. Theoretical Model," *CEGB Report, RD/B/N 3249*, (1974).

[16] Board, S. J. and Hall, R.W., "Propagation of Thermal Explosion; Part 1. Tin/Water Experiments," *CEGB Report, RD/B/N 2350*, (1974).

[17] Hess, P. D. and Brondyke, K. J., "Causes of Molten Aluminum-Water Explosions and their Prevention," *Metals Progress*, **95**, pp 93, (1962).

[18] Mosey, D., "Reactor Accidents; Nuclear Safety and the Role of Institutional Failure," *Nuclear Engineering International Special Publications*, (1990).

[19] Corradini, M. L. and Swenson, D. V., "Probability of Containment Failure Due to Steam Explosions Following a Postulated Core Meltdown in an LWR," *Report SAND 80-2132*, (Jun. 1981).

[20] Steam Explosion Review Group, "A Review of Current Understanding of the Potential for Containment Failure Arising from In-Vessel Steam Explosion," *NUREG-1116*, U.S. Nuclear Regulatory Commission, (1985).

[21] Turland, B. D., Fletcher, D. F., Hodges, K. I. and Attwood, G. J., "Quantification of the Probability of Containment Failure Caused by an In-vessel Steam Explosion For the Sizewell BPWR," *CSNI-FCI Specialists Meeting*, Santa Barbara, CA, January 5~8 (1993).

[22] Theofanous, T. G. and Yuen W. W., "The Probability of ALPHA-Mode Containment Failure Updated," *Proceedings of the CSNI Specialists Meeting on Fuel-Coolant Interactions, NUREG/CP-0127*, Santa Barbara, CA, USA, pp 330~342, (1993).

[23] Spies, T.P. and Basu, S., "Fuel-Coolant Interaction Phenomena in Reactor Safety: Current Understanding and Future Research Needs," *Proceedings of the CSNI Specialists Meeting on Fuel-Coolant Interactions, NEA/CSNI/R(97)26*, Tokai-Mura, Japan, pp 23~35, (1997).

[24] Basu, S. and Ginsberg, T., "A Reassessment of the Potential for an Alpha-Mode Containment Failure and a Review of the Current Understanding of Broader Fuel-Coolant Interaction Issues," Second Steam Explosion Review Group Workshop *NUREG-1524*, U.S. Nuclear Regulatory Commission, (1996).

[25] Buxton, L. D. and Nelson, L. S., "Core-Meltdown Experimental Review," *SAND74-0382*, Chapter 6, (1975).

[26] El-Genk, M. S., Matthews, R. B. and Bankoff, S. G., "Molten Fuel-Coolant Interaction Phenomena with Application to Carbide Fuel Safety," *Progress in Nuclear Energy*, Vol. **20**, No. 3, pp 151~198, (1987).

[27] Fletcher, D. F., "A Review of the Available Information on the Triggering Stage of a Steam Explosion," *Nuclear Safety*, Vol. 35, No. 1 (1994).

[28] Spencer, B. W., Wang, K., Blomquist, C. A., McUmber, L. M., and Schneider, J. P., "Fragmentation and Quench Behavior of Corium Melt Streams in Water," *NUREG/CR-6133, ANL-93/32*, (1994).

[29] Spencer, B. W., Sienicki, J. J., McUmber, L. M., "Hydrodynamics and Heat Transfer Aspects of Corium-Water Interaction," *EPRI NP-5127*, (1987).

[30] Wang, S. K., Blomquist, C. A., Spencer, B. W., McUmber, L. M., and Schneider, J. P., "Experimental Study of the Fragmentation and Quenching Behavior of Corium Melts in Water," *Fifth Proceedings of Nuclear Thermal Hydraulics Meeting*, San Francisco, November 26~30, *Report CONF-891103-53*, (1989).

[31] Fry, C. J. and Robinson, C. H., "Experimental Observations of Propagating Thermal Interactions in Metal/Water Systems," *Fourth CSNI Specialists' Meeting on FCI in Nuclear Reactor Safety*, Bournemouth, UK, (Apr. 1979).

[32] Bird, M. J., "An Experimental Study of Scaling in Core Melt/Water Interactions," *22nd National Heat transfer Conference, 84-HT-17*, Niagara Falls, N.Y., USA, August 5~8, (1984).

[33] Fletcher, D. F., "The Particle Size Distribution of Solidified Melt Debris from Molten Fuel-Coolant Interaction Experiments," *Nuclear Science and Design*, **1056.**, pp 313~319, (1988).

[34] Denham, M. K., Tyler A. P. and Fletcher, D. F., "Experiments on the Mixing of Molten Uranium Dioxide with Water and Initial Comparison with CHYMES Code Calculations," *Nuclear Science and Engineering*, **146**, pp 97~108, (1994).

[35] Fletcher, D. F. and Denham, M. K., "Validation of the CHYMES Mixing Model," *Proceedings of the CSNI Specialists Meeting on Fuel-Coolant Interactions, NUREG/CP-0127*, Santa Barbara, CA, USA, pp 89~98, (1993).

[36] Buxton, L. D. and Benedick, W. B., "Steam Explosion Efficiency Studies," *Report NUREG/CR-0947 (SAND-79-1399)*, (1978).

[37] Buxton, L. D., Benedick, W. B. and Corradini, M. L., "Steam Explosion Efficiency Studies: Part II. Corium Melts," *Report NUREG/CR-1746 (SAND-80-1324)*, (1980).

[38] Corradini, M. L., "Analysis and Modeling of Steam Explosion Experiments," *Report NUREG/CR-2072 (SAND-80-2131)*, (1980).

[39] Mitchell, D. E., Corradini, M. L. and Tarbell, W. W., "Intermediate Scale Steam Explosion Phenomena: Experiments and Analysis," *Report NUREG/CR-2145 (SAND-81-0124)*, (1981).

[40] Berman, M., "Light Water Reactor Safety Research Program Quarterly and Semiannual Report," January-December 1980 *SAND-80-1304*, (1980); January-March 1981 *SAND-81-1216*, (1981); April-September 1981 *SAND-82-0006*, (1981); October 1981-March 1982 *SAND-82-1572*, (1982); April-September 1982 *SAND-83-1576*, (1983); October 1982-March 1983 *SAND-84-0688*, (1983); October 1983-March 1984 *SAND-85-2500*, (1984).

[41] Mitchell, D. E., Evans, N. A., "Steam Explosion Experiments at Intermediate Scale: FITSB Series," *Report NUREG/CR-3983 (SAND-83-1057)*, (1986).

[42] Marshall, Jr., B. W., "Recent Fuel-Coolant Interaction Experiments Conducted in the FITS Vessel," *ANS Proceedings of the 25th National Heat Transfer Conference*, Huston, Texas, USA, (Jul. 1988).

[43] Sugimoto, J., Yamano, N., Maruyama, Y., Hidaka, A. and Soda, K., "Fuel-Coolant Interaction Experiments in ALPHA Program," *Proc. 5th Int. Topical Meeting on Nuclear Reactor Thermal Hydraulics ; NURETH-5*, Salt Lake City, UT, USA, pp 890~897 (1992).

[44] Yamano, N., Maruyama, Y., Kudo, T., Sugimoto, J., "Phenomenological Studies on Fuel-Coolant Interactions for Light Water Reactor," *Proceedings of the International Seminar on Physics of Vapor Explosion; Oji Seminar*, Tomakomai, Hokkaido, Japan, Oct 25~29, pp 175~186 (1993).

[45] Yamano, N., Maruyama, Y., Kudo, T., Moriyama, K. and Sugimoto, J., "Current Status of ALPHA Program and Recent Progress of the Steam Explosion Experiments," *presented at Severe Accident Research in Japan*, October 31~ November 1, Tokyo, Japan, (1994).

[46] Meeting Summary, *Proceedings of the CSNI Specialists Meeting on Fuel-Coolant Interactions, NUREG/CP-0127*, Santa Barbara, CA, USA, pp MS-1~MS-11, (1993).

[47] Hohmann, H., Magallon, D., Schins, H. and Yerkess, A., "FCI Experiments in the Aluminum Oxide/Water System," *Proceedings of the CSNI Specialists Meeting on Fuel-Coolant Interactions, NUREG/CP-0127*, Santa Barbara, CA, USA, pp 193~203 (1993).

[48] Hohmann, H., Magallon, D., Huhtiniemi, I., Annunziato, A. and Yerkess, A., "Advance in the FARO/KROTOS Melt Quenching Test Series," *Trans. of the 22nd Water Reactor Safety Information Meeting, NUREG/CP-0139*, Bethesda, Maryland, October 24~26, USA, (1994).

[49] Magallon, D., Hohmann, H., "High Pressure Corium Melt Quenching Tests in FARO," *Proceedings of the CSNI Specialists Meeting on Fuel-Coolant Interactions, NUREG/CP-0127*, Santa Barbara, CA, USA, pp 1~13, (1993).

[50] Buxton, L. D. and Nelson, L. S., "Core-Meltdown Experimental Review; Chapter 6 Steam Explosion," *SAND74-0382*, (1975).

[51] Nazaré, S., Ondracek, G. and Schulz, B., "Properties of Light Water Reactor Core Melts," *Nuclear Technology*, Vol. **32**, pp 239~246, (1977).

[52] Dullforce, T. A., Buchanan, D. J. and Peckover, R. S., "Self-triggering of Small-Scale Fuel-Coolant Interactions: I. Experiments," *J. Phys. D: Appl. Phys.*, Vol. 9, pp 1295~1303, (1976).

[53] Dullforce, T. A., "The Influence of Solid Boundaries in Inhibiting Spontaneously Triggered, Small-Scale Fuel Coolant Interactions," *the 4th CSNI Specialist Meeting on Fuel Coolant Interaction in Nuclear Reactor Safety*, Bournemouth, U.K., 2~5 April, *Culham Laboratory Report : CLM-P587*, (1979).

[54] Asher, R. C., Bullen, D. and Davies, D., "Vapor Explosions (Fuel-Coolant Interactions) resulting from the Sub-Surface Projection of Water into Molten Metals: Preliminary Results," *AERE Harwell Report AERE-M-2772*, (1976).

[55] Board, S. J., Farmer, C. L. and Poole, D. H., "Fragmentation in Thermal Explosions," *International Journal of Heat and Mass Transfer*, Vol. **17**, pp 331~339, (1974).

[56] Ciccarelli, G. and Frost, D. L., "Fragmentation Mechanisms Based on Single Drop Experiments Using Flash X-ray Photography," *Proc. 5th Int. Topical Meeting on Nuclear Reactor Thermal Hydraulics ; NURETH-5*, Salt Lake City, UT, USA, pp 615~626, (1992).

[57] Ciccarelli, G., "Investigation of Vapor Explosions with Single Molten Metal Drops in Water using Flash x-ray," PhD Thesis, McGill University, Montreal, Quebec, Canada, (1992).

[58] Nelson, L. S. and Duda, P. M., "Steam Explosion Experiments with Single Drops of Iron Oxide Melted with a CO_2 Laser," *High Temperatures-High Pressures*, Vol. *14*, pp 259~282, (1982).

[59] Nelson, L. S., Duda, P. M., Fröhlich, G. and Anderie, M., "Photographic Evidence for the Mechanism of Fragmentation of a Single Drop of Melt in Triggered Steam Explosion Experiments," *Journal of Non-Equilibrium Thermodynamics*, Vol. *13*, pp 27~55, (1988).

[60] Hall, R. W., Board, S. J. and Baines, M., "Observations of Tin/Water Thermal Explosions ina Long-tube Geometry; Their Interpretation and Concequences for the Detonation Model," *Proc. 4th CSNI Specialists Meeting on Fuel-Coolant Interactions in Nuclear Reactor Safety*, 2, 450~476, Bournemouth, England, April 2~5, (1979).

[61] Briggs, A. J., "Experimental Studies of Thermal Interactions at AEE Winfrith," *3rd Specialists' Meeting on Sodium Fuel Interaction*, Tokyo, Japan, *Report PNC-N251,-76-12 (Vol. 1) (CONF-760328-P1)*, pp 75~96, (1976).

[62] Baines, M., "Preliminary Measurements of Steam Explosion Work Yields in a Constrained System," *1st U.K National Heat Transfer Conference on Heat Transfer, Inst. Chem. Eng. Symp.*, No. 86, pp 97~108, Leeds, (1984).

[63] Bürger, M., Miller, K., Buck, M., Cho, S. H., Schatz, A., Schins, H., Zeyen, R. and Hohmann, H., "Analysis of Thermal Detonation Experiments by means of a Transient Multiphase Detonation Code," *Proc. 4th Int. Topical Meeting on Nuclear Reactor Thermal Hydraulics ; NURETH-4*, Karlsruhe, K. F. G., pp 304~311, (1989).

[64] Schins, H., "Characterization of Shock Triggers Used in Thermal Detonation Experiments," *Nuclear Engineering and Design*, 94., pp 93~98, (1986).

[65] Park, H. S., Yoon, C., Bang, K. H. and Corradini, M. L., "Vapor Explosion Escalation/Propagation Experiments and Possible Fragmentation Mechanisms," *Proceedings of the International Seminar on Physics of Vapor Explosion; Oji Seminar*, Tomakomai, Hokkaido, Japan, Oct 25~29, pp 187~196 (1993).

[66] Nelson, L. and Guay, K. P., "Suppression of Steam Explosions in Tin and $Fe - Al_2O_3$ Melts by Increasing the Viscosity of the Coolant," *High Temperatures-High Pressures*, Vol. *18*, pp 107, (1986).

[67] Kim, H. I., "Single Droplet Vapor Explosions; Effect of Viscosity," *Proc. 4th Int. Topical Meeting on Nuclear Reactor Thermal Hydraulics ; NURETH-4*, Karlsruhe, K. F. G., (1989).

[68] Baker, M., "The Effects of Surfactants on Single Droplet Vapor Explosions", M.S. Thesis, University of Wisconsin, Madison, WI (1993).

[69] Dowling, M. F., Ip, B. M. and Abdel-Khalik, S. I., "Suppression of Vapor Explosions by Dilute Aqueous Polymer Solutions," *Nuclear Science and Engineering*, Vol *113*, pp 300~313, (1993).

[70] Nelson, L. S., Eatough, M. J. and Guay, K. P., "Why Does Molten Aluminum Explode at Underwater or Wet Surfaces ?," *Light Metals, edited by Campbell, P. G., The Minerals, Metals, and Materials Society*, pp 951~961, (1989).

[71] Ip, B. M., Dowling, M. F. and Abdel-Khalik, S. I., "An Experimental Investigation of the Effects of Polymeric Additives on the Likelihood and Severity of Steam Explosion," *Proc. 5th Int. Topical Meeting on Nuclear Reactor Thermal Hydraulics ; NURETH-5*, Salt Lake City, UT, USA, (1992).

[72] Kowal, M. G., Dowling, M. F. and Abdel-Khalik, S. I., "Effects of Surfactants on the Likelihood and Severity of Steam Explosion," *Proceedings of the CSNI Specialists Meeting on Fuel-Coolant Interactions, NUREG/CP-0127*, Santa Barbara, CA, USA, pp 251~258, (1993).

[73] Kotchaphakdee, P. and Williams, M. C., "Enhancement of Nucleate Pool Boiling with Polymeric Additives," *International Journal of Heat and Mass Transfer*, Vol. *13*, pp 835~848, (1970).

[74] Paul, D. D. and Abdel-Khalik, S. I., "Nucleate Boiling in Drag-Reducting Polymer Solutions," *Journal of Rheology, 27(1)*, pp 59~76, (1983).

[75] Rouai, N. M. and Abdel-Khalik, S. I., "Pool Boiling of Drag-Reducting Polymer Solutions," *Applied Scientific Research, 40*, pp 209~222, (1983).

[76] Flory, K., Paoli, R. and Mesler, R., "Molten Metal-Water Explosions," *Chemical Engineering Progress*, Vol. *65*, No. 12, pp 50~54, (1969)

[77] Frost, D. L., Bruckert, B. and Ciccarelli, G., "The Role of Confinement in the Propagation of Vapor explosions," *Proceedings of the International Seminar on Physics of Vapor Explosion; Oji Seminar*, Tomakomai, Hokkaido, Japan, Oct 25~29, pp 128~138, (1993).

[78] Park, H. S., Yoon, C., Bang, K. H. and Corradini, M. L., "Experiments on the Trigger Effect for 1-D Large Scale Vapor Explosion," *Proc. New Trends in Nuclear System Thermodynamics*, Pisa, Italy, May 30~June 2, pp 271~280, (1994).

[79] Fletcher, D. F. and Anderson, R. P., "A Review of Pressure-induced Propagation Models of the Vapor Explosion Process," *Progress in Nuclear Energy*, Vol. **23**, No. 2, pp 137~179, (1990).

[80] Fletcher, D. F., "A Review of Coarse Mixing Models," *Culham Laboratory Report : CLM-251*, (1985).

[81] Fauske, H. K., "The Role of Nucleation in Vapor Explosion," *Trans. Am. Nucl. Soc.*, **15**, pp 813, (1972).

[82] Fauske, H. K., "on the Mechanism of Uranium Dioxide-Sodium Explosive Interactions," *Nuclear Science and Engineering*, **51.**, pp 95~101, (1973).

[83] Cho, D. H., Fauske, H. K. and Grolmes, M., "Some Aspects of Mixing in Large-Mass, Energetic Fuel-Coolant Interactions," *Proc. Meeting on Fast Reactor Safety*, Cicago, (1976).

[84] Corradini, M. L. and Moses, G. A., "Limits to Fuel/Coolant Mixing," *Nuclear Science and Engineering*, **90.**, pp 19~27, (1985).

[85] Henry, R. E. and Fauske, H. K., "Required Initial Conditions for Energetic Steam Explosions," *Journal of Heat Transfer*, **19.**, pp 99~107, (1981).

[86] Tong, L. S., Boiling Heat Transfer in Two-Phase Flow, Wiley and sons, New York, (1965).

[87] Park, G. C. and Corradini, M. L., "Estimates of Limits to Fuel/Coolant Mixing," *National Heat Transfer Conference AIChE Symposium Series*, No. 283, Vol. **87**, pp 8~18, (1991).

[88] Wallis, G. B., One-dimensional Two-phase Flow, McGraw-Hill Company, New York, (1969).

[89] Theofanous, T. G. and Saito. M, "An Assessment of Class-9 (Core-Melt) Accidents for PWR Dry-Containment Systems," *Nuclear Science and Engineering*, **66.**, pp 301~332, (1981).

[90] Drumheller, D. S., "The Initiation of Melt Fragmentation in Fuel-Coolant Interactions," *Nuclear Science and Engineering*, **72.**, pp 347~356, (1979).

[91] Corradini, M. L., "Modeling Film Boiling Destabilization Due to a Pressure Shock Arrival," *Nuclear Science and Engineering*, **84.**, pp 196~205, (1983).

[92] Inoue, A., Ganguli, A. and Banloff, S. G., "Destabilization of Film Boiling Due to Arrival of a Pressure Shock: Part I. Experimental," *Report No. C00-2512-13*, Chemical Engineering Dept., Northwestern University, Evanston, Illinois, USA, (1978).

[93] Henry, R. E., "Externally Triggered Steam Explosion Experiments: Amplification or Propagation," *Proceedings of the CSNI Specialists Meeting on Fuel-Coolant Interactions, NUREG/CP-0127*, Santa Barbara, CA, USA, pp 173~179, (1993).

[94] Plesset, M. S. and Chapman, R. B., "Collapse of an Initially Spherical Vapor Cavity in the Neighborhood of a Solid Boundary," *Journal of Fluid Mechanics*, 47(2), pp 283~290, (1971).

[95] Hicks, E. P. and Menzies, D. C., "Theoretical Studies on the Fast Reactor Maximum Accident," *Proceedings of the conference on Safety, Fuels and Core Design in Large Fast Power reactors, ANL-7120*, pp 654~670, (1965).

[96] Cline, D. D., Pong, L. T., Beck, D. F. and Berman, M., "An Equation of State Formulation for Hicks-Menzies FCI Efficiencies," *Nat. Heat Tran. Conf. AIChE Sym. Series*, No. 269, Vol. **85**, pp 48~53, (1989).

[97] Bang, K. H. and Corradini, M. L., "Thermodynamic Analysis of Vapor Explosions; Comparison of Models," *Proc. 5th Int. Topical Meeting on Nuclear Reactor Thermal Hydraulics; NURETH-5*, Salt Lake City, UT, USA, (1992).

[98] Hall, A. N., "Outline of New Thermodynamic Model of Energetic Fuel-Coolant Interactions," *Nuclear Engineering and Design*, **109.**, pp 407~415, (1988).

[99] Sharon, A. and Bankoff, S. G., "Propagation of shock waves in a fuel-coolant mixture," *In Topics in Two-phase Heat transfer and Flow*, S. G. Bankoff (ed.), ASME, (1978).

[100] Frost, D. L., Lee, J. H. S. and Ciccarelli, G., "The Use of Hugoniot Analysis for the Propagation of Vapor Explosion Waves," *Shock Waves*, **1**, pp 99~110, (1993).

[101] Fletcher, D. F., "Vapour Explosions: Multiphase Detonations or Deflagrations ?," *Shock Waves*, 3:181-192, (1994).

[102] Cho, D. H. and Ivins, R. O., "A Rate-Limited Model of Molten-Fuel/Coolant Interactions; Model Development and Preliminary Calculations," *ANL-7919*, (1972).

[103] Cho, D. H., Chen, W. L. and Wright, R. W., "A Parametric Study of Pressure Generation and Sodium-Slug Energy from Molten-Fuel-Coolant Interactions," *ANL-8105*, (1974).

[104] Chen, W. L., Cho, D. H. and Kazimi, M. S., "Recent Additions to the Parametric Model of Fuel-Coolant Interactions," *ANL-8130*, (1974).

[105] Oh, M. D., "Thermal-Hydraulic Modeling and Analysis for Large Scale Vapor Explosions," PhD Thesis, University of Wisconsin, Madison, Wisconsin, USA, (1985).

[106] Fletcher, D. F. and Thyagaraja, A., "The CHYMES Coarse Mixing Model," *Progress in Nuclear Energy*, **26** pp 31~61, (1991).

[107] Hall, R. W. and Fletcher, D. F., "Validation of CHYMES; Simulant Studies," *Proceedings of the CSNI Specialists Meeting on Fuel-Coolant Interactions, NUREG/CP-0127*, Santa Barbara, CA, USA, pp 70~88, (1993).

[108] Fletcher, D. F. and Thyagaraja, A., "Multiphase Detonation Modelling Using the CULDESAC Code," *12th Int. Col. on Dynamics of Explosions and Reaction Systems*, Ann Arbor, Michigan, 23-28 July, 1989; *Culham Laboratory Report : CLM-P855*, (1988).

[109] Amarasooriya, W. H. and Theofanous, T. G., "Premixing of Steam Explosions: a Three-Fluid Model," *Nuclear Engineering and Design*, **126** pp 23~29, (1991).

[110] Angelini, S., Yuen, W. W. and Theofanous, T. G., "Premixing-related Behavior of Steam Explosions," *Proceedings of the CSNI Specialists Meeting on Fuel-Coolant Interactions, NUREG/CP-0127*, Santa Barbara, CA, USA, pp 99~133, (1993).

[111] Medhekar, S., Abolfadl, M. and Theofanous, T. G., "Triggering and Propagaion of Steam Explosions," *Nuclear Engineering and Design*, Vol *126*, pp 41, (1991).

[112] Yuen W. W. and Theofanous, T. G., "The Prediction of 2D Thermal Detonations and Resulting Damage Potential," *Proceedings of the CSNI Specialists Meeting on Fuel-Coolant Interactions, NUREG/CP-0127*, Santa Barbara, CA, USA, pp 233~250, (1993).

[113] Young, M. F., "IFCI: an Integrated Code for Calculation of All Phases of Fuel-Coolant Interactions," *NUREG/CR-5084*, (1987).

[114] Davis, F. J. and Young, M. F., "Integrated Fuel-Coolant Interaction (IFCI 6.0) Code: User's Manual," *SAND94-0406, NUREG/CR-6211*, (1994).

[115] Chu, C. C., "One-Dimensional Transient Fluid Model for Fuel-Coolant Interactions," Ph.D Thesis, Unversity of Wisconsin-Madison, Madison, Wisconsin. (1986).

[116] Young, M. F., "The TEXAS Code for Fuel-Coolant Interaction Analysis," *Proc. ANS/ENS Fast Reactor Safety Conference*, July, Lyon, France, (1982).

[117] Tang, J. and Corradini, M. L., "Modeling of the complete Process of one-dimensional Vapor Explosions," *Proceedings of the CSNI Specialists Meeting on Fuel-Coolant Interactions, NUREG/CP-0127*, Santa Barbara, CA, USA, pp 204~217, (1993).

[118] Chang, S. K., "Hydrodynamics of liquid jet sprays : physicochemical analysis and computer simulation," PhD Thesis, University of Wisconsin-Madison, (1991).

[119] Taylor, G. I., "The Shape and Acceleration of a Drop in a High Speed Air Stream," *The Scientific Papers of G. I. Taylor, III, G. K. Batchelor (ed.)*, CUP, (1963).

[120] Bang, K. H., "The Role of Fragmentation Rate in Vapor Explosion Propagation: Comparison of Models," *Proceedings of the International Seminar on Physics of Vapor Explosion; Oji Seminar*, Tomakomai, Hokkaido, Japan, Oct 25~29, pp 229~233 (1993).

[121] Huh, K. and Corradini, M. L., "Dimensional Analysis of Small-Scale Steam Explosion Experiments," *Nuclear Science and Engineering*, **93**., pp 97~104, (1986).

[122] Amarasooriya, W. H. and Theofanous, T. G., "Scaling Considerations in Steam Explosions," *ANS Proceedings of National Heat Transfer Conference*, Vol. 2, pp 58~67, (1987).

[123] Ishii, M. and No, H. C., "Stepwise Integral Scaling Method for Severe Accident Analysis and Its Application to Corium Dispersion in Direct Containment Heating," *Proc. 6th Int. Topical Meeting on Nuclear Reactor Thermal Hydraulics; NURETH-6*, Grenoble, France, pp 960~971, (1993).

[124] Waldman, G. D., Reinecke, W. G. and Glenn, D. C., "Raindrop Breakup in the Shock Layer of a High Speed Vehicle," *AIAA J.*, **10**, pp 1200~1204, (1972).

[125] Berthoud, G. and Valette, M., "Calculations of the Premixing Phase of an FCI with the TRIO MC Code," *Proceedings of the CSNI Specialists Meeting on Fuel-Coolant Interactions, NUREG/CP-0127*, Santa Barbara, CA, USA, pp 27~36, (1993).

[126] Pilch, M. and Erdman, C. A., "Use of Breakup Time Data and Velocity History Data to Predict the Maximum Size of Stable Fragments for Acceleration-Induced Breakup of a Liquid Drop," *International Journal of Multiphase Flow*, **13**, pp 741~757, (1987).

[127] Pilch, M., "Acceleration Induced Fragmentation of Liquid Drops," PhD Thesis of University of Virginia, (1981).

[128] Hohmann, H. and Field, M., "KROTOS; Description of the experimental facility," Institute for Safety Technology Reactor Safety Programme Draft, (Apr. 1992).

[129] Molyneux, P., "Water-Soluble Synthetic Polymers: Properties and Behaviors," Vol. *1*, CRC Press, pp 12~45, (1982).

[130] Cho, D. H., Ivins, R. O. and Wright, R. W., "Pressure Generation by Molten Fuel-Coolant Interaction under LMFBR Accident Conditions," *Proc. of Conf. on New Develpments in Reactor Mathematics and Applications*, Idaho Falls, CONF-71032 (Vol.1), pp 25~49, (Mar. 1971).

[131] Bang, K. H. and Corradini, M. L., "An Experimental Study of Vapor Explosions in a Stratified Contact Mode," *International ENS/ANS Conference on Thermal Reactor Safety*, Avignon, France, October 2~7, pp 2362~2371, (1988).

[132] Bang, K. H., "On the Leidenfrost Temperature in a Dilute Polymer Solution and Implications for the Suppression of Vapor Explosions," *Proceedings of the Korean Nuclear Society Autumn Meeting*, Seoul, Oct, Korea, (1994).

[133] Farawila, Y. M. and Abdel-Khalik, "On the Calculation of Steam Explosion Conversion Ratios from Experimental Data," *Nuclear Science and Engineering*, **104**., pp 288~295, (1990).

[134] Board, S. J., Hall, R. W. and Hall, R. S., "Detonation of Fuel Coolant Explosions," *Nature*, Vol. **254**, pp 319~321, (1975).

[135] Shamoun, B. I. and Corradini, M. L., "Analysis of Supercritical Vapor Explosion Using Thermal Detonation Wave Theory," *submitted to 7th International Meeting on Nuclear Reactor Thermal-Hydraulics*, Saratoga, Spring, NY, USA, September 10~15, (1995).

[136] Carey, V. P., Liquid-Vapor Phase-Change Phenomena, Hemisphere Publishing Corporation, Washington, USA, (1992).

Appendix A

Experimental Data for the Debris

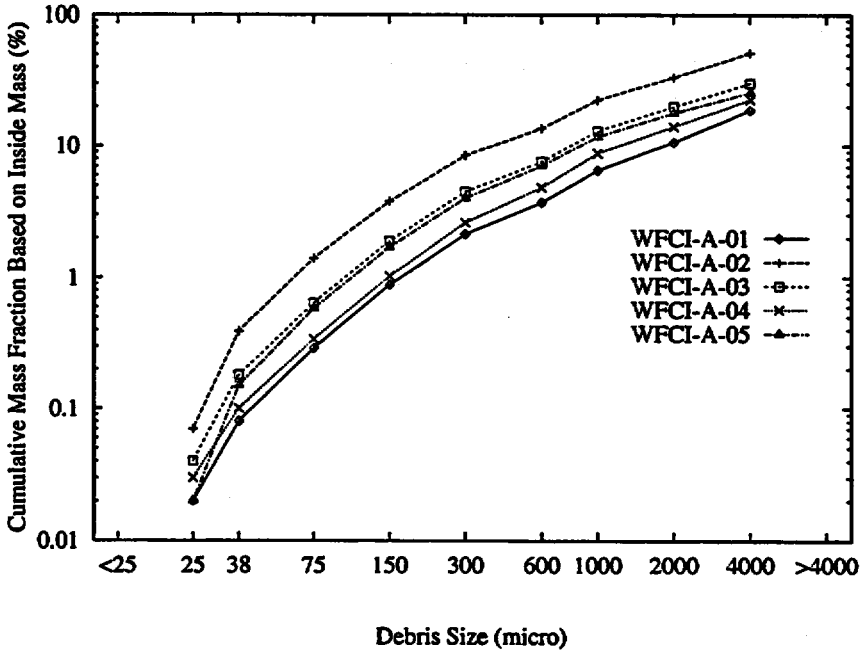

Figure A.1: Cumulative Debris Distribution for the WFCI-A Series

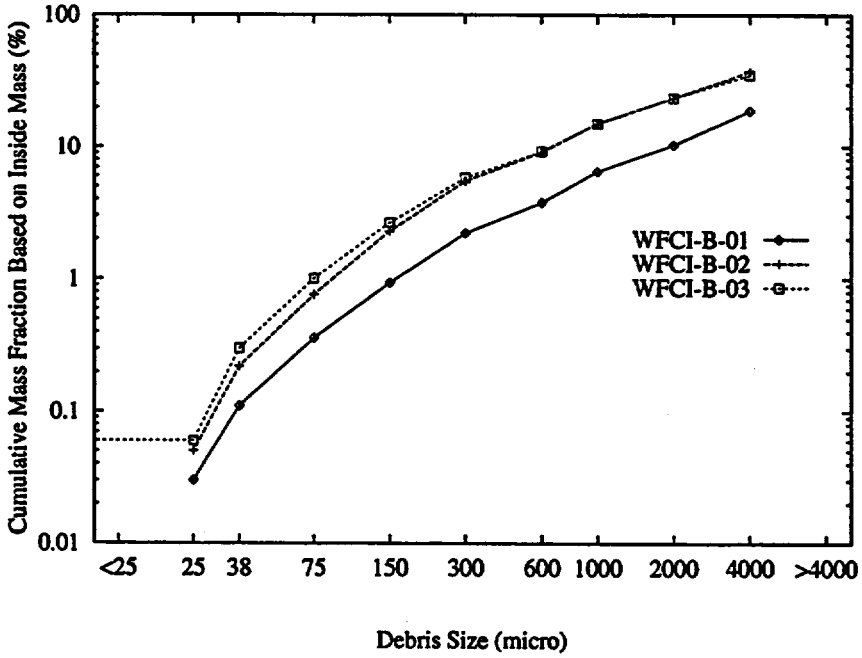

Figure A.2: Cumulative Debris Distribution for the WFCI-B Series

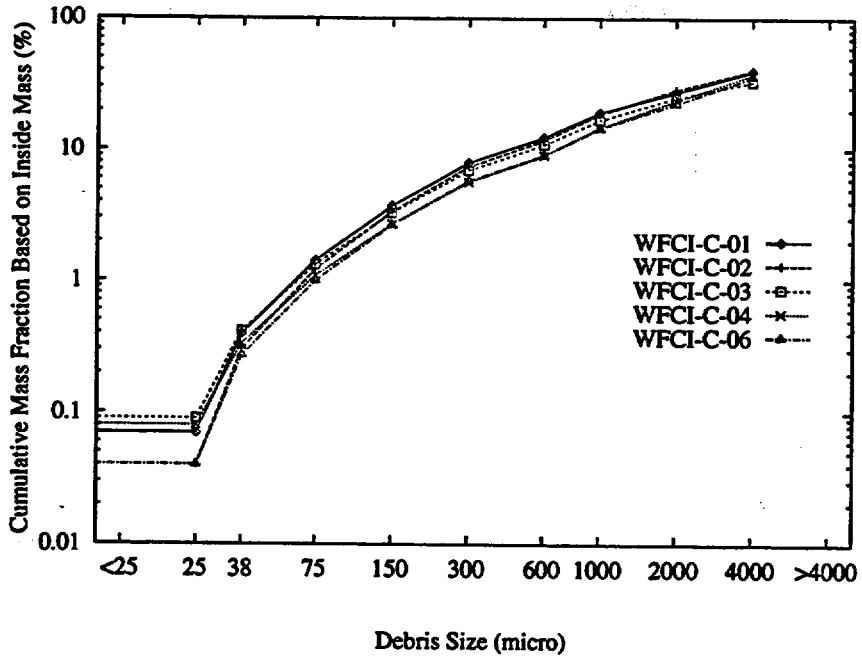

Figure A.3: Cumulative Debris Distribution for the WFCI-C Series

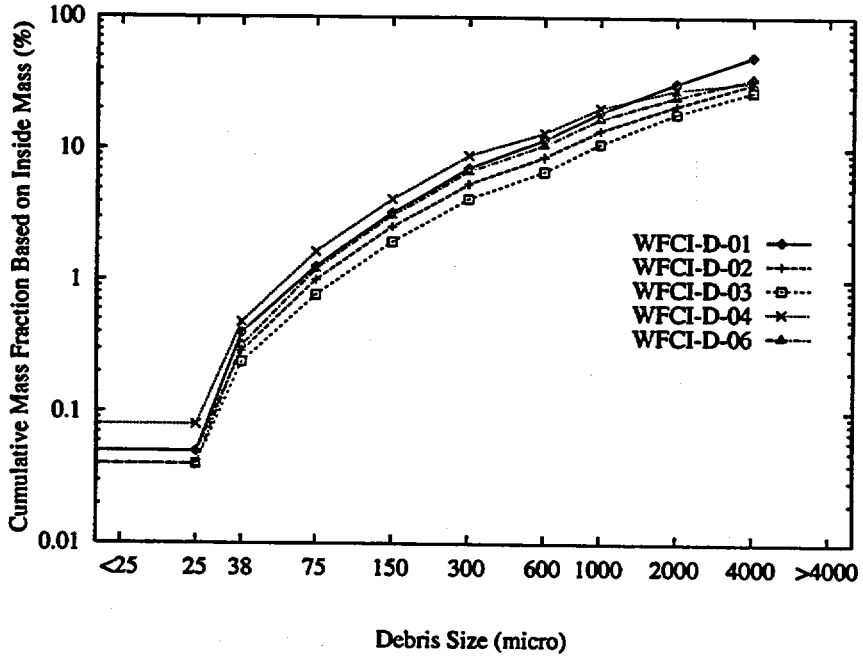

Figure A.4: Cumulative Debris Distribution for the WFCI-D Series

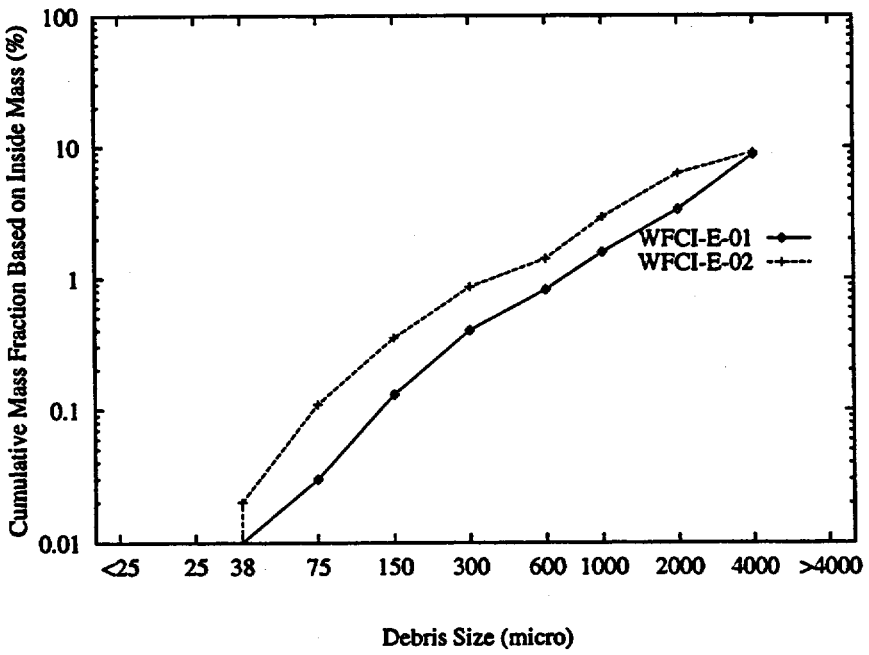

Figure A.5: Cumulative Debris Distribution for the WFCI-E Series

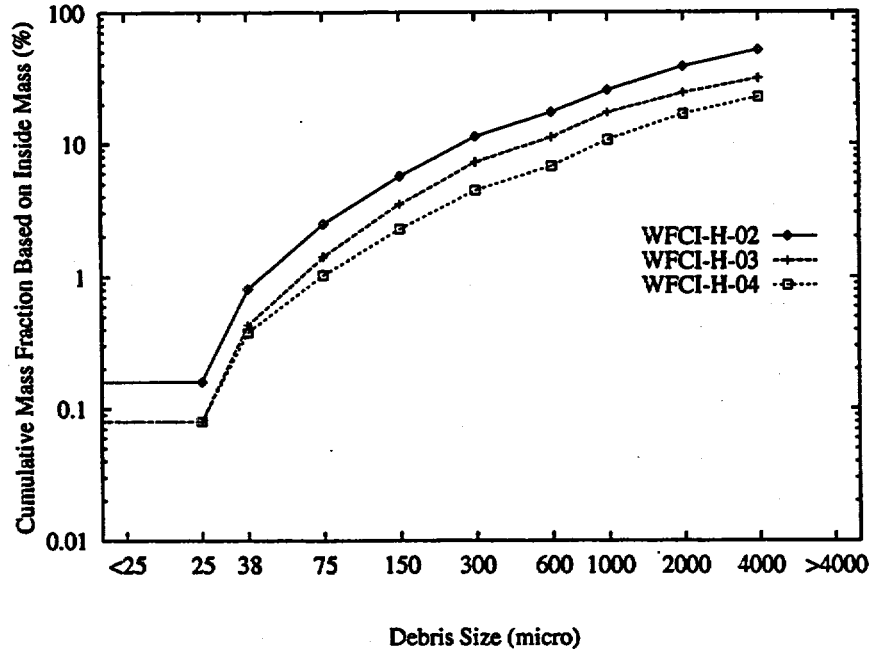

Figure A.6: Cumulative Debris Distribution for the WFCI-H Series

Appendix B

Melt Preparation and Delivery

Introduction

A key part of the WFCI series K experiments is the delivery of about a kilogram of molten iron oxide to a test section filled with water. This is accomplished with a specially designed furnace mounted directly above the test section. The furnace is constructed of several concentric cylindrical layers of insulation made of alumina (Al_2O_3) and silicon dioxide (SiO_2) to create a 6 inch thick layer on all sides. The inner cavity is approximately 13 inches tall and 12 inches in diameter, and is heated to over 1700 EC with eight radiative heating elements. Placed in the center of this cavity is a cylindrical crucible made of boron nitride (BN). This material was chosen because it seemed to resist erosion by molten iron oxide better than other materials tested, was reasonably affordable (when compared to platinum or iridium), and was easily machinable. The melt is delivered through a hole in the bottom of the crucible that is plugged from above by a pneumatically actuated plunger (also made of BN). The crucible used in experiment K-01 was 5 inches in diameter with 0.5 inch thick walls. A second crucible (used in experiment K-02) was larger with a 6 inch diameter. The walls in this second crucible were designed to extend the crucible lifetime by being much thicker in the regions that would be in contact with the molten fuel. This crucible was used for six experiments before it was replaced with a new one. The bottom portion of the crucible (where the greatest amount of erosion occurred) was cut away and replaced.

After tests K-01 and K-02, significant damage to the bottom of the furnace chamber was discovered. During test K-01, the smaller (5 inch) crucible cracked open, and much of the molten iron oxide leaked out onto the insulation, which caused serious damage to three upper layers. In test K-02, the melt bubbled over the top of the crucible, and again did serious damage to the furnace. A detailed chemical analysis was performed on the residues with the hope of understanding what caused the melt to bubble or foam over in test K-02 so furnace damage will be limited in future tests. Another reason was to give a quantitative measure of the amount of boron removed from the crucible after each melt, which could aid increasing the life of the crucible and preventing a failure (such as in test K-01) which could cause severe furnace damage.

Samples were taken from three different locations in both tests. Since the greatest amount of residue was a very hard rocky substance of heterogenous composition located on the floor of the furnace, samples were taken there (designated K1F and K2F). The samples taken were removed from the top layer, and were expected to contain iron from the melt leakage, aluminum and silicon from the furnace insulation, and possibly some boron from the crucible. Samples of the small gray colored pieces that remained inside the crucible were taken as well (designated K1C and K2C). These would be expected to contain only iron and boron. The third set of samples came from the melt that was dropped into the test section (designated K1T and K2T). These samples also would be expected to contain only iron and boron.

Several different types of chemical analyses were performed on these samples. A quantitative analysis of iron and boron composition using inductively coupled plasma - atomic emission spectroscopy (ICP-AES) was performed on all six samples at the UW Chemistry Department. In addition, an X-ray powder diffraction analysis was done at the UW Chemistry

Department on sample K2F to look for particular iron and boron compounds. Finally, an electron microprobe analysis and scanning electron microscope imaging was performed on the upper surface of sample K2F at the UW Geology Department to determine the structure and to also give a quantitative compositional analysis of the different regions of the heterogenous furnace residue.

Atomic Emission Spectroscopy Analysis

Atomic emission spectroscopy is a method used to determine amounts of specific elements in a sample by resolving the intensity of the light emitted at certain wavelengths when an element is burned. A diffraction grating in combination with a phototube detector is used for this purpose. The diffraction grating is rotated to scan a region of wavelengths that corresponds to the values of known emission peaks for a particular element. The amplitude of the peaks correspond to the intensity of the emitted light, which is proportional to the amount of the element present in the sample. To determine the quantitative amount of the element in the sample, a standard solution with a known amount of the element must be analyzed at several different concentrations. This allows the generation of a relation between concentration and light intensity, which is used to determine the concentration of the element in the unknown samples.

An ICP-AES analysis requires that the sample be in liquid form for injection into the plasma generated inside the instrument. This proved to be difficult, since the samples were composed mostly of ceramic materials that do not dissolve easily. The method chosen for the sample preparation was a hydrofluoric acid (HF) fusion. First the samples were powdered for easier dissolution, then they were placed in a platinum crucible with hydrofluoric acid and heated until no visible residue remained. The liquid was then diluted with water. Sodium tetraborate

($Na_2B_4O_7X10H_2O$) was used as the standard solution for the boron analysis since boron nitride would not dissolve in a HF fusion. Pure hematite (Fe_2O_3) was used as the standard in the iron analysis. Boron only had a single resolvable peak while iron had five, therefore the iron data was in the form of a range of values, since each peak gives a slightly different result.

X-Ray Powder Diffraction Analysis

This method of analysis simply involves scattering x-rays off the sample and measuring the corresponding scattering angle and peak intensity at that angle. This resolves molecules instead of atoms, and is not quantitative. It can be used as a fingerprint to indicate the presence of a particular compound in an unknown sample. A large database of diffraction data is available for almost every compound known, but cross referencing is not available, so knowledge of what compounds might be in the sample is necessary. In this case, some of the compounds found to be present in a powdered sample of K2F were Fe_2O_3, Fe_3O_4, Al_2O_3, SiO_2, B_2O_3, and $AlFeO_3$.

Electron Microprobe Analysis

A scanning electron microscope can produce very detailed images by scanning a surface and bombarding it with electrons. If the backscattered electrons are evaluated, a detailed image results. If the corresponding x-rays are analyzed, some indication of the composition of the area given which can also used to measure the quantitative elemental composition of a sample at a particular point. The regions scanned are on the order of microns in size, so to get a representation of the entire sample, a combination of both of the above methods must be used. The K2F sample to be analyzed was first mounted in a resin and polished smooth. Then an image close to the upper surface of the sample was taken. Four distinct compositions in this area were observed. Then the instrument was set to search for iron, silicon, and boron over the same

area. Boron is an element that is not able to be evaluated quantitatively, so all other elements known to be present were measured, and whatever remained was assumed to be boron. Further quantitative analyses of each composition were then done

Conclusions

These analyses have given some insight into the chemical interactions that occur inside the furnace upon heating. These interactions are responsible for eroding the crucible to a point where is cracks open (K-01) as well as causing the melt to bubble over the top of the crucible and leak onto the furnace floor (K-02). They will be addressed individually.

The erosion of the boron nitride is an unavoidable consequence of heating iron oxide in air at such a high temperature. The ICP-AES results show that between 14 and 22% of the material dropped into the test section is boron. This is supported by the fact that residues inside the crucible are between 14 and 21% boron (ICP-AES) and residues on the furnace floor are 10 to 30% boron (SEM). This means that for every kilogram of melt, approximately 200 grams of boron, or 460 grams of BN could be lost. From earlier observation of the smaller crucible, approximately 1/8 inch of the wall was eroded each time in the region of the molten liquid. This is a significant amount, which motivated the design of the second crucible to have thicker walls.

It is not completely understood why the iron oxide bubbled over the top of the crucible in test K-02. It is highly unlikely that the melt reached boiling temperatures, but it is known that gases are given off as the iron oxide is heated. Fe_2O_3 is the equilibrium state between iron and oxygen at normal temperatures and pressures, but at over 1650 EC, the equilibrium state shifts and oxygen will be given off. This off-gassing might be responsible for the melt bubbling out. This hypothesis is supported by the fact that the x-ray diffraction found evidence of Fe_3O_4 in the

furnace residue. Another explanation would be that any oxygen given off will form B_2O_3 with the crucible material, and nitrogen gas will be given off, which again could cause bubbling. This hypothesis is supported by the fact that B_2O_3 was also found in the furnace floor residue. In either case, little can be done to prevent the interaction. The possibility of using magnetite (Fe_3O_4) instead of hematite as a fuel was considered since it was thought that choosing a fuel that was closer to the stoichiometrically stable state at 1700 EC would limit oxygen generation. This was rejected after small scale tests showed no improvement. It is possible that the magnetite becomes hematite during heating, which would then lead to no reduction on oxygen production once melting occurred. The other possibility is that the primary reason for the foaming of the fuel is the nitrogen off-gassing.

It was decided that the only way to prevent serious furnace damage was to attempt to prevent the molten fuel from contacting the furnace floor. A 1" thick boron nitride plate (Carborundum, Grade A) was placed underneath the crucible to catch any iron oxide that bubbled over the top. In addition, for the last few tests, and expendable alumina ring was placed on top of the plate as a type of wall that would slow the melt even more. These improvements only marginally helped, and damage to the furnace was almost always inevitable.

NRC FORM 335 (2-89) NRCM 1102, 3201, 3202

U.S. NUCLEAR REGULATORY COMMISSION

BIBLIOGRAPHIC DATA SHEET

(See instructions on the reverse)

1. REPORT NUMBER (Assigned by NRC, Add Vol., Supp., Rev., and Addendum Numbers, if any.)

NUREG/CR-6623

2. TITLE AND SUBTITLE

Vapor Explosions in a One-Dimensional Large Scale Geometry with Simulant Melts

3. DATE REPORT PUBLISHED

MONTH	YEAR
October	1999

4. FIN OR GRANT NUMBER

W6183

5. AUTHOR(S)

H.S. Park, R. Chapman, and M.L. Corradini

6. TYPE OF REPORT

Technical

7. PERIOD COVERED *(Inclusive Dates)*

April 1994 to September 1999

8. PERFORMING ORGANIZATION - NAME AND ADDRESS *(If NRC, provide Division, Office or Region, U.S. Nuclear Regulatory Commission, and mailing address; if contractor, provide name and mailing address.)*

Nuclear Safety Research Center
University of Wisconsin - Madison
Madison, Wisconsin 53706

9. SPONSORING ORGANIZATION - NAME AND ADDRESS *(If NRC, type "Same as above"; if contractor, provide NRC Division, Office or Region, U.S. Nuclear Regulatory Commission, and mailing address.)*

Division of Systems Analysis and Regulatory Effectiveness
Office of Nuclear Regulatory Research
U.S. Nuclear Regulatory Commission
Washington, D.C 20555-0001

10. SUPPLEMENTARY NOTES

S. Basu, NRC Project Manager

11. ABSTRACT *(200 words or less)*

In light water reactors after a prolonged lack of cooling, vapor explosions could occur when molten fuel is generated and contacts residual water coolant within the reactor vessel or below in the containment reactor cavity. The objectives for this work were to obtain well-characterized experimental data for the explosion propagation/escalation phases using different melt simulants and to investigate the effects of a comprehensive set of initial and boundary conditions on the explosion energetics; i.e., trigger strength, fuel mass, composition and temperature, coolant mass, viscosity and temperature, and system constraint.

This experimental work has yielded a number of results that have potentially important safety implications. First, it has provided evidence of the reproducibility of vapor explosion energetics for a controlled set of initial and boundary conditions. Second, the experiments have demonstrated that if geometric scaling is properly specified, it is possible to extrapolate the results of laboratory scale experiments to reactor scale predictions. Finally and most importantly, the experimental data suggests that once the fuel-coolant initial conditions are within an envelope for triggered events, the energetics is much less than thermodynamic limit, apparently due to the small amount of fuel that participates in the explosion time scale. This envelope of triggerability is much smaller for a simulant molten oxide with low superheat, such as molten iron-oxide in the tests described in the report and corium in the KROTOS tests.

12. KEY WORDS/DESCRIPTORS *(List words or phrases that will assist researchers in locating the report.)*

fuel-coolant interactions (FCI), steam explosions, vapor explosions, simulant melts, molten tin, molten iron oxide, corium, zirconium-containing melt, chemical augmentation, explosion propagation/escalation, explosion energetics, explosivity, thermodynamic limit, triggering envelope, initial and boundary conditions trigger strength, fuel mass and composition, superheat, subcooling, viscosity, system constraint, severe accident, nuclear reactor safety

13. AVAILABILITY STATEMENT

unlimited

14. SECURITY CLASSIFICATION

(This Page) unclassified

(This Report) unclassified

15. NUMBER OF PAGES

16. PRICE

Federal Recycling Program